

# **Bose-Einstein Condensation of Molecules**

**Dissertation**

zur Erlangung des Doktorgrades an der  
naturwissenschaftlichen Fakultät  
der Leopold-Franzens-Universität Innsbruck

vorgelegt von

**Selim Jochim**

durchgeführt am Institut für Experimentalphysik  
unter der Leitung von  
Univ.-Prof. Dr. Rudolf Grimm

2004



## Zusammenfassung

Im Rahmen dieser Arbeit wurde ein Bose-Einstein-Kondensat (BEC) aus Molekülen realisiert. Ausgangspunkt waren optisch gefangene, ultrakalte fermionische  ${}^6\text{Li}$ -Atome, deren Wechselwirkung untersucht wurde. Durch gezielte Manipulation der Wechselwirkung mithilfe einer Feshbach-Resonanz konnten die fermionischen Atome zu bosonischen  ${}^6\text{Li}_2$ -Molekülen gepaart werden, die durch evaporatives Kühlen kondensiert wurden.

Um eine große Anzahl von  ${}^6\text{Li}$ -Atomen aus einer magneto-optischen Falle zu laden, wurde eine neuartige optische Dipolfalle entwickelt, die die resonante Überhöhung in einem optischen Resonator ausnutzt, um mit nur zwei Watt Leistung eines Nd:YAG Lasers eine tiefe Falle mit großem Volumen zu erzielen.

Eine breite Feshbach-Resonanz für eine Mischung der zwei niedrigsten Spinzustände des  ${}^6\text{Li}$ -Grundzustands führt zu resonanter quantenmechanischer Streuung in Magnetfeldern um 800 G. Die elastischen Stößeigenschaften in Magnetfeldern bis 1500 G wurden zunächst durch Evaporationsverluste beobachtet, wobei ein Nulldurchgang der Streulänge bei 530(3) G bestimmt werden konnte, bei dem keine Evaporationsverluste auftraten.

In den nachfolgenden Experimenten gelang es, durch gezielte Abstimmung der Wechselwirkung in der Nähe der Feshbach-Resonanz durch Dreikörper-Rekombination stabile, schwach gebundene  ${}^6\text{Li}_2$ -Moleküle zu bilden. Um diese Moleküle evaporativ zu kühlen wurde eine zweite optische Dipolfalle aufgebaut, die aus einem fokussierten Laserstrahl besteht, dessen Leistung sich von 10.5 W präzise um mehr als vier Größenordnungen reduzieren lässt. Die niedrigen inelastischen und hohen elastischen Stoßraten der Moleküle ermöglichten es, das molekulare Gas zur Bose-Kondensation zu kühlen. Die Existenz des Kondensats konnte durch die Anregung eines kollektiven Schwingungszustands und die Abstimbarkeit der Wechselwirkungsenergie des Kondensats über das Magnetfeld bestätigt werden. Der Phasenübergang zum BEC manifestierte sich in einer bimodalen räumlichen Verteilung in der Falle, die aus einem schmalen, kondensierten Anteil und einer breiteren thermischen Verteilung besteht.

Das molekulare Kondensat, das den Abschluss dieser Arbeit bildet, repräsentiert das stark gekoppelte Extrem des sogenannten BEC-BCS-Übergangs. Weiterführende Experimente konnten zeigen, dass die Stärke der Kopplung durch das Magnetfeld adiabatisch verringert werden kann und der Übergang zu einem schwach wechselwirkenden, hoch entarteten Fermigas möglich ist. Dieses abstimmbare Quantengas ist ein ideales Modell für vielfältige physikalische Systeme wie Neutronensterne, Hochtemperatursupraleiter, und für schwere Kerne.



## Abstract

This thesis reports on the first Bose-Einstein condensation (BEC) of molecules starting from optically trapped fermionic  ${}^6\text{Li}$  atoms. The control of the interaction properties by means of a Feshbach resonance allowed us to pair the fermionic atoms to bosonic  ${}^6\text{Li}_2$  molecules that were Bose condensed by evaporative cooling.

To load a large number of  ${}^6\text{Li}$  atoms from a magneto-optical trap, a novel optical dipole trap was developed that employs the resonant enhancement in an optical resonator to achieve a very large trap depth and trapping volume from moderate two Watts of laser power.

A broad Feshbach resonance for a mixture of the two lowest spin states of the  ${}^6\text{Li}$  ground state leads to resonant quantum mechanical scattering at magnetic fields near 800 G. The elastic collision properties in magnetic fields up to 1500 G were initially observed through evaporative loss of atoms from our dipole trap. In that way we could observe a zero crossing in the scattering length at 530(3) G that manifested itself through the absence of evaporative loss.

In subsequent experiments, the tunability of the interactions in the vicinity of the Feshbach resonance proved to be ideal to form stable weakly bound  ${}^6\text{Li}_2$ -molecules through three-body recombination. The high collisional stability of these molecules together with an expected very large elastic collision rate allowed us to evaporatively cool the molecules into a molecular BEC in a second focused beam optical dipole trap. Two independent manifestations of the presence of the condensate were the excitation of a characteristic collective oscillation mode, and the tunability of the mean field of the condensate using the magnetic field. The phase transition to the BEC was observed by imaging the characteristic bimodal spatial distribution of our cloud that represents a narrow condensed fraction and a broader thermal distribution.

The molecular condensate that was the final achievement of this thesis represents the strong-coupling limit of the so-called BEC-BCS crossover. Subsequent experiments showed that by tuning the magnetic field, the coupling strength can be adiabatically reduced and a crossover to a weakly interacting highly degenerate Fermi gas can be realized. This tunable quantum gas is an ideal model for such diverse systems as neutron stars, high- $T_c$  superconductors, and heavy nuclei.



# Contents

|          |   |           |
|----------|---|-----------|
| <b>1</b> | <b>Introduction</b>   | <b>9</b>  |
| <b>2</b> | <b>Interactions in an ultracold gas</b>                     | <b>11</b> |
| 2.1      | Elastic scattering . . . . .                                | 11        |
| 2.2      | Feshbach resonances and weakly bound molecules . . . . .    | 15        |
| <b>3</b> | <b>Degenerate quantum gases</b>                             | <b>23</b> |
| 3.1      | Bose-Einstein condensation . . . . .                        | 24        |
| 3.1.1    | BEC of an ideal gas . . . . .                               | 24        |
| 3.1.2    | Interacting Bose gas . . . . .                              | 26        |
| 3.1.3    | BEC at finite temperature - bimodal distributions . . . . . | 28        |
| 3.2      | Degenerate Fermi gas . . . . .                              | 30        |
| <b>4</b> | <b>Experimental setup</b>                                   | <b>35</b> |
| 4.1      | Vacuum and atomic beam . . . . .                            | 35        |
| 4.2      | Magneto-optical trap . . . . .                              | 40        |
| 4.3      | Optical dipole traps . . . . .                              | 45        |
| 4.3.1    | Optical resonator . . . . .                                 | 45        |
| 4.3.2    | Focused beam dipole trap . . . . .                          | 50        |
| 4.3.3    | Intensity stabilization . . . . .                           | 54        |
| 4.4      | High-field magnets . . . . .                                | 56        |
| 4.5      | Diagnostic tools . . . . .                                  | 60        |
| 4.5.1    | Fluorescence measurement . . . . .                          | 60        |
| 4.5.2    | Absorption imaging . . . . .                                | 61        |
| 4.5.3    | Microwave and radio frequency transitions . . . . .         | 64        |
| <b>5</b> | <b>Tuning elastic collisions</b>                            | <b>67</b> |
| 5.1      | Elastic collisions . . . . .                                | 68        |
| 5.2      | Experimental procedure . . . . .                            | 69        |

## Contents

|          |  |            |
|----------|--|------------|
| <b>6</b> | <b>Weakly bound molecules near a Feshbach resonance</b>                                      | <b>77</b>  |
| 6.1      | Three-body recombination . . . . .   | 78         |
| 6.2      | Formation and detection of molecules . . . . .   | 82         |
| 6.3      | Stern Gerlach selection of molecules . . . . .   | 88         |
| 6.4      | Molecular Lifetime . . . . .   | 89         |
| <b>7</b> | <b>Bose-Einstein condensation of molecules</b>   | <b>95</b>  |
| 7.1      | Evaporative cooling towards a molecular BEC . . . . .  | 96         |
| 7.2      | First experiments with the Bose-Einstein condensate . . . . .                                | 99         |
| 7.2.1    | Imaging the molecules at high magnetic field . . . . .                                       | 99         |
| 7.2.2    | Bimodal distributions of a BEC with large scattering length .                                | 100        |
| 7.2.3    | Studying a BEC without imaging . . . . .   | 107        |
| <b>8</b> | <b>Outlook</b>   | <b>111</b> |
| <b>A</b> | <b>Lithium properties</b>  | <b>115</b> |
| A.1      | Chemical properties . . . . .  | 115        |
| A.2      | Atomic structure . . . . .   | 116        |
| <b>B</b> | <b>Resonator-enhanced optical dipole trap for fermionic lithium atoms</b>                    | <b>119</b> |
| <b>C</b> | <b>Low-cost mechanical shutter for light beams</b>   | <b>125</b> |
| <b>D</b> | <b>Magnetic Field Control of Elastic Scattering in a Cold Gas of Fermionic Lithium Atoms</b> | <b>131</b> |
| <b>E</b> | <b>Pure Gas of Optically Trapped Molecules Created from Fermionic Atoms</b>                  | <b>137</b> |
| <b>F</b> | <b>Bose-Einstein Condensation of Molecules</b>   | <b>143</b> |
| <b>G</b> | <b>Crossover from a Molecular Bose-Einstein Condensate to a Degenerate Fermi Gas</b>         | <b>149</b> |
| <b>H</b> | <b>Collective Excitations of a Degenerate Gas at the BEC-BCS Crossover</b>                   | <b>155</b> |
| <b>I</b> | <b>Observation of the Pairing Gap in a Strongly Interacting Fermi Gas</b>                    | <b>161</b> |
|          | <b>References</b>  | <b>167</b> |



# Chapter 1

## Introduction

Nature divides all particles into two distinct categories depending on their intrinsic angular momentum, the spin. Depending on whether the spin is half-integer or integer, particles are called fermions or bosons. Their distinct properties become apparent when identical particles get so close to each other that they can no longer be distinguished because their wave packets overlap. Fermions then tend to repel each other, while bosons “socialize” and tend to accumulate in the same state. For this reason, bosons confined in a trap at very low temperatures undergo a phase transition where all particles condense into a single, macroscopic matter wave, a Bose-Einstein condensate (BEC). BEC is a purely statistical phenomenon where no interaction is required for the phase transition to occur.

The first Bose-Einstein condensates of bosonic atoms could be produced in 1995 [And95, Bra95, Dav95] and their study proved to be extremely exciting in the following years. While studying their Bose-Einstein condensates, physicists were impressed again and again of how fundamental ideas of the early days of quantum mechanics could be realized and proven to be true in experiments. Among some of the greatest achievements were the observation of macroscopic matter wave interference [And97], the creation of vortices [AS01], dark [Den00, Bur99] and bright [Kha02, Str02] solitons. The observation of the Mott insulator transition [Gre02] was particularly exciting as it opened new avenues for research and applications.

Trapped Fermi gases at ultralow temperatures behave fundamentally different from Bose gases. Without any interaction present, fermions simply fill up the lowest quantum states of the trap one by one up to the Fermi energy, forming a degenerate Fermi gas. For a phase transition to a superfluid state, an attractive interaction is required that leads to the formation of pairs which then behave like bosons because of their integer total angular momentum and Bose condense. Bardeen, Cooper and Schrieffer (BCS) were able to explain superconductivity by the formation of pairs of electrons, so-called Cooper pairs that form a superfluid [Bar57]. At ultralow energies identical fermions do not interact (see chapter 2.1). Therefore it is generally required that a mixture of

## 1 Introduction

particles be present to form pairs, which is in most cases a mixture of two spin states of the same particle.

The interactions are of crucial importance in a Fermi gas. For weak interactions, the critical temperature depends exponentially on the interaction strength, and if it is made strong enough to support a two-body bound state, bosonic molecules are formed that can form a BEC. In fact a Bose-Einstein condensate of bosonic atoms is nothing else than a BEC of tightly bound pairs of fermionic ions and electrons. The most interesting regime is the crossover regime between the BCS-type gas of weakly interacting fermions and the BEC of molecules. There exist many physical systems that are in this regime, for example high- $T_c$  superconductors and neutron stars. However, it is very difficult to study most of these systems experimentally as very few parameters can be varied. With ultracold atomic Fermi gases, the interactions can be tuned widely through so-called Feshbach resonances, near which the scattering properties can be tuned by varying an external magnetic field. For the first time a physical system is available that allows a systematic study of the properties of the BEC-BCS crossover.

During the past years, researchers working towards atomic Fermi gases concentrated mainly on  $^6\text{Li}$  and  $^{40}\text{K}$ , as they can be cooled and trapped by established laser cooling techniques. Both atoms feature a Feshbach resonance in a stable spin mixture that can be trapped in an optical trap. The spin mixture of interest in  $^6\text{Li}$  has its Feshbach resonance at 834 G and is more than 100 G wide, while the Feshbach resonance in  $^{40}\text{K}$  is at 201 G and is only a few Gauss wide. For lithium, which we chose for our experiments, there is the challenge to produce the large fields required to access the resonance.

This thesis is structured in the following way. In chapters 2 and 3 the main physical concepts of interactions in ultracold gases and of BEC and degenerate Fermi gases are presented. These two chapters are meant as a summary of the well-known ideas, and references are given for a more detailed description of the topics. Chapter 4 describes the experimental setup with a strong emphasis on those parts that were set up during this thesis and that have not been described elsewhere. The following chapters describe the experimental results that were obtained during this thesis. The magnetic-field tunability of the interactions in our lithium spin mixture is described in chapter 5, the major result being the determination of a zero crossing of the scattering length at 530 G. In subsequent experiments we exploited the tunability of the interactions to produce a molecular gas of  $^6\text{Li}_2$  (chapter 6). The major achievement of this thesis is then presented in chapter 7, where evaporative cooling of our molecules to a Bose-Einstein condensate is described. The Bose-Einstein condensation of molecules has paved the way for new exciting experiments with strongly interacting Fermi gases. In chapter 8 I summarized the major achievements of our experiment since I started writing this thesis and some ideas for future experiments.

# Chapter 2

## Interactions in an ultracold gas

The control over the interaction properties of ultracold particles plays an important role in every stage of our experiment. A so-called Feshbach resonance gives us the ability to tune collisions over a broad range. While the atoms are evaporatively cooled in the optical dipole trap, we would like the elastic collision cross section to be as large as possible to accelerate thermalization. At the same time, inelastic collisions leading to loss from the trap have to be minimized to achieve a high evaporation efficiency. Moreover, the possibility to resonantly tune the interactions is used to produce weakly bound dimers with tunable binding energy that are eventually cooled into a Bose-Einstein condensate (BEC) of molecules formed from fermionic atoms. It is the unique tunability of its interactions which make this BEC a very special one. By tuning the binding energy, the Bose-condensed cloud of bosonic molecules can be continuously transformed into a highly degenerate cloud of fermionic atoms.

This chapter summarizes the basic concepts of ultracold scattering. An elementary introduction to low energy scattering theory can be found for example in [Sak94]. An excellent introduction to collisions in ultracold atomic gases is given by [Dal99b]. A quite comprehensive review of cold collisions in both experiments and theory is given in [Wei99], but being published in 1999, the developments of the last five years are not covered. More recent treatments can be found in [Chi01, Bur02].

### 2.1 Elastic scattering

We are interested in the scattering process of two particles with energy  $E_k = \hbar^2 k^2 / (2m_r)$  in a potential  $V(\mathbf{r})$  with the relative coordinate  $\mathbf{r}$ , where  $m_r = m/2$  is the reduced mass of the particles. We therefore look for a solution of the Schrödinger equation

$$\left( \frac{\mathbf{p}^2}{2m_r} + V(\mathbf{r}) \right) \psi_k(\mathbf{r}) = E_k \psi_k(\mathbf{r}). \quad (2.1)$$

## 2 Interactions in an ultracold gas

For a spherically symmetric potential, the asymptotic form of the solution can be written in the form

$$\psi_k(\mathbf{r}) \sim e^{ik \cdot \mathbf{r}} + f(k, \theta) \frac{e^{ik \cdot \mathbf{r}}}{r}. \quad (2.2)$$

The first term of this expression is the incoming plane wave, while the second term describes the outgoing wave. All the physics is contained in the scattering amplitude  $f(k, \theta)$ , which depends on the scattering energy through  $k$  and on the scattering angle  $\theta$  between the incoming particle and the observation direction. The total scattering cross section is then obtained by integrating  $f(k, \theta)$  over the solid angle  $\Omega$ ,

$$\sigma(k) = \int_{\Omega} |f(k, \theta)|^2 d\Omega. \quad (2.3)$$

For studying the low-energy collision limit, it is useful to expand the wave function in terms of partial waves  $l = 0, 1, 2, \dots$ , also named  $s, p, d, \dots$ . One can then write down a one-dimensional (1-D) Schrödinger equation for each angular momentum state  $u_{k,l}(r)$ ,

$$\frac{\partial^2 u_{k,l}(r)}{\partial r^2} + \left( k^2 - \frac{2m_r}{\hbar^2} \left( V(r) + \frac{\hbar^2 l(l+1)}{2m_r r^2} \right) \right) u_{k,l}(r) = 0. \quad (2.4)$$

In this 1-D representation the higher partial waves experience an effective potential  $V_{\text{eff}} = V(r) + E_c$  that includes a repulsive centrifugal barrier  $E_c = \hbar^2 l(l+1)/(2m_r r^2)$ . An illustration of this is shown in Fig. 2.1. If the collision energy is much lower than this barrier, particles with angular momentum  $l > 0$  cannot see the potential  $V(r)$ , and thus cannot be scattered\*.

### The zero-energy limit

The different partial waves acquire different phases  $\delta_l$  that determine the scattering process. The total cross sections are given by [Sak94]

$$\sigma_l(k) = \frac{4\pi}{k^2} (2l+1) \sin^2 \delta_l, \quad (2.5)$$

assuming nonidentical particles. One finds [Sak94] that these phases are proportional to

$$\delta_l \propto k^{2l+1}, \quad (2.6)$$

causing the scattering cross section for higher partial waves to drop as  $\sigma_l \propto k^{4l}$ , when  $k$  approaches zero while  $\sigma_0$  becomes independent of the collision energy. The cross section can now be written as

$$\lim_{k \rightarrow 0} \sigma_0(k) = 4\pi a^2, \quad (2.7)$$

---

\*For lithium, this centrifugal barrier is  $\sim k_B \times 7 \text{ mK}$  [Jul92]

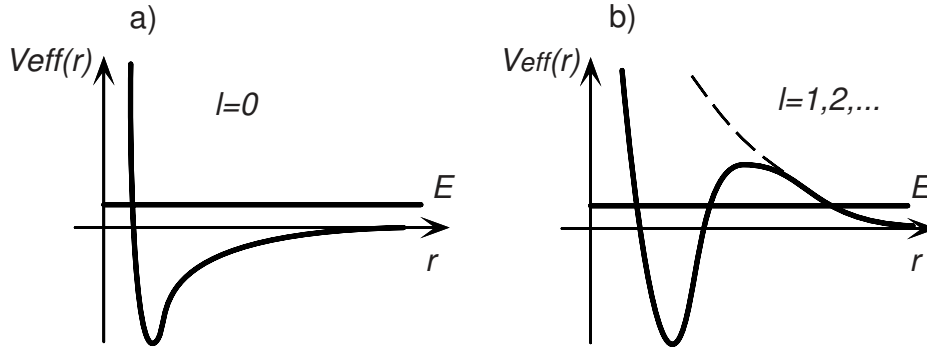


**Figure 2.1:** Schematic of the effective potential of the 1D radial Schrödinger equation. a) Shows the situation for s-wave scattering, in b) the centrifugal barrier  $E_c = \hbar^2 l(l+1)/2m_r r^2$  is added. If the collision energy  $E$  is much lower than this barrier, collisions with  $l > 0$  are suppressed (figure adapted from [Dal99b]).

where the scattering length  $a$  is defined by

$$a = -\lim_{k \rightarrow 0} \frac{\tan \delta_0(k)}{k}. \quad (2.8)$$

In the following, only  $s$ -wave scattering will be considered because all collision energies in the experiments described in this thesis are well below the centrifugal barrier. Typical  $s$ -wave scattering lengths for alkali atoms are on the order of  $10 - 100a_0$ . The exact value of the scattering length is very sensitive to the long-range van der Waals potential [Dal99b], which is described by the  $C_6$ -coefficient as  $V_{\text{vdW}} = C_6/r^6$ . Especially when a bound state lies just below or above the continuum the scattering length is large and positive or large and negative, respectively. A small change in the  $C_6$ -coefficient can then have a very large effect on the scattering length, it can even change from large and positive to large and negative.

### Energy dependence of the cross section

The scattering cross section is given by the zero-energy limit, equation 2.7, as long as  $\sin^2 \delta_0 \ll 1$ . At higher collision energies, the scattering cross section has to be limited, as  $\sin^2 \delta_0$  cannot become larger than unity. Assuming that characteristic radius of interaction  $r_c$  is much smaller than the scattering length and the de Broglie wavelength, which is true for most cases, one can approximate the potential by a point-like so-called contact potential [Dal99b]

$$V_{\text{cp}} = g\delta(r), \quad (2.9)$$

where the coupling constant  $g$  depends on the scattering length  $a$  as

$$g = \frac{4\pi\hbar^2}{m}a. \quad (2.10)$$

## 2 Interactions in an ultracold gas

The phase shift  $\delta_0$  and thus the total cross section can then be calculated as [Dal99b]

$$\sigma(k) = \frac{4\pi a^2}{1 + k^2 a^2}. \quad (2.11)$$

For  $k^2 a^2 \ll 1$ , one recovers the expected zero-energy limit  $\sigma = 4\pi a^2$ , whereas the limit  $k^2 a^2 \gg 1$  yields the so-called unitarity limit  $\sigma_u(k) = 4\pi/k^2$ , which is the maximum possible cross section for s-wave collisions that is obtained when  $\sin^2 \delta_0 = 1$ . This result is not surprising, as  $\sigma_u(k)$  is just about as large as the spread of the wave packet and a larger cross section would have to involve nonzero angular momentum.

### Identical particles

For the above considerations we assumed that the two colliding particles were distinguishable, which is not the case if one considers identical particles. In this case, the two scattering processes shown in Fig. 2.2 cannot be distinguished, and thus the two corresponding scattering amplitudes interfere. This leads to an extinction of the scattering cross section for the symmetric even partial waves in the case of fermions and of the symmetric odd partial waves in the case of bosons, while the remaining cross sections are doubled. An important conclusion of this is that at very low temperatures, identical fermions do not collide and form an ideal gas. The absence of s-wave scattering in an ultracold fermi gas was observed for the first time in  $^{40}\text{K}$  in D. Jin's group at JILA [DeM99a], which enabled them to observe the  $\sigma_p \propto E^2$  threshold law for p-wave collisions.

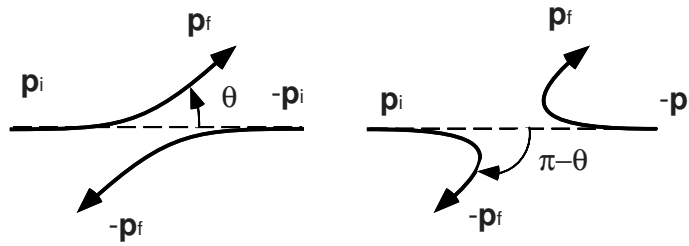


**Figure 2.2:** The two different scattering processes are indistinguishable for identical particles, causing their scattering amplitudes to interfere (adapted from [Dal99b]).

### Mean-field interaction

At high densities and very low thermal energies as for example in a BEC, the collisions lead to an interaction energy that is considerably larger than other energies of the system such as the thermal energy. This interaction energy can be approximated

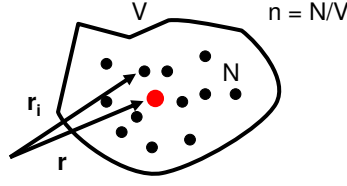


**Figure 2.3:** The red particle experiences a mean field due to the presence of the neighboring particles

by a mean field, even if the interparticle separation is much larger than the range of the potentials. In this case we can again use the approximation that the scattering is due to a point-like potential as in equation 2.9. Then we can easily calculate the mean field that is experienced by an atom immersed in a gas with density  $n$ , as depicted in Fig. 2.3\*:

$$V_{\text{mf}} = \lim_{V \rightarrow 0} \frac{1}{V} \sum_{i=1}^N \int g \delta(\mathbf{r} - \mathbf{r}_i) d\mathbf{r} = gn = \frac{4\pi\hbar^2}{m} a n. \quad (2.12)$$

It should be noted that the approximations used here are only valid in the dilute gas regime, when  $na^3 \ll 1$ .

## 2.2 Feshbach resonances and weakly bound molecules

In the last few years, so-called Feshbach resonances have emerged as a versatile tool to manipulate the scattering properties in ultracold gases [Ino98]. Using an external magnetic field, the scattering length can be tuned to arbitrarily large positive and negative values. This has been exploited already in various experiments. In  $^{85}\text{Rb}$  for example, tuning the scattering length from negative to positive made evaporative cooling to a BEC possible [Cor00] and intriguing dynamics of the condensate could be studied by altering the scattering length in the condensed cloud [Don01, Don02]. With  $^7\text{Li}$  Khaykovich *et al.* [Kha02] and Strecker *et al.* [Str02] were able to create matter wave solitons when they changed the interaction from repulsive to attractive. O'Hara *et al.* [O'H02a] tuned the scattering length of their  $^6\text{Li}$  spin mixture to create the first strongly interacting Fermi gas where the scattering length exceeds the inverse Fermi wave number  $1/k_F$ .

Feshbach resonances opened the way for the study of ultracold molecular gases. Pioneering work was done at JILA where  $^{40}\text{K}_2$  molecules were formed [Reg03]. These findings triggered a race to form Bose-Einstein condensates of molecules [Joc03a,

---

\*Due to the exchange symmetry, this mean field interaction has to be multiplied by a factor of two for identical, noncondensed particles [Gri96].

## 2 Interactions in an ultracold gas

Gre03, Zwi03], which now serve as a starting point to study the strongly interacting regime in ultracold fermionic gases [Bar04c, Reg04, Zwi04, Bar04b, Kin04a, Chi04a].

The concept of Feshbach resonances was first studied in nuclear physics by Herman Feshbach [Fes58]. The main idea of a magnetic-field Feshbach resonance, as they are used in ultracold atom experiments is illustrated in Fig. 2.4 a) [Tie93]. Consider a pair of atoms scattering in their mutual potential, which we call the open channel. For the same pair of atoms in different internal states, the potential can be different and represent so-called closed channels if their continuum lies above the incident scattering energy. When the atoms are scattered in the open channel, they may be coupled to the closed channel for example through hyperfine interactions. But as the continuum of the closed channel lies above the total energy, the atoms have to finally end up in the open channel, leading to a second-order coupling. If now the closed channel has a different magnetic moment than the open channel, the two potentials are tuned against each other by  $\Delta E = \Delta\mu \times B$  by applying an external magnetic field  $B$ . Tuning a bound state in the closed channel into degeneracy with the continuum results in resonant scattering if there is a coupling between the two states. The scattering length can then be written in the form

$$a(B) = a_{\text{bg}} \left( 1 + \frac{\Delta}{B - B_0} \right), \quad (2.13)$$

where  $a_{\text{bg}}$  is the off-resonant background scattering length,  $\Delta$  the width and  $B_0$  the position of the resonance.

The coupling mixes the continuum of the open channel and the bound state in the closed channel to form two new states as shown in Fig. 2.4 b). In analogy to the avoided crossing in a two level system, the resulting molecular state is connected adiabatically to the free-atom continuum, when the closed channel is tuned into the continuum. This means that by adiabatically ramping the magnetic field across the resonance, pairs of atoms can be converted into molecules and vice versa. Such experiments could recently be performed in a number of groups [Reg03, Her03, Dür04, Cub03, Str03, Xu03]. However, there is an important difference to the case of a simple two-level crossing as here, one of the states is a continuum state. This means that a stable molecular state can only exist below the continuum, while the molecular state embedded in the continuum can only be a virtual state.

### Feshbach resonances in $^6\text{Li}$

Between the two lowest hyperfine states  $|1\rangle$  and  $|2\rangle$  of  $^6\text{Li}^*$ , an exceptionally broad Feshbach resonance was first predicted in 1998 by Houbiers *et al.* [Hou98] at  $\sim 850$  G,

---

\*At low magnetic field, these two states correspond to the states  $|F = 1/2; m_F = \pm 1/2\rangle$ , well above 30 G, they are defined as  $|s = 1/2, m_s = -1/2; I = 1, m_I = 1\rangle$  and  $|s = 1/2, m_s = -1/2; I = 1, m_I = 0\rangle$  in the Paschen-Back regime, see A.2



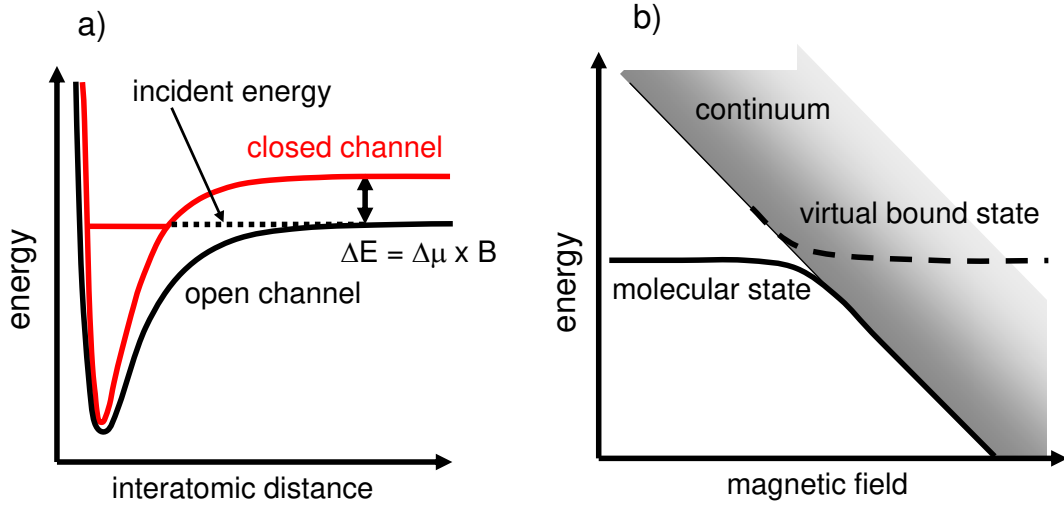


**Figure 2.4:** a) A Feshbach resonance occurs, when a bound state of a closed channel is tuned into degeneracy with the continuum of the open scattering channel using an external magnetic field. b) The coupling of the two channels leads to an avoided crossing, adiabatically connecting the molecular state with the free-atom state.

that modifies the scattering length in a range of several hundred Gauss (Fig. 2.5). Being zero at zero magnetic field, the scattering length first decreases with increasing magnetic field to a local minimum of  $\sim 300a_0$  at  $\sim 325$  G. It then increases again and crosses zero at  $530(3)$  G [Joc02] before diverging on the broad Feshbach resonance near 850 G. Throughout this thesis, I will use the values obtained from a calculation by V. Venturi *et al.* [Ven01] for the scattering length near the Feshbach resonance that was found to be at  $\sim 856$  G. Recent results from our experiment locate the Feshbach resonance at 834 G [Bar04d] and allow a more accurate determination of the scattering length. However, for most experimental results presented in this thesis, the resulting differences in scattering length are not significant. Above the resonance the scattering length then approaches from  $-\infty$  the anomalously large triplet scattering length of  $\sim 2200a_0$  [Abr97] above  $\sim 1500$  G. A second, very narrow resonance was discovered later [Die02, O'H02b, Str03]. It is marked by the vertical line at  $\sim 543$  G and is  $\sim 100$  mG wide.

To understand how these two resonances come about, let us first look at the scattering state. At low magnetic fields, the scattering state is a superposition of the singlet and triplet states due to the hyperfine coupling of the atoms in the Zeeman regime. At high fields  $\gg 30$  G in the Paschen-Back regime, the scattering potential is almost completely determined by the electronic  $m_s = -1/2$  state of the two atoms and consequently, the scattering potential is triplet in nature. The off-resonant background scat-

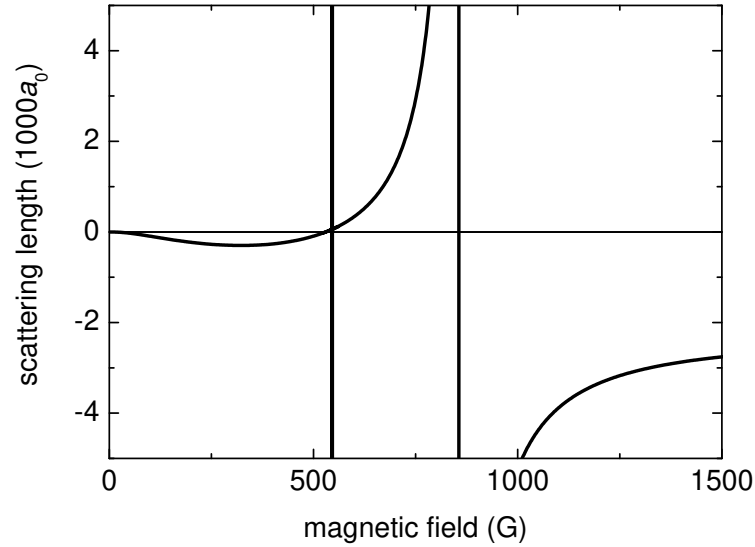


**Figure 2.5:** S-wave scattering length between the two lowest spin states  $|1\rangle$  and  $|2\rangle$  of the  ${}^6\text{Li}$  ground state as a function of the magnetic field. The broad resonance at  $\sim 834$  G tunes the scattering length over a wide range. The vertical line at 543 G marks another, very narrow Feshbach resonance. Beyond 1500 G, the scattering length is well approximated by the near-resonant triplet scattering length of  $\sim 2200a_0$  (The data shown are calculated by V. Venturi *et al.* [Ven01]).

tering length is then determined by the singlet and triplet scattering lengths that have been determined spectroscopically in photoassociation measurements at Rice University to be  $+45a_0$  and  $-2200a_0$ , respectively [Abr97]. This causes the background scattering length to vary smoothly from zero to the large triplet scattering length as the magnetic field is increased. The large triplet scattering length stems from a virtual bound state just above the resonance. Consequently this scattering length is very sensitive to the triplet potential. Less than a  $10^{-3}$  change of the potential depth would cause the scattering length to change sign!

The two Feshbach resonances occur when the highest vibrational state  $\nu = 38$  in the singlet potential coincides with the continuum of the scattering state. This singlet state is split into two hyperfine states that give rise to the two Feshbach resonances. The hyperfine splitting results from the coupling of the two nuclear spins of the atoms. Their unity nuclear spins add to either  $I = 0$  or  $I = 2$ , resulting in total angular momenta  $F = 0, M_F = 0$  and  $F = 2, M_F = 0$ , respectively. In principle, the nuclear spins can also couple to  $I = 1$ , but this state is symmetry forbidden as it is antisymmetric. The antisymmetric singlet electron wave function requires the nuclear spin wave function to be symmetric to result in a totally antisymmetric wave function.

The Zeeman energies of the continuum state and the molecular states are shown in Fig. 2.6. The scattering potential above 500 G is almost perfectly triplet in nature. The

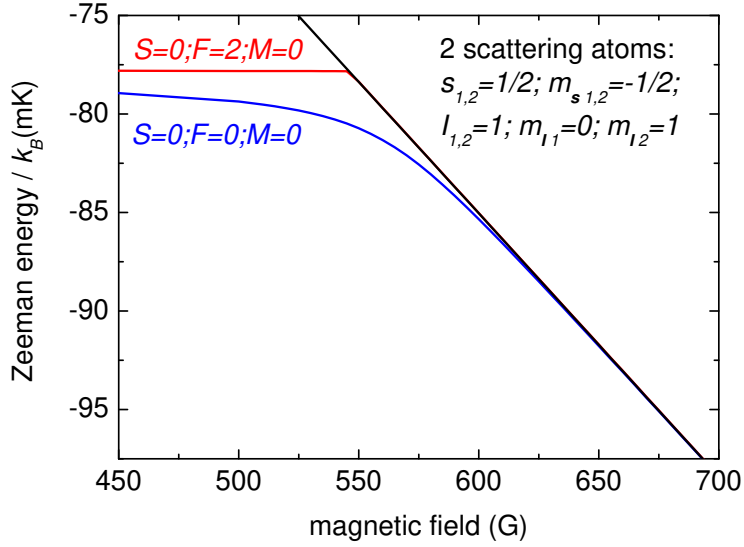


**Figure 2.6:** Zeeman energies of a pair of free  ${}^6\text{Li}$  atoms in the two lowest spin states and the two highest singlet molecular states with vibrational quantum number  $\nu = 38$ . They cross into the continuum above the free atom pair at 543.3 G and at 834 G respectively, where the two Feshbach resonances occur (The data shown represent calculations by V. Venturi *et al.* [Ven01]).

coupling to the triplet state leads to the bending down of the initially purely singlet states, in particular the  $F = 0$  state, causing the actual resonance position associated with that state to occur at 834 G, outside the range of Fig. 2.6.

The large width of the 834-G Feshbach resonance is caused by the large triplet scattering length, as the  $F = 0$  molecular state is adiabatically connected to the virtual triplet state, which is approached asymptotically, slowly crossing the continuum threshold [Mar04].

### Weakly bound molecules

A resonantly large scattering length is always caused by a bound molecular state that is very close to the continuum. The binding energy of this state can be calculated to be [Lan77]

$$E_B = \frac{\hbar^2}{ma^2}. \quad (2.14)$$

This formula is correct as long as the scattering length is much larger than the extent of the van der Waals potential between the atoms. The range of the van der Waals potential is characterized by the effective range, defined as

$$r_{\text{eff}} = \left( \frac{mC_6}{\hbar^2} \right)^{1/4}, \quad (2.15)$$

## 2 Interactions in an ultracold gas

where  $C_6$  determines the van der Waals potential as  $V_{\text{vdW}} = -C_6/r^6$ . For lithium,  $C_6$  has been calculated to be  $C_6 = 1.3340 \times 10^{-76} \text{ Jm}^6$  [Yan96], resulting in an effective range of the potential of  $r_{\text{eff}} = 62.5a_0$ . According to Gribakin and Flambaum [Gri93], the validity of equation 2.14 can be extended to lower values of  $a$  by subtracting a so-called mean scattering length  $\bar{a}$  from  $a$  that is given by

$$\bar{a} = \frac{\Gamma(3/4)}{2\sqrt{2}\Gamma(5/4)}r_{\text{eff}} \approx 0.478r_{\text{eff}} \quad (2.16)$$

which accounts for the finite extent of the scattering potential. For lithium atoms,  $\bar{a}$  is  $\approx 29.9a_0$ . The resulting binding energy is given by [Gri93]

$$E_B = \frac{\hbar^2}{m(a - \bar{a})^2}. \quad (2.17)$$

For the broad Feshbach resonance in the  $^6\text{Li}$  spin mixture, the binding energy calculated using Eq. 2.17 is shown in Fig. 2.7. By changing the magnetic field over a range of  $\sim 200 \text{ G}$ , the binding energy can be tuned continuously by more than two orders of magnitude, from  $E_B < k_B \times 1 \mu\text{K}$  to  $E_B > k_B \times 100 \mu\text{K}$ . Below  $\sim 600 \text{ G}$ , the approximation of Eq. 2.17 starts to fail as the zero crossing in the scattering length at  $530 \text{ G}$  is approached. Above  $800 \text{ G}$ , the uncertainty of the resonance position makes it impossible to obtain a good estimate for the binding energy. The properties of this unique, highly excited molecular state were studied theoretically by D. Petrov [Pet03a, Pet04]. Our experimental study is presented in chapter 6, including the formation, the magnetic moment, and the surprisingly long lifetime of these molecules against decay into lower-lying vibrational states.

## 2.2 Feshbach resonances and weakly bound molecules

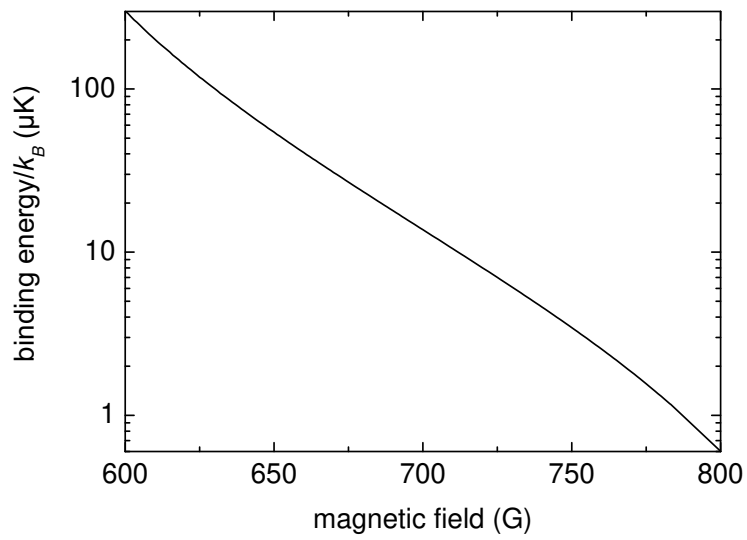


**Figure 2.7:** Binding energy of the weakly bound molecular level below the Feshbach resonance at 830 G, calculated from the scattering length in Fig. 2.5 using equation 2.17.



# Chapter 3

## Degenerate quantum gases

The statistics of a gas is governed by quantum mechanics as soon as the wave packets of the individual particles start to overlap, which means that the phase space density, defined as

$$D = \lambda_{\text{dB}}^3 n, \quad (3.1)$$

approaches unity. In this equation,

$$\lambda_{\text{dB}} = \sqrt{\frac{2\pi\hbar^2}{mk_{\text{B}}T}} \quad (3.2)$$

is the thermal de Broglie wavelength and  $n$  the density of the gas. The quantum mechanical properties are a result of the indistinguishability of identical particles and lead to drastically different behavior depending on whether the particles are bosons or fermions. A qualitative illustration is shown in Fig. 3.1. When a classical gas is cooled down, particles no longer behave like billiard balls, their collisions are governed by quantum mechanics as described in the previous chapter. By further cooling the gas to quantum degeneracy, the strikingly different behavior of bosonic and fermionic gases becomes apparent. While bosons quickly condense into the ground state of the trap, forming a BEC, the fermions slowly start filling up the lowest lying states of the trap with unity occupation, forming a Fermi sea. Experiments in Houston [Tru01] and Paris [Sch01] showed this in a very beautiful way by producing a mixture of a BEC of  $^7\text{Li}$  atoms and a Fermi sea of  $^6\text{Li}$  atoms.

As there is extensive literature available covering degenerate gases, this chapter summarizes only the main findings that are important for this thesis. The textbooks by Pitaevskii and Stringari [Pit03], Pethik and Smith [Pet02] as well as the experimental and theoretical review articles by Ketterle *et al.* [Ket99] and Dalfovo *et al.* [Dal99a] provide an excellent introduction to this field.

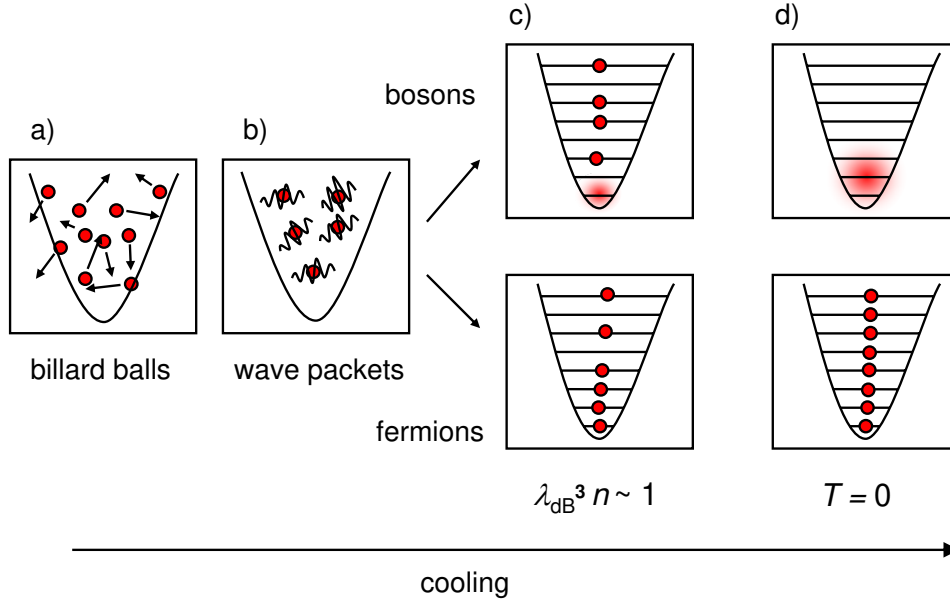


**Figure 3.1:** A gas of identical particles at different temperatures: a) At high temperatures, the particles behave like classical “billiard balls”. b) By lowering the temperature, the wave packet nature of the particles leads to quantum mechanical scattering. c) When  $\lambda_{\text{dB}}^3 n \sim 1$ , bosons start to condense into the ground state of the trap, while fermions avoid each other and start filling up the lowest lying states of the trap. d) At zero temperature, the bosons are fully condensed in a single, macroscopic matter wave, while the fermions form a Fermi sea filling the trap potential up to the Fermi energy.

## 3.1 Bose-Einstein condensation

### 3.1.1 BEC of an ideal gas

For trapped, non-interacting bosons in thermal equilibrium, the mean occupation number for a given quantum state  $r$  is given by the Bose distribution function

$$N_{r,\text{Bose}} = \frac{1}{\exp\left(\frac{\epsilon_r - \mu}{k_B T}\right) - 1}, \quad (3.3)$$

where  $\epsilon_r$  is the energy of the respective state and  $\mu$  is the chemical potential. It is fixed by the constraint that the sum over all states  $r$  must yield the total particle number,  $N = \sum_r N_r$ .

For a specific trap, the chemical potential depends on the particle number and the temperature. At high temperatures, when the mean occupation number of the ground state is much smaller than one, the chemical potential must be much smaller than  $\epsilon_0$  to reflect this low ground state population. But once the temperature is lowered, the



### 3.1 Bose-Einstein condensation

chemical potential has to approach  $\epsilon_0$  to fulfill the normalization condition  $N = \sum_r N_r$ . At this point, the occupation of the ground state becomes non-negligible.

Let us write the number of particles in the form  $N = N_0 + N_T$ , where  $N_T(\mu, T) = \sum_{r=1}^{\infty} N_r$  is the number of excited particles. For a given temperature,  $N_T$  reaches its maximum when  $\mu \rightarrow \epsilon_0$ . Thus, the maximum number of excited particles is

$$N_{T,\max} = \sum_{r=1}^{\infty} \frac{1}{\exp\left(\frac{\epsilon_r - \epsilon_0}{k_B T}\right) - 1}. \quad (3.4)$$

Once this number drops below the total number  $N$ , a macroscopic number of particles has to be in the  $N_0$  ground state. The temperature for this to occur is the critical temperature  $T_c$  for Bose-Einstein condensation. Note that for a large number of particles,  $k_B T_c$  is in most cases much larger than the energy level spacing and the ground state energy  $\epsilon_0$ , which also defines the chemical potential. We therefore assume the chemical potential to be zero in the following discussion. In a harmonic trap with trap frequency  $\omega$ , we can now write equation 3.4 in an integral form using the known density of states  $g(\epsilon) = \epsilon^2/(2\hbar^3 \omega^3)$ . The maximum number of thermal atoms then becomes

$$N_{T,\max} = \int_0^{\infty} \frac{\epsilon^2}{2\hbar^3 \omega^3 \left(\exp\left(\frac{\epsilon}{k_B T}\right) - 1\right)} d\epsilon. \quad (3.5)$$

Solving the integral and setting  $N_T = N$  yields

$$T_c = \frac{\hbar\omega}{k_B} \left(\frac{N}{\zeta(3)}\right)^{1/3} \approx 4.5 \left(\frac{\omega/2\pi}{100\text{Hz}}\right) N^{1/3} \text{ nK}, \quad (3.6)$$

where  $\zeta(3) \approx 1.202$  is Riemann's Zeta function,  $\zeta(x) = \sum_{k=1}^{\infty} k^{-x}$ . The peak phase space density for a classical gas in a harmonic trap is

$$D(T) = N \left(\frac{\hbar\omega}{k_B T}\right)^3. \quad (3.7)$$

If we calculate  $D$  at  $T_c$  we get

$$D(T_c) = N \left(\frac{\hbar\omega}{k_B T_c}\right)^3 = \zeta(3) \approx 1.202. \quad (3.8)$$

This means that Bose-Einstein condensation occurs when the mean occupation number in the center of the trap becomes larger than one.

The fraction of condensed atoms  $N_0/N = (N - N_T)/N$  is also readily calculated using equation 3.5, the result is

$$\frac{N_0}{N} = 1 - \left(\frac{T}{T_c}\right)^3 \quad (3.9)$$

### The wave function of an ideal gas BEC

For an ideal gas with no interactions, we have the very simple Hamiltonian  $H = -\hbar^2/2m \nabla^2 + U(\mathbf{r})$ . The wave function of a pure BEC is the same as for a single particle in the ground state, which is

$$\Phi(\mathbf{r}) = \sqrt{N} \left( \frac{1}{\sqrt{\pi} a_{\text{ho}}} \right)^{3/2} \exp\left(-\frac{\mathbf{r}^2}{2a_{\text{ho}}^2}\right), \quad (3.10)$$

where  $a_{\text{ho}} = \sqrt{\hbar/(m\omega)}$  is the harmonic oscillator length. The density distribution is simply given by the square of the wave function,  $n(\mathbf{r}) = \Phi^2(\mathbf{r})$ .

### 3.1.2 Interacting Bose gas

The density of a non-interacting BEC increases linearly with the atom number as can be seen from equation 3.10. With increasing density, even a very weak interaction must become important. Let us calculate the ratio between kinetic energy  $E_{\text{kin}}$  and interaction energy  $E_{\text{int}}$ , for simplicity omitting factors of order unity. While the kinetic energy per particle stays constant at  $\sim \hbar\omega$ , the interaction energy per particle increases as  $g \times \bar{n}$  (see Eq. 2.12), the mean density  $\bar{n}$  being of order  $1/a_{\text{ho}}^3$ . One can then estimate to zeroth order the ratio of the interaction and kinetic energies to be [Dal99a]

$$\frac{E_{\text{int}}}{E_{\text{kin}}} \sim \frac{N a}{a_{\text{ho}}}. \quad (3.11)$$

For our  $^6\text{Li}_2$  molecules  $a_{\text{ho}} \approx 3 \mu\text{m}$  for a trap with a typical vibration frequency of  $\sim 100$  Hz, whereas the scattering length is on the order of  $\sim 100$  nm. This means that for a typical number of particles, the interaction energy will be much higher than the kinetic energy. Therefore in most cases Eq. 3.10 will not be a good approximation to the wave function.

In most BECs, a repulsive mean field  $V_{\text{mf}}$  (Eq. 2.12), as a result of a positive scattering length, limits the density of the BEC, which is crucial for its stability. A negative mean-field energy resulting from a negative scattering length leads to a strong increase in density. Consequently, the BEC collapses above a certain atom number, when the zero-point energy can no longer balance the attractive mean field interaction. Important studies on the collapse of a gas with negative scattering length have been done with  $^7\text{Li}$  in Randy Hulet's group [Bra97, Ger00]. For this thesis, only the case of positive scattering length is of relevance, and in the following, the discussion will be limited to that case.

### The Gross-Pitaevskii equation

Introducing a mean-field interaction into the Hamiltonian we can write down a Schrödinger equation for an interacting BEC,

$$i\hbar \frac{\partial}{\partial t} \Phi(\mathbf{r}, t) = \left( -\frac{\hbar^2}{2m} \nabla^2 + U(\mathbf{r}) + g|\Phi(\mathbf{r}, t)|^2 \right) \Phi(\mathbf{r}, t), \quad (3.12)$$

which is called the Gross-Pitaevskii equation [Gro61, Pit61]. It is important to note that the description of the interaction as a mean field, as it is done in the Gross-Pitaevskii equation is only valid for a dilute gas, where  $na^3 \ll 1$ . For a time independent representation, one can write  $\Phi(\mathbf{r}, t) = \phi(\mathbf{r}) \exp(-i\mu t/\hbar)$ , resulting in

$$\mu \phi(\mathbf{r}) = \left( -\frac{\hbar^2}{2m} \nabla^2 + U(\mathbf{r}) + g\phi^2(\mathbf{r}) \right) \phi(\mathbf{r}). \quad (3.13)$$

$\phi(\mathbf{r})$  is now a real function,  $\phi^2(\mathbf{r}) = n(\mathbf{r})$  representing the density with the constraint that  $\int d\mathbf{r} \phi(\mathbf{r}) = N$ .

### The Thomas-Fermi approximation

The nonlinear Gross-Pitaevskii equation is in general very hard to solve analytically. But we have seen previously that for most cases the kinetic energy is completely negligible as compared to the interaction energy. In this regime, the Thomas-Fermi approximation can be applied, in which the kinetic energy term in equations 3.12 and 3.13 is omitted. The solution of equation 3.13 is then straightforward. It becomes

$$\mu = U(\mathbf{r}) + gn(\mathbf{r}). \quad (3.14)$$

This means that the BEC density will be such that the interaction energy and the potential energy add up to the chemical potential of the sample. To achieve this, the density has to compensate the potential. This gives a density distribution of

$$n(\mathbf{r}) = \begin{cases} \frac{\mu - U(\mathbf{r})}{g} & \text{for } \mu - U(\mathbf{r}) > 0, \\ 0 & \text{otherwise.} \end{cases} \quad (3.15)$$

The chemical potential can be calculated using the normalization condition  $N = \int d\mathbf{r} n(\mathbf{r})$ . In a harmonic potential, the chemical potential is then [Pit03]

$$\mu = \frac{\hbar\omega}{2} \left( \frac{15Na}{a_{\text{ho}}} \right)^{2/5}. \quad (3.16)$$

By setting  $\mu = U(R_{\text{TF}})$ , one obtains the Thomas-Fermi radius, where the condensate wave function becomes zero:

$$R_{\text{TF}} = \sqrt{\frac{2\mu}{m\omega^2}} = a_{\text{ho}} \left( \frac{15Na}{a_{\text{ho}}} \right)^{1/5}. \quad (3.17)$$

### 3 Degenerate quantum gases

The peak density is also readily obtained as

$$n_{\max} = \frac{\mu}{g} = \frac{1}{8\pi} \left( \frac{15^2 N^2}{a_{\text{ho}}^{12} a^3} \right)^{1/5}. \quad (3.18)$$

#### 3.1.3 BEC at finite temperature - bimodal distributions

The derivations for a zero temperature BEC can in many cases be generalized to partially condensed samples in a very simple way, treating the condensed cloud and the thermal gas as separate components.

##### Noninteracting gas

For the case of a non-interacting gas one can describe the condensed and noncondensed clouds independently. The density of the BEC is simply given by equation 3.10 and the thermal density is given by [Pit03]

$$n_T(\mathbf{r}) = \frac{1}{\lambda_{\text{dB}}^3} g_{3/2}(e^{-U(\mathbf{r})/k_B T}), \quad (3.19)$$

where  $\lambda_{\text{dB}}$  is the thermal de Broglie wavelength defined by Eq. 3.2 and  $g_p(z) = \sum_{k=1}^{\infty} z^k / k^p$  is the Bose function with  $p = 3/2$  describing the effects of Bose statistics in the thermal gas. Note that the peak thermal density  $n_{T,\max} = \zeta(3/2)/\lambda_T^3$  calculated from equation 3.19 is fixed only by the temperature and does not depend on the trap parameters. This is due to the fact that the presence of a noninteracting BEC constrains the chemical potential to be zero, and the thermal atom number is fixed by the condensate fraction. In experiments the characteristic bimodal distributions of the typically very narrow condensed part and the much wider thermal wings can be observed both in the spatial distribution by *in situ* imaging and in the momentum distribution by time-of-flight imaging. This gives the opportunity to clearly differentiate between the condensed and the thermal part of the cloud.

##### Interacting gas

When interactions in the gas become significant as is the case for most BECs, the separation into two components is less straight forward. The action of the BEC on the thermal cloud and of the thermal cloud on the BEC have to be considered. This leads to two coupled equations describing the density of the two components [Pit03]:

$$n_0(\mathbf{r}) = \frac{\mu - U(\mathbf{r}) - 2gn_T(\mathbf{r})}{g} \theta(\mu - U(\mathbf{r}) - 2gn_T(\mathbf{r})) \quad (3.20)$$

$$n_T(\mathbf{r}) = \frac{1}{\lambda_{\text{dB}}^3} g_{3/2}(e^{-(U(\mathbf{r}) + 2g[n_0(\mathbf{r}) + n_T(\mathbf{r})])/k_B T}). \quad (3.21)$$

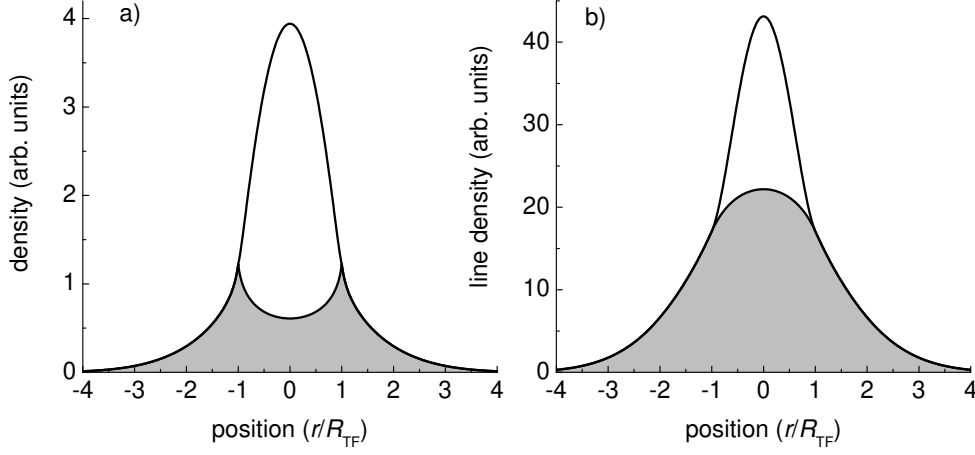


**Figure 3.2:** Typical bimodal distribution of a BEC just below the critical temperature with a condensate fraction of  $\sim 25\%$ . The shaded area shows the thermal component, while the condensed part is the area above the thermal component. a) shows the density while in b) the radially integrated density profile is shown. The radial position is scaled with the Thomas-Fermi radius (3.17).

Note that these two equations describe a weakly interacting gas in which the approximations for Eq. 2.12 are fulfilled. In general, one would have to solve these two equations in a self-consistent way, but no analytical solution is available. In most cases however, one can describe a partly condensed gas in a semi-ideal way, where the condensed part is described as an interacting BEC in the Thomas-Fermi limit at zero temperature, whereas the thermal component is described as an ideal gas. This makes use of the fact that in most cases, one can neglect the contributions due to the thermal density in the two equations above, as it is generally much lower than that of the condensed sample. The equations then become

$$n_0(\mathbf{r}) = \frac{\mu - U(\mathbf{r})}{g} \theta(\mu - U(\mathbf{r})) \quad (3.22)$$

$$n_T(\mathbf{r}) = \frac{1}{\lambda_{\text{dB}}^3} g_{3/2}(e^{-(U(\mathbf{r}) + 2gn_0(\mathbf{r}))/k_B T}). \quad (3.23)$$

Obviously, this approximation is only valid as long as the mean field due to the thermal cloud  $E_{\text{int,therm}} = 2gn_T$  is much smaller than the chemical potential and the thermal energy  $k_B T$ . In these equations, only  $\mu$  needs to be determined. In our semi-ideal approach, the chemical potential is simply determined by the condensed part,

$$\mu = \frac{\hbar\omega}{2} \left( 15N_0 \frac{a}{a_{\text{ho}}} \right)^{2/5} = \frac{\hbar\omega}{2} \left( 15N \frac{a}{a_{\text{ho}}} \right)^{2/5} \left( \frac{N_0}{N} \right)^{2/5}, \quad (3.24)$$

which reduces the problem to determining the condensate fraction. In general, the condensate fraction can only be determined numerically as has been done by Min-

### 3 Degenerate quantum gases

guzzi *et al.* for example [Min97]. Analytical solutions can be obtained by treating the interactions as a perturbation, using the scaling parameter [Pit03]

$$\eta = \frac{\mu(T=0)}{k_B T_c^0} = \frac{1}{2} \zeta(3)^{1/3} \left( 15 N^{1/6} \frac{a}{a_{ho}} \right)^{2/5} \simeq 1.57 \left( N^{1/6} \frac{a}{a_{ho}} \right)^{2/5}, \quad (3.25)$$

which is determined by the ratio of the chemical potential at  $T = 0$  and the critical temperature  $T_c^0$  for noninteracting particles in the same trap\*. As  $\eta$  depends only very weakly on the particle number ( $\eta \propto N^{1/15}$ ), its magnitude is mainly determined by the ratio  $a/a_{ho}$ . While in typical BEC experiments,  $\eta$  is typically 0.3 to 0.4, in our molecular BEC  $\eta$  can become on the order of 1 by tuning the scattering length of our molecules to values comparable to the harmonic oscillator length near the Feshbach resonance. Using the approximation that  $\eta$  is a small quantity, Giorgini *et al.* determined the reduction of the critical temperature as compared to a noninteracting gas to be [Gio96]

$$\frac{\delta T_c}{T_c^0} = -1.32 \frac{a}{a_{ho}} N^{1/6} = -0.43 \eta^{5/2}. \quad (3.26)$$

Naraschewski *et al.* [Nar98] used this approximation to calculate the condensate fraction:

$$\frac{N}{N_0} = 1 - \left( \frac{T}{T_c^0} \right)^3 - \eta \frac{\zeta(2)}{\zeta(3)} \left( \frac{T}{T_c^0} \right)^2 \left[ 1 - \left( \frac{T}{T_c^0} \right)^3 \right]^{2/5}. \quad (3.27)$$

Using equations 3.24 and 3.23 one obtains an analytical description of the semi-ideal Bose gas.

Fig. 3.2 a) shows an example of such a density distribution. Where the density of the condensed fraction goes to zero at the Thomas-Fermi radius, the thermal density exhibits a sharp peak. Here, the assumption of a dilute thermal gas is the least fulfilled. The repulsive interaction leads to a smoothing of this peak. By imaging the density distribution, one usually acquires column or line densities as shown in Fig. 3.2 b), where the thermal density peak is not visible.

## 3.2 Degenerate Fermi gas

In contrast to the case of bosons, where the quantum statistics by itself leads to the condensation into a superfluid phase below a critical temperature, this is not the case for fermions. Fermi-Dirac statistics governs the Fermi distribution function,

$$N_{r,\text{Fermi}} = \frac{1}{\exp\left(\frac{\epsilon_r - \mu}{k_B T}\right) + 1}, \quad (3.28)$$

---

\* $\eta$  can be expressed in terms of various parameters, such as the following:  $\eta = 2.24(n_{T=0,\text{max}} a^3) = 1.59 \left( \frac{k_B T_c^0}{\hbar^2 / m a^2} \right)^{11/5}$ .

### 3.2 Degenerate Fermi gas

where the +1 instead of the -1 in the denominator makes all the difference to the Bose case (3.3). It is convenient to write 3.28 in an integral form as has been done with 3.3 in the previous section. I will simply state here the most important quantities that can be readily obtained (see for example [Pit03]). Noninteracting trapped fermions will at zero temperature simply fill the trap up to the Fermi energy  $E_F = \mu$ ,

$$E_F = \hbar\omega(6N)^{1/3} = k_B T_F = k_B \times 405 \frac{\omega/2\pi}{100 \text{ Hz}} \left( \frac{N}{10^5} \right)^{1/3} \text{ nK} \quad (3.29)$$

in an isotropic harmonic trap with trap frequency  $\omega$ .  $N$  is the number of identical particles, so if there are several spin states present, there is a separate Fermi energy for each state. From the Fermi energy, one gets immediately the size of the cloud in the trap. It is

$$R_F = \sqrt{\frac{2E_F}{m\omega^2}} = \sqrt{\frac{\hbar}{m\omega}} (48N)^{1/6} = a_{\text{ho}} (48N)^{1/6}. \quad (3.30)$$

This is the analog of the Thomas-Fermi radius of a BEC (3.17). Note that both have a weak dependence on the particle number, the size of the BEC scaling with  $N^{1/5}$ . The maximum density in the center of the trap is given by

$$n(0) = \frac{2}{\sqrt{3}\pi^2} \frac{\sqrt{N}}{a_{\text{ho}}^3}. \quad (3.31)$$

Expressing the Fermi wavenumber  $k_F = \sqrt{2mE_F}/\hbar$  in terms of the density, one gets

$$k_F = (6\pi^2 n(0))^{1/3}. \quad (3.32)$$

Beside the constant factor of  $(6\pi^2)^{1/3}$ , the Fermi wave number simply corresponds to the inverse interparticle separation!

The Fermi temperature  $T_F = E_F/k_B$  marks the crossover to a Fermi degenerate gas, where the mean occupation number in the center of the trap approaches unity. Below  $T_F$ , the gas is governed by Fermi statistics, and the gas behaves different from a normal Bose gas. For the first time, such a gas could be studied at JILA with  $^{40}\text{K}$  atoms [DeM99b], where an excess energy of the trapped Fermi gas as compared to a classical gas with the same temperature could be observed. Fermi statistics leads to a reduction of the collision rate and at the time limited evaporative cooling to a temperature of  $\sim 0.5T_F$ . The collision rate is reduced as the density of a degenerate Fermi is smaller than that of a classical or Bose gas of the same temperature and because Pauli blocking inhibits collisions as the mean occupation number approaches unity, leading to a collisionless gas near zero temperature.

#### Weakly interacting ultracold fermions, Cooper pairing

While noninteracting fermions exhibit no phase transition to a superfluid state, it can be induced by an effectively attractive interaction. Bardeen, Cooper and Schrieffer

### 3 Degenerate quantum gases

(BCS) were able to explain superconductivity in metals by a pairing mechanism that leads to electrons being paired to Cooper pairs in momentum space [Bar57]. The BCS theory successfully describes Fermi systems with weak interactions, the mean distance between paired atoms being much larger than the interparticle spacing. Associated with Cooper pairing is a gap in the excitation spectrum of the gas, which has been calculated to be [Gor61, Pit03]

$$\Delta_0 = \frac{1}{2} \left( \frac{2}{e} \right)^{7/3} E_F \exp \left( -\frac{\pi}{2k_F|a|} \right) \quad (3.33)$$

at zero temperature for a homogeneous system. In the case of a trapped gas, one can use this result for a local density approach [Kin04b], which leads to a broadening of the excitation spectrum as observed in recent experiments in our group [Chi04a]. The critical temperature for the transition to a BCS state is proportional to the gap energy at zero temperature. For a harmonically trapped gas it is [Gor61, Car04]

$$T_{\text{BCS}} = \frac{e^\gamma}{\pi} \left( \frac{2}{e} \right)^{7/3} T_F \exp \left( -\frac{\pi}{2k_F|a|} \right) \approx 0.277 T_F \exp \left( -\frac{\pi}{2k_F|a|} \right), \quad (3.34)$$

where  $\gamma$  is Euler's constant. It should be noted however that this formula is only correct for the weakly interacting case, where  $k_F|a| \ll 1$ . Such temperatures are now routinely achieved in current experiments with ultracold fermions when Feshbach resonances are used to tune  $k_F|a| \geq 1$ . So far, no smoking gun of superfluidity has been found in these experiments, but there is strong presumptive evidence, that they have indeed entered the superfluid Fermi gas regime [Bar04c, Reg04, Zwi04, Kin04a, Bar04b, Chi04b].

#### Crossover to a BEC of molecules

The major interest of the experiments mentioned above is to tune the interactions into a regime where  $k_F|a| \gg 1$  and the gas is strongly interacting, which was first achieved at Duke university [O'H02a]. Using a Feshbach resonance, a weakly interacting gas can be tuned to infinite values of  $k_F|a|$ , where a two-body bound state appears, and Cooper pairs paired in momentum space are converted into molecules that are correlated in position space, which form a BEC. Other than the Cooper pairs which exist only in a many-body picture, the molecules form a two-body bound state. The crossover between the BCS and the BEC regimes has been of considerable interest for theorists in recent decades [Eag69, Leg80, Che04] because high- $T_c$  superconductors are based on strongly interacting electron gases. A quantitative description of the strongly interacting regime is a great challenge for theory because the interactions cannot be treated in a perturbative way. The crossover regime is difficult to study experimentally in solid state systems, as the interactions cannot be tuned easily. Ultracold atomic Fermi gases now enable the experimenter for the first time to study this regime extensively. First



experiments indicate that there is an adiabatic and reversible connection between the superfluidity of bosons in a BEC and the superfluid state of interacting fermions.

#### Universal behavior of a strongly interacting Fermi gas

A particularly interesting system is a gas with unitarity limited interactions that can be realized when  $k_F|a|$  diverges to infinity, as it is the case on a Feshbach resonance. One enters a universal regime, where the properties of the gas become completely independent of any particularities of the atomic interaction properties. The only relevant length scale in the system is then the mean interparticle spacing  $n^{-1/3}$  [Bak99, Hei01, Car03, Ho04], which is proportional to  $1/k_F$ .

To fulfill the above conditions, the Fermi wave number has to be much larger than the effective range of the potential. While such conditions can now be achieved on a Feshbach resonance in ultracold Fermi gases, they also determine the physics of neutron stars.

As the mean field energy due to the unitarity limit scales as

$$E_{\text{mf}} \propto \frac{n}{k_F} \propto k_F^2 = \beta E_F, \quad (3.35)$$

it simply rescales the Fermi energy to a smaller effective energy

$$E_{\text{eff}} = (1 + \beta)E_F. \quad (3.36)$$

Here,  $\beta$  is expected to be a universal constant. It has been estimated theoretically to be between -0.67 [Bak99, Hei01] and -0.43 [Bak99], the most recent value was determined in a Monte-Carlo Simulation to be -0.56(1)[Car03]. Experiments have determined  $\beta$  to -0.26(7) [O'H02a, Geh03b], -0.64(15) [Bou04], and  $-0.68^{+0.13}_{-0.1}$  [Bar04c].

A very exciting aspect of the universal regime is that the critical temperature for superfluidity is expected to be extremely high, on the order of the Fermi temperature  $T_F$ . A lot of theoretical work has been done on this so-called resonance superfluidity using different approaches that all lead to similar results [Hol01, Tim01, Oha02].



# Chapter 4

## Experimental setup

All the experiments described in this thesis are performed in an ultra-high vacuum (UHV) environment of  $<10^{-10}$  mbar. Fig. 4.1 provides an overview of the apparatus: A Zeeman slower decelerates atoms from a thermal atomic beam produced in an oven at a temperature of  $340^{\circ}\text{C}$  on a distance of  $\sim 45$  cm from up to 600 m/s to a few 10 m/s before being trapped in a magneto-optical trap (MOT) at temperatures as low as  $160\text{ }\mu\text{K}$ . The trapped atoms are then transferred into a deep, large volume optical dipole trap that is created using an optical resonator. In a final stage, the atoms are transferred into a focused beam dipole trap that allows precise control of the trap parameters over several orders of magnitude in trap depth. At the lowest trap depths, temperatures as low as  $\sim 10$  nK are achieved. To control the interactions between our trapped atoms and to finally convert them into molecules we apply magnetic fields up to 1500 G. Most of the vacuum apparatus, the MOT lasers and the resonator trap have been described thoroughly in previous diploma theses [Joc00, Els00, Mor01, Hen03]. I will here only summarize the main points and focus on the new parts of the system, the precise magnetic field and laser intensity control, and new diagnostic tools such as imaging at high magnetic fields.

### 4.1 Vacuum and atomic beam

#### Oven and oven chamber

Lithium atoms are evaporated from an oven to produce an atomic beam that has enough flux to load  $\sim 10^8$  atoms into the MOT within a few seconds. Fig. 4.2 illustrates the setup of the oven chamber. The oven itself consists of a small, hollow copper cube with dimensions  $32 \times 22 \times 22\text{ mm}^3$ . A small UHV compatible button heater (0.32" UHV Button Heater, HeatWave Labs) is attached to the back and also serves as a holder for the oven inside the chamber. The oven position can be adjusted through a tripod via a flexible-bellows construction. A thermocouple is attached to the oven to control

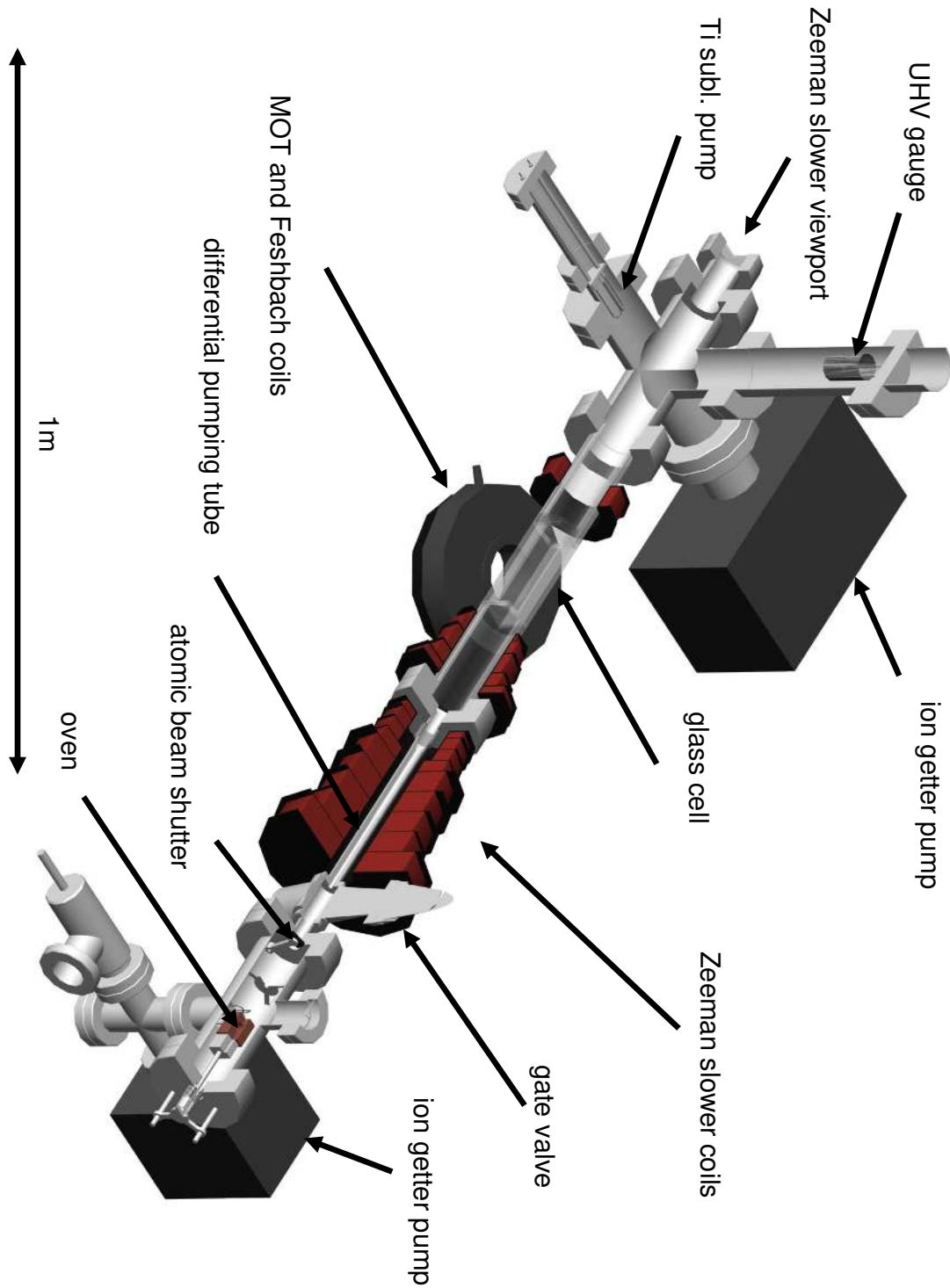


**Figure 4.1:** Overview of the vacuum chamber

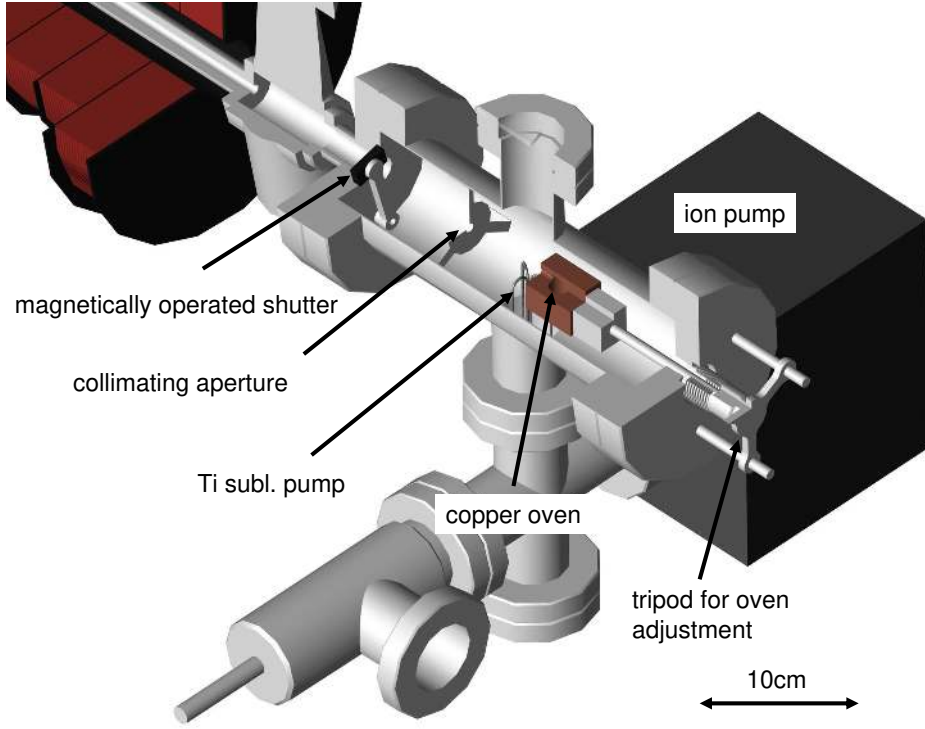


**Figure 4.2:** A view into the oven chamber

its temperature. Copper was chosen as an oven material as its high heat conductivity ensures a uniform temperature across the oven. A disadvantage is that the oven cannot be heated to higher temperatures than  $\sim 400^\circ\text{C}$ , as around that temperature, Copper and lithium start to form an alloy and the oven is destroyed. But for most experiments, our oven is operated at  $340^\circ\text{C}$ , as this already provides an adequate loading rate of our MOT. A low oven temperature has the advantage that the amount of lithium deposited on the entrance window for the Zeeman slowing beam is kept low, which maintains a high transparency of this window.

An important advantage of our design is that only a very limited surface inside the vacuum is at high temperature, minimizing negative effects on the vacuum. Only 5 W of electrical power are required to maintain the temperature of the oven. The lithium escapes through a 1 mm-hole on the front side of the oven. It is filled with about 0.2 g of  $^6\text{Li}$  enriched to 95%. Before passing through the gate valve that can be seen in the upper left corner of Fig.4.2, the beam is collimated by an aperture to protect the valve from any contamination with lithium that might affect its operation. A magnetically operated shutter is used to block the atomic beam when it is not needed. The oven chamber consists of a standard four-way reducing cross with two CF-40 and two CF-64-flanges. On the top CF-40 flange, a viewport is installed to be able to monitor adjustment of the oven position. Through the bottom CF-40, the titanium filaments of

#### 4 Experimental setup

a sublimation pump protude into the chamber, and a 20 l/s ion pump (StarCell, Varian) as well as a right angle valve for roughing are attached to the chamber.

We have no pressure gauge inside the oven chamber, but from the current in our ion pump we estimate the pressure to be  $\sim 10^{-8}$  mbar. The main limitation for the pressure in the oven chamber is hydrogen that is evaporated from the oven and which is extremely hard to get rid of. Details on this subject can be found in F. Schreck's PhD thesis [Sch02].

Beside the fact that we had to replace the oven several times shortly after it was first installed because of some user errors including operating it at too high temperatures, it had been working reliably for about two years now. Nevertheless, an oven with the same or even better performance could probably be built with a lot less effort. A simple single-ended tube that is heated from outside the vacuum would certainly work at least as well, especially if only moderate temperatures are required.

#### **UHV glass cell and differential pumping**

The  $\sim 10^{-8}$  mbar-vacuum of the oven chamber is obviously incompatible with the life-time requirements in our optical traps, where we wish to have at least several tens of seconds, for which one needs a pressure of  $\sim 10^{-10}$  mbar. The 45 cm-long Zeeman slower tube, in which the atomic beam is decelerated can work as an ideal differential pumping tube. The tube's inner diameter is matched to the diameter of the slightly focused slowing beam and the diverging atomic beam. On the first 10 cm, the diameter is 2 mm, for the next 10 cm it is 3 mm, before getting much larger because of an edge-welded bellow that is meant to protect the UHV glass cell from any mechanical stress (see Fig. 4.1). The calculated conductance of this tube is 0.02 l/s, making it possible to maintain a more than 100-fold difference in vacuum across the tube.

The UHV glass cell has outer dimensions of  $4 \times 4 \times 12$  cm<sup>3</sup> with a wall thickness of 4 mm. When designing the glass cell, the following parameters were especially taken care of:

- The losses of light passing through the glass cell at Brewster's angle have to be as low as possible as an optical resonator is used to enhance the intensity of our standing wave dipole trap. For this purpose, high purity fused silica was used (Spectrosil 2000, Saint-Gobain Quartz). The losses within our resonator are only determined by the surfaces of the glass cell, they are measured to be lower than 1‰ per surface.
- The wall thickness of 4 mm is much larger than what is needed to avoid significant leakage of He through the surface. Its thickness was chosen to avoid any optical birefringence due to mechanical stress that might occur when the cell is evacuated.

#### 4.1 Vacuum and atomic beam

- The inner diameter of the glass-to-metal transitions was chosen very large to achieve high pumping speeds for a good vacuum.
- The glass cell is not anti-reflection coated. The reason for not doing it was that it was only possible to coat the outside surfaces which would only reduce the reflections by 50% and the cost for that was rather high. After four years of experimental experience, this has proven not to be a wise decision, especially because the reflections of the two surfaces lead to interference fringes that would otherwise be significantly suppressed.

The ultra-high vacuum in the glass cell is maintained through a “pumping chamber” that is set up on the other end of the glass cell. It consists of a five-way cross that has attached a 55 l/s ion pump (StarCell, Varian), a titanium sublimation pump and a Bayard-Alpert vacuum gauge to monitor the pressure. The atomic beam is also dumped in this pumping chamber. It hits the sapphire viewport through which the Zeeman slowing beam enters the chamber. This viewport is made from sapphire, because glass or quartz are not resistant against lithium, especially at temperatures above  $\sim 100^\circ\text{C}$ . We heat this window continuously to about  $80^\circ\text{C}$  to evaporate lithium that is being deposited by the beam. The Bayard-Alpert gauge indicates a pressure of  $2 \times 10^{-11}$  mbar. It is not obvious that there is the same pressure in the glass cell, but one can expect that the vacuum there is better than  $10^{-10}$  mbar, which is consistent with maximum lifetimes observed in a magnetic quadrupole trap of up to 140 s.

### 4.2 Magneto-optical trap

The magneto-optical trap (MOT) is loaded from a Zeeman-slowed atomic beam. All the laser power for the MOT comes from diode lasers that have a maximum power of 30 mW (CQL806/D3, Philips, discontinued). Two laser frequencies are needed for the MOT to drive the cooling and repumping transitions from the two  $F = 3/2$  resp.  $F = 1/2$  ground states that are 228 MHz apart (see A.2). An additional laser frequency has to be provided for the Zeeman slower which is detuned 65 MHz to the red of the cooling light. Frequency stabilized light from grating stabilized diode lasers is used to injection lock three free running laser diodes of the same type that deliver the laser power needed for the experiment. A detailed description of the setup can be found in [Joc00, Hen03]. In the following, only the main features of the setup will be described.

#### Laser system

An overview of the current setup of the laser system for the MOT is shown in Fig. 4.3. Saturation spectroscopy of lithium vapor produced in a heat pipe provides the frequency reference for the experiment. One grating stabilized laser is locked to the heat pipe on a crossover line of the  $^7\text{Li}$  D1 line. This line is 698 and 469 MHz blue detuned from the  $^6\text{Li}$  D2 lines that are used in the experiment [Joc00]. To lock this laser we use frequency modulation spectroscopy. It is especially simple to implement with diode lasers because the modulation can be directly applied to the laser diode current and does not require any additional optical elements to modulate the beam. This has the slight disadvantage however, that the frequency modulation is present on all the laser light of this laser and not only on the part of the light that is used for spectroscopy.

To be able to shift our laser light over a wide frequency range, a second laser is locked relative to the first one using a simple scheme described in Ref. [Sch99]. It is based on recording the beat note between the two lasers using an avalanche photodiode. A simple radio frequency circuit generates an error signal that can be tuned to the desired frequency using a voltage controlled oscillator. It is configured such that it can be tuned between  $\pm 800$  Mhz and  $\pm 900$  Mhz using a programming voltage between 0 V and 10 V, but is can be easily adapted to span a much wider range.

Two AOMs operated in double pass configuration at frequencies of  $\sim 200$  MHz and  $\sim 80$  MHz produce the two light frequencies for cooling and repumping, respectively. In order to have enough intensity available for the MOT, two injection locked “slave” laser diodes amplify the two frequencies to  $\sim 20$  mW each.

#### Heat pipe for saturation spectroscopy

A lithium vapor cell for spectroscopy is quite a bit more difficult to build as compared to cesium or rubidium, where an evacuated glass cell at room temperature containing



## 4.2 Magneto-optical trap

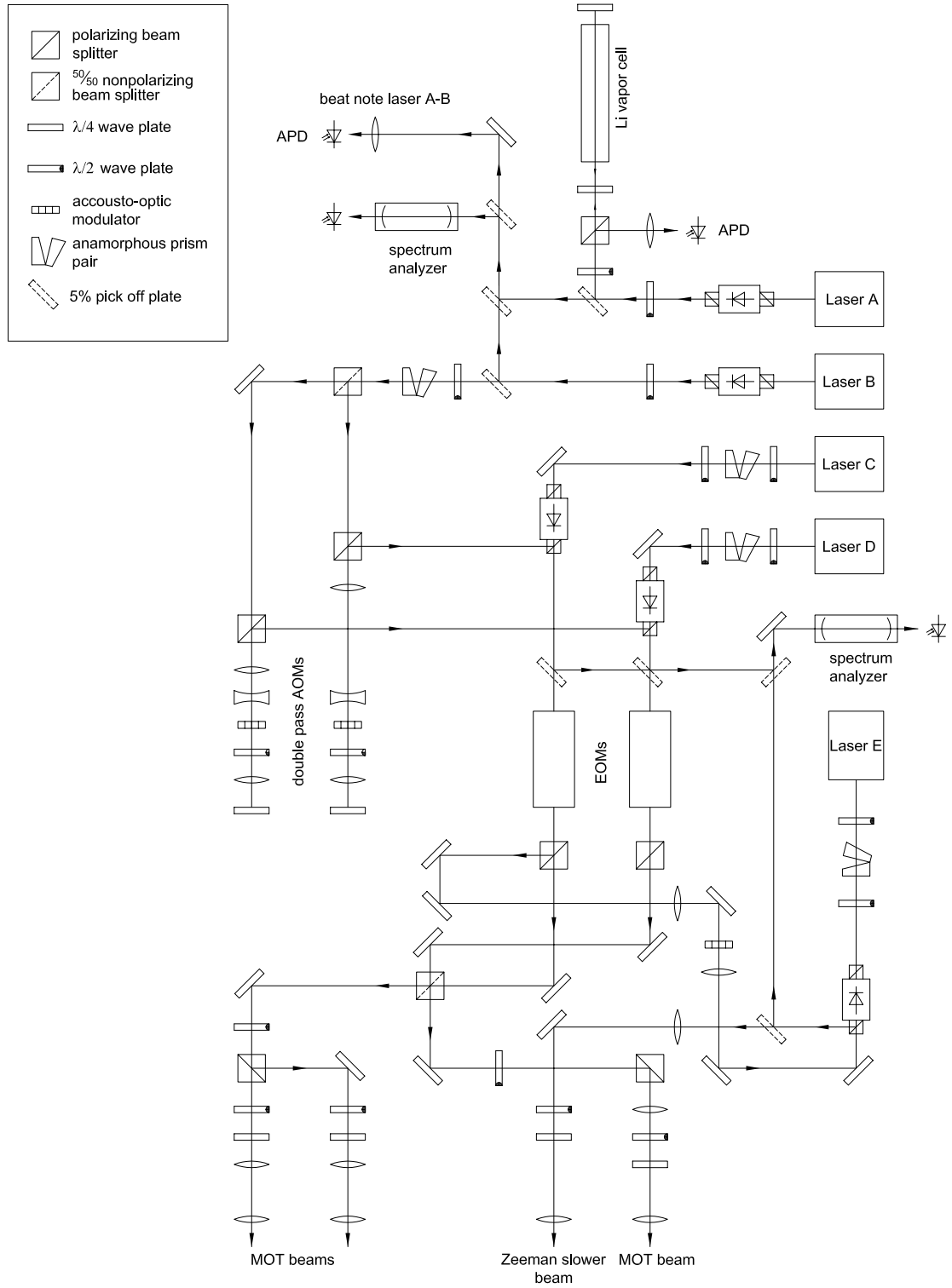


**Figure 4.3:** Schematic overview of the MOT laser optics.

#### 4 Experimental setup

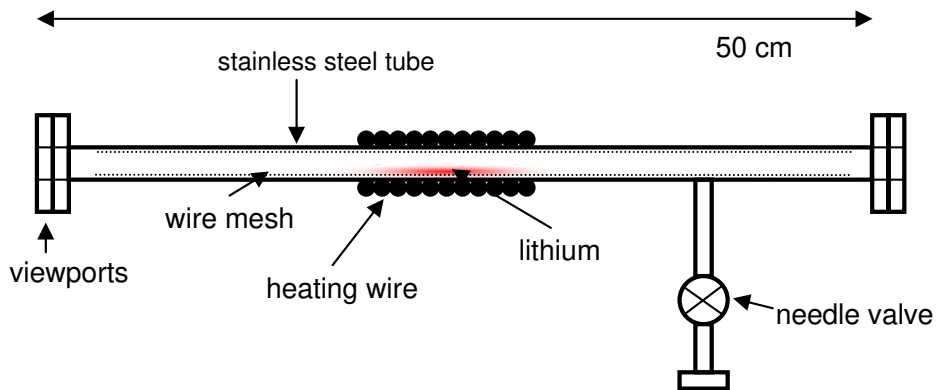


**Figure 4.4:** Schematic of the heat pipe used for the lithium saturation spectroscopy

a small amount of the metal has a sufficient vapor pressure to be able to perform spectroscopy on it. Lithium has to be heated to at least  $280^{\circ}\text{C}$  to achieve a high enough vapor pressure (Eq. A.1). A heated glass cell with a tantalum shield inside to keep the lithium away from the windows had been used in the early stages of the experiment. However, the glass cell's life time did never exceed about one year, because the lithium deposited on the hot glass destroyed the cell.

A new heat pipe was designed that follows the design described in G. Xu's PhD thesis [Xu01]. A schematic of our heat pipe is shown in Fig. 4.4. It consists of a long stainless steel tube with two CF-16 viewports on both ends. Near one end, a needle valve is attached to occasionally pump the pipe to maintain the vacuum. The pipe is only heated in the center part using a coaxial heating wire. Care has to be taken that the current in the heating does not lead to a magnetic field inside the pipe, because the Zeeman effect would lead to a fluctuating signal when the heating is switched on and off. The length of the tube of  $\sim 50$  cm is chosen such that the lithium vapor is limited by its mean free path in a buffer gas to the center part of the pipe, protecting the viewports from getting coated with lithium. The inside walls of the tube are covered with a stainless steel wire mesh, with a  $\sim 1$  mm spacing. It is intended to keep the hottest part of the tube, where most lithium is evaporated covered with lithium through the capillary effect. Following the ideas described in Ref. [Xu01], we experimented with an argon buffer gas. We increased the argon pressure until we could detect a significant pressure broadening of our saturation spectrum to minimize the mean free path length in our lithium vapor without sacrificing performance. It turned out however, that a very similar pressure established in our pipe when it was no longer pumped. We attribute this pressure to hydrogen evaporating from the lithium and concluded that an argon buffer gas is not really needed to operate the heat pipe. An appreciable absorption signal of a few per cent is obtained at a temperature just below  $300^{\circ}\text{C}$ . Above  $400^{\circ}\text{C}$ ,

the optical density is so large that no resonant light is transmitted. The pipe is water cooled at the ends and around the heating wires. This is not really necessary, but it avoids a considerable amount of heat being dissipated on the optical table.

### **Zeeman slower, MOT loading**

A decreasing-field Zeeman slower is used to decelerate the atomic beam from our 340°C-oven. While the mean velocity of the atoms at that temperature is  $\sim 900$  m/s, our Zeeman slower has a designed maximum capture velocity of 600 m/s for which an initial magnetic field of  $\sim 560$  G is needed. The magnetic field is produced by a set of 14 individual coils spread on 46 cm along the atomic beam. They are designed to produce an optimum shape of the magnetic field. On the last few centimeters, the Zeeman slower field is smoothly matched with the quadrupole field for the MOT ensuring that the atomic beam is decelerated efficiently on the last few centimeters before it is captured in the MOT.

To have enough laser power available for the Zeeman slowing beam, another slave laser diode is injected with  $\sim 0.2$  mW of the cooling light that is frequency shifted by 65 MHz using an AOM. Experimentally it turned out that adding some repumping light did not increase the loading rate very much. It turned out however that modulating the current of the slave laser diode for the Zeeman slower at a frequency of  $\sim 45$  MHz would double the loading rate. A possible explanation for this is that the broadening of the laser leads to an effective broadening of the transition line width. This in return makes the slowing more robust, as it becomes less likely that atoms do not scatter enough photons for a short period and then get out of resonance with the slowing beam. The current modulation of the slave laser diode has to be carefully optimized. It depends strongly on the amount of seeding light used for the injection lock, as the seeding light suppresses any modulation that is performed on the current of the slave diode. Our current setup produces maximum loading rates on the order of  $7 \times 10^6$  atoms/sec when the trapping lasers are tuned 4-5 natural linewidths to the red of the resonance at an oven temperature of 340°C. The large detuning creates a large-volume, box-like trap for the atoms. In the trap center, the cold atoms are out of resonance because of the large detuning and only when the magnetic field is large enough to compensate for the detuning the atoms scatter light that pushes them back into the center of the trap. In this configuration a large number of atoms can be accumulated and due to the low density and photon scattering rates, losses are rather small, the lifetime of the MOT is limited to  $\sim 40$  s mainly by collisions with the background gas that is probably dominated by atomic beam

## 4 Experimental setup

### Maximizing phase space density

The highest densities and lowest temperatures are achieved when the detuning of the MOT lasers is only about half a linewidth (3 MHz) and the intensity much smaller than the saturation intensity. For stable operation, both frequency and intensity have to be well controlled. To reduce the intensity smoothly and without changing the beam profiles, two EOMs are used (Model LM0202, Linos Photonics). A temperature of  $\sim 160\mu\text{K}$  [Hen03] and max. density of roughly  $10^{11}$  atoms/cm<sup>3</sup> can be achieved. However, under such conditions inelastic losses are extremely high [Kaw93] and these parameters can only be maintained for several milliseconds. This is enough to load our optical dipole trap efficiently, if carefully optimized ramps on the laser frequency and intensity are applied. See 4.3.1 for a timing diagram.

### 4.3 Optical dipole traps

Optical dipole traps have emerged in recent years as ideal and versatile tools to confine ultracold atomic and molecular gases [Gri00]. They rely on the electric polarizability of the particles in the light field. Depending on whether the induced dipole oscillates in phase (below the atomic resonance frequency) or at opposite phase (above the resonance), the resulting potential is negative or positive, respectively. The key quantities to consider are the potential depth given by

$$U_{\text{dip}}(\mathbf{r}) = -\frac{3\pi c^2}{2\omega_0^3} \left( \frac{\Gamma}{\omega_0 - \omega} + \frac{\Gamma}{\omega_0 + \omega} \right) I(\mathbf{r}) \quad (4.1)$$

and the associated spontaneous photon scattering rate

$$\Gamma_{\text{dip}}(\mathbf{r}) = -\frac{3\pi c^3}{2\hbar\omega_0^3} \left( \frac{\omega}{\omega_0} \right)^3 \left( \frac{\Gamma}{\omega_0 - \omega} + \frac{\Gamma}{\omega_0 + \omega} \right)^2 I(\mathbf{r}). \quad (4.2)$$

In these two formulas,  $\omega_0$  is the atomic resonance frequency,  $\omega$  is the laser frequency and  $\Gamma$  is the spontaneous decay width of the atomic transition which is 5.9 MHz for lithium. Note that as the laser frequency is tuned away from the atomic resonance, the photon scattering rate is reduced faster than the trapping potential. Therefore, it is advantageous to work at very large detuning, if one wants to have a low photon scattering rate for a given potential depth.

In our experiment, a combination of two dipole traps is used that both employ light tuned far below the atomic resonance to provide a potential well at the intensity maximum. The first trap is a deep large-volume trap designed to load a large number of atoms from the MOT. It is a standing wave trap that requires only moderate laser power through enhancing the intensity of the standing wave in an optical resonator [Els00, Mos01]. A second, focused beam dipole trap is loaded from the standing wave trap. Its main advantage is that the trap depth can be precisely controlled over more than four orders of magnitude. This was the key for successful evaporative cooling of the trapped particles starting from almost 100  $\mu\text{K}$  to tens of nanokelvins.

#### 4.3.1 Optical resonator

The two main design criteria for the dipole trap were a low heating rate due to photon scattering and a large atom number. In order to achieve a reasonable transfer efficiency from the MOT into the dipole trap, its trap depth should exceed the mean kinetic energy of the atoms in the MOT. At the same time, there should be a good spatial overlap between the spread of the atoms in the MOT and the size of the dipole trap. To fulfill all of these requirements simultaneously one has to use very far detuned light and thus, very high intensity is required. To achieve a reasonable size of the dipole

## 4 Experimental setup

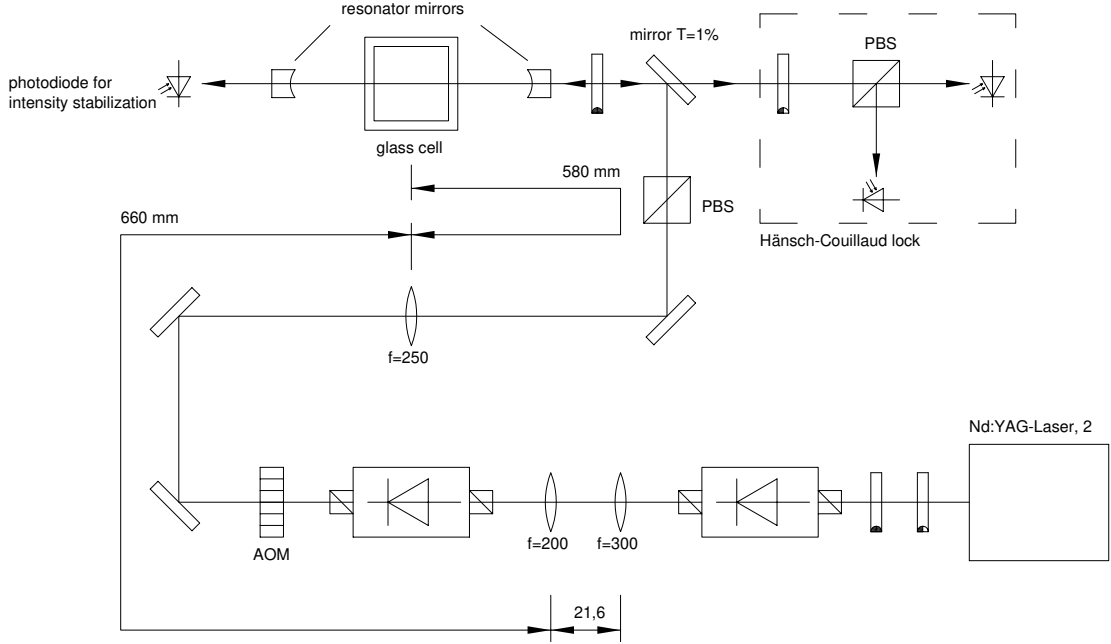


**Figure 4.5:** Setup for the optical resonator trap.

trap, one has to use quite a large amount of laser power. Using Nd:YAG laser light at 1064 nm, at least 100 W of laser power would be required to create a reasonable trap from a running wave beam. That is why for this experiment, we decided to make use of the resonant enhancement of the intensity in an optical resonator. Using a 2-W single frequency Nd:YAG laser we create a trap that is  $\sim 1$  mK deep while the waist of the resonator beam is  $159 \mu\text{m}$ , which provides a rather large trapping volume. The confinement along the resonator axis is provided by the standing wave structure in the resonator that forms pancake shaped microtraps with a half-wavelength spacing of 532 nm. A schematic of the resonator setup is shown in Fig. 4.5.

### Geometry

We use a linear resonator in almost confocal geometry. This configuration produces a rather large beam waist needed for efficient loading of the atoms from the MOT. Because all transverse modes in a confocal resonator have exactly the same resonance frequency, it is difficult to align it such that there is only the  $\text{TEM}_{00}$  mode excited. That is why in this experiment we chose to increase the length of the cavity by a few millimeters such that the degeneracy of the transverse modes is lifted and one is left with an essentially pure  $\text{TEM}_{00}$  mode. In the final design, two mirrors of radius  $R=150$  mm are used at a distance of  $L = 153$  mm. The beam waist for the  $\text{TEM}_{00}$

mode is given by

$$w_0 = \sqrt{\frac{\lambda L}{2\pi}} \sqrt{\frac{2R}{L} - 1}. \quad (4.3)$$

This is readily derived from Gaussian beam optics [Els00]. In our case,  $w_0$  is  $159 \mu\text{m}$ . The Rayleigh range in which the waist is smaller than  $\sqrt{2}w_0$  stretches out to  $r = \pi w_0^2/\lambda = 75 \text{ mm}$  from the center of the resonator. This means that the waist of the resonator mode does not vary noticeably near the center where we trap the atoms spread out over approximately 1500 individual wells.

#### Finesse and mode matching

To couple as much laser power as possible into the resonator, the incoming beam needs to be mode matched to the resonator mode. Also, the reflectivity of the incoupling mirror has to be chosen such that the incoupled power just compensates the loss from the resonator due to finite reflectivity of the mirrors and losses on all surfaces. The loss for one round trip in the resonator is on the order of  $10^{-3}$ . To determine the loss, a 99% input coupler was used and based on the finesse achieved in this test setup, a specially made  $R = 99.4\%$  mirror was ordered (Laser Components HR1064HT671). For convenience, this mirror was also antireflection coated at 671 nm because there existed some ideas to shine resonant light along the resonator axis for sideband cooling in the resonator lattice. The second, high-reflecting mirror is not coated for 671 nm.

#### Trapping potential

The laser light needed for our resonator trap comes from an ultrastable diode-pumped Nd:YAG-Laser that emits 2 W at a wavelength of 1064 nm (Mephisto 2000, Innolight). The depth of the potential per Watt of laser power for our lithium atoms in our standing wave is

$$U_{\text{sw}} = 8.4 \times 10^{-29} \text{ J/W} \times P = 6.12 \mu\text{K/W} \times k_{\text{B}} \times P, \quad (4.4)$$

where  $k_{\text{B}}$  is Boltzmann's constant and  $P$  is the running wave power. To transfer our atoms efficiently from the MOT in which we can achieve a minimum temperature of  $160 \mu\text{K}$ , the trap depth has to be much larger than the thermal energy of the atoms. This is achieved by the enhancement of the power in the optical resonator which is on the order of 150, while  $\sim 1 \text{ W}$  is actually coupled into the resonator. This results in a trap depth of  $\sim 1 \text{ mK}$ .

The trap potential can be approximated harmonically at the trap center. The trap frequencies are given by

$$\omega_{\text{rad}} = \frac{2}{w_0} \sqrt{\frac{U_{\text{sw}}}{m}} = 74.4 \text{ Hz } \mu\text{K}^{-1/2} \times \sqrt{\frac{U_{\text{sw}}}{k_{\text{B}}}} \quad (4.5)$$

#### 4 Experimental setup

$$\omega_z = \frac{2\pi}{\lambda} \sqrt{\frac{U_{\text{sw}}}{m}} = 49.4 \text{ kHz } \mu\text{K}^{-1/2} \times \sqrt{\frac{U_{\text{sw}}}{k_B}} \quad (4.6)$$

for the radial and the axial degrees of freedom, respectively [Els00]. At a trap depth of 1 mK, they become  $\omega_{\text{rad}} = 2.35 \text{ kHz}$  and  $\omega_z = 1.56 \text{ MHz}$ . Note the very high trap frequency of more than one Megahertz in the axial direction, which is 664 times larger than the radial frequency.

#### A 2-D trap

This trap configuration is ideally suited to study 2D quantum degenerate gases [Pet00, Pet01], especially also for degenerate Fermi gases [Pet03b]. One expects to observe 2-D behavior when the temperature of the gas becomes lower than the vibrational energy in the axial direction and the axial ground state population approaches unity. The axial ground state population can then be calculated to be

$$n_{0,\text{ax}} = 1 - e^{-\frac{\hbar\omega}{k_B T}}. \quad (4.7)$$

Many often-used quantities are different in the 2-D regime, we just summarize the most important differences here that we will need later:

- The 3-D density  $n_{3\text{D}}$  calculated from particle number  $N$ , trap frequencies  $\omega_i$  and temperature  $T$  is

$$n_{3\text{D}} = N \sqrt{\frac{m}{\pi}}^3 \frac{\omega_{\text{ax}} \omega_{\text{rad}}^2}{(k_B T)^{3/2}} \times \exp\left(-m \frac{\omega_{\text{ax}}^2 z^2 + \omega_r^2 r^2}{2k_B T}\right). \quad (4.8)$$

In the 2-D case, the density is modified in the axial direction, yielding

$$n_{2\text{D}} = N \sqrt{\frac{m}{\pi}}^3 \sqrt{\frac{\omega_{\text{ax}}}{\hbar}} \frac{\omega_{\text{rad}}^2}{k_B T} \times \exp\left(-m \left(\frac{\omega_r^2 r^2}{2k_B T} + \frac{\omega_{\text{ax}} z^2}{2\hbar}\right)\right). \quad (4.9)$$

The peak densities are obviously just the prefactors of the exponentials.

- The peak phase space density is also modified from the 3-D case: Instead of the 3-D formula,

$$D(3\text{-D}) = N \frac{\hbar^3 \omega_{\text{ax}} \omega_{\text{rad}}^2}{(k_B T)^3}, \quad (4.10)$$

it now becomes

$$D(2\text{-D}) = N \left(1 - \exp\left(-\frac{\hbar\omega_{\text{ax}}}{k_B T}\right)\right) \left(\frac{\hbar\omega_{\text{rad}}}{k_B T}\right)^2. \quad (4.11)$$



#### Locking technique

For locking of optical resonators, there exist two well established techniques: The method by Pound and Drever employs a phase modulation of the incoupled beam [Dre83]. It uses the fact that the phase of the modulated frequency in the reflected light changes sign on the resonance of the optical cavity. This is a very robust technique, but the laser light that is coupled into the cavity has to be modulated and thus additional optical components like an electro-optical modulator are required. Conceptually much more simple is the technique by Hänsch and Couillaud [Hän80]. The basic idea behind this technique is to compare the phase of light that is transmitted through the incoupling mirror of the resonator with the phase of light that is reflected and not coupled into the resonator. The main trick then is that the polarization inside the resonator is defined by some polarizing element, which in our case is the UHV glass cell at Brewster's angle. Now, the polarization of the incoming beam can be slightly tilted with respect to this polarization axis. The polarization component perpendicular to the one in the resonator is always reflected and serves as a phase reference for the light being transmitted out of the resonator. As the two beams have perpendicular polarization, any phase difference between the two leads to an elliptically polarized beam that can be analyzed using a standard circular analyzer setup. On the cavity resonance, the elliptical polarization changes sign, and thus, this can be used as an error signal to stabilize the cavity.

#### Loading the trap from the MOT

An efficient transfer of the atoms from the MOT into the dipole trap relies on a high density and a low temperature of the atoms in the MOT. This can be achieved at small detuning of the trapping lasers from the resonance and very low intensity. At such parameters inelastic loss from the MOT is tremendous [Kaw93]. That is why the timing during the transfer is very critical and the ramps that go from the MOT loading parameters to the transfer parameters have to be optimized carefully. A diagram showing the timings of all relevant parameters during the transfer is shown in Fig. 4.6. The dipole trapping light is always kept on during the transfer. During  $\sim 30$  ms ramps, we extinguish the MOT beams and at the same time reduce their detuning to about one half of the natural line width. To increase the density of the cloud we also compress the MOT by increasing the magnetic field gradient to about 50 G/cm. To pump the atoms into the  $F = 1/2$  ground state that is collisionally stable, the cooling light is switched off more slowly than the repumping light. Both  $m_F = \pm 1/2$  are populated equally within a few per cent during this procedure. About 20 % of the atoms in the MOT can be transferred to the dipole trap with an initial temperature of  $\sim 160 \mu\text{K}$  [Hen03], which is quite good as compared to the Doppler temperature of  $140 \mu\text{K}$ .

An appreciable lifetime in the dipole trap can only be achieved when there is absolutely no resonant light present at the position of the trap. For this purpose, we

## 4 Experimental setup

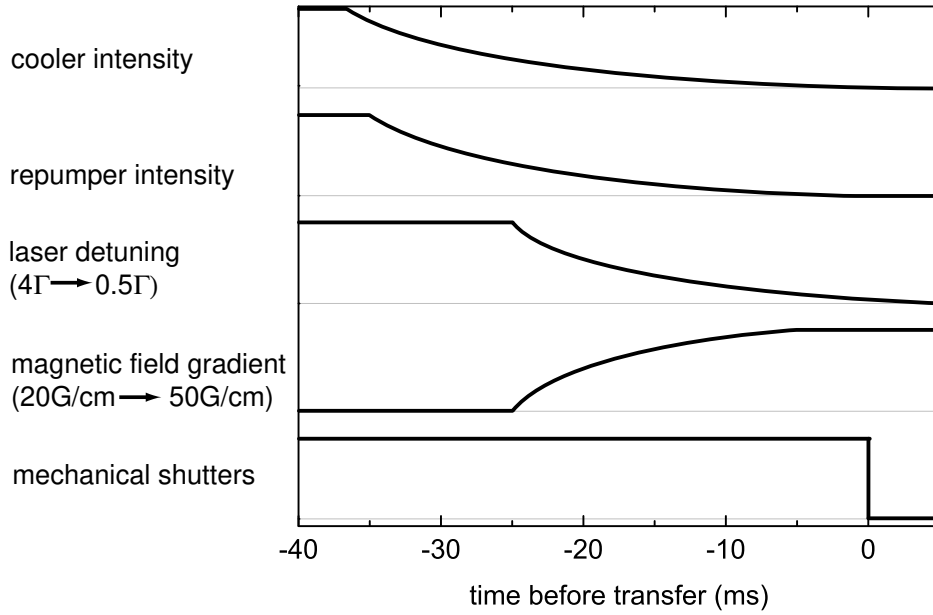


**Figure 4.6:** Timing diagram of the most important parameters during the transfer from the MOT into the dipole trap

quickly extinct the MOT beams with high-speed mechanical shutters that are made from loudspeakers [Sin02].

As the atoms are transferred into a standing wave trap, not only the total number of atoms that can be loaded into the trap is of interest, but especially the number of atoms per lattice site which will determine the density. We can typically load about  $8 \times 10^6$  atoms totally with a maximum of 1500 atoms per lattice site.

### 4.3.2 Focused beam dipole trap

In first experiments on evaporative cooling it turned out that the resonator trap had certain limitations that were difficult to overcome. First of all, the stability of the trap decreased while going to low power levels on the order of 1% of the full trap depth. But there is also the fundamental limitation that atoms start to tunnel along the lattice direction of the trap because the tunneling rate along the lattice direction for the axial ground state of the trap becomes important. The simplest trap to circumvent these problems is a focused beam running wave trap. However, in order to have sufficient axial confinement, the focus has to be rather tight. The aspect ratio of a focused beam trap is [Gri00]

$$\frac{\omega_{\text{rad}}}{\omega_{\text{ax}}} = \sqrt{2} \pi \frac{w_0}{\lambda}. \quad (4.12)$$

We designed the waist of our “dimple trap” to be  $\sim 20 \mu\text{m}$  with an aspect ratio of  $\sim 100$ .

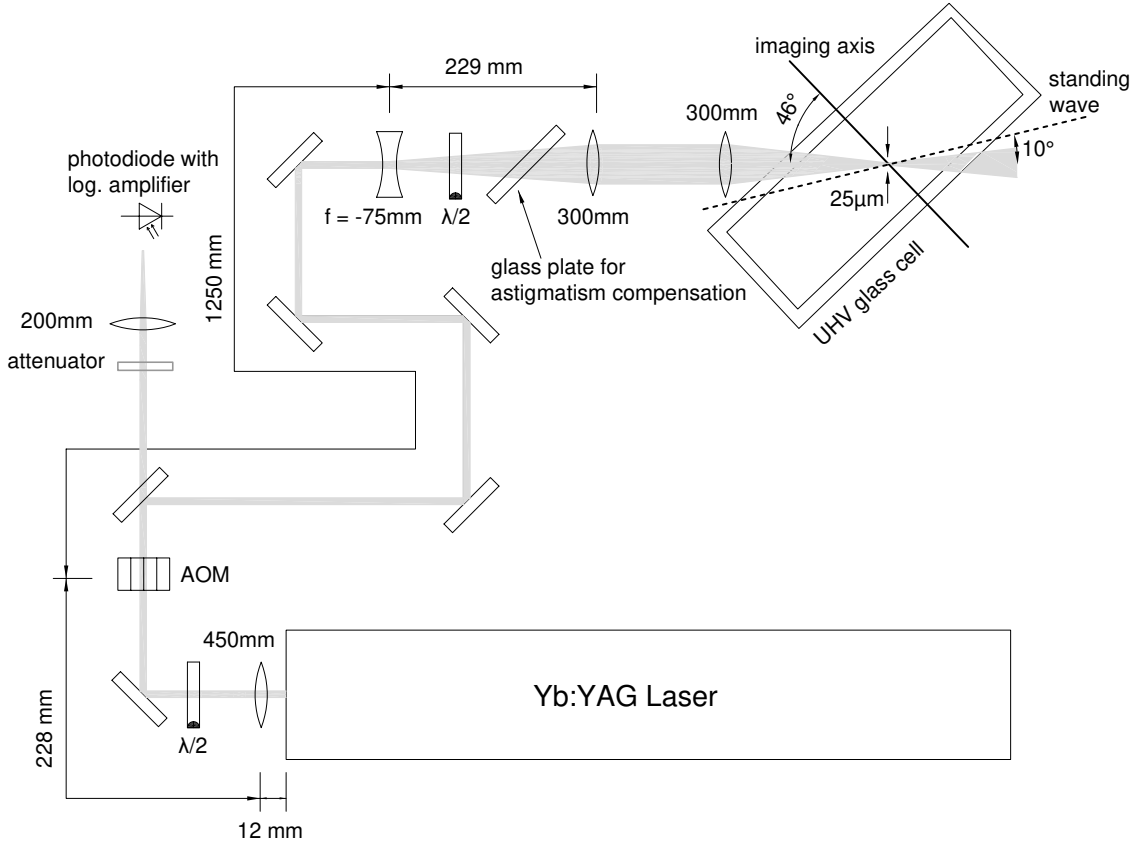


**Figure 4.7:** Setup for the focused beam dipole trap

### Trap setup

For the focused beam trap a 15-W Yb:YAG laser emitting its light at 1030 nm is used (VersaDisk by ELS). Focused to a waist of  $w_0 = 23 \mu\text{m}$ , one can achieve a trap depth on the order of 1 mK. The optical setup for the focused beam is shown in Fig. 4.7. For forced evaporative cooling, the power has to be reduced tremendously, which is done using an AOM. A lot of care has to be taken to align the AOM such that it induces only minor astigmatism in the diffracted beam and only insignificant beam deviations while changing the diffracted power drastically. In a test setup outside the UHV glass cell we measured a beam waist of  $23 \mu\text{m}$  and  $25 \mu\text{m}$  in the vertical and horizontal axes, respectively, with no noticeable astigmatism at very low laser power. At power levels above 1% of the total power, the minimum waist travels by as much as  $300 \mu\text{m}$  caused by thermal effects in the AOM. Another source of astigmatism is our glass cell that our focused beam crosses at an angle of about  $46^\circ$ . This induces an astigmatism of several hundred micrometers on the tightly focused beam. We compensated for this by inserting a fused silica glass plate into the beam where it is expanding (see Fig. 4.7).

#### 4 Experimental setup

The calculated trap parameters in our focused beam trap are

$$\omega_{\text{rad}}/2\pi = \frac{1}{\pi w_0} \sqrt{\frac{U_{\text{dimple}}}{m}} = 369 \text{ Hz } \mu\text{K}^{-1/2} \times \sqrt{\frac{U_{\text{dimple}}}{k_{\text{B}}}} \quad (4.13)$$

and

$$\omega_z/2\pi = \frac{1}{\lambda} \sqrt{\frac{U_{\text{dimple}}}{m}} = 5.19 \text{ Hz } \mu\text{K}^{-1/2} \times \sqrt{\frac{U_{\text{sw}}}{k_{\text{B}}}}. \quad (4.14)$$

A 1 mK deep trap then has the trap frequencies  $\omega_{\text{ax}} = 164 \text{ Hz}$  and  $\omega_{\text{rad}} = 16.2 \text{ kHz}$ .

#### Transfer of atoms from the standing wave

The focused beam is installed at a relative angle of about  $10^\circ$  with respect to the standing wave trap, the smallest angle possible in our setup to get a maximum overlap between the two traps. A false color image of the calculated trapping potential is shown in Fig. 4.8. The overlap of the two traps of about 1 mm is just enough to transfer almost all the atoms from the standing wave into the focused beam trap. The timing for the transfer from the standing wave trap into the dimple trap did not seem to be critical, we load about 2 million atoms into the trap. We ramp up the power in the focused beam trap within 2 s after switching off the MOT. After 1 s, we turn off the standing wave trap in a 1-s ramp. During the transfer of the atoms we apply a magnetic field of 300 G to achieve efficient collisional loading. Loading the focused beam directly from the MOT resulted in a much lower number of atoms, the intermediate step loading the standing wave is indeed crucial!

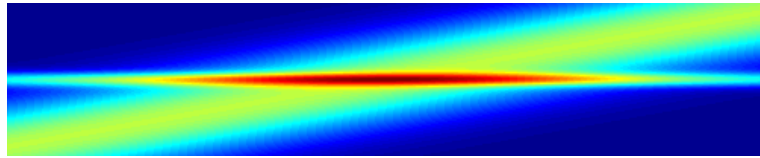


**Figure 4.8:** False color image showing the calculated potential in the combined focused beam and standing wave traps. The size of the image is  $2 \times 0.4 \text{ mm}^2$ . Note that due to the standing wave structure the particles are localized in the lattice direction, the maximum trap depth along the lattice is shown.

#### Magnetic confinement

At very low trapping power, the trapping potential is no longer determined only by the light intensity of the trapping beam, but also by residual magnetic field gradients and gravity. The weak axial confinement of the dipole trap is especially susceptible to such

### 4.3 Optical dipole traps

distortions, and in fact, the magnetic offset field applied in most of our experiments has a curvature that gives rise to an additional trapping potential which is

$$U_{\text{mag}} = -\frac{1}{2}\mu B'' x^2, \quad (4.15)$$

where  $x$  is the axial direction of the trap and  $\mu = \mu_B$  is the magnetic moment of our atoms at high magnetic field. From this, one can calculate the trap frequency to be

$$\omega_{\text{mag}} = \sqrt{\frac{\mu_B B''}{m}} \quad (4.16)$$

The curvature of the magnetic field is calculated to be  $B'' = -0.0255 \text{ cm}^{-2} \times B$  in the horizontal plane. As the optical trap and the magnetic field are centered precisely in the horizontal plane, the optical and the magnetic trap frequencies can be added quadratically.

#### Measured trap parameters

We measured the trap frequencies experimentally by observing the sloshing motion of our atomic cloud in our trap and calibrated the trap frequencies to be [Rie04, Bar04a]

$$\omega_{\text{ax}} = \sqrt{\omega_{\text{dip}}^2 + \omega_{\text{mag}}^2} = 2\pi \sqrt{\frac{0.6B}{\text{G}} + \frac{0.94P}{\text{mW}}} \text{ Hz}, \quad (4.17)$$

$$\omega_{\text{rad}} = 2\pi 110 \text{ Hz} \sqrt{P/\text{mW}}, \quad (4.18)$$

and the trap depth is

$$\frac{U_{\text{at}}}{k_B} = \frac{U_{\text{mol}}}{2k_B} = 0.072 \frac{P}{\text{mW}} \mu\text{K}, \quad (4.19)$$

where  $P$  is the laser power in mW and  $B$  is the magnetic offset field in Gauss. This calibration will be used throughout this thesis. Below  $\sim 50$  mW of Laser power, the axial confinement is purely magnetic and provides a perfectly harmonic potential with a trap frequency of  $\omega_{\text{ax}} = 2\pi(0.6B/\text{G})^{1/2} \text{ Hz}$ . At very low laser power, gravity begins to tilt the trap significantly. This can be compensated for by applying a magnetic field gradient of  $B' = mg/\mu = 1.06 \text{ G/cm}$  in the vertical direction. The applied gradient is optimized experimentally by minimizing trap loss at very low trap depths. During this procedure, any misalignment of the trap with the center of the magnets is also compensated for in the vertical direction. In the horizontal plane, perpendicular to our offset field, no such correction is possible and the trapping beam has to be aligned extremely well with respect to the center of the magnetic field coils, so that the curvature of the magnetic field does not result in a field gradient along the radial axis of the trap.

### 4.3.3 Intensity stabilization

Controlling the intensity of the trapping lasers is a major challenge as for evaporative cooling in optical dipole traps, the power needs to be controlled over a wide range. In all cases we measure the trapping power using a photodiode and use a servo loop to stabilize the intensity using an AOM.

#### Logarithmic amplifier for photodiodes

To measure the photodiode current precisely and reliably over a range of more than four orders of magnitude, we use a logarithmic transimpedance amplifier that converts the photodiode current into a logarithmic voltage. As logarithmic amplifier we use a single chip device by Analog Devices (AD8305). It employs a standard design using two matched transistors to eliminate offset drifts and also uses an active temperature compensation for the logarithmic slope of the transistors which is proportional to absolute temperature. Used in an appropriate way, these devices can be used over more than five orders of magnitude in photodiode current. The logarithmic slope and the DC offset of the voltage output can be set using very few external resistors. These should be selected with care to encompass the range that is needed for the experiment. As for low intensities the  $\sim 10$  MHz bandwidth is reduced and the  $\sim 1\%$  intensity noise increases, the photodiode should be operated at as high as possible maximum intensities. These should typically be on the order of 1-5 mW depending on the sensitivity of the photodiode that is being used. To save the work of designing a new circuit board for the AD8305 we simply use an evaluation board available from Analog Devices, where only a few resistors have to be adapted.

#### Controlling the intensity using an AOM

The signal from the logarithmic amplifier is used to stabilize the intensity of the trapping light using an AOM by adjusting the RF power. It is essential that the RF driver used has enough dynamic range to be able to tune the intensity over the desired range. In our case, we can work with a dynamic range of about 50 dB of RF power, which depends on the characteristics of the AOM. A further complication is the nonlinearity of the feedback loop. This leads to a reduced bandwidth of the stabilization, which is limited in our case to  $\sim 10$  kHz. This is still fast enough for most situations, as a fast switch-off can be realized within  $< 1 \mu\text{s}$  by disabling the RF signal (using the disable input of a CLC410 operational amplifier).

#### Intensity control of the resonator trap

When the intensity in the resonator trap is reduced, the magnitude of the error signal is reduced by the same amount in the conventional Hänsch-Couillaud setup, and

### 4.3 Optical dipole traps

consequently the lock becomes less tight. To circumvent that problem we also use logarithmic amplifiers for the lock setup to obtain the log-ratio of the two diodes instead of the difference. In principle, the error signal is now independent of the intensity.

To control the power in the optical resonator, we monitor the light that is transmitted through the high reflecting mirror of our cavity which has a transmission of  $T \sim 10^{-4}$ . A closed loop feedback system stabilizes the intensity recorded on a photodiode using an AOM as described above. The AOM is adjusted such that its zeroth order is coupled into the resonator. This has the advantage that no intensity is lost due to the finite diffraction efficiency at full power. The beam profile of the zeroth order deteriorates when light is diffracted into higher orders by increasing the radio frequency power that is fed into the AOM. In our case however, the optical resonator cleans the mode and inside the resonator only the purely gaussian mode is present. However, the power that can be coupled into higher transverse modes is increased and thus the stability of the resonator lock is less stable at intensities below  $\sim 1\%$ . This can of course be circumvented by using the first order of the AOM, which would reduce the maximum available power by  $\sim 10\%$ .

### 4.4 High-field magnets

To be able to tune the scattering properties of our lithium gas over the full range of interest, we need to apply magnetic fields much larger than 1000 G. To produce such fields at the given constraints of spatial access is not a simple task. The closest that one could get to the atoms is 35 mm, which is given by the glass cell and the titanium support for the resonator mirrors. The main idea behind our coil design is to have as much current carrying copper as possible in the available volume because this will determine the maximum power that is needed. At the same time, the cooling of the wires has to be efficient. To meet these requirements we use flat copper wire from which we made two individual coils with a narrow gap between them as is shown in Fig. 4.9. In this gap, the cooling water circulates, and every single winding has direct contact to the cooling water, which results in efficient cooling. It was a challenge to construct a waterproof case and mounting for such a setup without wasting too much space. After a lot of experimenting with different materials, we made a PVC housing that was sealed using a special, mechanical and thermal shock resistant epoxy glue (Eccobond 45, Emerson & Cuming).

#### Magnetic field design

A very homogeneous field in the trapping region is essential for many experiments as all the trapped atoms should feel the same magnetic field. The best configuration to achieve this requirement is a Helmholtz setup, where the radius of the coils has to match the distance between the coils. Such a setup was not possible in our case because of the limited space. Using a simple seminumeric magnetic field simulation, we optimized the dimensions of our coils to have the lowest possible curvature achievable using the available space. Our coils can be operated continuously at up to 200 A which results in a magnetic field of 1470 G. The power dissipated in the two coils is then 6 kW. The inductance of the two coils is measured to be  $\sim 1.74(9)$  mH. As the housing of the coils is made from PVC, Eddy currents are avoided, which in principle can enable very fast controlled switching of the magnetic fields, limited only by the coil's inductance.

As the distance between the coils is larger than for a Helmholtz configuration, the magnetic field in the center of the coils now has a field minimum in the axial (vertical) direction and a maximum in the radial (horizontal) plane. The curvature of the magnetic field is proportional to the total magnetic field and was calculated to be  $0.0510 \text{ cm}^{-2}$  and measured to be  $0.0515(15) \text{ cm}^{-2}$  in the vertical direction before the coils were installed. In the radial direction, the curvature is exactly half as large due to the radial symmetry. While these values were estimated to be negligible for most experiments in the standing wave trap that were planned when designing the coils, it turned out that the magnetic potential that the atoms see due to the curvature is



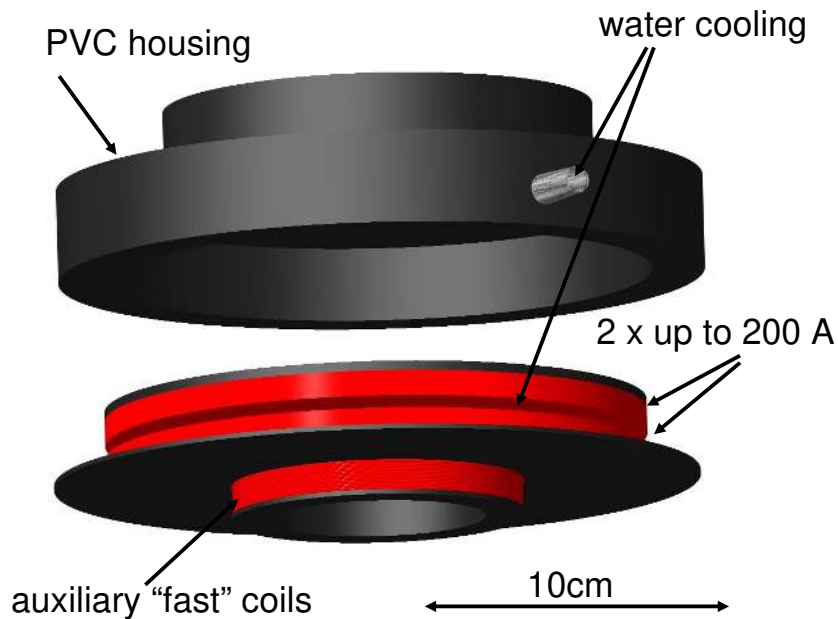


**Figure 4.9:** Drawing illustrating the coil design. Two individual coils made from flat 8×1-mm wire are placed at a distance of 2.5 mm from each other. The gap is used for efficient water cooling. The coils are installed in a water proof PVC housing. As there was still some space available very close to the glass cell, we added a small second coil which is not water cooled. Because of their small size they can be used for fast switching magnetic fields up to 300 G

essential for the experiments in the very shallow focused beam trap. Here, the axial optical confinement becomes extremely weak once the trap is reduced for evaporative cooling and at very low trap depth, the weak axial optical confinement can be neglected compared to the magnetic confinement. The details of the magnetic confinement are discussed in 4.3.2.

#### Auxiliary coils for fast switching

Between the large magnetic field coils and the mount for the optical resonator, there is space for another small coil. It consists of 322 windings of a 0.55 mm-wire and is not water cooled. But for a short time <1 s, this coil can produce fields in excess of 300 G in Helmholtz configuration and magnetic field gradients of >100 G/cm in anti-Helmholtz configuration at a current of 6 A. The dissipated power is at the above values ~200 W. Continuous operation is possible up to currents of 0.5A, producing a field of 25 G or alternatively 8.5 G/cm. The main advantage of these coils is that due to their small dimensions, they allow a fast switching of the magnetic fields over a considerable range. Due to the large amount of windings, the inductivity of the coils

#### 4 Experimental setup

is 23 mH, but as the coils produce  $\sim 50$  G/A, one can achieve magnetic field ramps in excess of 100 G/ms with a 80 V-5 A power supply. So far, these coils have only been used to compress the MOT during the transfer into the dipole trap and to apply precisely controlled magnetic field gradients to compensate for gravity and for residual magnetic field gradients that stem from a slight misalignment of the large coils with respect to the dipole trap in the vertical direction.

##### **Current and magnetic field stability**

A very high magnetic field stability is desired for many applications, such as radio frequency transitions, or controlling the scattering length near the  $\sim 100$ -mG wide Feshbach resonance at 543.3 G [O'H02b, Str03]. To drive coherent RF-transitions between different hyperfine states, the width of the transition has to be much smaller than its Rabi frequency. To achieve a high current stability in our offset field coils, we make use of the fact that the voltage programming bandwidth of our power supplies is much larger ( $\sim 1$  kHz) than the inductance-limited bandwidth of our coils, which is  $\sim 130$  Hz. We use a  $10^{-6}$ -precision current transducer (IT 600-S, LEM) to divide the 0-200 A primary current by a factor of 1500. This current is then converted into a  $\pm 10$  V signal to match the output of our D/A converter to which it is compared. The resulting error signal is used by a PID-controller to adjust the voltage of the power supply. Using this method, we achieve an accuracy of  $\pm 3$  mA or 22 mG, which corresponds to one single bit of the D/A-converter. By driving radio frequency transitions from the high-field seeking to the low-field seeking ground states, we calibrated our magnetic field. When the applied radio frequency is resonant with an allowed transition, we observe a loss of atoms that is due to spin changing collisions (see Fig. 4.10). From the corresponding radio frequency we can then infer the magnetic field the atoms experience using the Breit-Rabi formula A.2. From the width of the transitions we found that the magnetic field is as stable as our current, corresponding to 22 mG. This means that stray magnetic fields do not contribute significantly to the field stability in our setup.

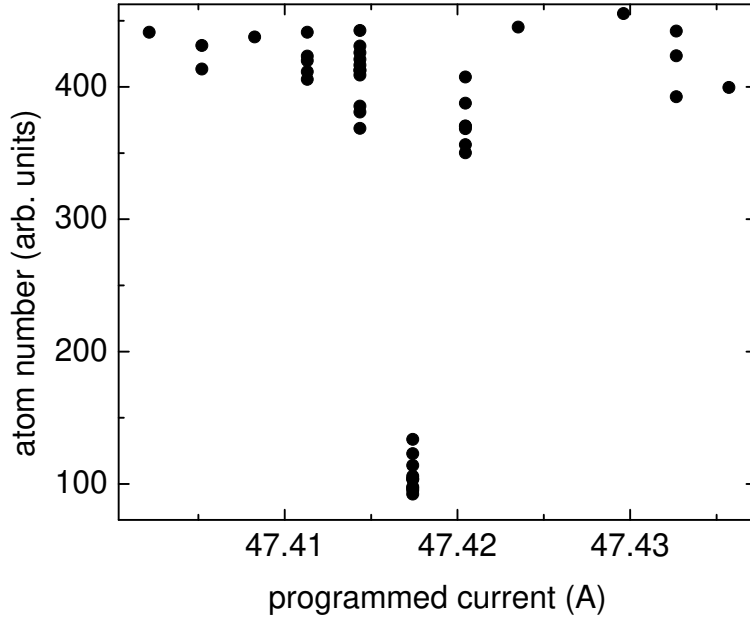


**Figure 4.10:** Remaining number of atoms after a 100-ms RF pulse with a frequency of 1141.99 MHz for varied magnetic field. For the transition from state  $|1\rangle$  to state  $|6\rangle$ , this frequency corresponds to a magnetic field of 349.334 G. The horizontal separation of the data points corresponds to a single bit of the 16-bit D/A-converter that we use, it corresponds to 3 mA of current and 22 mG of magnetic field.

## 4.5 Diagnostic tools

### 4.5.1 Fluorescence measurement

The most important parameter to know in our experiments is the total number of particles. The simplest and most robust way to measure the number of atoms present is to capture them in the MOT and to measure their fluorescence. A calibrated photodiode detects the light that is scattered at a rate  $\gamma_{\text{MOT}}$  per atom and collected from a solid angle  $\Omega$  using a lens with an aperture of  $d = 22$  mm placed at a distance of  $r = 70$  mm. The number of atoms is then determined by

$$N = \frac{\gamma_{\text{PD}}}{\gamma_{\text{MOT}}\Omega}, \quad (4.20)$$

where  $\gamma_{\text{PD}}$  is the rate of photons hitting the photodiode.

#### Photon scattering rate $\gamma_{\text{MOT}}$

It is rather difficult to estimate the photon scattering rate of atoms trapped in a MOT because the polarization of the atoms, their velocity distribution and other parameters are not well known. However, the maximum possible photon scattering rate is given by half the natural linewidth which is given by  $\gamma_{\text{max}} = \Gamma/2 = 2.95$  MHz for lithium. This limit can be approached by strong saturation and small detuning and provides an upper bound for the photon scattering rate. We usually measure the fluorescence of our atoms in a MOT about 3 MHz detuned from the atomic resonance. To estimate by how much  $\gamma_{\text{MOT}}$  is smaller as compared to  $\gamma_{\text{max}}$  we compare the fluorescence measured at constant detuning with the maximum value that is obtained while quickly ramping the laser frequency across the resonance. This maximum is observed to be a factor of  $1.43 \pm 10\%$  higher than the fluorescence at our constant detuning. Thus, we can be sure that

$$\gamma_{\text{MOT}} < \frac{1}{1.43} \gamma_{\text{max}} \pm 10\%, \quad (4.21)$$

which provides an upper limit of the scattering rate for our measurement at small detuning. To get a good estimate for the actual scattering rate, we tried to estimate the effective saturation  $S_{\text{eff}}$  of our atoms by measuring how the fluorescence changes when the intensity in the MOT beams is reduced to a fraction  $p$  of the total power and fitting it to the formula  $\gamma \propto pS_{\text{eff}}/(1 + pS_{\text{eff}})$ . From this we conclude that the saturation on resonance at maximum power is  $S_{\text{eff}} \sim 2.44 \pm 0.4$ . This means that the photon scattering rate on resonance is reduced by a factor of  $0.71 \pm 5\%$  as compared to the saturated transition. Therefore the effective photon scattering rate per atom can be estimated to be in our case

$$\gamma_{\text{MOT}} = 0.71/1.43 \times \gamma_{\text{max}} \pm 12\% \quad (4.22)$$

### Solid angle $\Omega$

The solid angle is readily determined from the aperture  $d = 22 \text{ mm} \pm 3\%$  of the lens and its distance  $r = 70 \text{ mm} \pm 10\%$  from the MOT. It is

$$\Omega = \frac{(d/2)^2}{4r^2} = 6.2 \times 10^{-3} \pm 21\%. \quad (4.23)$$

### Calibration of the photodiode to measure $\gamma_{\text{PD}}$

We calibrated our photodiode by two different techniques. Using the known sensitivity of the photodiode from the datasheet (Hamamatsu S-1223), which is  $0.46 \text{ A/W}$  at  $670 \text{ nm}$ , and multiplying that with the transconductance gain of the amplifier, which is  $47 \text{ V}/\mu\text{A}$ , we obtain a sensitivity of  $46.3 \text{ nW/V}$ . The effective sensitivity is still derated by a factor of  $0.85$  due to four uncoated glass surfaces, which lead to an effective sensitivity of  $54.3 \text{ nW/V}$ . In a second approach we used a laser beam with a power measured using a commercial power meter (Newport 835 with head 818/UV). Using this method we obtained an effective sensitivity of  $77.5 \text{ nW/V}$  taking into account the losses on two glass surfaces. We could also confirm the linearity over the whole range of interest for the experiment. The main uncertainty in the first method is the transconductance gain, which is determined by a  $47 \text{ M}\Omega$ -resistor that probably has a lower effective resistance. For the second method, the main error comes from the power measurement, which has a specified accuracy of  $2\%$ , so this one is much more reliable. Given the photon energy of  $hc/\lambda$ , we get

$$\gamma_{\text{PD}} = 2.61 \times 10^{11} \text{ photons s}^{-1} \text{V}^{-1} \pm 2\%. \quad (4.24)$$

In summary, we can give a lower bound for the atom number calibration which is

$$N_{\text{min}} = 2.1 \times 10^7 \text{ atoms/V} \pm 23\% \quad (4.25)$$

and a “best guess” atom number of

$$N = 2.85 \times 10^7 \text{ atoms/V} \pm 24\%*. \quad (4.26)$$

## 4.5.2 Absorption imaging

To image our atoms we use the well established technique of absorption imaging [Ket99]. The basic idea of this method is to image the intensity profile of a resonant laser beam that has been partially absorbed in the atomic cloud, and to deduct the column density  $\tilde{n}(x, y) = \int n dz$  from the transmitted light, where  $n$  is the atomic density. This method has the important advantage that in principle, the atomic column density can be determined only by taking the ratio of the intensity in two images, where most

---

\*Note that for most of our measurements, this signal was amplified  $10\times$  before being digitized, the effective conversion is then  $N = 2.85 \times 10^6 \text{ atoms/V} \pm 24\%$ .

#### 4 Experimental setup

systematic effects like the unknown sensitivity of the detector, losses on windows etc. drop out. In general, the relative transmission is simply given by

$$\frac{I}{I_0} = \exp(-\tilde{n}\sigma), \quad (4.27)$$

where  $\sigma$  is the absorption cross section, which is

$$\sigma = 3\lambda^2/2\pi \quad (4.28)$$

for a two-level system. The column density can then be obtained as

$$\tilde{n} = -\frac{1}{\sigma} \ln \frac{I}{I_0}. \quad (4.29)$$

Imaging lithium atoms is more delicate than the other, heavier alkali atoms for the following two reasons:

- Atoms are driven out of the atomic resonance by scattering only a few photons because of the large recoil energy.
- A strong repumper is required at low magnetic field to keep the atoms in resonance with the imaging beam, because there is no closed transition available at low magnetic field.

In our first imaging setup we used light resonant with the  $F = 3/2$  to  $P_{3/2}$  transition that is normally used to operate the MOT (see chapter A.2). This restricted us to imaging the atoms near zero magnetic field. To image our atoms in the  $F = 1/2$  ground state, the MOT repumping light was switched on a few microseconds before the imaging pulse. The timing in this setup was very complicated because it involved the time critical switching of several mechanical shutters.

In our experiments it proved to be rather important to be able to instantaneously image our atoms at large magnetic field over the whole width of the Feshbach resonance. For this purpose we set up a new imaging laser that can be frequency tuned over a wide range of  $\pm 1.8$  GHz with respect to our frequency reference laser. A detailed description of the setup will be given in [Rie04]. Besides the fact that the atoms can now be imaged at any magnetic field of interest for our experiment, the atoms are also imaged depending on their nuclear spin, so the actual spin mixture of the gas can be determined by imaging the two components separately. A closed  $\sigma^-$ -transition exists from our  $2S_{1/2}, m = -1/2$  state to the  $2P_{3/2}, m = -3/2$  (see appendix A.2). The magnetic moments of these two states are one and two Bohr magnetons, respectively. This means that the optical transition tunes by  $-\mu_B = -1.4$  MHz/G. To drive this  $\sigma^-$  transition with the proper polarization, one would have to use properly polarized light along the magnetic field which defines the quantization axis. As the axis parallel to the

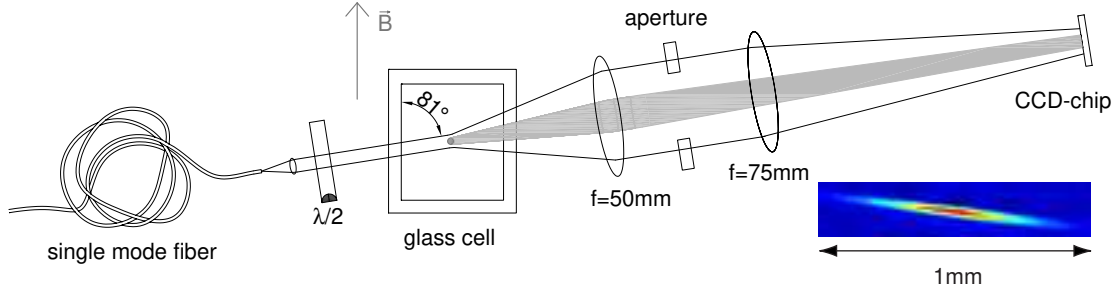


**Figure 4.11:** Optical setup of the imaging system. The two lenses result in a 1.5 $\times$ -magnification. The image in the right corner shows a typical *in situ* image of a cloud of trapped particles in the focused beam trap.

magnetic field is already used by a MOT beam, the imaging beam is set up at an angle of  $\alpha = 81^\circ$  degrees with respect to the symmetry axis (see fig. 4.11). The transmitted intensity in such a setup is calculated in ref. [Geh03a] and is given by

$$\frac{I}{I_0} = \left[ \frac{1}{2\zeta} (e^{-\tilde{n}\sigma\zeta} - 1) + 1 \right], \quad (4.30)$$

where  $\zeta = (1 + \cos^2 \alpha)/2$ . For typical imaging parameters where  $I/I_0 \geq 0.5$ , the formula 4.30 with our  $\alpha = 81^\circ$  can be approximated by the case where  $\alpha = 90^\circ$  with an error of less than 1 %. The formula then becomes

$$\frac{I}{I_0} = \exp\left(\frac{-\tilde{n}\sigma}{2}\right), \quad (4.31)$$

which is the same as 4.27 except for the factor 1/2 in the exponent. This means that in this configuration, the optical cross section is a factor of two lower compared to a setup where the light is properly polarized. So far, all of our images have been analyzed using 4.31. The observed atom number per pixel is  $N_{x,y} = \tilde{n}A_{\text{pix}}$ , where  $A_{\text{pix}} = (5\mu\text{m})^2$  is the area of one single pixel. To obtain the total particle number, one just has to sum over all pixels.

The optical setup of the imaging system is shown in Fig. 4.11. The beam coming from a single mode polarization maintaining fiber is collimated by a 35 mm-lens to form a beam with a diameter of approximately 0.8 cm and a power of a few  $10\mu\text{W}$ , well below saturation. This ensures a homogeneous intensity at the center of the beam. The imaging optics consist of two achromatic doublet lenses (Casix) with a focal length of 50 mm and 75 mm, respectively and a diameter of 25 mm. They are mounted in an adjustable focus lens tube setup (SM-series, ThorLabs), the active aperture being defined by an iris diaphragm (SM1D12, ThorLabs). Its maximum aperture of 12 mm results in a calculated diffraction limit of  $3.4\mu\text{m}$ . In the experiment, the resolution is limited to  $\sim 10\mu\text{m}$  by lens aberrations. The 1.5 $\times$ -magnification leads to an imaging

## 4 Experimental setup

pixel size of  $5\text{ }\mu\text{m}$  calculated from the  $7.5\text{ }\mu\text{m}$ -pixel spacing of the CCD chip (FT18, Philips; Camera: SIS1-p18, Theta System). This magnification was tested to be correct within 1% using the ruler of a microscope slide.

For most of our experiments, *in situ* imaging is preferred over time-of-flight imaging, because the axial magnetic confinement cannot be switched off without switching off the magnetic field. Thus, by switching off the dipole trap the cloud is only released radially and quantitative information is hard to extract. A typical *in situ* image in our focused beam dipole trap is shown as an inset of Fig. 4.11. The image is 200 pixels wide and thus represents a 1 mm-range. As is the case for most of our images, the spread of the cloud in the radial direction is only a few pixels wide and cannot be resolved accurately by the imaging optics. Thus, *in situ* imaging only provides information on the axial direction in our setup. For analysis of the axial density profile, we simply integrate the images in the vertical direction. To obtain the right scaling, the viewing angles have to be compensated for: The focused beam trap in which most images are taken is positioned at an angle of  $46^\circ \pm 1^\circ$  with respect to the camera in the horizontal plane. Neglecting any effect of the finite radial size of the cloud, which is a very good approximation in most cases, the real axial size is obtained by multiplying the size of the vertically integrated profile by a factor of  $1/\sin 46^\circ = 1.39 \pm 1.5\%$ . In Fig. 4.11, one can see slight interference fringes along the radial direction of the cloud. These can become quite a bit stronger, if the cloud is strongly compressed in a deep trap and its radial size becomes comparable to the wavelength. In this case it is advisable to release the particles from the trap a few hundred microseconds before the image is taken to let the cloud expand over a few micrometers.

It is interesting to note that very weakly bound molecules can be imaged using the same technique with no noticeable frequency shift of the optical transition (see section 7.2.1).

A mystery remains in the atom number measurement from the absorption images as the numbers calculated from the images are a factor of 4-8 smaller than the numbers obtained from the fluorescence measurement. A careful analysis of the source of error has not yet been done. As the fluorescence measurement is pretty robust and the results obtained in chapter 7 are inconsistent with such low atom numbers we calibrate the absorption images with the atom numbers obtained with the fluorescence measurement.

### 4.5.3 Microwave and radio frequency transitions

Radio frequency spectroscopy can provide useful information on the properties of the weakly bound molecules near a Feshbach resonance. The technique of photodissociating weakly bound molecules was first used in D. Jin's group at JILA [Reg03]. The main idea is that the transition frequency for a free atom is increased by the binding energy if a transition is driven from an atom that is initially in a bound state to an free



atom in a different hyperfine state. The distribution of final momentum states of the two dissociated atoms, provide information on the relative momentum distribution of the two bound atoms and thus the molecular wave function. This momentum spread is reflected in a characteristic broadening of the bound-free transition, which can be used to reconstruct the wave function. Well above 30 G, our lithium atoms are in the Paschen-Back regime, and we can either drive transitions flipping the electron spin or transitions flipping the nuclear spin, which are obviously much weaker. As the electronic transition tunes with two Bohr magnetons in the magnetic field, it is highly sensitive on the magnetic field stability, and the transition frequency at 1000 G is already 2.8 GHz. Our 20 mG magnetic field stability provides a resolution of  $2\mu_B \times 20 \text{ mG} \approx 50 \text{ kHz}$ . A much higher resolution can be obtained by flipping nuclear spins. At high magnetic field the transition frequencies are on the order of 80 MHz. For these transitions, we were able to observe peaks as narrow as 160 Hz. This high-precision technique proved to be a valuable tool for observing the pairing gap in the BEC-BCS crossover regime. It will be described in detail in [Bar04a].



# Chapter 5

## Tuning elastic collisions

In this chapter our study of elastic collisions in a thermal gas of our optically trapped spin mixture is described [Joc02]. Because of the small atom numbers that could be achieved for these experiments, our  $^6\text{Li}$  gas obeys classical statistics. The collisions however are governed by quantum mechanical low-energy scattering as described in chapter 2.1 at our temperatures below  $\sim 500\mu\text{K}$ . In this regime, only zero angular momentum  $s$ -wave scattering is relevant. It can be described by one single parameter, the scattering length  $a$ . In our experiments, we were able to tune the scattering length using the Feshbach resonance described in chapter 2.2 by applying an external magnetic field. We could observe the associated scattering cross section to vary between the fundamental maximum of  $\sigma_{\text{max}} = 4\pi/k^2$ , which is given by the unitarity principle, and exactly zero, where the scattering length crosses zero. The magnetic field value where this zero crossing occurs could be determined to be at 530(3) G and helped theorists to improve their calculations on the scattering length. Similar experiments were performed at the same time by O’Hara *et al.* in John Thomas’s group [O’H02b]. Their results are in full agreement with our findings.

For the experiments presented in this chapter the major experimental challenges were the following:

- The magnetic field coils to produce magnetic fields of up to 1500 G to cover the whole range of magnetic fields near the 834-G Feshbach resonance.
- No imaging of the atoms was available. Consequently, alternative methods to measure the temperature other than the established time-of-flight method had to be found. In fact, all the results presented in this chapter were obtained by measuring the atom number using a photodiode!
- By always taking data points in a random sequence and by sophisticated averaging of drifts, signals could be obtained that were often smaller than the noise level and relatively large drifts in atom number, which occurred over a period of typically 30 min.

## 5.1 Elastic collisions

The most established technique to determine the scattering cross section in a trapped ultracold gas is to excite the gas in one axis, and then observe the thermalization of the gas by measuring the temperature in another axis of the trap [Mon93, Lof02]. However, this technique was not suited for our standing wave trap, because the temperature in the lattice direction can not easily be derived from time-of-flight measurements.

Our approach was to start with an initially nonthermal ensemble of atoms with a thermal energy that is not much lower than the trap depth. When thermalization occurs, atoms are evaporated from the trap, reducing the temperature of the remaining gas. From the dynamics of this process, one can obtain information on the scattering cross section [Chi00]. An important advantage of this technique is that one is able to observe thermalization at very low scattering rates even much lower than the trap frequencies, where the above method fails because of ergodic mixing of the different degrees of freedom. Also, this technique is very easy to implement, because no imaging of the atoms is necessary as the main parameter to look for is a drop in particle number. On the other hand, it is very hard to actually extract numbers for a cross section as this would require careful modelling of the evaporation process.

### Resonant scattering cross section: What do we expect?

In the following, a few key points of section 2.1 are recalled: For most experiments with ultracold alkali atoms the scattering cross section for nonidentical particles can be approximated by the zero energy limit

$$\sigma = 4\pi a^2, \quad (5.1)$$

which holds as long as  $k^2 a^2 \ll 1$ . Obviously, in the vicinity of a Feshbach resonance, this condition is no longer fulfilled and the scattering becomes energy dependent. It can be described by

$$\sigma = 4\pi \frac{a^2}{1 + k^2 a^2}, \quad (5.2)$$

assuming that one can approximate the scattering potential to be point-like. This equation finally yields the unitarity limited cross section

$$\sigma_{\max} = \frac{4\pi}{k^2}, \quad (5.3)$$

when  $k^2 a^2 \gg 1$ .

From 5.2 it is obvious that very close to the Feshbach resonance, where the scattering length diverges, the scattering cross section will be unitarity limited even for very small temperatures. The collisions that we observe using our method described

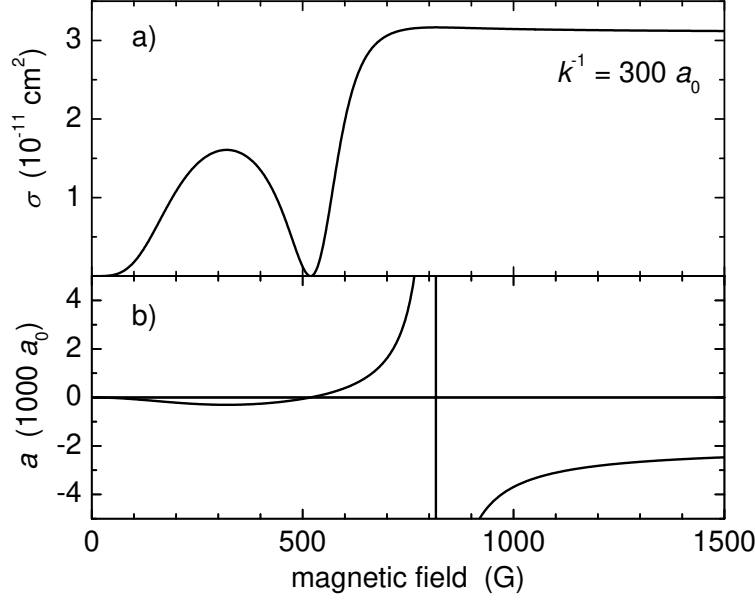


**Figure 5.1:** a) Calculated scattering cross section assuming the theoretically predicted scattering length b) and a collision velocity of  $k = (300 a_0)^{-1}$ .

above are collisions that lead to evaporation. Thus, it can be expected that the collision energies that we observe are on the order of the trap depth. A Monte Carlo simulation of our system that was done by Allard Mosk showed that the mean energy for collisions ejecting particles from the trap is about  $k_B \times 500 \mu K$ , slightly more than half the  $k_B \times 750 \mu K$  trap depth. Using this collision energy, which corresponds to  $k = (300 a_0)^{-1}$ , we calculate the expected scattering cross section from the theoretically expected scattering length using 5.2. The result is shown in Fig. 5.1.

## 5.2 Experimental procedure

### Starting conditions

We loaded typically  $5 \times 10^5$  atoms into our standing wave trap from the MOT that contained  $\sim 10^7$  atoms after a 10-15 s loading time. This resulted in about 350 atoms per lattice site in the central region of the trap, assuming a gaussian distribution of the atoms along the lattice with a width of  $\sigma \sim 0.4$  mm. The transfer of the unpolarized sample in the MOT leads automatically to an equal 50-50 mixture of the  $F = 1/2, m_F = \pm 1/2$  states, when the repumping light of the MOT is switched off just a few milliseconds before the cooling light. The atom number in the dipole trap is measured by quickly switching on the MOT and thereby recapturing the atoms, recording their fluorescence (see section 4.5.1).

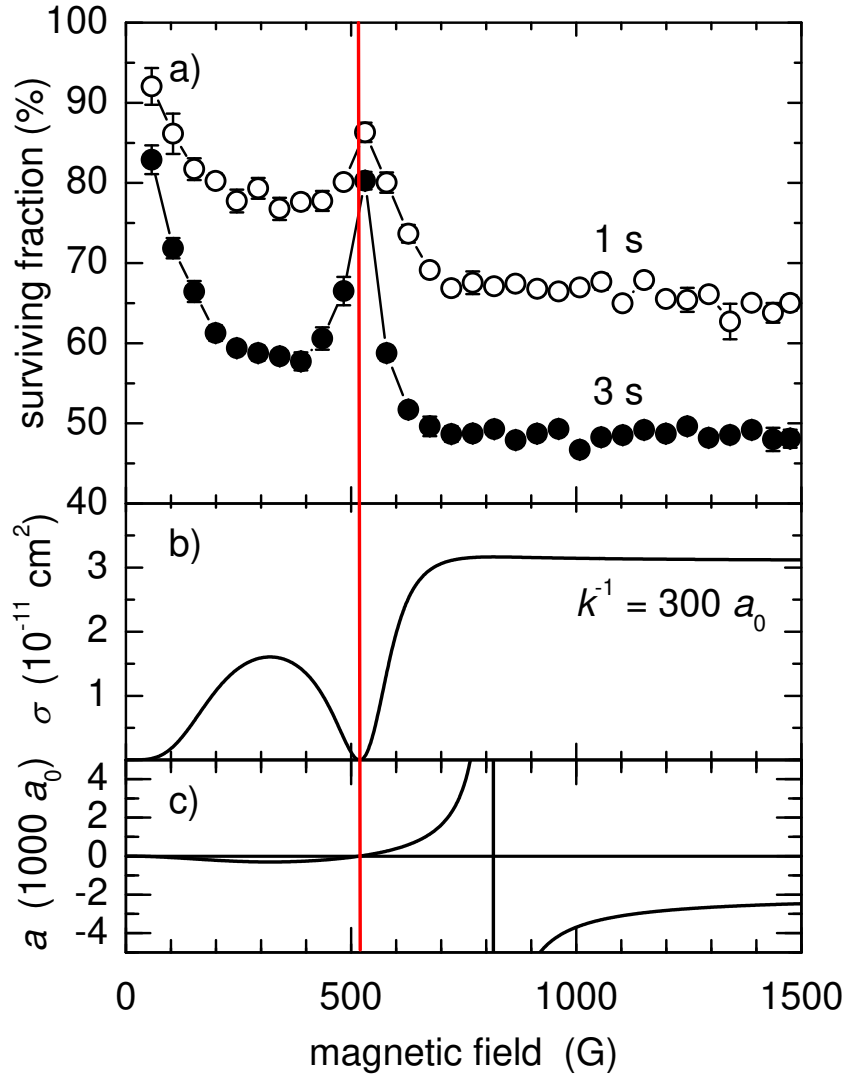


**Figure 5.2:** a) Evaporative loss measurements at constant trap depth over the full accessible magnetic field range. The data show the measured number of particles in the trap after 1 s (○) and 3 s (●) of plain evaporation. For comparison, Figs. b) and c) show again the expected scattering cross section and the scattering length.

### Plain evaporation

To study the dependence of the scattering cross section on the magnetic field, we loaded our dipole trap and then quickly applied a magnetic field in the range of 0-1500 G in a 100-ms ramp while keeping the trap depth constant at  $k_B \times 750 \mu\text{K}$ . After holding times of either 1 or 3 s we measured the number of atoms remaining in the trap. Figure 5.2(a) shows the result of about 1000 individual data points taken at 31 different magnetic field values. The error bars shown in the figure represent the statistical

fluctuations. To minimize the effects of any systematic drifts of the apparatus during the 6 h-acquisition time, the data points were taken in random order. The observed evaporation loss in Fig. 5.2(a) shows a pronounced dependence on the magnetic field which we compare with the expected cross section for elastic collisions ejecting atoms out of the trap (5.2(b)). After being very small at low magnetic fields, the loss increases for fields up to  $\sim 350$  G where an expected local maximum of evaporative loss is observed. The loss then decreases and disappears at about 530 G as a consequence of the predicted zero crossing of the scattering length. Here the slight observed loss in the 1 s curve is explained by the finite ramp time of the magnetic field. In the 100 ms ramping time some evaporation does already take place. At 530 G the decrease of the trapped atom number between 1 s and 3 s is fully explained by rest gas losses without any further evaporation. For higher magnetic fields evaporative loss rapidly rises until it levels off at about 700 G. Up to the maximum attainable value of 1.5 kG high evaporation loss is observed. A slight decrease of the atom number for fields exceeding 1 kG occurs which we attribute to technical reasons; we observed an increasing noise for currents higher than  $\sim 130$  A in the error signal of the resonator lock of the standing wave trap. The relatively large and constant evaporative loss for fields exceeding 700 G is consistent with the predicted behavior of the cross section.

### Temperature measurements

To confirm that the loss observed in the measurements presented above is actually due to evaporation, it is necessary to measure the temperature change of the gas while the losses occur.

Unfortunately, at the time we performed these measurements, we did not have absorption imaging implemented, so we were not able to use the standard technique of time-of-flight imaging to measure the temperature. For this reason we used a method that relies on controlled spilling of our atoms from the trap. We first switch off the magnetic field to avoid thermalization of the cloud and then reduce the trap depth adiabatically in a 1-s exponential ramp to spill atoms above a certain, well defined energy. We can fit the remaining fraction versus the relative trap depth with a model that takes into account the adiabatic cooling of the cloud while the trap potential is lowered to obtain directly the truncation parameter that is defined as the trap depth divided by the thermal energy,  $\eta = U_{\text{trap}}/k_{\text{B}}T$ . Two examples of such measurements are shown in Fig. 5.3 for the extreme cases of no cooling and plain evaporation for several seconds of evaporation at large magnetic field.

After transfer into the dipole trap, we determined an initial  $\eta$  of 1.9(3). We then looked at the change in  $\eta$  after 3 s of trapping at selected values of the magnetic field. At the zero-crossing at 530 G we observed only a slight increase of  $\eta$  to a value of 2.3(2) which is explained by the unavoidable evaporation during the magnetic field ramps. At 340 G close to the local maximum of  $|a|$  we found an increase of  $\eta$  to 4.2(3)

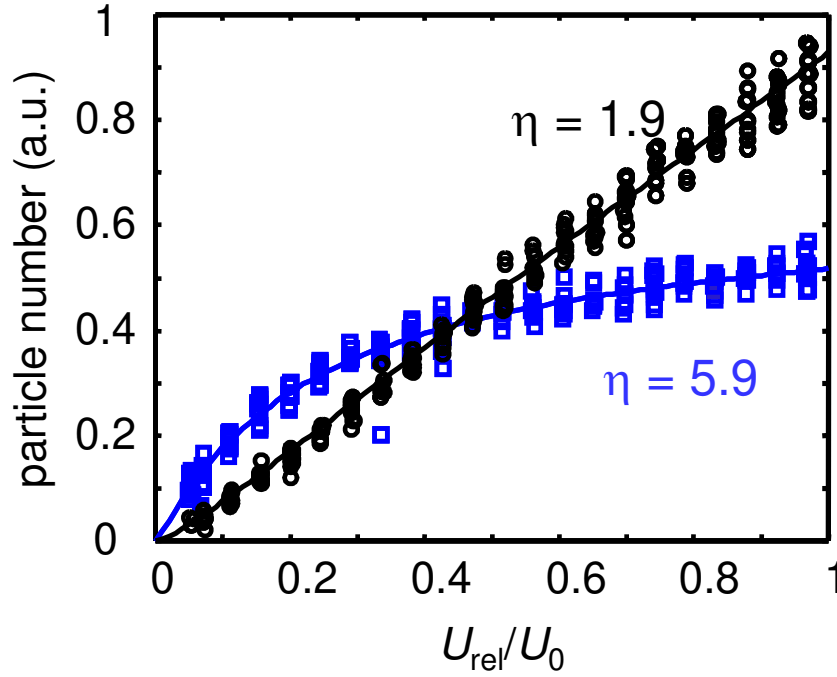


**Figure 5.3:** Determination of the truncation parameter  $\eta = U_0/k_B T$ . The data show the remaining number of particles as a function of trap depth for two different temperatures, before and after evaporative cooling. The solid lines represent calculated curves for  $\eta = 1.9$  and  $\eta = 5.9$ , respectively

as a clear evidence of evaporative cooling. At 720 G, i.e. in the case of a large positive scattering length, we measured a higher value of 5.5(2) showing deeper evaporative cooling. Essentially the same  $\eta$  of 5.3(2) was obtained at  $B = 1290$  G where scattering takes place in the triplet-dominated regime with a very large negative scattering length.

### Forced evaporation

Forced evaporation measurements provided complementary data to plain evaporation and allowed us to rule out a significant role of inelastic collisions. When the trap depth is ramped down, elastic collisions reduce trap loss in contrast to increased loss at constant trap depth. This can be understood by the spilling loss of energetic particles [Lui96]: Without elastic collisions the most energetic particles are spilled out of the trap when its depth is reduced. With elastic collisions the evaporative cooling effect decreases the temperature and thus reduces the spilling loss.

In these forced evaporation measurements we reduced the trap depth in 10 s to 20% of its initial value in an exponential ramp and measured the number of remaining atoms; the results are displayed in Fig. 5.4. At reduced intensity of the standing wave the magnetic field had to be restricted to 1 kG because of an increasing sensitivity of the



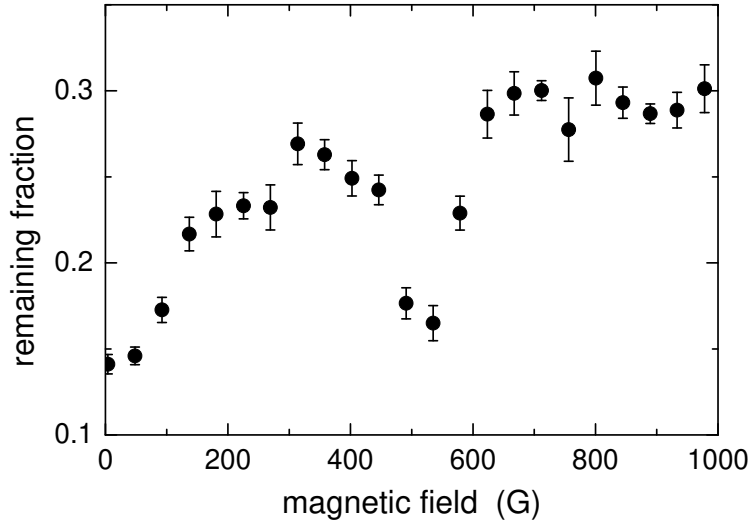


**Figure 5.4:** Fraction of atoms remaining after forced evaporation versus applied magnetic field. The trap depth is ramped down exponentially to 20% of the initial value in 10 s.

resonator lock to current-dependent noise. A minimum number of atoms was measured at 0 G and 530 G instead of the maximum observed with constant trap depth. The largest number of atoms is observed in the high-field region above 650 G as expected for the large scattering cross section.

### Inelastic collisions?

While the above experiments showed a strong dependence of the elastic scattering cross section on the magnetic field, the measurements of the temperature and on forced evaporation rule out significant inelastic loss near the Feshbach resonance that was the main signature of a Feshbach resonance in previous work [Ino98]. However, at much higher densities as compared to ours, other groups had already seen such inelastic loss [Die02, O’H02b] at magnetic field values significantly below the expected Feshbach resonance, at  $\sim 680$  G while working at densities of  $\sim 10^{13} \text{ cm}^{-3}$ . To observe such a loss under our conditions of higher temperature and much lower density we studied the long-time evolution of samples which were pre-cooled by forced evaporation and then recompressed into a  $750 \mu\text{K}$  deep trap to a temperature of  $\sim 150 \mu\text{K}$  and a density of  $5 \times 10^{10} \text{ cm}^{-3}$ . The magnetic field during the 60-s holding time was alternated for successive data points between 680 G and 300 G, the latter value corresponding to a very low loss rate in Ref. [Die02]. We found no significant difference in the number of remaining atoms, which lead to a clear upper bound to the two-body rate constant of  $1 \times 10^{-12} \text{ cm}^3/\text{s}$ . From the fact that we were not able to see any inelastic loss at our low density, we can conclude that for the experiments discussed in this chapter, inelastic

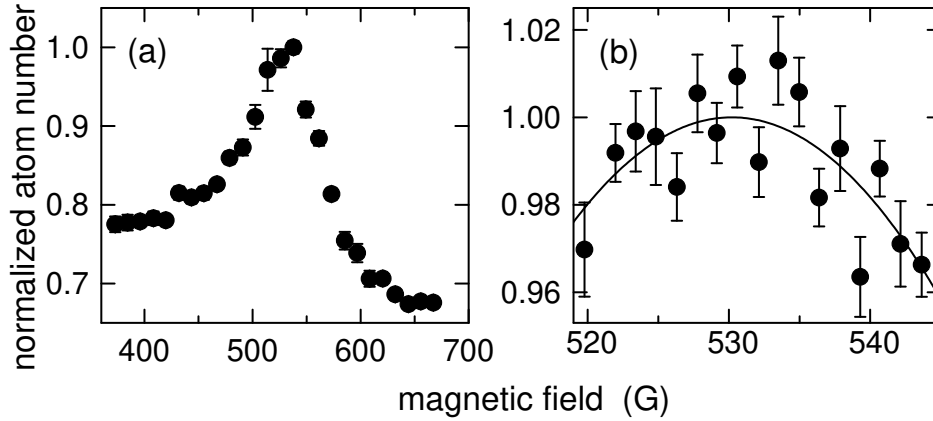


**Figure 5.5:** Accurate determination of the zero crossing of the scattering length. These measurements are performed in the same way as those of the 3 s-measurement in Fig. 5.2(a), but over a narrow range of magnetic fields. The quadratic fit in (b) yields 530(3) G for the zero crossing.

collisions are completely negligible.

### Zero crossing of the scattering length

While the position of the Feshbach resonance could not be determined using the above measurements, the magnetic field value where the scattering length crosses zero could be accurately determined. This value is an important parameter to further constrain the knowledge of the Li-Li potentials [O’H02b]. To determine the position of the zero crossing, we measured the minimum-loss feature of Fig. 5.2 in a closer range of magnetic fields. The data points in Fig. 5.5(a) were obtained from 500 individual measurements at a holding time of 3 s with the magnetic field randomly varied between 30 values in an interval between 370 G and 670 G. The data shown in Fig. 5.5(b) were obtained from 1000 measurements in the very narrow range between 520 G and 544 G. A quadratic fit to the very narrow region in Fig. 5.5(b) allowed us to determine the B-field for minimum evaporative loss to 530(3) G. The uncertainty contains the error from the fit of our data and the uncertainty of the magnetic field, which was 1 G at the time when these measurements were performed. A systematic shift of this value from the position of the scattering length is expected to occur due to the finite collision energy of our atoms. In an intuitive picture, one can imagine that the additional kinetic energy of the scattering state has to be compensated for by the difference in magnetic energies of the scattering and the molecular state. Because at 530 G, the molecular level associated with the Feshbach resonance is still almost singlet in nature, its magnetic moment is almost zero and the main contribution of the Zeeman shift comes from the free atom pair, which has a magnetic moment of two Bohr magnetons. The shift of the zero

## 5.2 Experimental procedure

crossing can thus be estimated to be

$$\Delta B_0 = E_C/2\mu_B = +0.74 \text{ G} \times E_C/(k_B \times 100 \mu\text{K}). \quad (5.4)$$

A more accurate calculation performed by V. Venturi *et al.* yields

$$\Delta B_0 = E_C/2\mu_B = +0.7 \text{ G} \times E_C/(k_B \times 100 \mu\text{K})[\text{Ven01}]. \quad (5.5)$$

For our collision energies, such an expected shift is well within our uncertainty of 3 G. Another source of systematic error would be a magnetic field dependent inelastic loss of atoms as it had been reported by [Die02, O'H02b]. As such a loss would occur above the zero crossing, this would shift the observed loss minimum to a lower magnetic field. But as we did not observe any inelastic loss due to our much lower density, we expect this shift to be negligible, and conclude that within our given uncertainty, our minimum in evaporative loss coincides with the zero crossing of the scattering length at 530(3) G.



## Chapter 6

# Weakly bound molecules near a Feshbach resonance

Research on ultracold molecules witnessed a rapid progress in 2003 after the formation of molecules using a Feshbach resonance was achieved in D. Jin's group at JILA [Reg03]. They established the technique of an adiabatic ramp across the Feshbach resonance to bind pairs of atoms to molecules. The molecules were observed by a loss of atoms that could be recovered by applying a reverse ramp across the resonance to break the molecules again. Within a relatively short time, a number of teams were able to produce degenerate molecules from bosonic atoms [Her03, Dür04], and later also in Ketterle's group [Xu03]. But the short lifetime of those molecules inhibited so far their thermalization to a BEC. The finding that molecules formed from fermionic  ${}^6\text{Li}$  atoms would be rather long-lived [Cub03, Str03, Joc03b] "sparked a hot race" [Cho03], that saw its first highlight in the Bose-Einstein condensation of molecules [Joc03a, Gre03, Zwi03, Bou04, Hul04]. This chapter describes our experiments that lead to the formation of molecules from our lithium spin mixture, which is summarized in [Joc03b]. Our approach makes use of the fact that three-body recombination to dimers is strongly enhanced near a Feshbach resonance. This enhanced recombination leads to the exclusive formation of the very weakly bound molecular state associated with the resonance. The binding energy and thus the released energy can be tuned using the magnetic field such that it is smaller than the trap depth to avoid loss and at the same time larger than the thermal energy of the gas so that the atom-molecule equilibrium favors the molecular state.

A number of important improvements of our setup were the key to success:

- Optimizing the transfer from the MOT into our standing wave dipole trap resulted in a more than five-fold increase in atom number and a factor of three lower initial temperature that enabled us to observe inelastic loss from our trapped spin mixture where the scattering length is large and positive, which was first reported in [Die02]. These inelastic losses were later identified to be

associated with molecule formation [Bou03].

- A much better control of the intensity of the standing wave, especially at very low intensities enabled us to perform efficient evaporative cooling by lowering the trapping potential. The evaporative cooling also resulted in a 2-D gas in our standing wave trap with more than 99% of all the particles in the axial ground state of the trap.
- A much more stable magnetic field by stabilizing the current of our power supplies by an external circuit that programs the voltage of the power supply in a feedback loop. The accuracy is now limited by the 16-bit resolution of our digital-to-analog converter to  $1.5 \times 10^{-5}$ , or 22 mG. It allows us to also resolve the narrow Feshbach resonance at 546 G described in chapter 2.2.
- Imaging of the atoms at zero magnetic field was implemented. This enabled us to measure temperatures with the standard time-of-flight techniques. As we could only image our atoms at zero field, no imaging of molecular clouds was available in the following chapter.
- Finally, we achieved a higher and eventually much more constant loading rate of our MOT: an additional laser diode was set up to amplify the Zeeman slower beam. This made experiments much more hassle free and was crucial for the quick success.

### 6.1 Three-body recombination

In our first experiments on the formation of molecules, we were looking for magnetic field dependent loss as it had already been observed at MIT in 2002 [Die02]. But as the loss dynamics suggested a two-body loss process instead of three-body recombination, this loss had not been attributed to molecule formation.

Three-body recombination has been studied extensively in theory and in experiments. The special case when there is a weakly bound state present that also determines the scattering length as  $E_B = \hbar^2/ma^2$  was studied by Fedichev *et al.* in [Fed96]. They found a rather strong scaling of the decay rate with the scattering length as  $\alpha_{\text{rec}} \propto a^4$  for bosonic atoms. This finding was confirmed in an intensive study on inelastic loss in cesium in our group [Web03]. For the case of fermions, three-body collisions are expected to be very strongly suppressed even in a two-state mixture. In a simple picture, the spatial wave function at ultralow temperatures has to be totally symmetric because no angular momentum is involved. This means that the spin part of the wave function of three particles of which two are identical has to be antisymmetric, which is not possible. A calculation by D. Petrov [Pet03a] finds however that three-body recombination of a fermionic spin mixture is indeed possible near a Feshbach

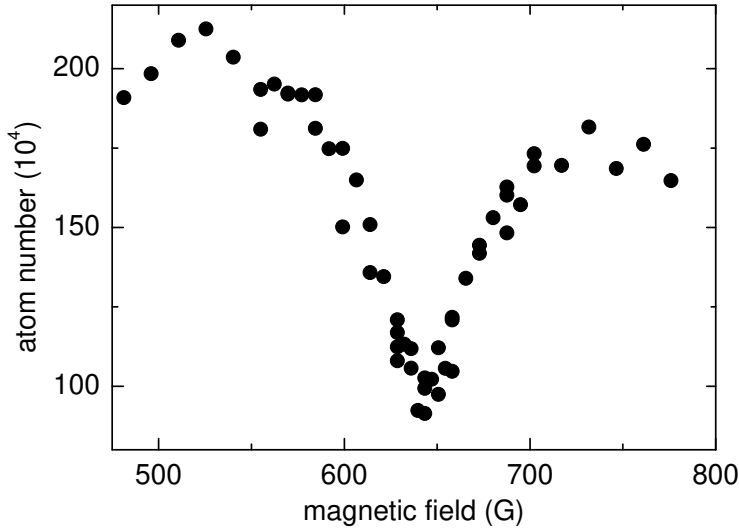


**Figure 6.1:** Loss of atoms from a precooled sample of  $\sim 2$  million atoms at  $30\,\mu\text{K}$  after 5 s in variable magnetic field. The maximum loss occurs at  $\sim 636$  G, where the scattering length is  $620a_0$  and the binding energy is  $83\,\mu\text{K}$ .

resonance where a weakly bound molecular level exists. The rate is calculated to be

$$\dot{n}/n = Ln^2 \approx 111n^2 a^6 \bar{\epsilon}/\hbar, \quad (6.1)$$

where  $L$  is the three-body loss coefficient and  $\bar{\epsilon}$  is the average kinetic energy of the particles. Formula 6.1 is valid when the kinetic energy is much lower than the binding energy,  $\bar{\epsilon} \ll \hbar^2/ma^2$ . It also assumes that the binding energy is much larger than the trap depth so that all three particles involved are lost from the trap. Furthermore, it neglects the presence of molecules, which will lead to an atom-molecule equilibrium as described in the next chapter. There are two major differences to the case of bosonic atoms: First, the loss rate scales with the scattering length to the sixth power, much stronger than in the bosonic case. Second, the recombination rate depends linearly on the kinetic energy of the particles, whereas for bosons, it is independent of the kinetic energy. Both effects are due to the fermionic suppression of such collisions and thus, such rates are expected to be much lower than in the bosonic case.

In the following, our experiments to observe such three-body recombination losses will be described. For these experiments we started with typically a few million atoms trapped in our standing wave trap. These atoms were first cooled to different temperatures by forced evaporative cooling at a field of 300 G where the scattering length is large and negative. We then ramped the magnetic field to arbitrary values in the vicinity of the Feshbach resonance in  $\sim 50$  ms. To observe the loss, we stored the atoms for typically 5-7 s at a given magnetic field before ramping the field back to zero and detecting the remaining fraction of the atoms. An example of such a measurement is

## 6 Weakly bound molecules near a Feshbach resonance

shown in Fig. 6.1. Here, the trap depth was  $500\,\mu\text{K}$  and the temperature  $\sim 30\,\mu\text{K}$ . Starting from about two million atoms, loss starts to set in at about 550 G, just above the zero crossing of the scattering length. A maximum of the loss then occurs at 636 G, disappearing again at  $\sim 750$  G. At the maximum loss of 636 G, the scattering length is  $620a_0$ , corresponding to a binding energy of  $83\,\mu\text{K}$ , which is only about a factor of three larger than the thermal energy. The same measurement was repeated again under similar conditions, but with varied trap depth and thus, also temperature, yielding comparable results (see table 6.1). The interpretation of these data is not straight forward. There are several factors complicating things here: First of all, for most of the magnetic field range of interest, any formed dimers will be trapped because the binding energy is smaller than the trap depth. This means that a mixture of atoms and molecules has to be considered. Here, the thermal equilibrium between atoms and molecules as well as the stability of the dimers against collisional decay play a role. However, the fact that the maximum loss of atoms occurs where the binding energy is just above the temperature can be explained qualitatively: The recombination rate depends on the scattering length to the sixth power. Thus it increases strongly with the magnetic field. At the same time, the thermal energy must be smaller than the binding energy in order to form a significant amount of molecules, a necessary requirement for losses to occur. Accordingly, the loss increases quickly until it reaches the maximum where the kinetic energy is just below the binding energy and then levels off again.

| Temperature       | Trap depth          |       | $a$      | $E_B$              |
|-------------------|---------------------|-------|----------|--------------------|
| $60\,\mu\text{K}$ | $1000\,\mu\text{K}$ | 629 G | $557a_0$ | $104\,\mu\text{K}$ |
| $30\,\mu\text{K}$ | $500\,\mu\text{K}$  | 636 G | $620a_0$ | $83\,\mu\text{K}$  |
| $22\,\mu\text{K}$ | $350\,\mu\text{K}$  | 644 G | $700a_0$ | $64\,\mu\text{K}$  |

**Table 6.1:** The magnetic field value where the maximum loss occurs varies with the temperature of the gas. Tabulated is the temperature, the magnetic field  $B$  where the maximum loss occurs and the corresponding scattering lengths  $a$  and molecular binding energies  $E_B$ .

### Narrow Feshbach resonance

Beside the inelastic losses associated with the broad resonance, we also observed losses near the narrow resonance at  $\sim 542$  G. Here, different phenomena can be studied because of the small width of  $\sim 100$  mG of the resonance. The result of measurements performed in the same way as those shown previously at higher field are shown in Fig. 6.2 at trap depths of 1 mK and  $20\,\mu\text{K}$ , with temperatures of approximately  $80\,\mu\text{K}$  and  $2.4\,\mu\text{K}$ , respectively. Note the very different scale, in Fig. 6.1, a 300-G range is shown, whereas Fig. 6.2 covers only a range of 3 G. Here, not only the loss maximum is shifted with temperature, the shape of the loss feature is dramatically different



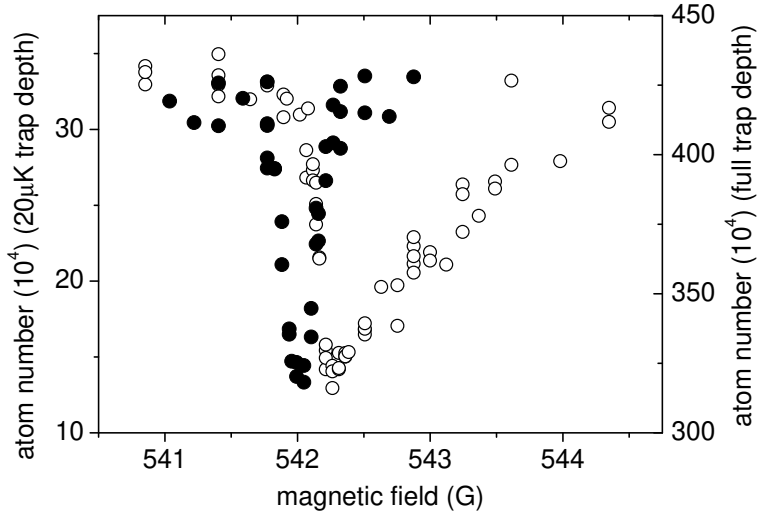


**Figure 6.2:** Inelastic loss at the narrow Feshbach resonance. The open circles are taken at  $\sim 1$  mK trap depth, the data represented by full circles are taken at a trap depth of  $20 \mu\text{K}$

as compared to the broad resonance. At high temperatures in the deep trap, the loss extends up to two Gauss to higher fields above the well defined loss at low temperature. A rather simple explanation for the effect of broadening to higher magnetic fields would be a shift of the resonance position as a function of the collisional energy in the same way as it was discussed for a possible shift of the zero crossing of the scattering length (see 5.2). A typical shift for a  $100\text{-}\mu\text{K}$  collision would then be  $0.7$  G, the loss at even higher magnetic fields coming from the tail of the Maxwell-Boltzmann distribution. It is also interesting to look at the left hand side of the loss features in Fig. 6.2. While both the low-temperature and the high-temperature data show the approximately the same slopes, these are shifted by  $\sim 250$  mG. Such a shift would come from a collision energy of  $k_B \times 35 \mu\text{K}$ . The ground state energy in the  $1\text{-mK}$  deep trap is  $1/2 \hbar \times 1.5 \text{ MHz} = k_B \times 36 \mu\text{K}$  due to the  $1.5 \text{ MHz}$  axial vibration frequency, while it is only  $k_B \times 5 \mu\text{K}$  in the shallow trap. The difference of  $k_B \times 31 \mu\text{K}$  coincides quite well with the observed shift. Thus, it could be interpreted as a signature of the 2-D nature of the trap leading to a shift of the position of the Feshbach resonance. The data presented in this section cannot be interpreted in a simple model such as three-body recombination leading to loss out of the trap. Instead, there seem to be many different effects involved: First, the recombination products remain trapped and an atom-molecule equilibrium establishes. The loss of atoms is then dramatically reduced and is basically governed by inelastic loss of molecules that decay into lower vibrational levels in two-body collisions. The time scale of this process together with the atom-molecule equilibrium strongly determine the dynamics of the system. To be able to do such studies conclusively, one needs a method to detect those atoms that are

not really lost but have formed molecules and remain trapped in the dipole trap. This will be the subject of the next section.

## 6.2 Formation and detection of molecules

This section describes our quest for a molecular gas of  ${}^6\text{Li}_2$  molecules. Inspired by previous work with potassium at JILA [Reg03], with cesium in our group [Her03] and with lithium in Paris [Cub03], that had produced molecules either from degenerate fermi gases or BECs, we started experiments to explore the possibility of creating molecules from a thermal gas of atoms.

### Preparation of the starting conditions

The ultracold gas was prepared by forced evaporative cooling after loading the standing wave trap at its initial depth of  $\sim 1$  mK with  $8 \times 10^6$  atoms from the MOT. The evaporation is performed by ramping down the light intensity in 1 s at a magnetic field of 1200 G. The evaporation initially proceeds with very high efficiency, as can be seen in Fig. 6.3, where the temperature is plotted versus the trap depth during the evaporation. The fact that the truncation parameter  $\eta = U/k_B T$  is always larger than ten, which corresponds to the dashed line, suggests that the evaporation is very efficient [O’H01].

At very low trap depth, the lifetime of the gas is reduced tremendously to well below 1 s and no further gain in phase space density is achieved. The main reasons for this loss are technical in nature: The stability of the resonator lock for our standing wave is reduced at very low power, which leads to heating of the gas, also the trap potential is tilted by gravity and some uncompensated magnetic field gradients. But there is also one effect that is fundamental and cannot be overcome in our standing wave trap: When the trap depth is lowered so much that there are only one or two bound states present in the trap, tunneling along the standing wave becomes important even for the axial ground state of the trap.

After evaporative cooling, the starting point for the following measurements was a sample of  $2.5 \times 10^6$   ${}^6\text{Li}$  atoms in our standing-wave optical dipole trap at a trap depth of  $k_B \times 27 \mu\text{K}$ . The axial and radial trap frequencies corresponding to this trap depth are 260 kHz and 390 Hz, respectively. The 50-50 spin mixture in the lowest two spin states was spread over  $\sim 1600$  individual lattice sites. In the central region of the trap, a single site contained typically 1800 atoms. Under these conditions, we achieved a temperature of  $2.5 \mu\text{K}$ . Peak values for the number density and phase-space density were then  $3 \times 10^{12} \text{ cm}^{-3}$  and 0.04 respectively. The spread of the atoms over many lattice sites will cause some complications later for quantitative analysis. This spread can be approximated by a gaussian distribution with a width of  $\sigma \approx 0.4$  mm.

An interesting aspect of these starting conditions is the 2-D character: Due to the

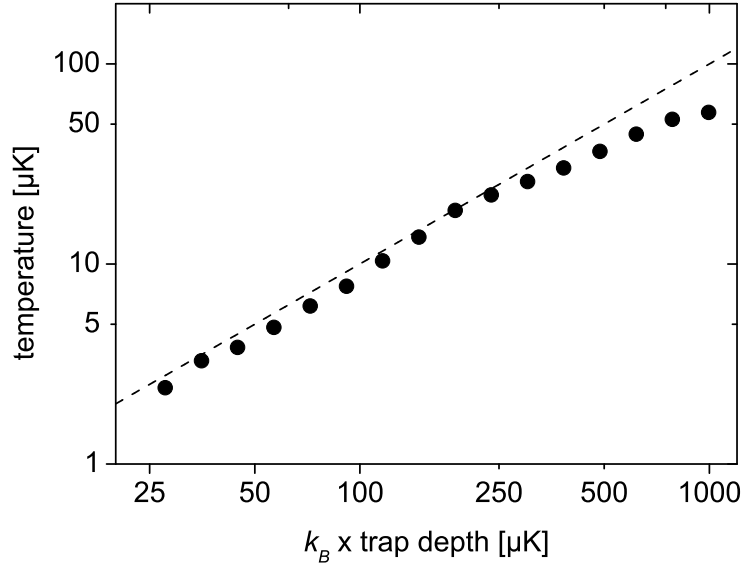


**Figure 6.3:** Evaporative cooling in the standing wave. The trap depth is lowered in an exponential ramp from 1 mK to 25  $\mu\text{K}$ . The temperature is plotted versus the trap depth. All the data points are below the dashed line that represents a thermal energy of one tenth of the trap depth. This indicates an extremely efficient evaporation.

high axial vibration frequency, the atoms are almost completely confined to the axial ground state of the trap. The ground state population for our conditions is

$$n_{0,\text{ax}} = 1 - e^{-\frac{\hbar\omega_{\text{ax}}}{k_B T}} = 99.3\%, \quad (6.2)$$

plugging in the numbers given above. Of course, also the number density and the phase space density have to be calculated taking that into account, the formulas to be used are given in section 4.3.1. It is also important to note that for the experimental conditions described here, the axial harmonic oscillator length is

$$a_{\text{ho,ax}} = \sqrt{\frac{\hbar}{m\omega_{\text{ax}}}} = 24.7 \text{ nm} = 466a_0. \quad (6.3)$$

This is in many cases smaller than the scattering length of our atoms near the Feshbach resonance and one can expect to observe some variations from a 3-D trap [Pet01].

### Observation of molecules

The loss measurements in atomic samples presented above indicate that dimers are being formed and trapped in our dipole trap. However a detection scheme is needed to actually observe the molecules that are expected to be in the highest vibrational

## 6 Weakly bound molecules near a Feshbach resonance

state that is associated with the Feshbach resonance. The JILA Group established two techniques for the observation of such molecules that both rely on dissociating the molecules into atoms again [Reg03]:

- The first technique is a simple magnetic field ramp across the Feshbach resonance, where no bound state exists, and thus, the molecules have to decay into free atoms.
- The second technique uses a radio frequency transition from the bound molecule to a pair of free atoms, where the hyperfine state of one of the atoms is changed. This technique also provides additional information, for example on the binding energy and the size of the molecule, which can be obtained from the frequency shift as compared to the free atoms and from the line shape of the molecule-atom transition.

In the measurements presented in this chapter, we used the first technique. For this purpose, we applied a ramp across the Feshbach resonance to fields of typically 1200 G at a speed of +6 G/ms. This brings the bound level above the scattering continuum and the molecules quickly dissociate. The dissociation turned out to be insensitive to variations of the ramp speed and the final field. After the dissociation ramp, we immediately ramped down to zero magnetic field. The ramp speed of -12 G/ms is fast enough to avoid molecule formation when crossing the region of positive scattering length. As an additional measure to avoid any loss of atoms during the ramp, we also cranked up the trapping potential to the full trap depth to heat the atoms so that for most of the ramp, the binding energy is smaller than the thermal energy. After reaching zero magnetic field we recaptured all atoms into the MOT to measure their number as described in section 4.5. This measurement provides the total atom number  $2N_{\text{mol}} + N_{\text{at}}$ , where  $N_{\text{mol}}$  and  $N_{\text{at}}$  denote the number of molecules and atoms after the production phase, respectively. To determine  $N_{\text{at}}$  we repeated the same measurement without the Feshbach dissociation ramp by immediately ramping down to zero from the production field. The ramp down to zero magnetic field increases the binding energy to a large value of about  $k_B \times 80$  mK and the molecules are lost without leading to any fluorescence light in the MOT. The number of molecules  $N_{\text{mol}}$  is then obtained by taking the difference in atom numbers measured in two subsequent runs with and without the dissociating Feshbach ramp.

After a lot of optimization, we found the following scheme to be most effective to produce molecules in our setup: We started at a magnetic field of 1200 G, where we performed evaporative cooling. We then quickly ramped down from the evaporation field to 690 G with a speed of -7.5 G/ms, where we find optimum production rates at a large positive scattering length of  $a = +1300a_0$ . In contrast to other experiments with fermionic atoms [Reg03, Cub03, Str03], the molecule formation during this ramp

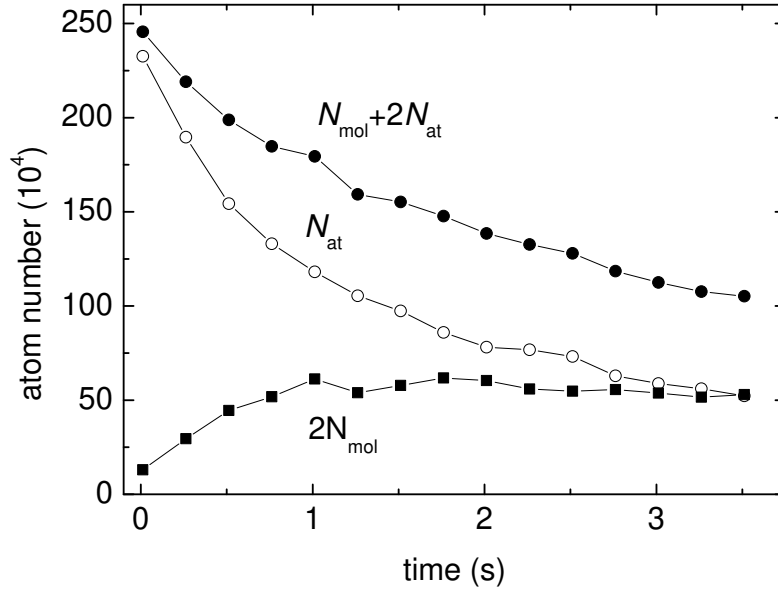


**Figure 6.4:** Formation of molecules at a fixed magnetic field of 690 G. The measured numbers  $N_{\text{at}} + 2N_{\text{mol}}$  and  $N_{\text{at}}$  are plotted as a function of time together with the resulting number of molecules  $2N_{\text{mol}}$ .

is negligible and the molecules are predominantly formed after the ramp at the fixed production field.

At the optimum production field of 690 G the molecular binding energy amounts to  $\sim k_{\text{B}} \times 18 \mu\text{K}$ , which is in between the thermal energy of  $k_{\text{B}} \times 2.5 \mu\text{K}$  and the trap depth of  $k_{\text{B}} \times 27 \mu\text{K}$  for the atoms. For the molecules the trap depth is a factor of two higher because of the two times larger polarizability. We have verified this fact by measuring the trap frequencies for atoms and molecules. We observed a  $\sim 5\%$  higher frequency for the molecules, which is well within the error of our measurement. After a three-body recombination event both the atom and the molecule remain trapped. We believe that the recombination heat is cooled away by evaporation of atoms out of the trap. Evaporative loss of molecules is strongly suppressed because of the higher trap depth.

The creation of molecules from the atomic gas is demonstrated in Fig. 6.4 for the optimum production field of 690 G. The time evolution of the measured numbers  $2N_{\text{mol}} + N_{\text{at}}$  and  $N_{\text{at}}$  is shown together with the corresponding number of molecules  $2N_{\text{mol}}$ . The formation of these molecules must be three-body in nature [Sun03, Pet03a], because two-body processes cannot lead to bound dimers as a third particle is required for energy and momentum conservation. The initial three-body molecule formation rate can be modeled with the equation  $\dot{n}_{\text{mol}}/n_{\text{at}} = M_3 n_{\text{at}}^2$ , which is the same equation as 6.1, where  $L = 3M_3$ , because any single three-body event is counted only once here,

## 6 Weakly bound molecules near a Feshbach resonance

while three atoms are lost in the case of 6.1. To express this equation in measured numbers, we have to integrate  $\dot{n}_{\text{mol}}(\mathbf{r})$  to get  $\dot{N}_{\text{mol}}$ ,

$$\dot{N}_{\text{mol}} = M_3 \int d\mathbf{r} n_{\text{at}}^3(\mathbf{r}). \quad (6.4)$$

This integral yields immediately for any Gaussian density distribution, such as 4.8 or 4.9,

$$\dot{N}_{\text{mol}} = \frac{M_3}{\sqrt{3}^3} n_{\text{max,at}}^2 N_{\text{at}}. \quad (6.5)$$

This gives the right solution for a single well, but in the standing wave trap we also have to average over the different atom numbers in the individual lattice sites. Assuming a gaussian distribution along the lattice, the factor  $\sqrt{3}^3$  has to be multiplied with another factor of  $\sqrt{3}$  so that the final equation for the standing wave potential is

$$\frac{\dot{N}_{\text{mol}}}{N_{\text{at}}} = \frac{M_3}{9} n_{\text{max,at}}^2 \quad (6.6)$$

From the initial molecule formation rate of  $\dot{N}_{\text{mol}} = 3.5 \times 10^5 \text{ s}^{-1}$  we thus derive a three-body formation coefficient of  $M_3 = 1 \times 10^{-25} \text{ cm}^6/\text{s}^{-1}$ . This value can only be an order of magnitude estimate for such a rate, as the peak density is not known to better than a factor of two due to the uncertainty in the particle number. This value is in the expected range if compared with the number  $M_3 \approx 1 \times 10^{-24} \text{ cm}^6/\text{s}^{-1}$  predicted by D. Petrov [Pet03a] for our conditions using equation 6.1 and using  $L = 3M_3$ .

For the large scattering length of  $1300a_0$ , which is more than twice as large as the harmonic oscillator length of  $466a_0$ , we also expect a modification of this rate due to the quasi 2-D nature of our gas. The maximum number of  $3 \times 10^5$  molecules is reached after about 1 s. For longer times, the fraction of atoms forming molecules approaches a value of  $\sim 50\%$ .

### Atom-molecule equilibrium

A model describing the thermal equilibrium of such a mixture of atoms and molecules is presented by C. Chin in [Chi04b]. A similar model that takes into account a quantum degenerate molecular gas is developed in [Kok04]. In the following, I will describe the basic idea of [Chi04b]. We expect that after a long enough thermalization time, we reach a thermal equilibrium between atoms and molecules that is independent of the precise formation process. This equilibrium should then be constrained only by the molecular binding energy, the temperature of the gas and the particle number in our trap.

In thermal equilibrium, the free energy  $F$  of the system,  $F = -k_B T \ln Z$  must be minimized. Here,  $Z$  denotes the partition function of the system. It can be constructed

## 6.2 Formation and detection of molecules

from the single particle partition functions of the atoms in the two spin states ( $Z_\uparrow$ ,  $Z_\downarrow$ ) and of the molecules ( $Z_{\text{mol}}$ ) to be

$$Z = \frac{Z_\uparrow^{N_\uparrow} Z_\downarrow^{N_\downarrow} Z_{\text{mol}}^{N_{\text{mol}}}}{N_\uparrow! N_\downarrow! N_{\text{mol}}!}. \quad (6.7)$$

We now constrain that we have an equal spin mixture of atoms so that  $N_\uparrow = N_\downarrow = N_{\text{at}}$ . The total number of particles  $N_0$  in each spin state is assumed to be conserved,  $N_0 = N + N_{\text{mol}}$ . The free energy then becomes:

$$F(N_{\text{at}}, T) = -k_B T (N_{\text{at}} \ln Z_\uparrow + N_{\text{at}} \ln Z_\downarrow + (N_0 - N_{\text{at}}) \ln Z_{\text{mol}} - 2 \ln N_{\text{at}}! - \ln(N_0 - N_{\text{at}})!). \quad (6.8)$$

Now,  $F(N_{\text{at}})$  has to be minimized. Using Stirling's rule  $\ln n! = n \ln n - n$ , we find

$$\frac{d}{dN_{\text{at}}} F(N_{\text{at}}) = 0 = \ln Z_\uparrow + \ln Z_\downarrow - \ln Z_{\text{mol}} - 2 \ln N_{\text{at}} + \ln(N_0 - N_{\text{at}}). \quad (6.9)$$

This can be written as

$$\frac{N_{\text{at}}^2}{Z_\uparrow Z_\downarrow} = \frac{N_{\text{mol}}}{Z_{\text{mol}}}, \quad (6.10)$$

which is a special case of the Saha-equation, that was originally derived by Saha for a partially ionized plasma [Lan80]. For us, the most interesting quantity to derive is the ratio of molecules to atoms,  $N_{\text{mol}}/N_{\text{at}}$  for a given temperature. In our optical trap, atoms independent of their spin state and also the molecules have the same trap frequencies and therefore have the same single particle partition function. We can therefore rewrite 6.10 as

$$\frac{N_{\text{mol}}}{N_{\text{at}}} = \frac{Z_{\text{mol}}}{Z_{\text{at}}} \frac{N_{\text{at}}}{Z_{\text{at}}}. \quad (6.11)$$

Because of the molecular binding energy we have  $Z_{\text{mol}} = Z_{\text{at}} \times \exp(E_B/kT)$ , and  $N_{\text{at}}/Z_{\text{at}}$  is the phase space density  $\phi_{\text{at}}$  of the atoms. We then get the result

$$\frac{N_{\text{mol}}}{N_{\text{at}}} = \phi_{\text{at}} \times e^{\frac{E_B}{kT}}. \quad (6.12)$$

We can now compare this result with our experimental data in Fig. 6.4. The best equilibration is after long times, so we take the data point at 3.5 s. We have at this time a mixture of  $\sim 2.5 \times 10^5$  atoms per spin state, assuming an equal mixture, and  $\sim 2.5 \times 10^5$  molecules. Assuming that the temperature stayed constant during the formation of the molecules because of evaporative cooling, the five-fold drop in atom number would lead to the same drop in atomic phase space density to  $8 \times 10^{-3}$ . Plugging in this number,  $2.5 \mu\text{K}$  for the temperature and  $19 \mu\text{K}$  for the binding energy, we get a molecule - atom ratio of 16, which is much higher than the observed ratio of one. But because the temperature of the mixture could not be measured, there is a rather large uncertainty.

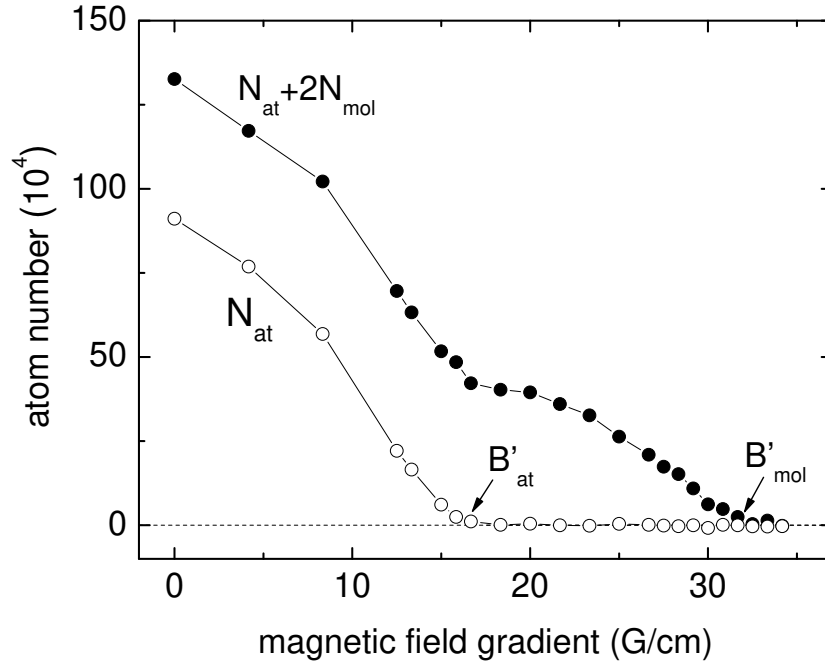


**Figure 6.5:** Stern-Gerlach selection by applying a magnetic field gradient to the trapped atom-molecule mixture at a magnetic field of 568 G and a trap depth of  $k_B \times 19 \mu\text{K}$ . Marked are the two gradients where all the atoms and all the molecules are lost.

This does not only affect the exponential factor in equation 6.12, but also our calculated phase space density in our 2-D trap depends quadratically on the temperature (see equation 4.11). If one assumes a temperature of  $3.5 \mu\text{K}$  with no change in other parameters, the calculated molecule - atom ratio becomes one. This means that within our knowledge of the temperature, the model described above yields the correct result.

### 6.3 Stern Gerlach selection of molecules

To purify the created molecules we used a Stern-Gerlach selection technique. We applied a magnetic field gradient perpendicular to the standing wave axis. This pulls particles out of the trap for which the magnetic force is larger than the trapping force. In order to be able to apply large enough field gradients, we lowered the trap depth to  $k_B \times 19 \mu\text{K}$  while applying the gradient for about 10 ms. Fig. 6.5 demonstrates such a purification at 568 G. While all the atoms are lost above  $B'_{\text{at}} = 17 \text{ G/cm}$ , the molecules start getting spilled at 20 G/cm, and are lost completely above  $B'_{\text{mol}} = 32.5 \text{ G/cm}$ . This means that under suitable conditions, we could remove all the atoms while keeping the molecule number constant.



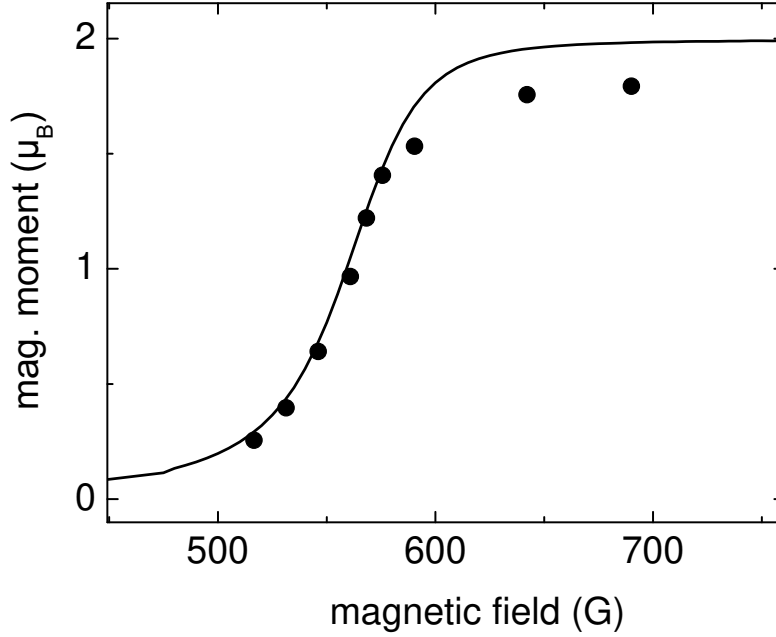


**Figure 6.6:** Determination of the magnetic moment of the molecules as a function of the magnetic field by taking the ratio  $B'_{\text{at}}/B'_{\text{mol}}$  where atoms and molecules, respectively, are expelled from the trap. The solid line shows the derivative of the Zeeman energy of the molecule as calculated by V. Venturi [Ven01]

The magnetic moment of the molecules, that we define as  $\mu_{\text{mol}}(B) = \partial E(B)/\partial B$  can be estimated from the spilling measurement described above by comparing it with the known magnetic moment of the atoms which equals Bohr's magneton  $\mu_B$  at fields much larger than 30 G. As the dipole trapping potential of the molecules can be estimated to be twice as large as that of the atoms, one expects that the potential gradient needed to spill all the molecules is twice as large as the one needed to spill all the atoms. The molecular magnetic moment can therefore be determined as  $\mu_{\text{mol}} = 2\mu_B B'_{\text{mol}}/B'_{\text{at}}$ . Fig. 6.6 shows the magnetic moments of the molecules determined in such a way at various magnetic fields. The data agree well with the magnetic field dependence expected from theory. The solid line shows the derivative of the Zeeman energy of the molecule as calculated by V. Venturi [Ven01]. We attribute the systematic deviation to slightly different trap parameters for atoms and molecules.

## 6.4 Molecular Lifetime

The surprisingly simple formation of molecules raised the question of how stable such a gas of molecules in the highest vibrational state would be. It is known from molecular physics that the vibrational energy very quickly thermalizes with the kinetic energy of

## 6 Weakly bound molecules near a Feshbach resonance

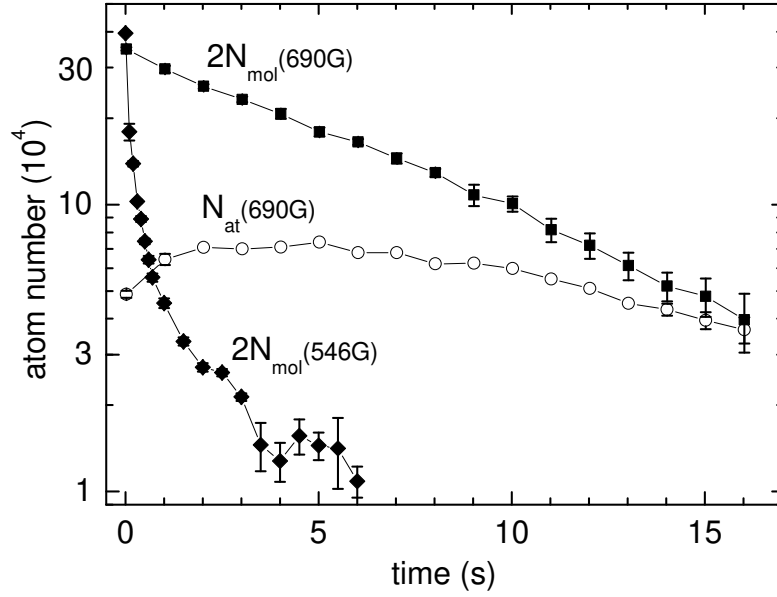


**Figure 6.7:** Evolution of an initially pure sample of molecules at two magnetic fields. While the molecules decay rapidly at 546 G, the sample exhibits a long lifetime of 10 s at 690 G. At the same time, molecules are partly dissociated into atoms in endoenergetic collisions.

the particles. In our case, any change in the vibrational state of the molecules would immediately lead to loss from the dipole trap, as the typical vibrational energies are on the order of Kelvins, very much larger than our trap depth. In this section, the surprising finding is reported that such highly excited molecules can be extremely stable if their binding energy is made very small close to the Feshbach resonance.

We started with a pure molecular sample, prepared as described above, and look at the time evolution in the trap. Corresponding decay curves are displayed in Fig. 6.7 for two different magnetic fields. At 546 G a rapid non-exponential decay is observed as a clear signature of inelastic molecule-molecule collisions. These are expected to be two-body in nature, where in a collision one molecule changes its vibrational state and the gain in kinetic energy kicks the particles out of the trap. A two-body loss can be modeled by  $\dot{n} = L_2 n^2$ . As we did before for the case of three-body losses (equation 6.5, one has to average over the density distribution to express this equation in absolute particle numbers. One gets

$$\frac{\dot{N}}{N} = \frac{L_2}{\sqrt{2}^3} n_{\text{peak}} \quad (6.13)$$

for a 3-D Gaussian distribution. To take into account the averaging along the standing wave, one has to divide by another factor of  $\sqrt{2}$ . From the first three points of the decay in Fig. 6.7, we derived a two-body loss coefficient of  $5 \times 10^{-11} \text{ cm}^3/\text{s}$ .

At 690 G, the observed behavior is strikingly different. The molecular sample shows a nearly exponential decay with a time constant as long as  $\sim 10$  s. As similar lifetimes were observed for trapped atom samples under conditions where trapped molecules cannot be created, the observed molecular lifetime can be fully attributed to one-body effects like heating in the optical trap. For a loss rate coefficient at 690 G our data provide an upper limit of  $3 \times 10^{-13}$  cm<sup>3</sup>/s, which is surprisingly low for inelastic collisions in a molecular system with many open exit channels.

This high stability against inelastic collisions had already been predicted by theory [Pet04]. In a simple picture, one can identify two mechanisms that lead to a suppression of the decay of these weakly bound molecules. The first one is the fact that the size of the weakly bound molecule is on the order of the scattering length, typically a few hundred to thousand Bohr radii, whereas all the other vibrational states are much more tightly bound and have a size that is on the order of the characteristic radius of interaction  $R_{\text{eff}}$ , which is  $62.5a_0$  for lithium. Thus, the spatial Franck-Condon overlap of the weakly bound state with any of the other states is rather small. This is an effect that applies in a similar way to all weakly bound molecules, also those formed from bosonic atoms. Experiments have shown however, that molecules formed from fermionic atoms are much more stable against collisional decay. There is a second mechanism that leads to suppression of the decay that applies only to fermions. This stems from the suppression of three-body s-wave collisions that was discussed previously in section 6.1. To actually form a tightly bound molecule, three atoms, either paired in molecules or free, have to come very close to each other, on the order of  $R_{\text{eff}}$ . This means that the mechanisms that allow the formation of weakly bound dimers [Pet03a] do not apply and as there is no angular momentum involved, such a process is symmetry forbidden if two identical fermions are involved. However, as the size of the weakly bound molecule is reduced by lowering the scattering length the above arguments are weakened and the decay rate increases, as observed in the experiment. Theory predicts the two-body decay rate of molecules to scale with the scattering length as  $a^{-2.55}$ .

The data at 690 G show another interesting collisional effect that does not occur at lower field. Atoms reappear after purification of the molecular cloud, see (○) in Fig. 6.7. For long storage times ( $\sim 15$  s) an atom-molecule mixture is reestablished with a similar fraction of molecules as observed in the initial formation process at the same magnetic field, see Fig. 6.4. But there is an important difference, the total particle number is a factor of ten lower, which of course would result in a ten-fold decrease in phase space density at constant temperature that would not be consistent with the model described above. Collisions producing atoms from molecules are endoergic in nature as kinetic energy is required to provide the dissociation energy, thereby cooling the gas. One can estimate a temperature of  $\sim 2.5$   $\mu$ K from the molecule-atom ratio of  $\sim 1$  at an atom number of  $\sim 50000$  per spin state. The kinetic energy to break so many

## 6 Weakly bound molecules near a Feshbach resonance

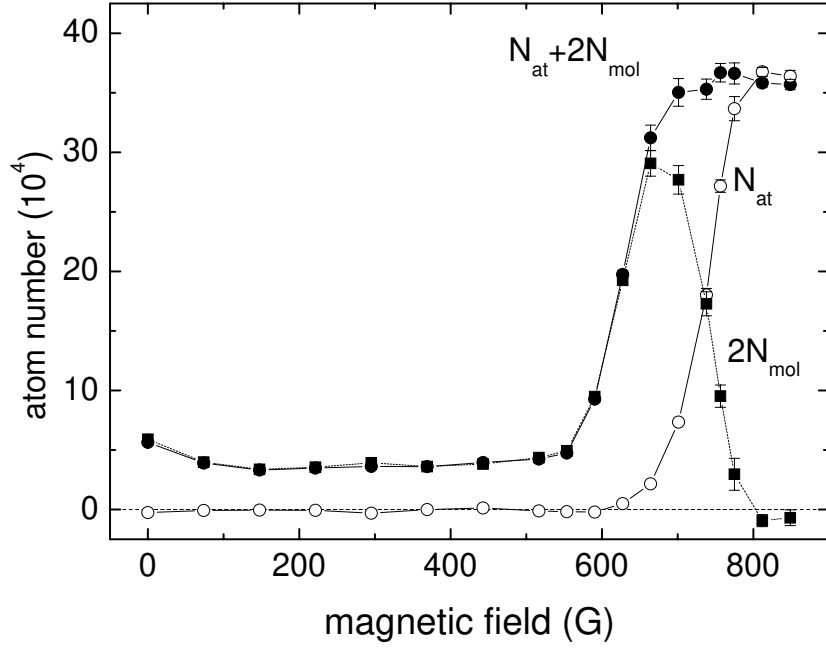


**Figure 6.8:** Remaining number of atoms  $N_{\text{at}}$ ,  $N_{\text{at}} + 2N_{\text{mol}}$ , and  $2N_{\text{mol}}$  after a 1-s hold time at variable magnetic field starting with a pure molecular ensemble.

molecules cannot stem from the initial temperature of the gas. There must be heating present that is probably associated with the stability of our standing wave dipole trap at low trap depth. The observed lifetime of  $\sim 10$  s that we also observe for a stable atomic gas in the same trap supports this interpretation. The increasing atom fraction does not lead to any increased loss. This shows that the gas is remarkably stable both against molecule-molecule and also atom-molecule collisions.

The dependence of the molecular decay on the magnetic field is shown in Fig. 6.8. Here we stored the initially pure gas of  $1.8 \times 10^5$  molecules at a variable magnetic field for a fixed holding time of 1 s before we measured the number of remaining molecules and atoms. A sharp transition occurs around 650 G. For fields below  $\sim 600$  G, where the binding energy is relatively large ( $> k_B \times 100 \mu\text{K}$ ), the observed decay is very fast and no atoms are found to reappear. Here inelastic collisions apparently lead to a rapid vibrational quenching. Furthermore, the kinetic energy of the molecules cannot provide the necessary energy for collisional dissociation. Consequently, we do not observe any atoms reappear.

For fields above  $\sim 680$  G a completely different behavior is observed. In this regime, no significant loss occurs in the total number  $2N_{\text{mol}} + N_{\text{at}}$ . However, an increasing atom fraction is observed as a result of collisional dissociation of the molecules. Here the binding energy approaches the thermal energy and the sample tends towards a thermal atom-molecule equilibrium. Close to the Feshbach resonance, where the binding en-

ergy becomes comparable to the thermal energy, the atomic fraction dominates in the atom-molecule mixture.

The incredible stability of the mixture provides the intriguing possibility of an extremely efficient production of molecules and great prospects for their evaporative cooling to a Bose-Einstein condensate. In fact, evaporative cooling of an atom-molecule mixture is expected to be especially effective as described in [Chi04b]. The basic idea here is that while for the molecules the trap is twice as deep as for the atoms, they will be in thermal equilibrium and thus have the same temperature. This means that by evaporative cooling, almost only atoms are lost. Atoms can then be dissociated from molecules, if the binding energy of the molecules is tuned appropriately to allow for an atom fraction to exist. Such a scheme would be a two step process in which every molecule that will be lost by evaporation is first dissociated into atoms. Thereby the binding energy is absorbed and then, two free atoms take with them typically up to  $\sim 10 \times k_B T$  of energy when they leave the trap, assuming a typical evaporative cooling scenario, where the trap depth is about a factor of ten higher than the temperature. This means that for every molecule lost from the trap, the loss of kinetic energy from the sample is  $\sim E_B + 2 \times 10 \times k_B T$  instead of the typical  $\sim 10 \times k_B T$ .



## Chapter 7

# Bose-Einstein condensation of molecules

The findings of the previous chapter that molecules can be formed efficiently from a thermal gas of fermionic atoms and the extremely high stability of these molecules against inelastic decay immediately suggested that such molecules would be ideal candidates to form a molecular Bose-Einstein condensate [Joc03b, Joc03a]. Our Bose-Einstein condensate is produced by forced evaporative cooling of our  $^6\text{Li}$  spin mixture in a specially designed focused beam dipole trap. During evaporative cooling, the atoms are efficiently converted into molecules as the thermal energy of the atoms falls below the binding energy of the weakly bound level associated with the broad Feshbach resonance at 834 G. While cooling the molecules further we observed typical bimodal distributions as the signature of Bose-Einstein condensation using high-field *in situ* absorption imaging. The long-lived nature of the molecular cloud of  $> 40$  s allowed us to produce a pure BEC with no noticeable thermal component.

Within a very short time, a number of groups were able to produce molecular condensates [Joc03a, Gre03, Zwi03, Bou04, Hul04] of either  $^6\text{Li}$  or  $^{40}\text{K}$  atoms. Such condensates open up new research opportunities with ultracold particles. For the first time, condensates of more complex systems than atoms had been made. Especially the weak, tunable binding energy of the molecules composed of two fermions opens new avenues of research [Bar04c, Reg04, Zwi04, Bou04, Bar04b, Kin04a, Chi04a] for experimentalists that had previously only been accessible in theory [Eag69, Leg80, Che04].

Among the major experimental challenges for the achievement of the molecular condensate and its observation were:

- A new focused beam optical dipole trap was designed (4.3.2) that provides a stable trapping potential which can be precisely controlled over more than four orders of magnitude. Together with the large scattering lengths close to the Feshbach resonance highly efficient evaporative cooling can be achieved.

- Unconventional methods were used to prove the presence of the condensate as initially, no imaging of the molecules was available. Most important, the precise control of the trap frequencies helped to get an accurate estimate of the number of quantum states in our extremely shallow trap that was a factor of 2 lower than the number of trapped molecules.
- Controlled spilling of our condensate using a magnetic field gradient to tilt a very shallow trap was used to demonstrate the tunability of the mean field of the condensate that depends on the magnetic field.

## 7.1 Evaporative cooling towards a molecular BEC

As evaporative cooling in our standing wave trap turned out not to be efficient below a certain trap depth, we designed a new focused beam optical dipole trap which we load from our standing wave trap. An important feature of this trap is that we can control the shape of the potential with excellent accuracy while changing the trap depth by four orders of magnitude. It is described in more detail in chapter 4.3.2 and in [Rie04, Bar04a]. We started the evaporation process with typically two million atoms at a temperature of  $\sim 80 \mu\text{K}$  trapped in our focused beam trap with a laser power of  $P = 10.5 \text{ W}$ , corresponding to a trap depth of  $U_{\text{at}}/k_{\text{B}} \approx 760 \mu\text{K}$ . The peak number density is calculated as  $\sim 10^{14} \text{ cm}^{-3}$  and the peak phase-space density is  $\sim 5 \times 10^{-3}$ . The calculated elastic collision rate is as high as  $\sim 5 \times 10^4 \text{ s}^{-1}$ . For evaporative cooling, we then ramped down the trapping potential in an exponential ramp with a  $1/e$  time between 0.23 s and 0.46 s. During evaporation, the interactions were tuned by applying a constant magnetic field. In the following discussion evaporative cooling towards a molecular BEC is described.

To test the performance of evaporative cooling in our dipole trap, we applied a magnetic field of 1176 G above the Feshbach resonance where the scattering length is very large and negative, but no inelastic loss or molecule production is expected. The evaporation proceeded in a very similar way as described in Refs. [Gra02, O’H01]. The measured atom number first follows a scaling law with the laser power  $P$ ,  $N/N_0 = P^\alpha$  [O’H01] with  $\alpha \approx 0.24$  (solid black line in Fig. 7.1). In this regime the temperature of the gas is typically a factor of ten below the trap depth [O’H01] and the elastic collision rate stays well above  $10^4 \text{ s}^{-1}$ . The crossover to Fermi degeneracy, where the thermal energy  $k_{\text{B}}T$  reaches the Fermi energy  $E_{\text{F}}$ , takes place at  $P \approx 0.5 \text{ W}$  where the trap depth is  $U_{\text{at}}/k_{\text{B}} \approx 36 \mu\text{K}$ . Below  $P \approx 50 \text{ mW}$ , the axial confinement is determined only by the magnetic potential as the optical potential is much weaker (see Eq. 4.17). The mean trap frequency  $\bar{\omega} = (\omega_{\text{rad}}^2 \omega_{\text{ax}})^{1/3}$  scales then as  $\bar{\omega} \propto E_{\text{F}} \propto U_{\text{at}}^{1/3} \propto P^{1/3}$ . As a consequence, the trap depth decreases faster than the Fermi energy and a threshold occurs when  $E_{\text{F}}$  reaches  $U_{\text{at}}$  and the trap is filled up to the “rim”. Further decrease



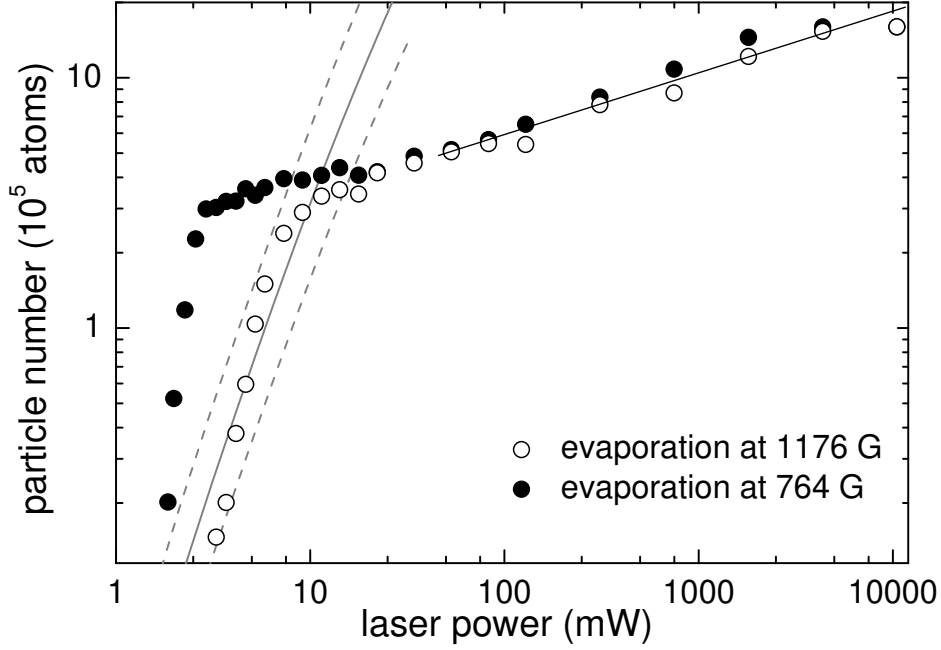


**Figure 7.1:** Evaporative cooling on both sides of the Feshbach resonance. We measure the number of trapped particles (the number of all atoms that are free or bound in molecules) as a function of the laser power  $P$  at the end of an exponential evaporation ramp  $P(t) = 10.5 \text{ W} \exp(t/230 \text{ ms})$ . The trap depth for atoms is  $U_{\text{at}}/k_B = P \times 72 \mu\text{K}/\text{W}$ , whereas for molecules it is two times larger ( $U_{\text{mol}} = 2U_{\text{at}}$ ). The measurements taken at 1176 G with a negative scattering length of  $a \approx -3500a_0$  ( $\circ$ ) show the spilling of a degenerate Fermi gas when the trap depth reaches the Fermi energy. The solid line shows the maximum number of trapped atoms in a two-component Fermi gas according to a numerical calculation of the number of quantum states in our trap. The dashed lines indicate the corresponding uncertainty range due to the limited knowledge of the experimental parameters. The measurements at 764 G with positive scattering length  $a \approx 3500a_0$  ( $\bullet$ ) exhibit a striking increase of the trapped particle number at low laser power, which is due to the formation of molecules.

of the laser power then leads to a spilling of atoms out of the trap and thus to a rapid decrease of the number of trapped atoms. Our data shown in Fig. 7.1 clearly show this spilling effect for  $P < 10 \text{ mW}$  corresponding to a trap depth of  $U_{\text{at}}/k_B < 720 \text{ nK}$ . Modeling the spilling curves provides us with an upper bound of  $k_B T < 0.2E_F$  for the temperature in terms of the Fermi energy. In the regime of a completely filled shallow trap, the number of atoms in the two-component spin mixture is given by two times the number of quantum states in the trap. A numerical calculation, shown in Fig. 7.1, confirms this interpretation of our data.

We performed the same evaporation procedure at a magnetic field of 764 G, where

the scattering length  $a \approx +3500a_0$  has a similar magnitude but opposite sign. Here the weakly bound dimers have a binding energy of  $\sim 2\mu\text{K}$ . Atoms are converted into molecules when the temperature of the gas drops below the binding energy as described in the previous chapter. In order to detect the molecules we dissociate them and measure the number of resulting atoms. For this purpose we abruptly turn on the full trap power which strongly heats the sample and leads to collisional dissociation. In order to ensure that we dissociate all molecules we also apply a magnetic field ramp across the Feshbach resonance. It turned out that the first step of the dissociation process was crucial, as even while all molecules might be dissociated during the ramp across the resonance, molecules could be formed again from a cold sample during the finite speed ramp back to zero magnetic field before detection. The same scheme was also used for switching off the field after evaporation above the resonance. Care also had to be taken that evaporative loss did not occur after heating the sample. This was done by minimizing the time for the magnetic field ramps so that the atoms would spend only negligible time in fields where the scattering length is large. The number of atoms measured after the dissociation process thus yields the number of free atoms together with atoms having formed molecules. Evaporation at 764 G initially proceeds in a very similar way as above the resonance. However, below  $P = 10\text{ mW}$  the measured atom numbers depicted by the filled circles in Fig. 7.1 show a striking difference in comparison with the case of the degenerate Fermi gas. Down to a power level of  $P = 3\text{ mW}$  ( $U_{\text{mol}}/k_B \approx 420\text{ nK}$ ) the trap holds almost all particles and contains up to 20 times more atoms than it would be possible for fermions. Hence, the trapped sample can no longer be an atomic Fermi gas. The trap is filled with bosonic molecules in the weakly bound state. The lifetime of the molecular ensemble, for which we measured about 20s at a fixed trap depth of  $U_{\text{mol}}/k_B \approx 500\text{ nK}$ , exceeds the time scale of elastic collisions ( $\sim 100\mu\text{s}$ ) by several orders of magnitude. This highlights that the molecular cloud exists in a thermal equilibrium state.

In the experiments described in the previous chapter, molecules were formed at constant trap depth and thus almost constant temperature. Here, the chemical atom-molecule equilibrium shifts from a pure atomic sample to a pure molecular sample. In the final stage of cooling all relevant energies, i.e. the thermal energy  $k_B T$  and the trap depths  $U_{\text{at}}$  and  $U_{\text{mol}}$ , are far below the binding energy  $\hbar^2/(ma^2)$  so that in chemical equilibrium one is left with an essentially pure sample of molecules. Furthermore, any residual atoms, also those that might be left in a single state due to an initially imperfect spin mixture are expected to evaporate quickly out of the trap, as they see only half the trap depth as compared to the molecules.

The observation that a large number of  $N_{\text{mol}} \approx 1.5 \times 10^5$  molecules are confined in our very shallow, only 420 nK deep trap under thermal equilibrium conditions already shows that a molecular BEC is formed. The trap offers about 10 times more quantum states for dimers as compared to the case of atoms discussed before. A factor

of eight comes from the fact that the trap depth for the molecules is twice as large as for the atoms and another factor of 1.24 is due to the lower magnetic confinement at 764 G. As we observe a factor of  $\sim 20$  more particles than for the degenerate atomic Fermi gas, the molecular gas is necessarily quantum degenerate. Because of the high elastic collision rates, which stay well above  $10^3 \text{ s}^{-1}$  even for very shallow traps, the sample is also thermalized. The temperature then must be a small fraction of the trap depth. According to standard evaporation theory [O'H01], we can typically assume  $T \approx 0.1 U_{\text{mol}}/k_B \approx 40 - 50 \text{ nK}$ . This is well below the critical temperature for BEC, for which we calculate  $T_c = 280 \text{ nK}$  using Eq. 3.6 from the above parameters. As the condensate fraction is given by  $1 - (T/T_c)^3$ , these arguments show that the molecular BEC must be almost pure.

## 7.2 First experiments with the Bose-Einstein condensate

In this section, the first experiments that were done with the molecular Bose-Einstein condensate are presented. Obviously, it was important to image the molecular cloud to be able to observe the phase transition to a BEC by imaging the bimodal distribution and watching the thermal component to disappear during evaporation.

Before we were able to image our molecular clouds, we used some unconventional techniques to study the properties of our BEC. By tilting the trap using a magnetic field gradient we could spill the BEC out of the trap in a controlled way. By performing the spilling at different magnetic fields, we could show that the mean field size of the BEC changes with the magnetic field in an expected way, proving that the shape of our molecular cloud is governed by its mean field energy, which can only be the case in a BEC.

### 7.2.1 Imaging the molecules at high magnetic field

There are several ways to image molecules produced at a Feshbach resonance. Most of them include dissociating the molecules into atoms and then, before the spatial distribution changes, imaging the atoms. The dissociation can either be done by a magnetic field ramp across the Feshbach resonance [Her03] or by applying a radio frequency pulse. In this case, one of the resulting atoms changes its hyperfine state and thus one can selectively image the molecules by imaging atoms in the respective state.

If the molecules have a very small binding energy, they can be imaged with the same light that would be used to image atoms at the same field, which is described in section 4.5.2. As the ground state energy shift of a few  $\mu\text{K}/k_B$  is much smaller than

the width of the atomic transition, only the shift of the excited state plays a role. The long-range excited state potential is [Wei99, Zwi03]

$$V_e(R) \simeq \hbar\Gamma \times \left(\frac{\lambda}{2\pi R}\right)^3, \quad (7.1)$$

where  $R$  is the distance between the two atoms. This means that as long as the inter-atomic distance is larger than  $\sim 100$  nm, the detuning of the molecular transition will be small compared to the atomic linewidth of 5.9 MHz. As the size of the molecule is on the order of the atomic scattering length, the molecules can be imaged as if they were free atoms down to a magnetic field of  $\sim 720$  G, which is consistent with our observation.

Our current imaging technique works only for very weakly bound molecules and is destructive, so one can only take one single shot per measurement. However, techniques like off-resonant phase contrast imaging [Ket99] should be readily applicable also for imaging molecules. With such a technique it should also be possible to image more strongly bound molecules on bound-bound transitions [Hul04].

## 7.2.2 Bimodal distributions of a BEC with large scattering length

The emergence of a narrow peak on top of the much broader thermal momentum or spatial distributions while cooling a dilute ultracold gas has emerged in the past years as a standard method to observe the phase transition to a Bose condensed gas (see 3.1.3, [Ket99]). In our experiment, the application of this technique is subject to a few constraints:

- First, the scattering length of our molecules is rather large, causing the usual assumptions of a dilute gas to be not as well fulfilled as for alkali atoms. Fortunately, the scattering length of our molecules can be tuned over a wide range, providing additional diagnostic possibilities. For the images presented in this chapter, the magnetic field is always ramped adiabatically to 676 G to tune the scattering length to a value as low as possible without affecting the lifetime of the BEC significantly.
- A second difficulty results from the axial magnetic confinement of the molecules in the focused beam trap. As this confinement is directly related to the magnetic offset field that determines the properties and the stability of our molecules, it cannot be switched off, and time-of-flight measurements along the axial direction are not possible.
- As a consequence, all the measurements presented in the following were done by analyzing *in situ* images. While the radial size on the order of  $\sim 1 \mu\text{m}$  is smaller than the  $\sim 10 \mu\text{m}$  resolution of our imaging system, the axial extent of the cloud

## 7.2 First experiments with the Bose-Einstein condensate

of roughly  $100\text{ }\mu\text{m}$  is well resolved, and radially integrated axial profiles will be analyzed in the following section.

### Analysis of the *in situ* images

In the following, images taken during evaporative cooling are analyzed. A set of images and their radially integrated profiles are shown in Fig. 7.2. One can see clearly that starting from the second image, a narrow peak appears on top of the broader thermal distribution with its Gaussian wings that are getting smaller and smaller as the temperature is reduced. For a quantitative analysis of the images we adopt the semi-ideal model [Nar98] as described in section 3.1.3, neglecting the interaction energy of the thermal component. The radially integrated line profiles obtained from the density distribution given in 3.22 and 3.23 are

$$n_0(z) = \begin{cases} \pi \frac{(\mu - \frac{1}{2}m\omega_z^2 z^2)^2}{g m \omega_r^2} & \text{for } \mu - \frac{1}{2}m\omega_z^2 z^2 > 0, \\ 0 & \text{otherwise.} \end{cases} \quad (7.2)$$

and

$$n_T(z) = \frac{2\pi}{\lambda_T^3} \frac{kT}{m\omega_r^2} \begin{cases} 2\zeta(5/2) - g_{5/2} \left( e^{-(\mu - \frac{1}{2}m\omega_z^2 z^2)/k_B T} \right) & \text{for } \mu - \frac{1}{2}m\omega_z^2 z^2 > 0, \\ g_{5/2} \left( e^{(\mu - \frac{1}{2}m\omega_z^2 z^2)/k_B T} \right) & \text{otherwise} \end{cases}, \quad (7.3)$$

where  $n_0(z)$  and  $n_T(z)$  now represent line densities \*. These calculated density profiles are now fitted to the measured profiles shown in Fig. 7.2. The profiles are obtained by summing the images shown on the right hand side in Fig. 7.2 along the vertical direction†. To obtain the correct axial cloud size, the observed axial dimension has been multiplied by  $1.39 \pm 1.5\%$  to compensate for the viewing angle (see 4.5.2). The resulting fits are shown in Fig. 7.2 as dark and light gray shading for the condensed and noncondensed fractions. The fit includes four independent parameters: The total molecule number given by the integrated signal, the temperature which is obtained from the width of the thermal cloud, the fraction of condensed atoms and the chemical potential of the BEC determined by the size of the condensed cloud  $\mu = 1/2 m \omega_{\text{ax}}^2 r_{\text{TF,ax}}^2$ . The resulting values are plotted in Fig. 7.3 a)-d) versus the final laser power of the evaporation ramp. A significant fraction of condensed molecules appears at a laser power of 30 mW ( $U_{\text{mol}} = k_B \times 4.3\text{ }\mu\text{K}$ ) at a temperature of  $\sim 600\text{ nK}$ . The condensate fraction reaches  $\sim 90\%$  at a laser power of  $\sim 5\text{ mW}$  ( $U_{\text{mol}} = k_B \times 720\text{ nK}$ ) and a temperature of  $\sim 100\text{ nK}$ . While lowering the trap depth further, the fit on the thermal wings acquires increasingly large errors, because the thermal wings get smaller and smaller and extend only very slightly beyond the condensate mean field.

\*To integrate equation 3.23 one has to make use of the identity  $dg_{p+1}(z)/dz = g_p(z)/z$ .

†Each image is the average of typically seven individual images to reduce noise.

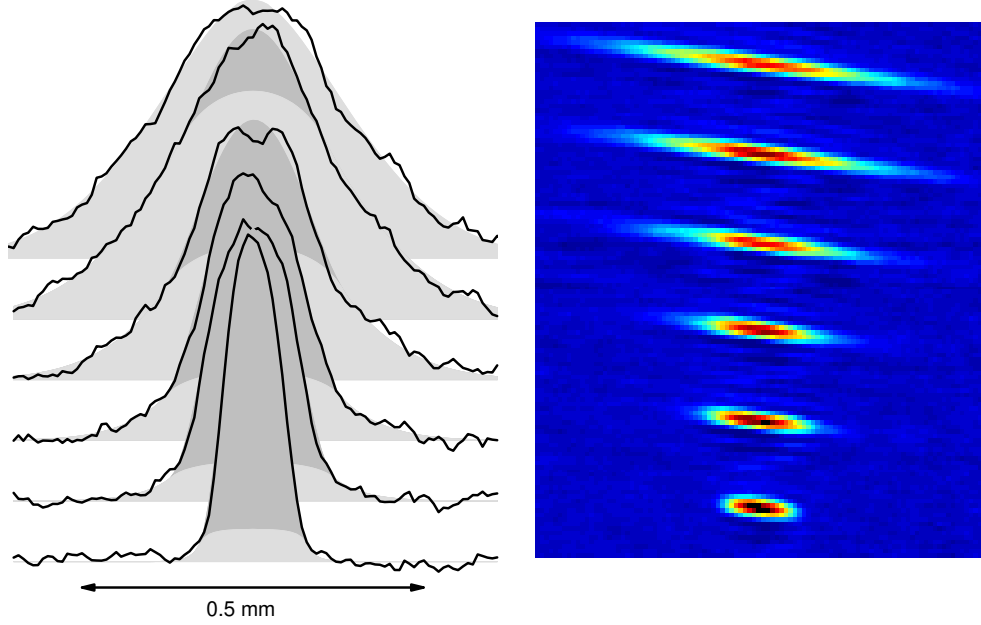


**Figure 7.2:** In-situ absorption images and axial profiles of the molecular cloud during evaporative cooling, starting at a laser power level of  $\sim 40$  mW, going down to  $\sim 1$  mW, with corresponding temperatures ranging from  $\sim 600$  nK to  $\sim 15$  nK. Bose-Einstein condensation occurs between the first two images. The bimodal fits to the data show the thermal (light gray) and condensed fractions (dark gray) of the sample.

### Determination of the scattering length

We calculate the scattering length from the chemical potential, the condensed molecule number and the trap frequencies, using equation 3.16:

$$a = \left( \frac{2\mu}{\hbar\bar{\omega}} \right)^{5/2} \frac{\bar{a}_{\text{ho}}}{15N_0} = \frac{(2\mu)^{5/2}}{15N\hbar^2\bar{\omega}^3 \sqrt{m}}, \quad (7.4)$$

$\bar{a}_{\text{ho}} = \sqrt{\hbar/m\bar{\omega}}$  being the harmonic oscillator length associated with the geometric mean vibration frequency  $\bar{\omega}$ . The result is shown in Fig. 7.3 e). The data at high trap depth have a very large error that comes from the fact that the small condensate fraction has a large relative error and also the chemical potential can not be determined very well. At laser powers between 20 mW and 5 mW, all the data yield a consistent value of the scattering length of  $\sim 400a_0$ , while at very low trap depths ( $P < 2$  mW), the calculated scattering length drops significantly, which can be attributed to anharmonicity of the radial trapping potential\*.

\*The chemical potential for these points is close to the trap depth and thus the BEC already sees the anharmonic gaussian shape of the trapping potential, which is also confirmed by the spilling loss that is

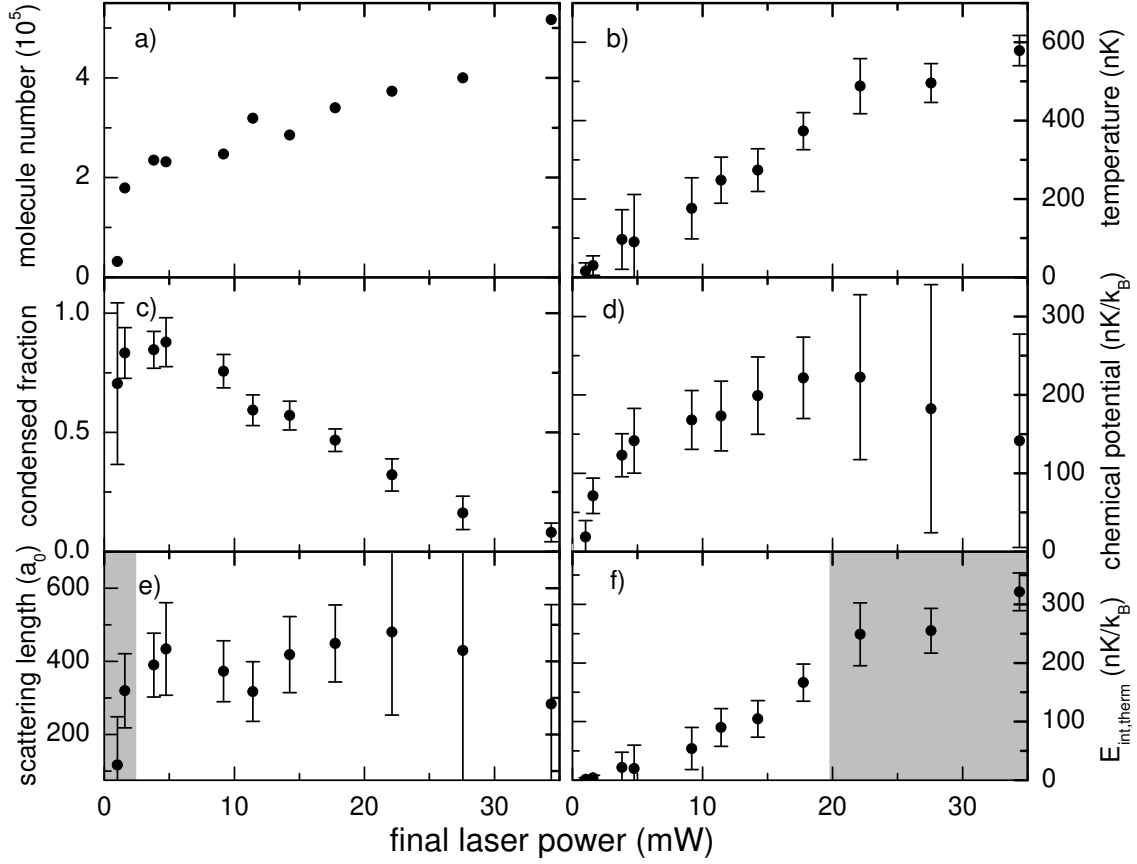


**Figure 7.3:** Parameters obtained from the fits to the data shown in Fig. 7.2 versus the final relative trap laser power: a) Total number of molecules remaining. b) Temperature of the molecules. c) Condensate fraction. d) Chemical potential. e) Scattering length calculated from molecule number and chemical potential. f) Maximum interaction energy per molecule in the thermal gas in the semi-ideal model [Nar98]. The areas shaded in gray in e) and f) indicate where quantitative analysis is not possible because of anharmonicity effects (e) or because the assumption of an ideal thermal gas breaks down (f).

In the semi-ideal model, we assumed that the interaction energy of the thermal component of the BEC does not play a role. To check how well this assumption is fulfilled, we calculate the maximum interaction energy per particle to zeroth order, neglecting any change in density from the noninteracting case. This energy is

$$E_{\text{int,therm}} = 2gn_T = \frac{8\pi\hbar^2 a}{m} \frac{\zeta(3/2)}{\lambda_T^3} \quad (7.5)$$

demonstrated with the lowest point in Fig. 7.3 a). The effectively lower radial trap frequency then leads to a lower chemical potential

and is plotted in Fig. 7.3 f) in units of  $k_B$ . These values are significant fractions of both the temperatures and the chemical potentials for high trap depths. Obviously, the interaction energy calculated using 7.5 is strongly overestimated as they neglect the repulsive effect of the mean field. But for the data above  $P = 20$  mW the effect on the density of both the condensed fraction ( $E_{\text{int,therm}} > \mu$ ) and the thermal cloud must be significant, and a quantitative description for these data using the above model is expected to fail. Excluding the data points in Figs. 7.3 e) and f) shaded in gray and for which we know that the our model will not yield the correct scattering length, we determine a scattering length of

$$a = 390 \pm 40a_0 \text{ at } 676 \text{ G} \quad (7.6)$$

by averaging the results from the remaining data. The error given here is the statistical error that does not include any systematic uncertainties, the largest one stemming from the molecule number that scales linearly with the scattering length (see 7.4), and which has an uncertainty of  $\sim 50\%$ . According to our current knowledge [Bar04d], assuming the Feshbach resonance to be at 834 G, the atomic scattering length at 676 G is  $1170a_0$ . The molecular scattering length can then be estimated to be  $a_{\text{mol}} = 0.6 \times a_{\text{at}} = 706a_0$ , which is a factor of 1.8 larger than the measured value, which can in part be explained by a 50%-error of the particle number calibration \*.

### Condensate fraction and critical temperature

Fig. 7.4 shows the measured condensate fraction versus the temperature divided by the critical temperature  $T_c^0$  as calculated for an ideal gas. This relation has been calculated by Naraschewski *et al.* [Nar98] for the condition that the interactions can be treated in a perturbative way (equation 3.27). The small quantity  $\eta$  used in this calculation is for our data

$$\eta = \frac{\mu(T=0)}{k_B T_c^0} = 1.57 \left( N^{1/6} \frac{a}{a_{\text{ho}}} \right)^{2/5} \simeq 0.5 - 0.6. \quad (7.7)$$

Assuming that  $\eta$  is small enough, Eq. 3.27 describes the condensate fraction. The gray shaded area in Fig. 7.4 describes the condensate fraction expected from Eq. 3.27 for values of  $\eta$  between 0.45 and 0.65. It fits the data well within the large error bars for the temperature despite of the relatively large value for  $\eta$ . The black solid line

---

\*Any other errors are supposed to be much smaller, among them are the calibration of the magnification of the imaging system including the angles between the cigar shaped cloud and the camera (1%): The chemical potential scales with the square of the magnification, and thus the scattering length scales with the fifth power. Consequently, it can account for a 5% error of the scattering length. A remaining source of error are the trap frequencies. The scattering length depends on the fourth power of the axial frequency, while it depends only on the second power of the radial frequency, which can be seen from 7.4, taking into account the  $\omega_z^2$ -dependence of the observed chemical potential. The error in scattering length due to the trap frequencies consequently amounts to about 10%.



shows the calculated condensate fraction expected for a noninteracting gas using 3.9. It can be seen clearly that there is a significant reduction of the condensate fraction due to interactions. As the determination of the scattering length suggested that the molecule number be a factor of 1.8 lower as compared to our calibration, the dashed line shows the expected condensate fraction for that case assuming  $\eta = 0.55$ . This line lies significantly below the data in Fig. 7.4. This in return suggests that the molecular scattering length at 676 G has to be smaller than the expected  $720a_0$ . But as 676 G is already quite far away from the Feshbach resonance, one could think of a deviation from the  $a_{\text{mol}} = 0.6a_{\text{at}}$  law [Pet04] that is only correct for large  $a$ .

Close to the critical temperature, one expects that the semi-ideal model breaks down, because the calculated chemical potential is smaller than the interaction energy per particle in the thermal gas. For our molecules, this interaction energy is even on the order of the thermal energy, as can be seen from Fig. 7.3 f). Especially the critical temperature is a value that is difficult to get right if  $\eta$  is not very small. The critical temperature for our trap and atom numbers has been calculated numerically by S. Kokkelmans. It is  $0.89 \times T_c^0$  or  $0.93 \times T_c^0$  for  $a = 700a_0$  and  $a = 400a_0$ , respectively. In Fig. 7.4, these two values are represented by two triangles. Unfortunately, the critical temperature is quite hard to determine experimentally, so that this prediction cannot be verified quantitatively in the experiment.

### Lowest achieved temperature (entropy) and prospect for a highly degenerate Fermi gas

For subsequent measurements it is interesting to know the final temperature after evaporative cooling. The errors for the temperature obtained from the fits shown in Fig. 7.4 are rather large and do not result in a good estimate. The large error results from the fact that both the condensate fraction and the temperature are used as free parameters in the fit. If one however constrains the condensate fraction to the temperature using Eq. 3.27, the uncertainty in the temperature can be greatly reduced. One then obtains for the data at 3 mW in Fig. 7.3 a temperature of 114(14) nK, corresponding to  $T/T_c = 0.42(5)$  and a condensate fraction of 0.85(3), the error of which also includes the limited knowledge of the scattering length within a factor of two. Errors not included above are due to the imaging and due to quantum depletion. Errors in the imaging are rather hard to get quantitative, but they tend to make the thermal wings look wider. Thus, image distortion will make the temperature appear higher. The same is true for quantum depletion [Tim97]. It will cause some atoms to be expelled from the condensate if the interaction is large. The fraction of depleted atoms is  $5\pi/8 \sqrt{na}^3$  [Tim97, Pit03], which is  $\leq 1\%$  for the image analyzed here. As these two errors both make the observed temperature larger, the temperature and condensate fraction determined above represent upper limits. The chemical potential under these conditions is determined from the fit as  $k_B \times 125(6)$  nK, which is comparable to the temperature.

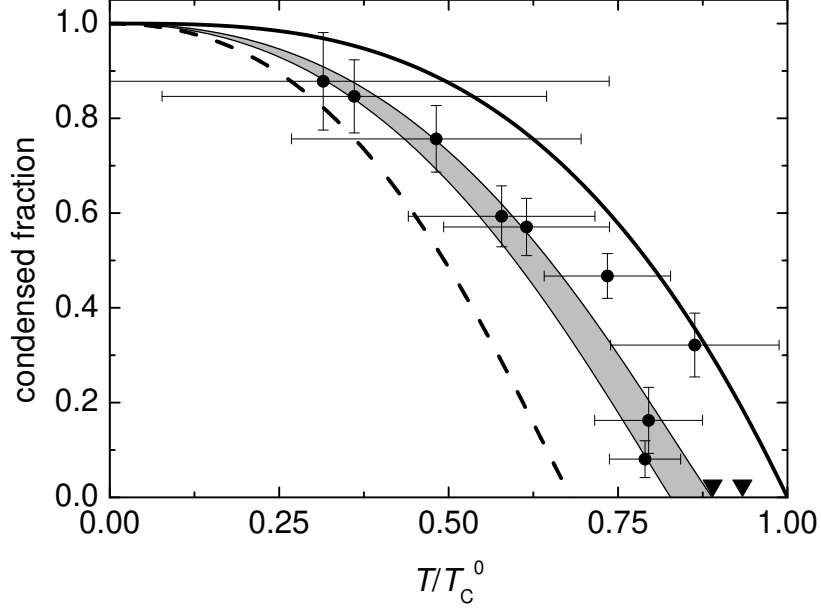


**Figure 7.4:** Condensate fraction versus temperature divided by the critical temperature calculated for an ideal gas. The gray shaded area represents the expectation using equation 3.27 for  $\eta$  between 0.45 and 0.65. The black solid line is the prediction for a noninteracting gas. The dashed line is calculated assuming a factor of 1.8 lower atom number with  $\eta=0.55$ . The two triangles represent the critical temperatures calculated by S. Kokkelmans assuming a scattering length of  $a = 700a_0$  ( $0.89 \times T_c^0$ ) and  $a = 400a_0$  ( $0.93 \times T_c^0$ ).

It is interesting to note that if the molecular BEC can be isentropically converted into a Fermi gas, it would be cooled significantly while the molecules are dissociated and the thermal energy is distributed on twice as many particles. This phenomenon was studied quantitatively in [Car04]. Carr *et al.* calculate the entropy of a noninteracting Fermi gas to be

$$S_{\text{Fermi}} = k_B N \pi^2 \frac{T}{T_F} + O(T^3), \quad (7.8)$$

and that of a (molecular) BEC in the Thomas-Fermi limit as

$$S_{\text{BEC}} \approx k_B N_{\text{mol}} \left( \frac{2\pi^4}{45\zeta(3)} + 3 \frac{\mu_{\text{mol}}}{k_B T} \right) \left( \frac{T}{T_c} \right)^3. \quad (7.9)$$

To obtain the analytic expression of Eq. 7.9, the entropy was expanded in terms of  $\mu_{\text{mol}}/k_B T$ . According to [Car04], Eq. 7.9 is accurate to within 10% for  $\mu_{\text{mol}}/k_B T \leq 10$ , well fulfilled for all our experiments. Equating the two entropies, one can obtain the

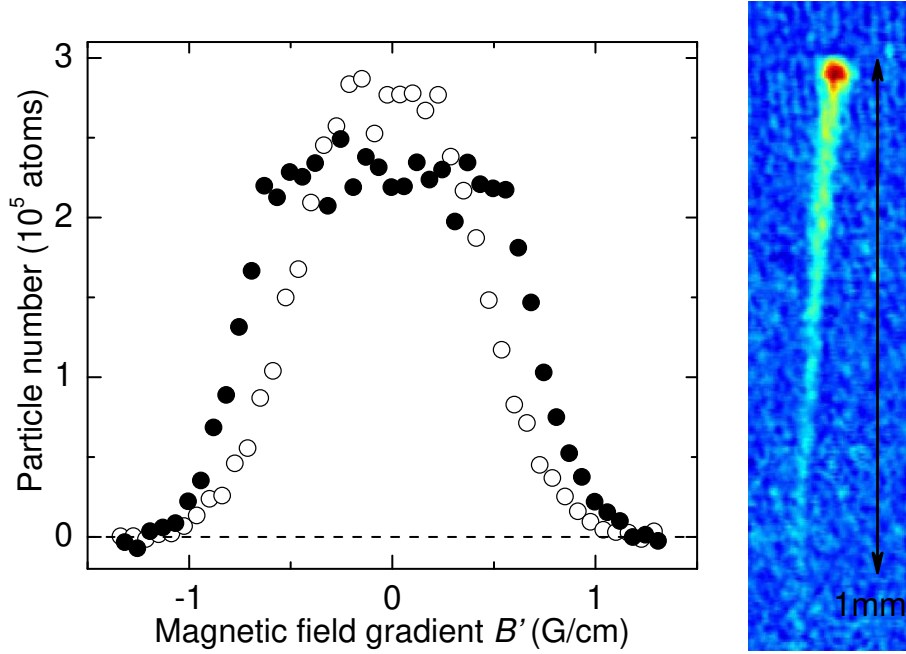


**Figure 7.5:** Controlled spilling of the BEC by application of a magnetic field gradient  $B'$ . This variable gradient was applied in addition to the constant gradient of 1.1 G/cm that we use for gravity compensation. The data are taken at two different magnetic fields,  $B_1 = 772$  G ( $\circ$ ) and  $B_2 = 731$  G ( $\bullet$ ), where the mean field of the BEC is different by a factor of  $\sim 2$ . The image on the right shows how molecules are spilled out of the trap in a controlled way, the spilling results in a molecule laser!

temperature of the Fermi gas,

$$\frac{T}{T_F} = \frac{1}{2\pi^2} \left( \frac{2\pi^4}{45\zeta(3)} + 3 \frac{\mu_{\text{mol}}}{k_B T} \right) \left( \frac{T}{T_{\text{BEC}}} \right)^3. \quad (7.10)$$

Plugging in the numbers given above, one gets  $T/T_F \leq 0.025(10)$ . Indeed, we could show later that the crossover to a Fermi gas proceeds with negligible increase of entropy [Bar04c] and one can expect to achieve such temperatures in the Fermi gas regime. This expected temperature of  $0.025T_F$  is a factor of two lower than the lowest temperatures reported previously [Had03]. At such temperatures, a Fermi gas with strong interactions should be deep in the superfluid regime.

### 7.2.3 Studying a BEC without imaging

#### Controlled spilling of the condensate

Before we were able to image our molecules we performed controlled spilling of the condensate to demonstrate the mean field of the molecular BEC and to investigate its

dependence on the magnetic field. After producing the BEC at a magnetic field of  $B_1 = 772$  G and a final laser power of 3.7 mW which corresponds to a trap depth of  $U_{\text{mol}}/k_B \approx 500$  nK we adiabatically tilted the vertical trapping potential by application of a magnetic field gradient  $B'$  that was smoothly ramped up within 50 ms. The magnetic field gradient was applied using the small auxiliary coils that are also used to compress the MOT during the loading of the dipole trap. A small additional gradient is always applied to compensate for gravity (1.06 G/cm) and stray magnetic field gradients. The number of remaining particles as a function of the applied field gradient (Fig. 7.5) shows the loss of molecules resulting from the reduced trap depth. When the magnetic field is kept at the evaporation field of  $B_1 = 772$  G, where the scattering length is  $a \approx 4100a_0$ , even very weak gradients lead to loss (open circles). This indicates that the chemical potential is close to the potential depth so that the trap is full. The chemical potential can be lowered by reducing the scattering length. For this purpose we ramped the magnetic field to a smaller value. A spilling curve taken at  $B_2 = 731$  G, where the scattering length is  $a \approx 2200a_0$ , indeed shows a markedly different behavior (filled circles in Fig. 7.5). Here small gradients do not lead to any loss and the curve thus shows a flat top. For gradients  $|B'|$  exceeding 0.65 G/cm atoms get spilled until everything is lost at  $|B'| = 1.3$  G/cm.

A comparison of the two spilling curves in Fig. 7.5 provides us with information on the ratio of the scattering lengths  $a_m$  at the two magnetic fields  $B_1$  and  $B_2$ . In the spilling region above  $|B'| = 0.65$  G/cm the trap is full in both cases, and the trapped particle number is inversely proportional to  $a_m$ . Comparing of the two spilling curves in that region we obtain a scattering length ratio of  $a_m(B_1)/a_m(B_2) = 2.4(2)$ . This factor is indeed close to the factor of 1.9 expected from the proportionality of atomic and molecular scattering lengths  $a_m \propto a$  [Pet03a] and the dependence of  $a$  with the magnetic field. This observation demonstrates the mean field of the molecular BEC together with its magnetic tunability.

After we had absorption imaging for the molecules available, we came back to the spilling experiment for a moment, to see how the spilling process would look like. The image shown on the right in Fig. 7.5 was taken right after the magnetic field gradient ramp, showing a continuous flow of molecules out of the trap. The properties of this molecular beam were not studied, but one can expect that this is the first molecule laser!

### Collective oscillations

For our cigar-shaped BEC in the Thomas-Fermi limit, the lowest frequency collective excitation mode is a quadrupolar mode which is expected at a frequency of

$$\omega_{\text{BEC}} = \sqrt{\frac{5}{2}} \omega_z = 2\pi \times 33.8 \text{ Hz. [Str96]} \quad (7.11)$$

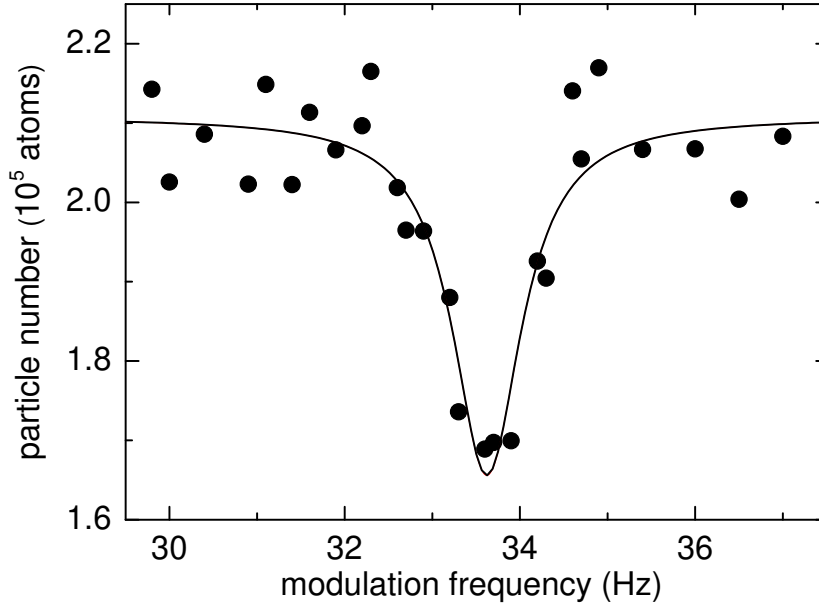


**Figure 7.6:** Resonance of a collective excitation mode at  $\sqrt{5/2}\omega_z$ . The oscillation is excited by magnetic modulation of the molecular BEC mean field. The solid curve shows a Lorentzian fit to the data.

We performed our measurement at  $\sim 3.7$  mW ( $U_{\text{mol}}/k_B \approx 500$  nK) with a trapped sample of  $\sim 10^5$  molecules at a magnetic field of 764 G. We applied a sinusoidal modulation to the magnetic field with an amplitude of 3.5 G. This resulted in a modulation of the molecular scattering length with a relative amplitude of about 5%, whereas the resulting amplitude in the axial trap frequency is only 0.2%. After two seconds of continuous excitation we measured the remaining number of particles in the trap. The resonance manifests itself in a sharp dip in the number of particles as shown in Fig. 7.6. The observed resonance frequency of 33.6 Hz is in remarkable agreement with the expectation. It is interesting to note that a non-condensed gas deep in the hydrodynamic regime would show a similar frequency of

$$\omega_{\text{hydro}} = \sqrt{\frac{12}{5}} \omega_z = 2\pi \times 33.2 \text{ Hz [GO99]}, \quad (7.12)$$

which differs only by 2% from that of a BEC. This measured collective excitation frequency rules out a gas in the collisionless regime, which would show its resonant loss at  $2\omega_z = 2\pi \times 42.8$  Hz. Without the ability to image the molecules, the observation of the collective excitation mode was a key argument to prove the presence of a BEC. The observed narrow resonance width of  $\sim 1$  Hz shows a very low damping rate and is consistent with an almost pure BEC [Jin97].



# Chapter 8

## Outlook

The almost pure molecular Bose-Einstein condensate that was realized during this thesis serves as an ideal starting point for further experiments. By tuning the binding energy of the molecular state above zero a strongly interacting Fermi gas can be realized, and a BCS-type superfluid is expected when the interactions become sufficiently weak. This so-called BEC-BCS crossover (see chapter 3.2 for details and references) has been under theoretical investigation for several decades and can now finally be studied experimentally.

Indeed after completion of the experimental work in the frame of this thesis we could show that the molecular BEC can be converted adiabatically and reversibly into a highly degenerate Fermi gas of atoms [Bar04c]. In a race to prove the superfluidity of the strongly interacting Fermi gas above the Feshbach resonance, a number of important experiments were performed in several groups. Regal *et al.* at JILA could show that pairs existed above the Feshbach resonance and that these pairs were Bose-condensed [Reg04], which was quickly confirmed by experiments performed by Zwierlein *et al.* at MIT. Collective excitation measurements performed with our experiment [Bar04b] and by Kinast *et al.* at Duke University [Kin04a] showed extremely low damping and provided further evidence that the strongly interacting gases studied by these groups are in a superfluid state also above the Feshbach resonance. The most recent progress in our group is the observation of the pairing gap in the Fermi gas [Chi04a], which is another strong indication of superfluidity. However, none of the above experiments were able so far to provide a real “smoking gun” for superfluidity, which represents the next great challenge for experimentalists.

In the following I will shortly summarize the results obtained with our experiment. They will be described in detail in Markus Bartenstein’s PhD thesis [Bar04a].

### **Crossover from a molecular BEC to a degenerate Fermi gas [Bar04c]**

The extraordinarily long lifetime of the molecular BEC of 40 s close to the Feshbach resonance immediately suggested that our strongly interacting gas should be very sta-

ble against any kind of inelastic decay. But the question remained whether the process of dissociating the molecules through a magnetic-field sweep across the Feshbach resonance would be reversible and a BEC of molecules would be recovered when the magnetic field is ramped back to its original value. Experiments showed that such magnetic-field ramps were indeed isentropic provided that the ramps were performed slow enough so that the gas would always remain in equilibrium. The first measurement of the axial cloud size as a function of the magnetic field in the crossover regime showed that the conversion to the Fermi gas is completely smooth, and the shape of the cloud is continuously transformed into that expected for an interacting Fermi gas.

### Collective excitations in the BEC-BCS crossover [Bar04b]

A well established technique to study the dynamic properties of a trapped gas is to excite collective oscillations and measure their frequencies and damping. Experimentally in our cigar-shaped trap the lowest axial and radial collective frequencies are the most straight forward to excite. The calculations for the collective modes in the strongly interacting regime are challenging. In December 2003, S. Stringari summarized the status of theoretical results in [Str04]. For the low-frequency axial mode, our results could very well reproduce the expectations. This was not the case for the radial mode where we found surprising features. In the strongly interacting molecular BEC regime, we observe a negative frequency shift with increasing coupling strength while a positive shift was expected. In the regime of a strongly interacting Fermi gas, an abrupt change in the collective excitation frequency occurs, which may be a signature for a transition from a superfluid to a collisionless phase.

### Observation of the pairing gap in a strongly interacting Fermi gas [Chi04a]

Experiments pioneered by Regal *et al.* showed that the weakly bound molecules formed on a Feshbach resonance could be dissociated by radio frequency spectroscopy to determine the binding energy [Reg03]. The main idea is that a radio frequency transition is driven from the weakly bound molecular state formed from one atom in state  $|1\rangle$  and one in state  $|2\rangle$  to a pair of free atoms in state  $|1\rangle$  and  $|3\rangle$ . Due to the small binding energy, this transition is only slightly upshifted as compared to the free-atom transition from state  $|2\rangle$  to state  $|3\rangle$ , which has a frequency of about 80 MHz at high magnetic field.

We extended this technique to the strongly interacting Fermi gas above the Feshbach resonance, where no two-body bound state exists. Here, an upshift in frequency represents the amount of energy that is needed to remove a single particle from the gas. Fig. 8.1 shows radio frequency spectra of our spin mixture at different magnetic fields and temperatures. Plotted is the fractional loss in state  $|2\rangle$  versus the frequency offset from the free-atom transition. The upper row shows the spectrum of a thermal gas



where the temperature is much larger than the binding energy and no molecules exist. In this case only the narrow atomic transition is observed. In the consequent rows the temperature is reduced in two steps to the lowest possible temperature in our setup. In the second row one can clearly observe a second peak appear above the atomic frequency while the position of the atomic peak is unchanged. Surprisingly, a double-peak structure also emerges on the Feshbach resonance and above, where no molecular bound state exists. Further cooling then leads to a complete extinction of the atomic signal indicating that all atoms are paired. Below the Feshbach resonance, the shape of the molecular peak is unchanged during the cooling process because the dissociation of the molecules into two free atoms is a simple two-body process. On resonance and above, the pairing mechanism is many-body in nature and therefore, the pair-breaking energy depends on the temperature and the Fermi energy of the system. The spectra observed in the crossover region are in beautiful agreement with a theoretical model developed by Kinnunen *et al.* [Kin04b]. The appearance of the double peak structure early in the evaporative cooling process suggests that our full evaporation brings the strongly interacting system deep into a superfluid state.

### **New experimental challenges: A “smoking gun” for superfluidity**

While the experiments described above provide strong evidence for the presence of a superfluid phase in our strongly interacting Fermi gas, none of them is a clear manifestation of superfluidity. The next great experimental challenge will be to find direct evidence for superfluidity. The beautiful experiments that have been performed with atomic BECs can provide ideas and incentives: One of the most stunning effects would be the excitation of vortices [AS01]. Other interesting experiments would be the observation of matter-wave interference [And97] to show the phase coherence of the gas. Bragg diffraction [Ste99] or optical lattice experiments [And98, Gre02] could also give new insight into the properties of deeply degenerate Fermi gases. The first optical lattice experiments are already on the way in Florence [Mod03] and in Zurich.

All of the above ideas are already being actively pursued in several groups around the world and experimenters will definitely have a lot of fun producing more exciting results already in the coming months.

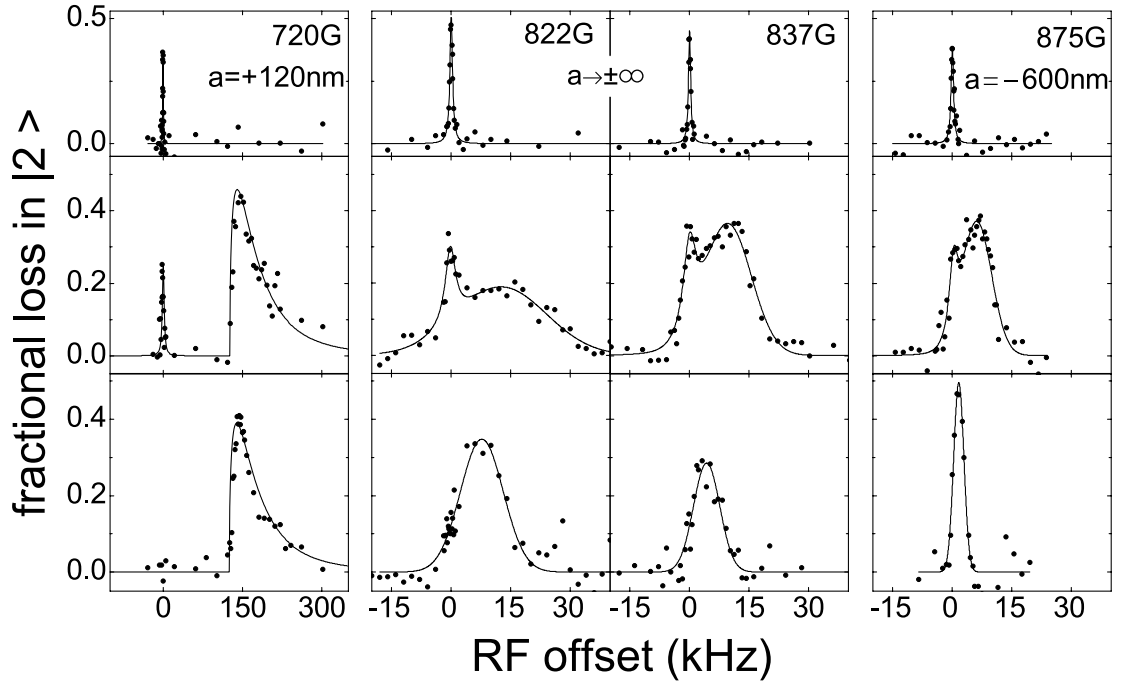


**Figure 8.1:** RF spectra for various magnetic fields and different degrees of evaporative cooling. The RF offset ( $k_B \times 1 \mu K = \hbar \times 20.8 \text{ kHz}$ ) is given relative to the atomic transition  $|2\rangle \rightarrow |3\rangle$ . The molecular limit is realized for  $B = 720 \text{ G}$  (first column). The resonance regime is studied for  $B = 822 \text{ G}$  and  $837 \text{ G}$  (second and third column). The data at  $875 \text{ G}$  (fourth column) explore the crossover on the BCS side. Upper row, signals of unpaired atoms at  $T' \approx 5T_F$  ( $T_F = 18 \mu K$ ); middle row, signals for a mixture of unpaired and paired atoms at  $T' = 0.5T_F$  ( $T_F = 3.4 \mu K$ ); lower row, signals for paired atoms at  $T' < 0.2T_F$  ( $T_F = 1.2 \mu K$ ). Note that the true temperature  $T$  of the atomic Fermi gas is below the temperature  $T'$  which was always measured in the BEC limit (see chapter 7.2.2 and Eq. 7.10). The solid lines are introduced to guide the eye.

# Appendix A

## Lithium properties

In this appendix, only the most important properties of lithium are summarized. A more elaborate treatment can be found in [Geh03a] for example.

### A.1 Chemical properties

Lithium (Greek lithos, meaning “stone”) was discovered by the Swedish chemist Johann Arfvedson in 1817. Arfvedson found the new element within minerals, which gave the element its name. Lithium in its pure form is a soft, silver white metal, that oxidizes very rapidly in air and water. It is the lightest solid element with a density only about half that of water.

Industrially, lithium is used for heat transfer applications due to its large heat capacity, and for batteries because of its high electrochemical potential.

Being the lightest of all alkali atoms, it features the highest melting point of 181°C and also the lowest vapor pressure. It can be approximated by [Lid92]

$$p_{\text{Li}} = 10^{8.061-8310/T} \text{ mbar}, \quad (\text{A.1})$$

where  $T$  is measured in Kelvins. At 300°C, it is  $3.6 \times 10^{-7}$  mbar, at 400°C it is  $5.2 \times 10^{-5}$  mbar. This low vapor pressure makes magneto-optic trapping of lithium atoms from a background gas impossible, and a slowed atomic beam has to be used to achieve a reasonable loading rate of the magneto-optical trap.

Lithium has two stable isotopes. Naturally abundant lithium consists of 92.5%  ${}^7\text{Li}$  and 7.5%  ${}^6\text{Li}$ . The  ${}^6\text{Li}$  isotope is an important ingredient of the thermonuclear hydrogen bomb, where  ${}^6\text{Li}$  serves as a source for tritium, which has a finite lifetime of 12 years and is thus not suitable for long-time storage. For this reason isotope separation was performed on a large scale in the mid-1950s and early 1960s.

## A.2 Atomic structure

As an alkali atom, lithium has a hydrogen-like atomic level structure with the single  $2S_{1/2}$  valence electron determining most of its properties. The two main optical transitions are the two dipole 671-nm transitions to the  $2P_{1/2}$  and the  $2P_{3/2}$  excited states that have a splitting of  $\sim 10$  GHz.

The nuclear spin of either  $F = 1$  ( $^6\text{Li}$ ) or  $F = 3/2$  ( $^7\text{Li}$ ), which is added to the spin  $S = 1/2$  of the electronic ground state lead to an either half-integer ( $^6\text{Li}$ ) or integer ( $^7\text{Li}$ ) total angular momentum. This causes the  $^6\text{Li}$  atom to be a fermion and the  $^7\text{Li}$  atom to be a boson. The coupling of the nuclear spin with the electron spin also gives rise to a hyperfine splitting, which is 228.20526 MHz for  $^6\text{Li}$  and 803.50487 MHz for  $^7\text{Li}$  [Ari77].

Fig. A.1 shows the Zeeman energy of those states of the  $^6\text{Li}$  atom that are relevant for the experiments in this thesis, the  $2S_{1/2}$  ground state and the  $2P_{3/2}$  excited state.

### $^6\text{Li}$ ground state

The  $I = 1$  nuclear spin of the  $^6\text{Li}$  atom couples to the electron spin and leads to a hyperfine splitting of the  $2S_{1/2}$  ground state resulting in total angular momentum states of  $F = 1/2$  and  $F = 3/2$  that are split by 228 MHz.

When magnetic fields are applied, the Zeeman shift is linear only in a small magnetic field range  $\ll 30$  G because of the weak hyperfine coupling and the Breit-Rabi formula [Bre31] has to be used to calculate the magnetic field dependent energies of the hyperfine states:

$$E_{\text{HFS}}(B, F = 1 \pm \frac{1}{2}, m_F) = -\frac{1}{6}\Delta E_0 + m_F g_N \mu_B B \pm \frac{\Delta E_0}{2} \left( 1 + \frac{2}{3} m_F x + x^2 \right)^{1/2}, \quad (\text{A.2})$$

where

$$x = \frac{(g_J - g_N)\mu_B}{\Delta_0} B, \quad (\text{A.3})$$

with  $g_J = 2.0023010$  and  $g_N = -0.0004476540$  [Ari77].

At high magnetic field  $\gg 30$  G, the nuclear spin is completely decoupled from the electron spin, the atom is in the Paschen-Back regime. Depending on the electron spin, the atom is either a high-field seeker ( $m_S = -1/2$ ) or a low-field seeker ( $m_S = +1/2$ ) with a magnetic moment of  $\sim \mu_B$ . The nuclear spin leads to a splitting of the electronic states by approximately 80 MHz with  $m_I = \pm 1, 0$  (see Fig. A.1).

In our experiments, we use a spin mixture of the two lowest-lying levels to avoid any two-body decay channels.

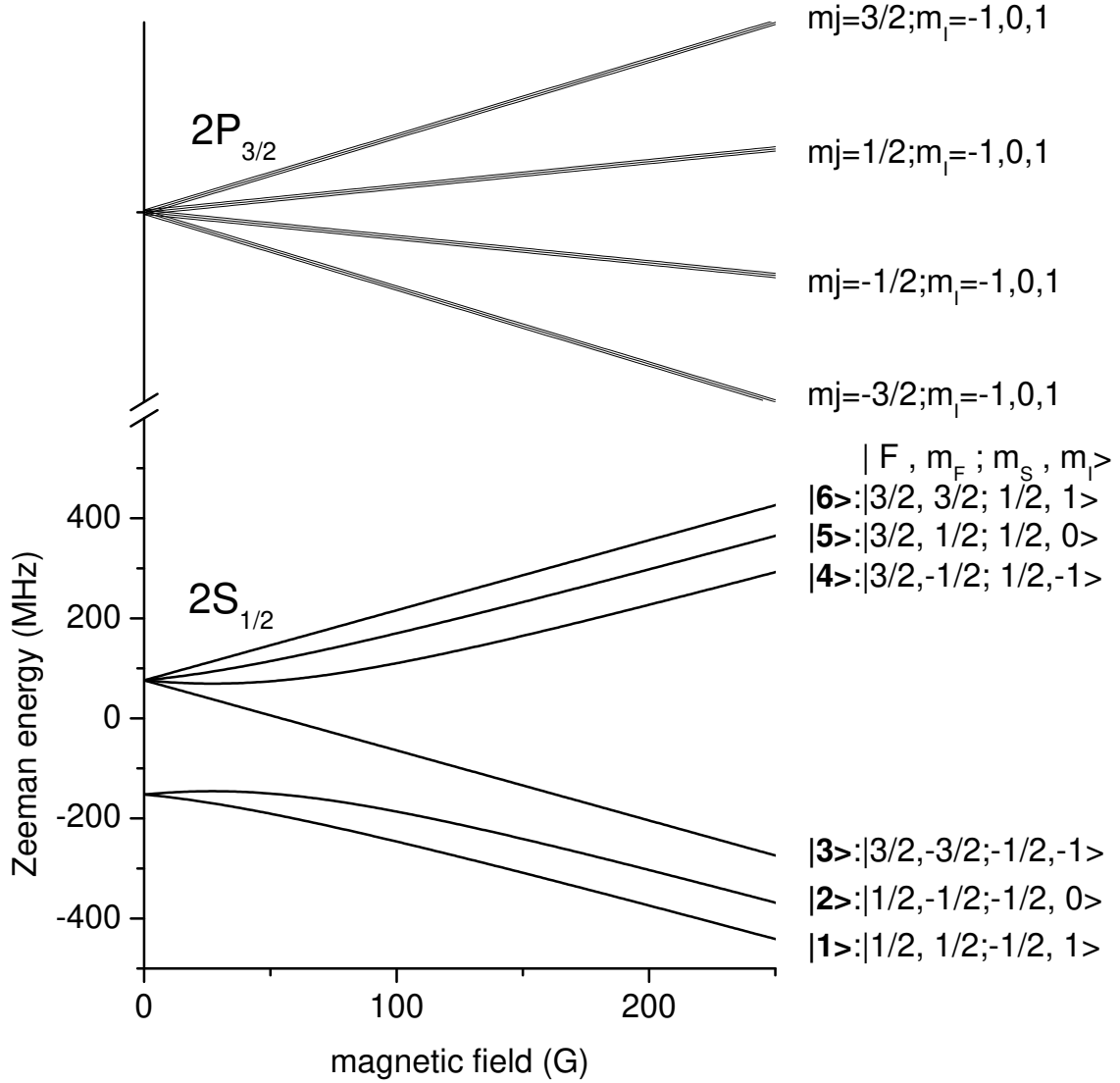


**Figure A.1:** Schematic of the Zeeman energy of those states of the  ${}^6\text{Li}$  atom that are of interest for this thesis: The  $2S_{1/2}$  ground state and the  $2P_{3/2}$  excited state. While the hyperfine splitting of the ground state of 228 MHz is important, the hyperfine splitting of the excited state is smaller than the width of the optical transition of 5.9 MHz.

### Optical transitions for trapping and imaging

In alkali atoms, there exists a closed (cycling) transition from a stretched ground state to a stretched excited state. In lithium, this is the transition from the  $F = 3/2; m_F = 3/2$  ground state to the  $F' = 5/2; m_F' = 5/2$  excited state, from which it can only decay back into its original state. Unfortunately, the hyperfine splitting between the  $F' = 5/2$  and the  $F' = 3/2$  excited states is only  $\sim 3$  MHz, about half the natural linewidth of the

## *A Lithium properties*

transition of 5.9 MHz. This means that light resonant with the  $F = 3/2 \rightarrow F' = 5/2$  transition is also resonant with the  $F = 3/2 \rightarrow F' = 3/2$  transition, from which the atoms can decay to the  $F = 1/2$  ground state. Therefore, the continuous scattering of photons at zero magnetic field always requires the simultaneous excitation from both the  $F = 3/2$  and the  $F = 1/2$  states, and two sources with a frequency splitting of 228 MHz are required, both for imaging or for trapping the atoms.

At high magnetic field in the Paschen-Back regime, an almost closed transition exists from any ground state, as now the nuclear spin is decoupled from the electron, and thus it cannot be flipped in an electric dipole transition. For our atoms in the two lowest states with  $m_S = -1/2$ , the transition to the  $m_j = -3/2$  is a closed transition preserving  $m_I$ . Moreover, due to the splitting of  $\sim 80$  MHz between the different hyperfine ground states, these can be selectively excited by tuning the laser frequency. This is very useful for imaging as the atoms in the different states can be selectively imaged.

## **Appendix B**

### **Resonator-enhanced optical dipole trap for fermionic lithium atoms**





# Resonator-enhanced optical dipole trap for fermionic lithium atoms

A. Mosk, S. Jochim, H. Moritz, Th. Elsässer, and M. Weidemüller

Max-Planck-Institut für Kernphysik, Postfach 103980, 69029 Heidelberg, Germany

R. Grimm

Institut für Experimentalphysik, Universität Innsbruck, 6020 Innsbruck, Austria

Received May 7, 2001

We demonstrate a novel optical dipole trap that is based on enhancement of the optical power density of a Nd:YAG laser beam in a resonator. The trap is particularly suited for experiments with ultracold gases, as it combines a potential depth of the order of 1 mK with storage times of several tens of seconds. We study the interactions in a gas of fermionic lithium atoms in our trap and observe the influence of spin-changing collisions and off-resonant photon scattering. A key element in reaching long storage times is the use of an ultralow-noise laser. The dependence of storage time on laser noise is investigated. © 2001 Optical Society of America

OCIS codes: 020.7010, 020.2070.

Optical dipole traps that are detuned far from resonance are rapidly becoming standard tools for atomic physics at ultralow temperatures.<sup>1</sup> They permit trapping of practically any atomic species, as well as molecules. In the field of quantum gases they permit trapping of mixed-state and mixed-species ensembles. The coupling of the atoms to the light field, which is weak for traps tuned far from resonance, can be strongly enhanced with an optical resonator. Indeed, in cavity quantum-electrodynamics experiments, single atoms have been trapped by classic light fields<sup>2</sup> and by light fields that correspond to a single photon.<sup>3,4</sup> Optical resonators have also been used for sensitive detection of optical fields in a quantum nondemolition way with cold atoms<sup>5</sup> and even open up new possibilities for optical cooling of atoms and molecules.<sup>6,7</sup>

In this Letter we demonstrate a resonator-enhanced dipole trap (REDT) for use in experiments with ultracold gases. We take advantage of the resonant enhancement of the optical power density and the corresponding trap depth. To suppress photon scattering and reach storage times of several tens of seconds, the trap light is detuned far from atomic resonance. At the same time the trap's volume and potential depth are large to facilitate the transfer of many atoms into the trap. We expect that the high optical power density reached in the REDT will be useful in many contexts, for instance, for trapping earth-alkali atoms, buffer-gas-cooled atoms, and cold molecules.

Our primary interest is in spin mixtures of fermionic <sup>6</sup>Li as a promising candidate system for the formation of Cooper pairs in an atomic gas.<sup>8,9</sup> In particular, we aim to study Feshbach scattering resonances, which may provide a binding mechanism for the Cooper pairs.<sup>10</sup>

To suppress photon scattering sufficiently requires that the trap light be detuned from the 670-nm *D*

lines of Li by a few hundred nanometers. In addition, capturing atoms from a magneto-optical trap (MOT) requires an optical trap with a similar spatial extension and a depth of ~1 mK. Without resonant enhancement, such a trap can be created only by use of a high-power laser. Indeed, trapping of <sup>6</sup>Li in a high-power CO<sub>2</sub> laser trap as well as evaporative cooling were recently reported.<sup>11</sup>

Our REDT requires only a 1.2-W Nd:YAG laser ( $\lambda = 1064$  nm) whose power density is resonantly enhanced 130-fold in a 15-cm near-confocal resonator (see Fig. 1). The resonator mirrors are placed outside the vacuum, which facilitates adjustment of the resonator and at the same time avoids the problems associated with optics in ultrahigh vacuum (UHV). The MOT overlaps approximately 1000 antinodes of the standing wave, which act as separate microtraps, with an axial separation of  $\lambda/2 = 532$  nm and a radial extension given by the beam waist,  $w_0 = 160$   $\mu$ m. The resonator's length is increased by ~3 mm from the confocal condition to lift the degeneracy of the higher-order modes. The optical losses at the vacuum windows are minimized by use of a high-purity fused-silica UHV cell and by transversing of all intracavity glass surfaces at

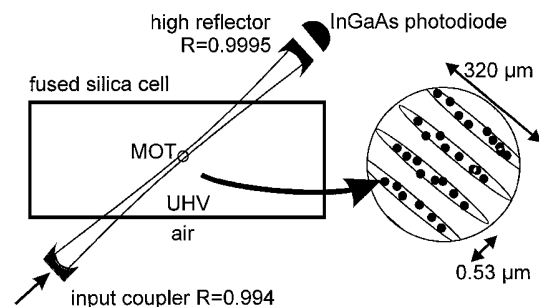


Fig. 1. Schematic of the resonator trap. The atoms are trapped in ~1000 antinodes of the standing wave.

Brewster's angle. The small residual round-trip loss  $\mathcal{L}$  permits a maximal resonant enhancement  $A = 1/\mathcal{L}$ , where the resonant enhancement factor  $A$  is defined as the ratio of the intracavity intensity to the intensity of the standing wave in a retroreflected beam. For maximum enhancement, reflectivity  $R$  of the input coupler must match  $\mathcal{L}$ . For our UHV cell we measured  $\mathcal{L} = 0.004(2)$  in a test resonator, and correspondingly we chose  $R = 0.9940(2)$ . Using these values theoretically would permit an enhancement factor of 240 at a calculated finesse  $\mathcal{F} = 600$ . We typically measure  $A = 130 \pm 15$  at  $\mathcal{F} = 650 \pm 60$ , where the loss is due to incomplete mode matching.

A rigid resonator body, which is acoustically decoupled from mechanical vacuum pumps, provides passive stability. In addition, a piezomechanical actuator compensates for changes in cavity length caused, e.g., by thermal drifts and acoustical noise. This servo loop, with a bandwidth of 8 kHz, uses the Hänsch-Couillaud method to derive an error signal<sup>12</sup>; the Brewster windows act as the intracavity polarizer. No high-bandwidth stabilization proved to be necessary. The drive laser for the resonator trap is a commercially available ultralow-noise 1.2-W diode-pumped solid-state Nd:YAG laser (Innolight Mephisto). Two Faraday rotators provide a 70-dB reduction of feedback of the resonator to the laser, and an acousto-optical modulator provides control over the laser power admitted to the cavity. Approximately 20% of the laser power is lost in these elements.

The energy density inside the cavity is the same as in a retroflected 130-W beam, which leads to a calculated trap depth<sup>13</sup> of  $0.8 \text{ mK} \times k_B$ . The corresponding photon-scattering rate in the intensity maximum is calculated to be  $\sim 1 \text{ s}^{-1}$ . In the harmonic approximation of the potential near the trap center we calculate axial and radial trap frequencies  $\omega_{\text{ax}}/2\pi = 1.4 \text{ MHz}$  and  $\omega_{\text{rad}}/2\pi = 2.0 \text{ kHz}$ , respectively. The trap, however, is anharmonic, and atoms in higher vibrational states oscillate at lower frequencies.

Our source of cold atoms is a MOT based on diode lasers,<sup>14</sup> which consists of a cooler beam, detuned  $-20 \text{ MHz}$  from the  $2^2S_{1/2}F = 3/2 \rightarrow 2^2P_{3/2}F = 5/2$  transition, and a repumper at  $\sim -20 \text{ MHz}$  from  $2^2S_{1/2}F = 1/2 \rightarrow 2^2P_{3/2}F = 3/2$ . In the MOT we collect approximately  $2 \times 10^7$  atoms in 10 s from a Zeeman slowed beam. We then cool and compress the atoms, by reducing the detuning, to a density of  $\sim 10^{11} \text{ cm}^{-3}$  at a temperature of  $\lesssim 1 \text{ mK}$ . The MOT light beams and magnetic fields are turned off after 20 ms of compression. The REDT remains on permanently during the MOT phase, as it does not influence the loading of the MOT. Approximately 0.5% of the atoms remain in the REDT after the MOT is turned off; the remainder are lost in the first 60 ms. We detect atoms that remain in the REDT by turning on the MOT fields again and subsequently measuring the fluorescence. The fluorescence is proportional to the number of atoms in an optically thin MOT, with an uncertainty of 50% in the calibration.

The storage time of atoms in an optical trap is usually limited by rest-gas collisions, interatomic processes, off-resonant photon scattering, or heating

caused by laser noise. In our apparatus, at a pressure of  $3 \times 10^{-11} \text{ mbars}$  the decay rate that is due to rest-gas collisions, measured with magnetically trapped Li atoms, is  $8 \times 10^{-3} \text{ s}^{-1}$ .

Interatomic collisions in  $^6\text{Li}$  strongly depend on the hyperfine state of the atoms. We pump the atoms into the  $F = 1/2$  state by turning off the MOT repumper several milliseconds before the cooler, or into the  $F = 3/2$  state by leaving the repumper on longer. Atoms in the  $F = 3/2$  state are lost from the trap as a result of spin-changing collisions with a second-order decay rate  $\dot{N}/N^2 = 2 \times 10^{-5} \text{ s}^{-1}$  (Fig. 2). Because the initial density of the trapped atoms is of the order of  $10^9 \text{ cm}^{-3}$ , the measured decay rate implies a rate constant of the order of  $10^{-9} \text{ cm}^3/\text{s}$ , in agreement with theoretical predictions.<sup>10</sup>

The atoms in the  $F = 1/2$  hyperfine ground state are noninteracting to a good approximation, as the  $s$ -wave scattering length between the two Zeeman sublevels is small in a low magnetic field<sup>10,11</sup> and  $p$ -wave scattering is expected to be strongly suppressed. The data show an initial fast decay of the order of 10 s, followed by a long storage time; that time is well described by an exponential decay with a time constant of  $\sim 50 \text{ s}$ . The initial decay can be explained as follows: Because the density of trapped states in our potential is strongly peaked just below the trap edge, a large fraction of atoms occupies states that are only weakly bound. A single photon recoil momentum then suffices to transfer such an atom into an untrapped state; therefore the number of weakly bound atoms decays strongly in the first few photon-scattering times. We numerically modeled the effect of photon scattering and rest-gas collisions on the distribution of the atoms, starting from a distribution that matches the density of states in the trap. The model curve (dashed curve in Fig. 2), which has no adjustable parameters except for the initial number of atoms, agrees with our measurements.

Laser intensity noise, especially at twice the axial trap frequency, causes heating of the atomic gas.<sup>15</sup> The resonator has a mode-cleaning effect:

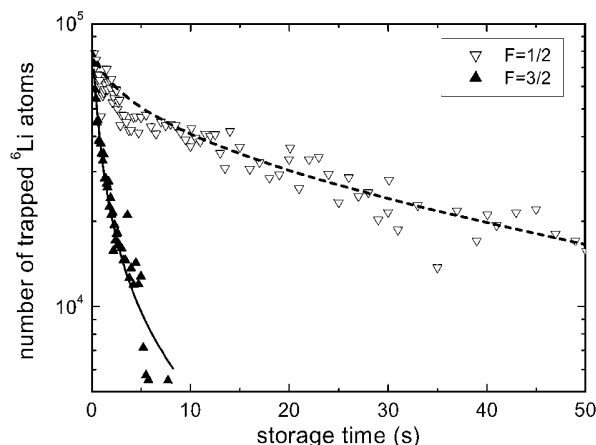


Fig. 2. Evolution of the number of trapped atoms in the upper ( $F = 3/2$ ) and lower ( $F = 1/2$ ) hyperfine ground states. Solid curve, second-order decay fit to the  $F = 3/2$  data; dashed curve, modeled loss owing to off-resonant photon scattering and rest gas.

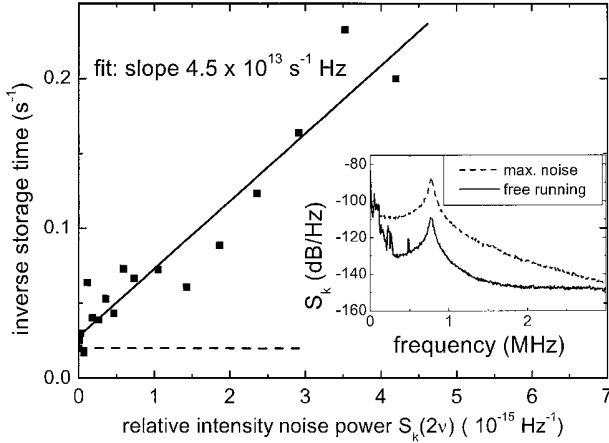


Fig. 3. Influence of laser intensity noise on storage time. Dashed horizontal line, storage time with active stabilization of the laser output power; solid line, linear fit through the data. Inset, noise spectrum with the active intensity stabilization of the laser turned off (solid curve) and with the additional intensity noise modulation (dashed curve). Shot noise at the photodiode exceeds the normal laser noise.

Pointing and shape fluctuations of the laser beam do not affect the shape of the trap potential. However, these fluctuations are converted into intensity noise. Great care must therefore be taken in choosing the drive laser: The absence of laser noise, especially at frequencies near  $2\omega_{ax}$ , is crucial. An estimate of the relevant loss rate can be found from a harmonic oscillator model<sup>16</sup>:  $\Gamma = \pi^2 \nu^2 S_k(2\nu)$ , where  $\nu$  is the relevant oscillation frequency and  $S_k$  is the one-sided power spectrum of relative intensity noise (RIN) as defined in Ref. 16.

In preliminary experiments with a different single-frequency diode-pumped Nd:YAG laser, with a relative intensity noise of  $S_k(2\nu_{ax}) = 10^{-10} \text{ Hz}^{-1}$ , we were able to trap atoms, but storage times were less than 1 s. The Mephisto laser, which has  $S_k(2\nu_{ax}) \leq 10^{-14} \text{ Hz}^{-1}$ , is much more suitable as a drive laser and facilitates the long storage time shown in Fig. 2. To study the strong dependence of the storage time on laser noise we modulated the laser output power with white noise (bandwidth, 5 MHz). The resultant intracavity relative intensity noise was measured on an InGaAs photodiode behind the resonator end mirror. Figure 3 shows that the storage time is inversely proportional to the intensity noise level,  $\tau^{-1} = (4.5 \times 10^{13} \text{ s}^{-1}) \times S_k(2\nu_{ax}) \times \text{Hz}$ . The measured storage times agree with the model of Ref. 16 within a factor of 2.

In conclusion, we have demonstrated a resonator-enhanced dipole trap that traps approximately

$10^5$  fermionic Li atoms. Although this type of trap is sensitive to laser noise, a storage time of several tens of seconds can be reached by use of an ultralow-noise laser. On this time scale, atoms are lost as a result of photon scattering and rest-gas collisions.

The storage time in our system greatly exceeds the expected collision times in the Li gas at fields of  $\sim 0.08 \text{ T}$ , which are of the order of 1 s.<sup>10</sup> Thermalization and loss measurements in our trap will characterize the interactions in the vicinity of the Feshbach resonance.

The research of A. Mosk is supported by a Marie-Curie Fellowship from European Community program IHP under contract CT-1999-00316. We thank InnoLight GmbH for the loan of a Mephisto 1200 laser system. We are indebted to D. Schwalm for encouragement and support. A. Mosk's e-mail address is allard.mosk@mpi-hd.mpg.de; that of R. Grimm is rudolf.grimm@uibk.ac.at.

## References

1. R. Grimm, M. Weidemüller, and Y. B. Ovchinnikov, *Adv. At. Mol. Opt. Phys.* **42**, 95 (2000).
2. J. Ye, D. W. Vernooy, and H. J. Kimble, *Phys. Rev. Lett.* **83**, 4987 (1999).
3. C. J. Hood, T. W. Lynn, A. C. Doherty, A. S. Parkins, and H. J. Kimble, *Science* **287**, 1447 (2000).
4. P. W. H. Pinkse, T. Fischer, P. Maunz, and G. Rempe, *Nature* **404**, 365 (2000).
5. A. Sinatra, J. F. Roch, K. Vigneron, Ph. Grelu, J.-Ph. Poizat, K. Wang, and P. Grangier, *Phys. Rev. A* **57**, 2980 (1998).
6. P. Horak, G. Hechenblaikner, K. M. Gheri, H. Stecher, and H. Ritsch, *Phys. Rev. Lett.* **79**, 4974 (1997).
7. V. Vuletić and S. Chu, *Phys. Rev. Lett.* **84**, 3787 (2000).
8. A. G. Truscott, K. E. Strecker, W. I. McAlexander, G. B. Partridge, and R. G. Hulet, *Science* **291**, 2570 (2001).
9. F. Schreck, G. Ferrari, K. L. Corwin, J. Cubizolles, L. Khayovich, M.-O. Mewes, and C. Salomon, *Phys. Rev. A* **64**, 011402 (2001).
10. M. Houbiers, H. T. C. Stoof, W. I. McAlexander, and R. G. Hulet, *Phys. Rev. A* **57**, R1497 (1998).
11. K. M. O'Hara, M. E. Gehm, S. R. Granade, S. Bali, and J. E. Thomas, *Phys. Rev. Lett.* **85**, 2092 (2000).
12. T. W. Hänsch and B. Couillaud, *Opt. Commun.* **35**, 441 (1980).
13. This calculation is based on a two-level approximation that takes into account rotating and counterrotating terms of the *D* lines of Li.<sup>1</sup>
14. U. Schünemann, H. Engler, M. Zielonkowski, M. Weidemüller, and R. Grimm, *Opt. Commun.* **158**, 263 (1998).
15. G. M. Bruun and C. W. Clark, *Phys. Rev. A* **61**, 061601 (2000).
16. M. E. Gehm, K. M. O'Hara, T. A. Savard, and J. E. Thomas, *Phys. Rev. A* **58**, 3914 (1998).



## **Appendix C**

### **Low-cost mechanical shutter for light beams**



## Low-cost mechanical shutter for light beams

Kilian Singer,<sup>a)</sup> Selim Jochim,<sup>b)</sup> Marcel Mudrich, Allard Mosk,<sup>c)</sup> and Matthias Weidemüller  
*Max-Planck-Institut für Kernphysik, P.O. Box 10 39 80, D-69029 Heidelberg, Germany*

(Received 22 May 2002; accepted 18 September 2002)

We present a simple design of a fast mechanical shutter for light beams using a low-cost personal computer loudspeaker. The shutter is capable of closing an aperture of 5 mm at a maximum speed of 1.7 mm/ms with a timing jitter of less than 10  $\mu$ s. When combined with polarization optics, our device can also be used as an alterable switch and adjustable attenuator. © 2002 American Institute of Physics. [DOI: 10.1063/1.1520728]

Switching light beams with high speed and timing precision can be accomplished with electro-optical or acousto-optical modulators. These nonmechanical devices do not fully extinguish the light and provide only finite transmission. For infinite attenuation of a laser beam, mechanical shutters are the only option. Most widely known are iris shutters as used in photo cameras. In most cases, their unipolar design only allows one to switch the light beam either on or off with sufficient speed ( $\sim 1$  ms). Commercial shutters<sup>1</sup> without this deficiency are available at rather high cost ( $\sim \$1000$ ). When placed in a laser laboratory, delicate optical devices such as interferometers might be perturbed by the acoustic vibrations created by the iris diaphragm. Mechanical shutters based on piezoelectric actuators have been demonstrated to achieve switching times of 10  $\mu$ s, but the extinction ratio was limited to 300:1 for an aperture size of only 10  $\mu$ m.<sup>2</sup> Chopper wheels permit exposure times of 10  $\mu$ s for 1 mm slits but cannot be triggered asynchronously.<sup>3–5</sup> Shutters based on thermal expansion of Ni–Cr wires allow switching times of 100  $\mu$ s for 1 mm slits but the repetition rate is limited to 5 s due to the thermal recovery time of the wire.<sup>6</sup>

We developed a simple bipolar mechanical shutter which combines fast switching, high timing precision, and ultimate extinction. The design is shown in Fig. 1. The device is based on a standard loudspeaker ( $\sim \$5$ ) as used in personal computers. Loudspeakers with attached retroreflectors have already been used as pathlength varying elements in low-cost interferometric femtosecond autocorrelators.<sup>7</sup> In our design, all membranes are removed so that the voice coil freely moves out of the permanent magnet of the loudspeaker. A stiff nontransparent flag, which is attached to the top of the voice coil, serves as the movable beam stop. The flag is made of a light, nontransparent material (plastic or aluminum foil). The copper leads on the remaining membrane pieces of the loudspeaker are reinforced by glue. An upper mechanical stopper is mounted above the voice coil. To minimize acous-

tic noise, damping material (felt, in our design) is glued below the upper stopper and on top of the permanent magnet. A little hole is cut in the middle of the remaining membrane on top of the voice coil to further reduce acoustic noise and to increase speed. By minimizing the mass of the moving parts, we achieve high acceleration and low acoustic noise.

The driving circuit for the shutter device as depicted in Fig. 2 consists of four transistor switches. The supply voltage should range between 2 and 5 V and needs to support 500 mA. In order to accelerate the shutter in the desired direction, the supply voltage for the voice coil can be reversed by changing the transistor–transistor logic (TTL) level (low=0 V, high=5 V). A low TTL level switches transistors *Q2* and *Q4* to a conducting state and *Q1* and *Q3* to a nonconducting state. The situation is reversed for a high TTL level.

The motion of the flag was measured by shining an expanded laser beam (diameter 30 mm) through a vertical slit (horizontal width 2 mm and vertical width 10 mm) placed directly in front of the shutter device. The transmitted light intensity is measured with a photodiode. When the shutter vertically moves into the light beam (positive *x* direction), part of the expanded light beam is stopped by the flag so that the light intensity transmitted through the slit is proportional to the displacement of the flag. Knowing the maximum displacement (5.3 mm for our device), the relative displacement of the flag can be derived from the measured light intensity. The result of such a measurement is shown in Fig. 3. For *t* < 0, the TTL signal connected to the driving electronics is set to high keeping the flag in the elevated position. The supply

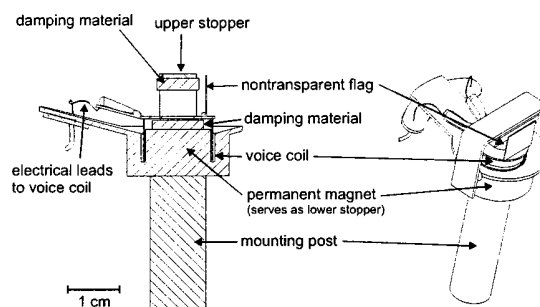


FIG. 1. Shutter design based on a standard loudspeaker as used in personal computers.

<sup>a)</sup>Electronic mail: kilian.singer@mpi-hd.mpg.de

<sup>b)</sup>Present address: Institut für Experimentalphysik, Universität Innsbruck, 6020 Innsbruck, Austria.

<sup>c)</sup>Present address: FOM Instituut voor Plasmafysica Rijnhuizen, P.O. Box 1207, 3430 BE Nieuwegein, The Netherlands.

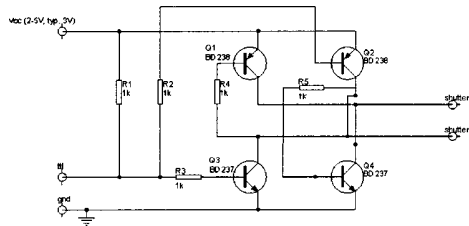


FIG. 2. Electric driving circuit of the shutter device.

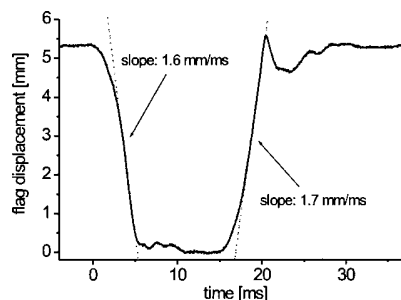
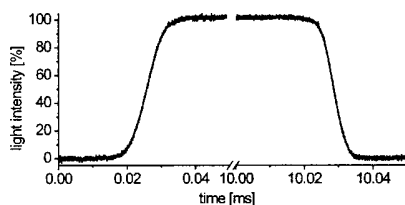
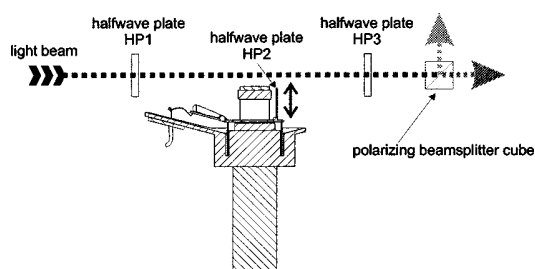
FIG. 3. Displacement of the shutter flag. At  $t=0$  and  $t=15$  ms, TTL input to the driving circuit was changed.FIG. 4. Measurement of the extinction time. The flag is moved into ( $t=0$ ) and out of ( $t=10$  ms) the focus of a laser beam with  $10\text{ }\mu\text{m}$  waist.

FIG. 5. Switchable attenuator for laser beams.

voltage is 4 V resulting in a current of 300 mA. At  $t=0$ , the level of the TTL signal was changed to low. As a consequence, the loudspeaker coil with the attached flag starts to accelerate into the negative  $x$  direction. After 2.5 ms, the flag has reached its final velocity of 1.7 mm/ms as derived by a linear fit to the displacement curve. At  $t=5$  ms, the flag motion is stopped by the damping material on top of the permanent magnet. The vibrations caused by the stopping of the flag are damped within 5 ms. At  $t=15$  ms, the TTL level is changed to high causing the flag to move into the positive  $x$  direction with similar characteristics. As an important feature of our design, the speed of the flag is equally high in the upward direction as in the downward direction.

For fast interruption of a laser beam, the shutter is placed in the focal plane of a lens. To provide a measure of typical shutter times, we have focused a laser beam to a waist of  $10\text{ }\mu\text{m}$ . Figure 4 shows the light intensity measured while the shutter is opening and closing. Within  $10\text{ }\mu\text{s}$ , the laser beam can be fully transmitted or extinguished. Due to the transverse Gaussian intensity distribution of the laser beam, the measured data are well described by an error function. For a known waist of the laser beam, the fit yields an independent measurement of shutter velocity. We find that 1.7 mm/ms is in agreement with the measurement discussed in the previous paragraph. The delay to the electronic TTL signal is 3.5 ms with a jitter of less than  $10\text{ }\mu\text{s}$ . The minimum delay between an opening and closing pulse applied to the shutter is determined by the time that the flag has come to a complete rest (roughly 5 ms, see Fig. 3). In order to create controlled light pulses with duration down to  $50\text{ }\mu\text{s}$ , one may place two shutters in series. Trigger pulses are applied to each shutter in such a way that the first shutter opens the beam at a given time while the second one interrupts it after the duration time.

We also employ our fast switching device to place optical elements into the light beam, like, e.g., a waveplate or a grayfilter. In this way, one creates optical switches or switchable attenuators. Instead of the flag, the optical element is simply glued on the movable loudspeaker coil. A switchable rotation of polarization is realized by moving a halfwave plate into a light beam with linear polarization. The rotation angle of the polarization is twice the angle between the polarization and the optical axis of the halfwave plate. If the light polarization is turned by  $90^\circ$  the light beam can be switched between two ports of a polarizing beam splitter.

Since the waveplate has to be glued to the loudspeaker coil, it can no longer be freely rotated. This limitation can be overcome by placing the movable halfwave plate HP2 between two stationary, but rotatable, halfwave plates HP1 and HP3 as schematically depicted in Fig. 5. The light transmitted through the polarizing beam splitter can then be switched between two freely adjustable intensity levels. The first intensity level (without HP2 in the beam) is set by rotating the halfwave plates HP1 and HP3. Note, that for two halfwave plates placed in series, the total rotation angle of the polarization is determined only by the difference of the rotation angles of the two waveplates. The second intensity level is then adjusted by moving HP2 into the beam and simulta-



neously rotating HP1 and HP3 by equal angles, thus keeping the difference angle between HP1 and HP3 constant. In this way, the intensity switch replaces considerably more expensive devices such as electro-optic modulators.

The authors thank D. Schwalm for generous support in many respects. The work of one of the authors (A.M.) is supported by a Marie-Curie fellowship from the European Community program IHP under Contract No. CT-1999-

00316. The project is partly funded by the Deutsche Forschungsgemeinschaft (WE 2661/1-1).

<sup>1</sup><http://www.uniblitz.com>

<sup>2</sup>C. S. Adams, Rev. Sci. Instrum. **71**, 59 (2000).

<sup>3</sup>P. C. Miles and R. S. Barlow, Meas. Sci. Technol. **11**, 392 (2000).

<sup>4</sup>S. Yatsiv and J. J. Ewing, Rev. Sci. Instrum. **45**, 705 (1975).

<sup>5</sup>P. M. Selzer and W. M. Yen, Rev. Sci. Instrum. **47**, 749 (1976).

<sup>6</sup>M.-F. Ye, D.-Y. Jiang, and C. S. Wong, Rev. Sci. Instrum. **61**, 203 (1990).

<sup>7</sup>A. Watanabe, H. Saito, T. Tokizaki, Y. Ishida, and T. Yajima, Rev. Sci. Instrum. **58**, 1852 (1987).



## **Appendix D**

### **Magnetic Field Control of Elastic Scattering in a Cold Gas of Fermionic Lithium Atoms**



# Magnetic Field Control of Elastic Scattering in a Cold Gas of Fermionic Lithium Atoms

S. Jochim, M. Bartenstein, G. Hendl, J. Hecker Denschlag, and R. Grimm

*Institut für Experimentalphysik, Universität Innsbruck, Technikerstrasse 25, 6020 Innsbruck, Austria*

A. Mosk

*FOM instituut voor plasmafysica Rijnhuizen, P.O. Box 1207, 3430 BE Nieuwegein, The Netherlands*

M. Weidemüller

*Max-Planck-Institut für Kernphysik, Postfach 103980, 69029 Heidelberg, Germany*

(Received 24 July 2002; published 18 December 2002)

We study elastic collisions in an optically trapped spin mixture of fermionic lithium atoms in the presence of magnetic fields up to 1.5 kG by measuring evaporative loss. Our experiments confirm the expected magnetic tunability of the scattering length by showing the main features of elastic scattering according to recent calculations. We measure the zero crossing of the scattering length at 530(3) G which is associated with a predicted Feshbach resonance at  $\sim 850$  G. Beyond the resonance we observe the expected large cross section in the triplet scattering regime.

DOI: 10.1103/PhysRevLett.89.273202

PACS numbers: 34.50.-s, 05.30.Fk, 32.80.Pj, 39.25.+k

In an ultracold atomic gas, the  $s$ -wave scattering length characterizes the elastic interactions and has a profound effect on the physical behavior. The scattering length can be conveniently tuned by using a magnetic field when a Feshbach resonance is present. For bosonic atoms, such resonances have been observed [1–3], and they have found particular applications for attainment and manipulation of a Bose-Einstein condensate in  $^{85}\text{Rb}$  [4,5] and for the production of bright solitons in bosonic  $^7\text{Li}$  [6,7].

For fermionic gases, Feshbach resonances in  $s$ -wave scattering of atoms in different spin states are of great interest to experimentally explore the rich physics of paired fermionic gases [8–11]. For obtaining superfluidity in a Cooper-paired gas, magnetic tuning allows one to raise the critical temperature [8] from values far below the Fermi temperature into a region that seems accessible with current experimental methods. With resonantly tuned interactions the fermionic superfluid is predicted [9,10] to perform a crossover from a superfluid of weakly coupled Cooper pairs to a Bose-Einstein condensate of strongly coupled molecules. Feshbach tuning also offers a possible way to detect this molecular coupling through oscillations induced by magnetic-field transients [10] analogous to a recent observation with coupled bosonic atoms [5]. Experimental control of different pairing regimes thus represents an intriguing prospect of a fermionic gas with magnetically tuned interactions.

A narrow Feshbach resonance between two different spin states of fermionic  $^{40}\text{K}$  was recently observed by Loftus *et al.* [12]. The other fermionic species currently used in several experiments,  $^6\text{Li}$ , is predicted to show a Feshbach resonance with strong modifications of  $s$ -wave interactions in a very wide magnetic-field range [13–15]. At relatively small fields, this dependence was recently used by Granade *et al.* to obtain a sufficient scattering

cross section for the all-optical production of a degenerate Fermi gas of lithium [16].

In this Letter, we experimentally explore the magnetic tunability of elastic scattering in an optically trapped spin mixture of fermionic lithium atoms in high magnetic fields up to 1.5 kG. Our results verify the expected dependence of  $s$ -wave interactions in the whole magnetic-field range of interest [13–15]. As a particular feature associated with the predicted Feshbach resonance [13], we observe the zero crossing of the scattering length at a field of 530 G. The exact location of this feature is of great interest as a sensitive input parameter to better constrain the uncertainty in the molecular potentials for more accurate theoretical calculations of the scattering properties of  $^6\text{Li}$ . Our measurements of elastic collisions are based on evaporation out of an optical dipole trap.

The scattering properties in different spin mixtures of fermionic lithium atoms were theoretically investigated by Houbiers *et al.* [13], Kokkelmans *et al.* [14], and Venturi and Williams [15]. Magnetic tunability, of particular interest for Cooper pairing in a Fermi gas [8,9], was predicted for the stable combination of the two lowest states  $|1\rangle$  and  $|2\rangle$ ; at low magnetic field these states correspond to  $F = 1/2$ ,  $m_F = +1/2$ , and  $m_F = -1/2$ , respectively. Most prominently, a broad Feshbach resonance at  $\sim 850$  G is expected to mark the transition from the low-field scattering regime to the high-field region. As a precursor of the Feshbach resonance, the  $s$ -wave scattering length  $a$  crosses zero in the range between 500 and 550 G. Beyond the resonance, scattering in higher fields is dominated by the triplet potential with a very large and negative scattering length of  $-2200a_0$ , where  $a_0$  is the Bohr radius. The available theoretical data [13–15] show the same behavior for  $a(B)$  within some variations due to the limited knowledge of the

molecular interaction parameters. Figure 1(a) illustrates these predictions for the scattering length  $a(B)$  by a corresponding model curve that approximates the results of Refs. [13–15].

In a cold gas at finite temperature the cross section for elastic scattering of nonidentical particles is unitarity limited to a maximum value of  $\sigma_{\max} = 4\pi/k^2$ , where  $k = mv/(2\hbar)$  is the wave number corresponding to a relative velocity  $v$  and a reduced mass  $m/2$ . Taking into account the B-field dependent scattering length  $a(B)$  and the unitarity limit, the resulting B-field dependent cross section can be written as  $\sigma = 4\pi a^2/(1 + k^2 a^2)$ . For the considered  $|1\rangle - |2\rangle$  spin mixture of  $^6\text{Li}$  the expected behavior of the cross section is shown in Fig. 1(b) for the example of a wave number  $k = (300a_0)^{-1}$  close to our experimental conditions. Most notably, as a consequence of the unitarity limit in combination with the very large scattering length for high magnetic fields, the Feshbach resonance does not appear as a pronounced feature in the cross section. The zero crossing of the scattering length, however, leads to a vanishing scattering cross section and thus shows up as a manifestation of the resonance.

Our dipole trap [17] makes use of the enhancement of the laser intensity inside a linear optical resonator to create a large and deep trapping volume for lithium atoms. The power provided by a 2-W Nd:YAG laser (Innolight Mephisto-2000) at a wavelength of 1064 nm is enhanced by a factor of 120 to create a far red-detuned 1D optical lattice trap with an axial period of 532 nm and a transverse  $1/e$  radius of 115  $\mu\text{m}$ . The maximum trap depth is of the order of 1 mK. To vary the trap depth the resonator-internal power is servo-controlled by an acousto-optical modulator in the incident laser beam. From a standard magneto-optical trap (MOT) operated with diode lasers we typically transfer  $5 \times 10^5$   $^6\text{Li}$  atoms into roughly 1000 individual wells at a temperature of

$\sim 400$   $\mu\text{K}$ . The resulting peak density is  $\sim 1.5 \times 10^{11} \text{ cm}^{-3}$ . By extinguishing the repumping light of the MOT 1 ms before the main trapping light is turned off, all atoms are pumped into the two states  $|1\rangle$  and  $|2\rangle$  to create a 50-50 spin mixture [16].

The magnetic field is produced by a pair of water-cooled coils outside of the glass vacuum cell of the trap. At a maximum continuous operation current of 200 A the coils produce a magnetic field of 1.5 kG with a curvature of only 75 G/cm<sup>2</sup> along the symmetry axis; the corresponding power dissipation is 6 kW. The setup allows for a maximum ramp speed of 5 G/ms within the full range. The magnetic field is calibrated by radio-frequency induced transitions from  $|2\rangle$  to the state that at  $B = 0$  corresponds to  $F = 3/2$ ,  $m_F = +1/2$ . The latter is unstable against inelastic collisions with  $|2\rangle$  which leads to easily detectable loss. With a fit to the Breit-Rabi formula we obtain a calibration of the magnetic field to better than 1 G over the full range.

The basic idea of our measurements is to observe elastic collisions through evaporative loss at a variable magnetic field [18]. The method is particularly well suited for measuring the position of a resonance by locating the corresponding zero crossing of the scattering length. With this sensitive experimental input for theoretical calculations, as is readily available in our case [13–15], precise knowledge of the magnetic-field dependent scattering length can be obtained. Our dipole trap is loaded under conditions where the effective temperature  $T$  of a truncated Boltzmann distribution [19] is only slightly below the trap depth  $U$ . A strongly nonthermal distribution is thus created with a small truncation parameter  $\eta = U/k_B T \approx 2$ . The thermal relaxation resulting from elastic collisions then leads to rapid evaporative loss and cooling of the sample, i.e., an increase of  $\eta$ . The trap depth can be kept constant to study plain evaporation or, alternatively, ramped down to force the evaporation process.

In a series of plain evaporation experiments performed at a constant trap depth of 750  $\mu\text{K}$  we measure evaporative loss over the maximum accessible range of magnetic fields up to 1.5 kG. After a fixed holding time the remaining atoms are retrapped into the MOT and their number is measured via the fluorescence signal by a calibrated photodiode. The signal is recorded after holding times of 1 and 3 s corresponding to the time scale of evaporation. These holding times are short compared with the rest-gas limited lifetime of 30 s. Figure 2 shows the result of 1000 different measurements obtained in an acquisition time of 6 h. The data points are taken in a random sequence for 31 magnetic field values equally distributed over the full range. Data points for 1 and 3 s are recorded alternately. This way of data taking ensures that the signal is not influenced by residual long-term drifts of the experimental conditions.

The observed evaporation loss in Fig. 2 shows a pronounced dependence on the magnetic field, which we

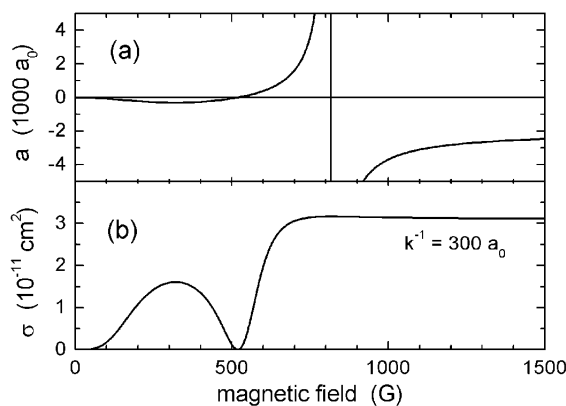


FIG. 1. (a) Model curve approximating the results of [13–15] for the  $s$ -wave scattering length of  $^6\text{Li}$  atoms in the two lowest spin states versus magnetic field. (b) Corresponding behavior of the scattering cross section at a finite collision energy with a relative wave number of  $k = (300a_0)^{-1}$ .

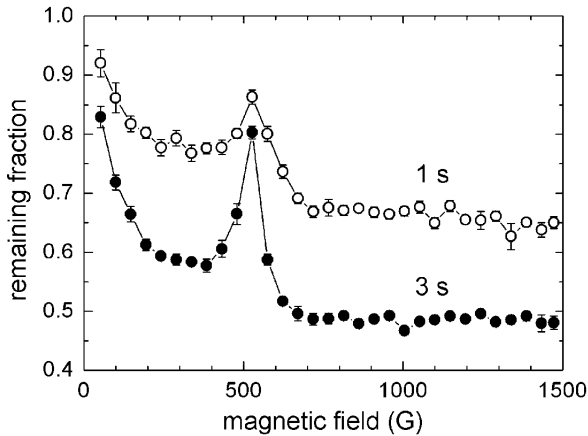


FIG. 2. Evaporative loss measurements over the full magnetic field range. The data points show the measured number of atoms remaining in the trap after 1 s ( $\circ$ ) and 3 s ( $\bullet$ ) of plain evaporation at a constant trap depth of 750  $\mu$ K.

compare with the expected cross section for elastic collisions ejecting atoms out of the trap. Figure 1(b) displays the cross section for  $k = (300a_0)^{-1}$ , which corresponds to a collision energy of about half the trap depth and thus to the relevant energies for evaporating collisions. After being very small at low magnetic fields, the observed loss increases for fields up to  $\sim 350$  G where the expected local maximum of evaporation shows up. The loss then decreases and disappears at about 530 G in agreement with the predicted zero crossing of the scattering length. Here the slight observed loss in the 1 s curve is explained by the finite ramp time of the magnetic field. In the 100 ms ramping time some evaporation does already take place. At 530 G the decrease of the trapped atom number between 1 and 3 s is fully explained by rest-gas losses without any further evaporation. For higher magnetic fields evaporative loss rapidly rises until it levels off at about 700 G. Up to the maximum attainable value of 1.5 kG high evaporation loss is observed. A slight decrease of the atom number for fields exceeding 1 kG occurs which we attribute to technical reasons; we observe an increasing noise for currents higher than  $\sim 130$  A in the error signal of the resonator lock. The relatively large and constant evaporative loss for fields exceeding 700 G is consistent with the predicted behavior of the cross section.

The evaporative cooling effect is confirmed by measuring the change of the truncation parameter  $\eta$  after 3 s of trapping at selected values of the magnetic field. For thermometry we turn off the magnetic field to avoid further elastic collisions and adiabatically lower the trap depth in a 1-s exponential ramp. The fraction of remaining atoms as a function of the relative depth then provides a good measure of  $\eta$ . At the zero crossing at 530 G we observe only a slight increase of  $\eta$  to a value of 2.3(3) which is explained by the unavoidable evaporation during

the magnetic-field ramps. At 340 G close to the local maximum of  $|a|$  we find an increase of  $\eta$  to 4.2(3) as a clear evidence of evaporative cooling. At 720 G, i.e., in the case of a large positive scattering length, a higher value of 5.5(4) is measured showing deeper evaporative cooling. Essentially the same  $\eta$  of 5.3(4) is obtained at  $B = 1290$  G where scattering takes place in the triplet-dominated regime with a very large negative scattering length.

We measure the minimum-loss feature in a closer range of magnetic fields to precisely determine the value of the magnetic field at which the zero crossing of scattering length occurs. The main data points in Fig. 3 are obtained with 500 individual measurements at a holding time of 3 s with the magnetic field randomly varied between 30 values in an interval between 370 and 670 G; the data shown in the inset are obtained with 1000 measurements in the very narrow range between 520 and 544 G. The results allow us to determine the B field for minimum evaporative loss, and thus the zero crossing of the scattering length to 530(3) G [20].

Forced evaporation measurements provide complementary data to plain evaporation and allow us to rule out a significant role of inelastic collisions. When the trap depth is ramped down, elastic collisions reduce trap loss in contrast to increased loss at constant trap depth. This can be understood by the spilling loss of energetic particles [19]: Without elastic collisions the most energetic particles are spilled out of the trap when its depth is reduced. With elastic collisions the evaporative cooling effect decreases the temperature and thus reduces the spilling loss.

In our forced evaporation measurements we reduce the trap depth in 10 s to 20% of its initial value in an exponential ramp and measure the number of remaining atoms; the results are displayed in Fig. 4. A minimum

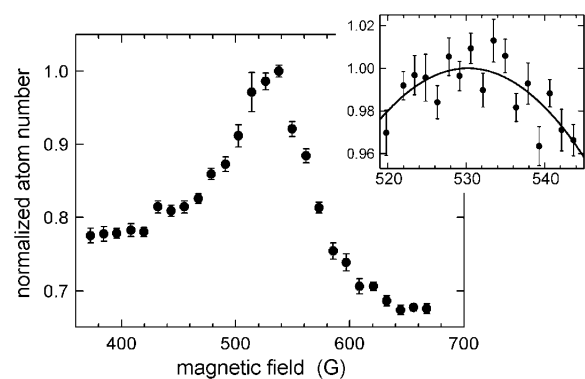


FIG. 3. Measurements on plain evaporation in magnetic fields close to the zero crossing of the scattering length under the same conditions as in Fig. 2 for a holding time of 3 s. Here the number of remaining atoms is normalized to the observed maximum value. The inset shows a series of measurements in a very narrow range around the maximum at 530(3) G together with a parabolic fit.

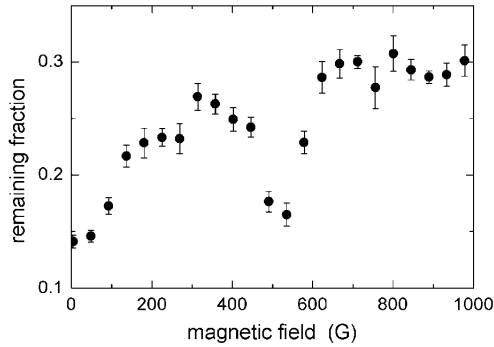


FIG. 4. Fraction of atoms remaining after forced evaporation versus applied magnetic field. The trap depth is ramped down exponentially in 10 s to 20% of the initial value.

number of atoms is now measured at 0 and 530 G instead of the maximum observed with constant trap depth. The largest number of atoms is observed in the high-field region above 650 G as expected for the large scattering cross section.

On a Feshbach resonance, enhanced inelastic loss can occur as a result of three-body collisions [1] or, if the system has internal energy, as a result of two-body decay [3]. For fermions, three-body processes are symmetry forbidden at ultralow energies when only  $s$ -wave collisions are involved. In a spin mixture at nonzero magnetic field, two-body decay is energetically possible (in our case with an energy release of  $k_B \times 3.5$  mK) but involves higher partial waves and relies on weak dipolar coupling. Consequently, inelastic loss can be expected to be weak in our experiments. Indeed, our data do not show any indication of inelastic loss even at the very center of the Feshbach resonance.

At much higher densities ( $\sim 10^{13}$  cm $^{-3}$ ) as compared to our conditions ( $\sim 10^{11}$  cm $^{-3}$ ), a recent experiment [21] has revealed inelastic loss with a maximum at 680 G. As our results support the predicted position of the  $s$ -wave resonance at  $\sim 850$  G, the explanation for the inelastic feature cannot be attributed to the Feshbach resonance in a simple way. The experiment [21] also provided evidence for a two-body nature of the underlying process with a rate constant of  $2 \times 10^{-12}$  cm $^3$ /s measured at  $\sim 20$   $\mu$ K. At a higher temperature of  $\sim 100$   $\mu$ K we derive an upper bound for the two-body rate constant of  $1 \times 10^{-12}$  cm $^3$ /s, whereas for a process involving higher partial waves one would expect the rate to increase with temperature. For three-body collisions our densities are too low to provide useful constraints. Obviously, inelastic loss in the fermionic spin mixture is an interesting problem that deserves more attention.

In conclusion, our measurements confirm the predicted magnetic tunability of the  $s$ -wave scattering length in a spin mixture of fermionic lithium atoms in the whole magnetic-field range of experimental interest. The ob-

served zero crossing of the scattering length at 530(3) G together with the large cross section observed for higher fields provides clear evidence of the predicted Feshbach resonance. Moreover, it enables more precise calculations of the  $^6\text{Li}$  scattering properties. The resonance itself is masked by unitarity-limited scattering and requires much deeper evaporative cooling for a direct observation. The fact that we do not see any significant effect of inelastic loss highlights the fact that the extremely large positive and negative scattering lengths attainable with fermionic lithium offer intriguing new possibilities for experiments on interacting Fermi gases.

We thank R.G. Hulet and H. Stoof for very useful discussions and V. Venturi for valuable input. Support by the Austrian Science Fund (FWF) within Project No. P15115 and SFB15 and by the Institut für Quanteninformation GesmbH is gratefully acknowledged.

Shortly before submission of the present Letter we learned about the measurements of the group of J.E. Thomas on the zero crossing of the scattering length which agree with our data.

- 
- [1] S. Inouye *et al.*, Nature (London) **392**, 151 (1998).
  - [2] P. Courteille *et al.*, Phys. Rev. Lett. **81**, 69 (1998).
  - [3] V. Vuletić, A. J. Kerman, C. Chin, and S. Chu, Phys. Rev. Lett. **82**, 1406 (1999).
  - [4] S. Cornish *et al.*, Phys. Rev. Lett. **85**, 1795 (2000).
  - [5] E. A. Donley, N. R. Claussen, S. T. Thompson, and C. E. Wieman, Nature (London) **417**, 529 (2002).
  - [6] L. Khaykovich *et al.*, Science **296**, 1290 (2002).
  - [7] K. Strecker, G. Partridge, A. Truscott, and R. Hulet, Nature (London) **417**, 150 (2002).
  - [8] H. T. C. Stoof, M. Houbiers, C. Sackett, and R. Hulet, Phys. Rev. Lett. **76**, 10 (1996).
  - [9] M. Holland, S. Kokkelmans, M. Chiofalo, and R. Walser, Phys. Rev. Lett. **87**, 120406 (2001).
  - [10] E. Timmermans, K. Furuya, P. W. Milonni, and A. K. Kerman, Phys. Lett. A **285**, 228 (2001).
  - [11] M. L. Chiofalo, S. J. J. M. F. Kokkelmans, J. L. Milstein, and M. J. Holland, Phys. Rev. Lett. **88**, 090402 (2002).
  - [12] T. Loftus *et al.*, Phys. Rev. Lett. **88**, 173201 (2002).
  - [13] M. Houbiers, H. T. C. Stoof, W. McAlexander, and R. Hulet, Phys. Rev. A **57**, R1497 (1998).
  - [14] S. Kokkelmans *et al.*, Phys. Rev. A **65**, 053617 (2002).
  - [15] V. Venturi and C. Williams (private communication).
  - [16] S. Granade, M. Gehm, K. O'Hara, and J. Thomas, Phys. Rev. Lett. **88**, 120405 (2002).
  - [17] A. Mosk *et al.*, Opt. Lett. **26**, 1837 (2001).
  - [18] C. Chin, V. Vuletić, A. J. Kerman, and S. Chu, Phys. Rev. Lett. **85**, 2717 (2000).
  - [19] O. J. Luiten, M. W. Reynolds, and J. T. M. Walraven, Phys. Rev. A **53**, 381 (1996).
  - [20] A finite collision energy  $E_C$  leads to a shift of  $+0.7G \times E_C/(k_B \times 100 \mu\text{K})$  [15], which for our data stays within the error.
  - [21] K. Dieckmann *et al.*, cond-mat/0207046v2.



## **Appendix E**

### **Pure Gas of Optically Trapped Molecules Created from Fermionic Atoms**



# Pure Gas of Optically Trapped Molecules Created from Fermionic Atoms

S. Jochim, M. Bartenstein, A. Altmeyer, G. Hendl, C. Chin, J. Hecker Denschlag, and R. Grimm

*Institut für Experimentalphysik, Universität Innsbruck, Technikerstraße 25, 6020 Innsbruck, Austria*

(Received 5 August 2003; published 8 December 2003)

We report on the production of a pure sample of up to  $3 \times 10^5$  optically trapped molecules from a Fermi gas of  $^6\text{Li}$  atoms. The dimers are formed by three-body recombination near a Feshbach resonance. For purification, a Stern-Gerlach selection technique is used that efficiently removes all trapped atoms from the atom-molecule mixture. The behavior of the purified molecular sample shows a striking dependence on the applied magnetic field. For very weakly bound molecules near the Feshbach resonance, the gas exhibits a remarkable stability with respect to collisional decay.

DOI: 10.1103/PhysRevLett.91.240402

PACS numbers: 03.75.Ss, 05.30.Fk, 32.80.Pj, 33.80.Ps

The formation of composite bosons by pairing of fermions is the key to many intriguing phenomena in physics, with superfluidity and superconductivity being prominent examples. In ultracold atomic gases, pairs of fermionic atoms can be combined to form bosonic molecules [1,2] or possibly Cooper pairs [3]. The pairing changes the properties of the gas, highlighted by the prospect of a molecular Bose-Einstein condensate or a Cooper-paired superfluid. The interatomic interactions play a crucial role for the nature of the pairing process. The ability to control the interaction via magnetically tuned Feshbach resonances [4–6] opens up exciting possibilities for experiments on ultracold fermionic gases, e.g., exploring superfluidity in different pairing regimes [7–10].

The formation of molecules near Feshbach resonances in ultracold gases has been reported for bosons [11–14] and fermions [1,2]. In the experiments [1,2,11,12], the molecules coexist with the atoms in a strongly interacting mixture. A generic feature of a Feshbach resonance is the existence of a bound molecular state with a magnetic moment that differs from that of the unbound atom pair. The binding energy thus depends on the magnetic field, and a properly chosen field can resonantly couple colliding atoms into the molecular state. The inherent difference in magnetic moments facilitates a Stern-Gerlach selection of molecules and atoms. Two recent experiments [13,14] demonstrate the separation of the molecular from the atomic cloud in free space.

In this Letter, we report the creation of a pure sample of up to  $3 \times 10^5$  optically trapped molecules from a fermionic gas of  $^6\text{Li}$  atoms. After the production of an atom-molecule mixture via three-body collisions, a Stern-Gerlach purification scheme efficiently removes all trapped atoms, while leaving all molecules trapped. This allows us to investigate the intriguing behavior of the pure molecular sample, which strongly depends on the magnetic field.

The lithium isotope  $^6\text{Li}$  is one of the two prime candidates in current experiments exploring the physics of fermionic quantum gases [15–19], the other one being

$^40\text{K}$  [1,20]. A spin mixture composed of the lowest two sublevels in the hyperfine manifold of the electronic ground state is stable against two-body decay and exhibits wide magnetic tunability of  $s$ -wave interactions via a broad Feshbach resonance at about 850 G [21]. A calculation of the corresponding scattering length  $a$  as a function of the magnetic field [22] is shown in Fig. 1(a) [23]. The large cross section for elastic scattering near the resonance can be used for efficient evaporative cooling, in particular, above the resonance at negative scattering length where inelastic loss is negligible [16]. In the region of positive scattering length below the resonance, loss features have been observed [24]. At large positive  $a$ , a weakly bound molecular level exists with a binding energy approximately given by  $\hbar/(ma^2)$ , where  $\hbar$  is Planck's constant and  $m$  denotes the atomic mass. For the region of interest, Fig. 1(b) shows this binding energy as calculated from the scattering length data [25].

The starting point of our experiments is a sample of  $2.5 \times 10^6$   $^6\text{Li}$  atoms in a standing-wave optical dipole trap realized with a Nd:YAG laser at a wavelength of 1064 nm [19,26]. The 50-50 spin mixture in the lowest two spin states is spread over  $\sim 1500$  individual lattice sites of the standing-wave trap. In the central region of the trap, a single site contains typically 1800 atoms. The

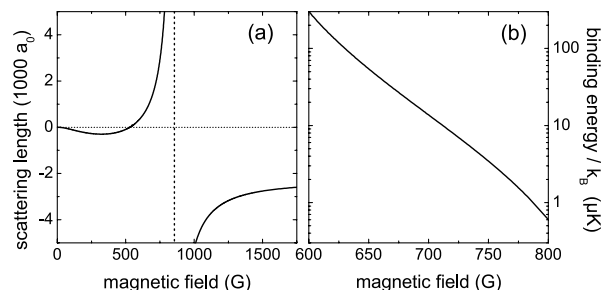


FIG. 1. (a) Magnetic-field dependence of the  $s$ -wave scattering length  $a$  in the  $^6\text{Li}$  spin mixture. An additional, narrow Feshbach resonance near 550 G [22] is omitted in the plot. (b) Binding energy of the weakly bound molecular level in the region of large positive  $a$ .

axial and radial trap frequencies are 260 kHz and 390 Hz, respectively. The trap depth is  $k_B \times 27 \mu\text{K}$  with  $k_B$  denoting Boltzmann's constant. At a temperature of  $2.5 \mu\text{K}$ , peak values for the number density and phase-space density are  $3 \times 10^{12} \text{ cm}^{-3}$  and 0.04 [27,28], respectively. The ultracold gas is prepared by forced evaporative cooling after loading the optical trap at an initial depth of  $\sim 1 \text{ mK}$  with  $8 \times 10^6$  atoms from a magneto-optical trap (MOT). The evaporation is performed by ramping down the light intensity in 1 s at a magnetic field of 1200 G. The evaporation initially proceeds with very high efficiency similarly to [16,29], but finally loses its efficiency when the tightly confining lattice potential does not support more than one or two quantum states.

We form molecules in the weakly bound level at a field of 690 G, where we find optimum production rates at a large positive scattering length of  $a = +1300a_0$ . Here  $a_0$  denotes Bohr's radius. To reach the production field of 690 G, we quickly ramp from the evaporation field of 1200 G down to this value with a speed of  $-7.5 \text{ G/ms}$ . In contrast to other experiments with fermionic atoms [1,2], the molecule formation during this ramp is negligible and the molecules are predominantly formed after the ramp at the fixed production field.

The molecules are detected by dissociating them into atoms [1,2,13,14] and measuring their fluorescence. For this purpose, we apply a ramp across the Feshbach resonance to fields of typically 1200 G (speed  $+6 \text{ G/ms}$ ). This brings the weakly bound level above the scattering continuum and the molecules quickly dissociate. The dissociation turns out to be insensitive to variations of the ramp speed and the final field. After the dissociation ramp, we immediately ramp down to zero magnetic field. The ramp speed of  $-12 \text{ G/ms}$  is fast enough to avoid molecule formation when crossing the region of positive scattering length. After reaching zero magnetic field, we recapture all atoms into the MOT. Their number is then determined by measuring the emitted fluorescence intensity using a calibrated photodiode [27]. This measurement provides the total atom number  $2N_{\text{mol}} + N_{\text{at}}$ , where  $N_{\text{mol}}$  and  $N_{\text{at}}$  denote the number of molecules and atoms after the production phase, respectively. To determine  $N_{\text{at}}$ , we repeat the same measurement without the Feshbach dissociation ramp by immediately ramping down to zero from the production field. The ramp down to zero magnetic field increases the binding energy to a large value of about  $k_B \times 80 \text{ mK}$  and the molecules are lost without leading to any fluorescence light in the MOT. The number of molecules  $N_{\text{mol}}$  is then obtained by taking the difference in atom numbers measured in two subsequent runs with and without the dissociating Feshbach ramp.

The creation of molecules from the atomic gas is demonstrated in Fig. 2 for the optimum production field of 690 G. The time evolution of the measured numbers  $2N_{\text{mol}} + N_{\text{at}}$  and  $N_{\text{at}}$  is shown together with the corresponding number of molecules  $2N_{\text{mol}}$ . We attribute the molecule formation to three-body recombination into the

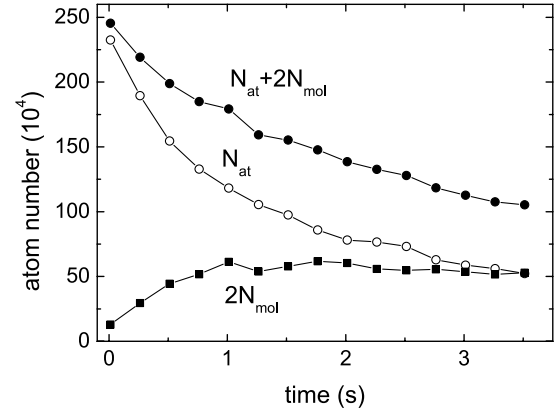


FIG. 2. Formation of molecules at a fixed magnetic field of 690 G. The measured numbers  $N_{\text{at}} + 2N_{\text{mol}}$  and  $N_{\text{at}}$  are plotted as a function of time together with the resulting number of molecules  $2N_{\text{mol}}$ .

weakly bound state [30,31]. Two-body processes cannot lead to bound dimers as a third particle is required for energy and momentum conservation. The three-body molecule formation process can be modeled with the differential equation  $\dot{N}_{\text{mol}}/N_{\text{at}} = M_3 \langle n_{\text{at}}^2 \rangle$ , where  $\langle n_{\text{at}}^2 \rangle$  denotes the mean quadratic density of the atoms. From the initial molecule formation rate of  $\dot{N}_{\text{mol}} = 3.5 \times 10^5 \text{ s}^{-1}$ , we thus derive a three-body formation coefficient of  $M_3 = 1 \times 10^{-25} \text{ cm}^6/\text{s}^{-1}$  [27]. The maximum number of  $3 \times 10^5$  molecules is reached after about 1 s. For longer times, the fraction of atoms forming molecules approaches a value of  $\sim 50\%$ .

At the optimum production field of 690 G, the molecular binding energy amounts to  $\sim k_B \times 18 \mu\text{K}$ , which is in between the thermal energy of  $k_B \times 2.5 \mu\text{K}$  and the trap depth of  $k_B \times 27 \mu\text{K}$  for the atoms. For the molecules, the trap depth is a factor of 2 higher because of the 2 times larger polarizability. We have verified this fact by measuring the trap frequencies for atoms and molecules to be equal within the experimental uncertainty of a few percent. After a three-body recombination event both the atom and the molecule remain trapped. We believe that the recombination heat is cooled away by an evaporation of atoms out of the trap. Evaporative loss of molecules is strongly suppressed because of the higher trap depth.

To purify the created molecules we use a Stern-Gerlach selection technique. We apply a magnetic field gradient perpendicular to the standing-wave axis. This pulls particles out of the trap for which the magnetic force is larger than the trapping force. In order to be able to apply large enough field gradients, we lower the trap depth to  $k_B \times 19 \mu\text{K}$  while applying the gradient for about 10 ms. Figure 3 demonstrates such a purification at 568 G. While all the atoms are lost above  $B'_{\text{at}} = 17 \text{ G/cm}$ , the molecules start getting spilled at  $20 \text{ G/cm}$ , and are lost completely above  $B'_{\text{mol}} = 32.5 \text{ G/cm}$ . This means that, under suitable conditions, we can remove all the atoms while keeping the molecule number constant.

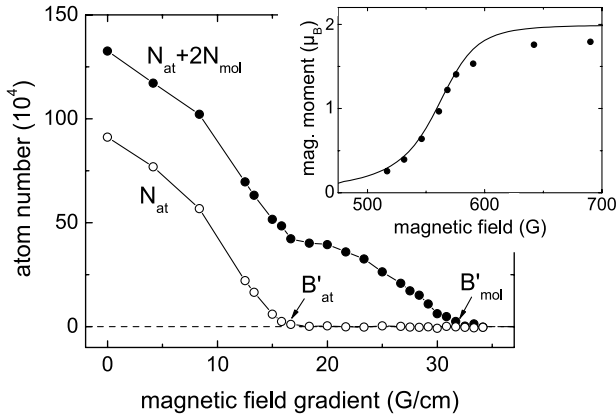


FIG. 3. Stern-Gerlach selection by applying a magnetic field gradient to the trapped atom-molecule mixture at 568 G and a trap depth of  $k_B \times 19 \mu K$ . Marked are the two gradients where all the atoms and all the molecules are lost. The inset shows the magnetic moment of the molecules estimated from the Stern-Gerlach selection at different magnetic fields together with the theoretical calculation.

The magnetic moment of the molecules  $\mu_{mol}$  can be estimated to be  $\mu_{mol} = 2\mu_{at}B'_{mol}/B'_{at}$ , where  $\mu_{at}$  is the magnetic moment of one free atom. At high magnetic field,  $\mu_{at}$  equals Bohr's magneton  $\mu_B$ . The inset of Fig. 3 shows the magnetic moments of the molecules determined at various magnetic fields. The data agree well with the magnetic field dependence calculated from theory (solid curve). We attribute the systematic deviation to slightly different trap parameters for atoms and molecules.

Starting with a pure molecular sample, we study its stability against inelastic molecule-molecule collisions. Corresponding decay curves are displayed in Fig. 4 for two different magnetic fields. At 546 G a rapid nonexponential decay is observed as a clear signature of inelastic molecule-molecule collisions. From the initial decay rate we derive a two-body loss coefficient of  $5 \times 10^{-11} \text{ cm}^3/\text{s}$  [27]. At 690 G, the observed behavior is strikingly different. The molecular sample shows a nearly exponential

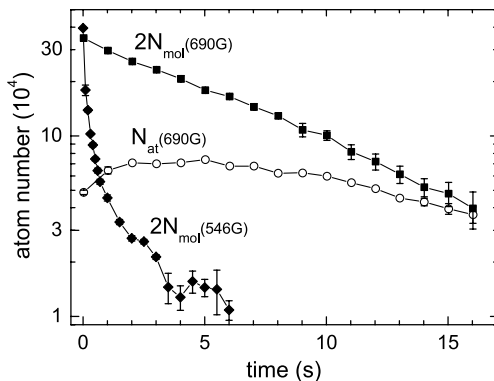


FIG. 4. Time evolution of an initially pure sample of molecules at 546 G (◆) and at 690 G (■). At 690 G, atoms are observed to reappear (○).

decay with a time constant as long as  $\sim 10$  s. As similar lifetimes are observed for trapped atom samples under conditions where trapped molecules cannot be created, the observed molecular lifetime can be fully attributed to one-body effects such as heating in the optical trap. For a loss rate coefficient at 690 G our data provide an upper limit of  $3 \times 10^{-13} \text{ cm}^3/\text{s}$  [27], which is surprisingly low for inelastic collisions in a molecular system with many open exit channels.

The data at 690 G show another interesting collisional effect. Atoms reappear after purification of the molecular cloud, see (○) in Fig. 4. For long storage times ( $\sim 15$  s), an atom-molecule mixture is reestablished with a similar fraction of molecules as observed in the initial formation process at the same magnetic field (see Fig. 2). Collisions producing atoms from molecules are endoergic in nature as kinetic energy is required to provide the dissociation energy. The increasing atom fraction does not lead to any increased loss. This shows that the gas is remarkably stable both against molecule-molecule and atom-molecule collisions.

The dependence of the molecular decay on the magnetic field is shown in Fig. 5. Here we store the initially pure gas of  $1.8 \times 10^5$  molecules at a variable magnetic field for a fixed holding time of 1 s before we measure the number of remaining molecules and atoms. A sharp transition occurs around 650 G. For fields below  $\sim 600$  G, where the binding energy is relatively large ( $> k_B \times 100 \mu K$ ), the observed decay is very fast and no atoms are found to reappear. Here inelastic collisions apparently lead to a rapid vibrational quenching. Furthermore, the kinetic energy of the molecules cannot provide the necessary energy for collisional dissociation. Consequently, we do not observe any atoms reappearing.

For fields above  $\sim 680$  G, a completely different behavior is observed. In this regime, no significant loss occurs in the total number  $2N_{mol} + N_{at}$ . However, an increasing atom fraction is observed as a result of collisional dissociation of the molecules. Here the binding energy

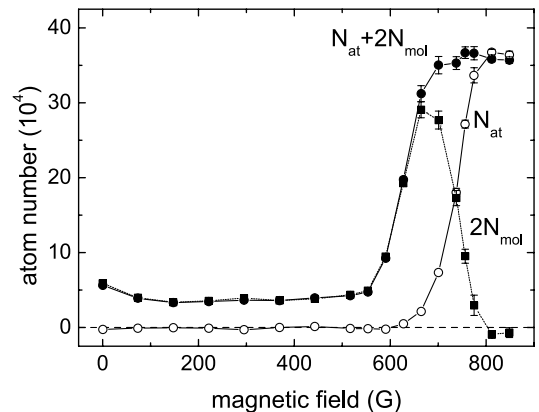


FIG. 5. Remaining number of atoms  $N_{at}$ ,  $N_{at} + 2N_{mol}$  and  $2N_{mol}$  after a 1-s hold time at variable magnetic field starting with a pure molecular sample.

approaches the thermal energy and the sample tends towards a thermal atom-molecule equilibrium. Close to the Feshbach resonance, where the binding energy becomes comparable to thermal energy, the atomic fraction dominates in the atom-molecule mixture.

In conclusion we have produced an ultracold, pure molecular gas of  $^6\text{Li}$  dimers in an optical dipole trap. Close to the Feshbach resonance, where the molecular binding energy is small, there is a strong coupling of the atomic gas and the molecules. Three-body collisions between atoms form molecules and collisions break up molecules to produce atoms. Our observations show that this exchange between atomic and molecular fraction can be nearly lossless. The long molecular lifetime along with a large elastic collision rate between the particles opens up great perspectives for further evaporative cooling of the molecular gas to Bose-Einstein condensation. Given the maximum molecule number of  $3 \times 10^5$  and a temperature of about  $2.5 \mu\text{K}$ , we reach a phase-space density of 0.01, only a factor of 4 lower than our initial atomic phase-space density. The molecular sample may be further cooled to condensation by efficient evaporation. Out of a mixture of atoms and molecules, mainly atoms will evaporate because they are more weakly trapped than the molecules. The gas is cooled further when molecules break up into atoms since this is an endoergic process. Once quantum degeneracy is accomplished it will be very interesting to cross the Feshbach resonance in order to observe the transition to a strongly interacting superfluid Fermi gas [7–10].

We thank G. Shlyapnikov for very stimulating discussions and V. Venturi for providing us with theoretical data on the scattering length and binding energy. We gratefully acknowledge support by the Austrian Science Fund (FWF) within SFB 15 (project part 15) and by the European Union in the frame of the Cold Molecules TMR Network under Contract No. HPRN-CT-2002-00290.

*Note added.*—After submission of the present Letter, molecule formation in  $^6\text{Li}$  using the narrow Feshbach resonance at 543 G was reported by Hulet's group [32].

- 
- [1] C. A. Regal, C. Ticknor, J. L. Bohn, and D. S. Jin, *Nature* (London) **424**, 47 (2003).
  - [2] J. Cubizolles, T. Bourdel, S. J. J. M. F. Kokkelmans, G. V. Shlyapnikov, and C. Salomon, preceding Letter, *Phys. Rev. Lett.* **91**, 240401 (2003).
  - [3] H. T. C. Stoof, M. Houbiers, C. Sackett, and R. Hulet, *Phys. Rev. Lett.* **76**, 10 (1996).
  - [4] H. Feshbach, *Ann. Phys. (Leipzig)* **19**, 287 (1962).
  - [5] S. Inouye, M. Andrews, J. Stenger, H.-J. Miesner, D. Stamper-Kurn, and W. Ketterle, *Nature* (London) **392**, 151 (1998).
  - [6] T. Loftus, C. Regal, C. Ticknor, J. Bohn, and D. Jin, *Phys. Rev. Lett.* **88**, 173201 (2002).
  - [7] M. Holland, S. J. J. M. F. Kokkelmans, M. Chiofalo, and R. Walser, *Phys. Rev. Lett.* **87**, 120406 (2001).
  - [8] E. Timmermans, K. Furuya, P. W. Milonni, and A. K. Kerman, *Phys. Lett. A* **285**, 228 (2001).
  - [9] M. L. Chiofalo, S. J. J. M. F. Kokkelmans, J. L. Milstein, and M. J. Holland, *Phys. Rev. Lett.* **88**, 090402 (2002).
  - [10] Y. Ohashi and A. Griffin, *Phys. Rev. Lett.* **89**, 130402 (2002).
  - [11] E. A. Donley, N. R. Claussen, S. T. Thompson, and C. E. Wieman, *Nature* (London) **417**, 529 (2002).
  - [12] C. Chin, A. J. Kerman, V. Vuletić, and S. Chu, *Phys. Rev. Lett.* **90**, 033201 (2003).
  - [13] J. Herbig, T. Kraemer, M. Mark, T. Weber, C. Chin, H.-C. Nägerl, and R. Grimm, *Science* **301**, 1510 (2003).
  - [14] S. Dürr, T. Volz, A. Marte, and G. Rempe, *cond-mat/0307440*.
  - [15] A. G. Truscott, K. E. Strecker, W. I. McAlexander, G. B. Partridge, and R. G. Hulet, *Science* **291**, 2570 (2001).
  - [16] K. O'Hara, S. Hemmer, M. Gehm, S. Granade, and J. Thomas, *Science* **298**, 2179 (2002).
  - [17] T. Bourdel, J. Cubizolles, L. Khaykovich, K. M. F. Magalhães, S. J. J. M. F. Kokkelmans, G. Shlyapnikov, and C. Salomon, *Phys. Rev. Lett.* **91**, 020402 (2003).
  - [18] S. Gupta, Z. Hadzibabic, M. Zwerle, C. Stan, K. Dieckmann, C. H. Schunck, E. G. M. van Kempen, B. J. Verhaar, and W. Ketterle, *Science* **300**, 1723 (2003).
  - [19] S. Jochim, M. Bartenstein, G. Hendl, J. Hecker Denschlag, R. Grimm, A. Mosk, and M. Weidemüller, *Phys. Rev. Lett.* **89**, 273202 (2002).
  - [20] G. Modugno, G. Roati, F. Riboli, F. Ferlaino, R. J. Brecha, and M. Inguscio, *Science* **297**, 2240 (2002).
  - [21] M. Houbiers, H. T. C. Stoof, W. McAlexander, and R. Hulet, *Phys. Rev. A* **57**, R1497 (1998).
  - [22] K. O'Hara, S. Hemmer, S. Granade, M. Gehm, J. Thomas, V. Venturi, E. Tiesinga, and C. Williams, *Phys. Rev. A* **66**, 041401(R) (2002).
  - [23] The exact resonance position is uncertain within a few 10 G [17], whereas the location of the zero-crossing has been determined to 529 G within 3 G [19,22].
  - [24] K. Dieckmann, C. Stan, S. Gupta, Z. Hadzibabic, C. Schunck, and W. Ketterle, *Phys. Rev. Lett.* **89**, 203201 (2002).
  - [25] From the scattering length data [22], we calculate the binding energy  $\hbar^2/[m(a - \bar{a})^2]$  including a correction with  $\bar{a} = 29.8a_0$  for lithium. See G. Gribakin and V. Flambaum, *Phys. Rev. A* **48**, 546 (1993).
  - [26] A. Mosk, S. Jochim, H. Moritz, T. Elsässer, M. Weidemüller, and R. Grimm, *Opt. Lett.* **26**, 1837 (2001).
  - [27] With fluorescence detection, we can determine the absolute atom number only within a factor of 2. All the derived quantities are subject to this systematic error.
  - [28] With a ground-state population of 99% in the tightly confined direction, each lattice site contains a quasi-2D gas. This fact is taken into account in our calculations of number and phase-space densities.
  - [29] S. R. Granade, M. E. Gehm, K. M. O'Hara, and J. E. Thomas, *Phys. Rev. Lett.* **88**, 120405 (2002).
  - [30] H. Suno, B. D. Esry, and C. H. Greene, *Phys. Rev. Lett.* **90**, 053202 (2003).
  - [31] D. Petrov, *Phys. Rev. A* **67**, 010703(R) (2003).
  - [32] K. E. Strecker, G. B. Partridge, and R. G. Hulet, *Phys. Rev. Lett.* **91**, 080406 (2003).

## **Appendix F**

# **Bose-Einstein Condensation of Molecules**





# Bose-Einstein Condensation of Molecules

S. Jochim,<sup>1</sup> M. Bartenstein,<sup>1</sup> A. Altmeyer,<sup>1</sup> G. Hendl,<sup>1</sup> S. Riedl,<sup>1</sup>  
C. Chin,<sup>1</sup> J. Hecker Denschlag,<sup>1</sup> R. Grimm<sup>1,2\*</sup>

We report on the Bose-Einstein condensation of more than  $10^5$   $\text{Li}_2$  molecules in an optical trap starting from a spin mixture of fermionic lithium atoms. During forced evaporative cooling, the molecules are formed by three-body recombination near a Feshbach resonance and finally condense in a long-lived thermal equilibrium state. We measured the characteristic frequency of a collective excitation mode and demonstrated the magnetic field-dependent mean field by controlled condensate spilling.

Since the first experiments on Bose-Einstein condensation (BEC) in ultracold atomic gases in 1995 (1–3), atoms of eight chemical elements have been condensed. BEC of more complex objects such as molecules or Cooper-paired atoms will open up many new avenues of research because they offer new degrees of freedom. An intriguing example is the fundamental change in quantum statistics when paired fermions form composite bosons. Recent experiments have demonstrated the formation of molecules in ultracold atomic gases of bosons (4–9) and fermions (10–13). Experiments starting with atomic BEC show the creation of molecular clouds at the threshold to quantum degeneracy (7) or clearly in that regime (9), but not in a thermal equilibrium state. In most of these experiments, weakly bound dimers are produced via magnetically tuned Feshbach resonances (14). Such a scattering resonance occurs when a free colliding atom pair energetically coincides with a bound molecular state. On the side of the resonance where the energy of the molecular level is below the dissociation limit, a weakly bound dimer state exists. The experiments indicate an important difference between weakly bound dimers composed of bosonic and of fermionic atoms. Dimers of bosons show a quick decay via inelastic atom-molecule or molecule-molecule collisions (9), so that quantum-degenerate molecular clouds can only be created in a transient regime. In contrast, the dimers of fermions exhibit a remarkable stability (11–13, 15). Such molecular gases have been observed with lifetimes far longer than the time scales for elastic collisions and thermalization. This fact has been explained by a fermionic suppression of vibrational quenching in molecule collisions (16). Their stability allows us to use bosonic mole-

cules composed of fermionic atoms to achieve molecular BEC in thermal equilibrium.

Our experiment is based on evaporative cooling of an optically trapped mixture of fermionic  $^6\text{Li}$  atoms in the two lowest spin states (11–13, 17–21). During the cooling process, a large number of bosonic dimers are formed by three-body recombination and finally condense into a molecular BEC. The spin mixture exhibits a broad Feshbach resonance at a magnetic field of about 850 G (18, 19, 22, 23), which leads to a pronounced magnetic field dependence of the scattering length  $a$  (Fig. 1) that characterizes the  $s$ -wave interactions. Dimers in a single weakly bound state can be formed in the range of large positive  $a$  with a binding energy of  $\hbar^2/(ma^2)$ , where  $\hbar$  is Planck's constant  $h$  divided by  $2\pi$  and  $m$  is the mass of a  $^6\text{Li}$  atom. This has been observed in magnetic field-dependent loss features (24) and changes in the interaction energy of the gas (21). Two recent experiments have directly demonstrated the presence of these molecules and investigated some of their properties (12, 13). For negative scattering length, no weakly bound dimer state exists. For negative scattering length, where a weakly bound dimer state does not exist, the  $^6\text{Li}$  gas exhibits a remarkable stability against collisional decay, and deeply degenerate Fermi gases have been created (20).

Our optical dipole trap is realized with a single Gaussian laser beam at a wavelength of 1030 nm, which is focused to a waist of 23  $\mu\text{m}$ . At the full power of  $P_0 = 10.5$  W, the radial and axial oscillation frequencies are  $\Omega_r/2\pi = 14.5$  kHz and  $\Omega_z/2\pi = 140$  Hz, respectively, and the atom trap is  $U_0 \approx k_B \times 800$   $\mu\text{K}$  deep ( $k_B$  denotes Boltzmann's constant). When the power  $P$  is reduced to a relative value  $p = P/P_0$ , the optical trap frequencies follow  $p^{1/2}\Omega_i$  ( $i = r, z$ ) and the trap depth for the atoms is  $U_{\text{at}} = pU_0$ . Our magnetic field  $B$  used for Feshbach tuning exhibits a curvature that gives rise to an additional contribution to the trapping potential. For the tight radial confinement of the optical trap, this effect is negligibly small. For the weak axis, however, a magnetic trap-

ping effect becomes important with decreasing  $p$ . Taking this into account, the axial trap frequency is given by  $\omega_z = \sqrt{p\Omega_z^2 + \omega_m^2}$ . Here  $\omega_m/2\pi = 24.5$  Hz  $\times \sqrt{B/k_B}$  is the magnetic contribution, which is precisely known for our coils. For weak traps with  $p \ll 0.03$  ( $U_{\text{at}}/k_B \ll 25$   $\mu\text{K}$ ), the magnetic contribution dominates, and the axial confinement is harmonic with a corresponding frequency known on the percent level. In this regime, the mean trap frequency is given by  $\bar{\omega} = (p\Omega_r^2\omega_m)^{1/3}$ . For the weakly bound  $^6\text{Li}$  dimers, all external forces are twice the ones on the individual atoms. Thus, the molecular trap is two times deeper than the atom trap ( $U_{\text{mol}} = 2U_{\text{at}}$ ), and the trap frequencies are identical. Gravity is compensated for by a magnetic field gradient of 1.1 G/cm.

We start the evaporation process with  $\sim 1.5 \times 10^6$  atoms at a temperature of  $\sim 80$   $\mu\text{K}$ , a peak number density of  $\sim 10^{14}$   $\text{cm}^{-3}$ , and a peak phase-space density of  $\sim 5 \times 10^{-3}$ . The mean elastic collision rate is as high as  $\sim 5 \times 10^4$   $\text{s}^{-1}$ . These excellent starting conditions are obtained by a two-stage loading process. The atoms are loaded into the dipole trap from another deep, large-volume standing wave trap (25), which itself is loaded from a magneto-optical trap. Forced evaporative cooling is then performed by reducing the trap power (17, 20). We use a simple exponential ramp with a relative power  $p(t) = \exp(-t/\tau)$ , where the time constant  $\tau = 0.23$  s is experimentally optimized. A feedback system allows us to precisely control the laser power to levels well below  $p = 10^{-4}$ .

BEC of weakly bound molecules occurs when we perform evaporative cooling at a large positive scattering length of  $a \approx +3500a_0$ , where  $a_0$  is Bohr's radius. In this case, the evaporation process shows a strikingly different behavior in comparison with the corresponding situation at large negative scattering length, where no dimers can be produced.

First we discuss the creation of a degenerate Fermi gas without the possibility of molecule formation at a magnetic field of 1176 G, where  $a \approx -3500a_0$  (23). Here the evaporation pro-

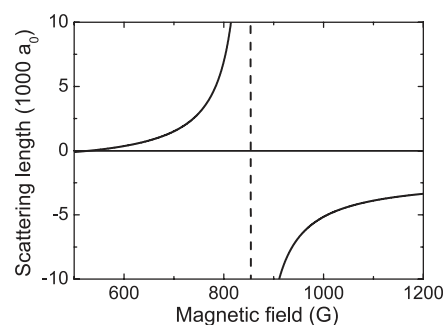


**Fig. 1.** Feshbach resonance at  $\sim 850$  G in a mixture of the two lowest spin states of  $^6\text{Li}$  (18). The  $s$ -wave scattering length  $a$  is plotted as a function of the magnetic field  $B$ .

<sup>1</sup>Institut für Experimentalphysik, Universität Innsbruck, Technikerstraße 25, 6020 Innsbruck, Austria.

<sup>2</sup>Institut für Quantenoptik und Quanteninformation, Österreichische Akademie der Wissenschaften, 6020 Innsbruck, Austria.

\*To whom correspondence should be addressed. E-mail: rudolf.grimm@uibk.ac.at

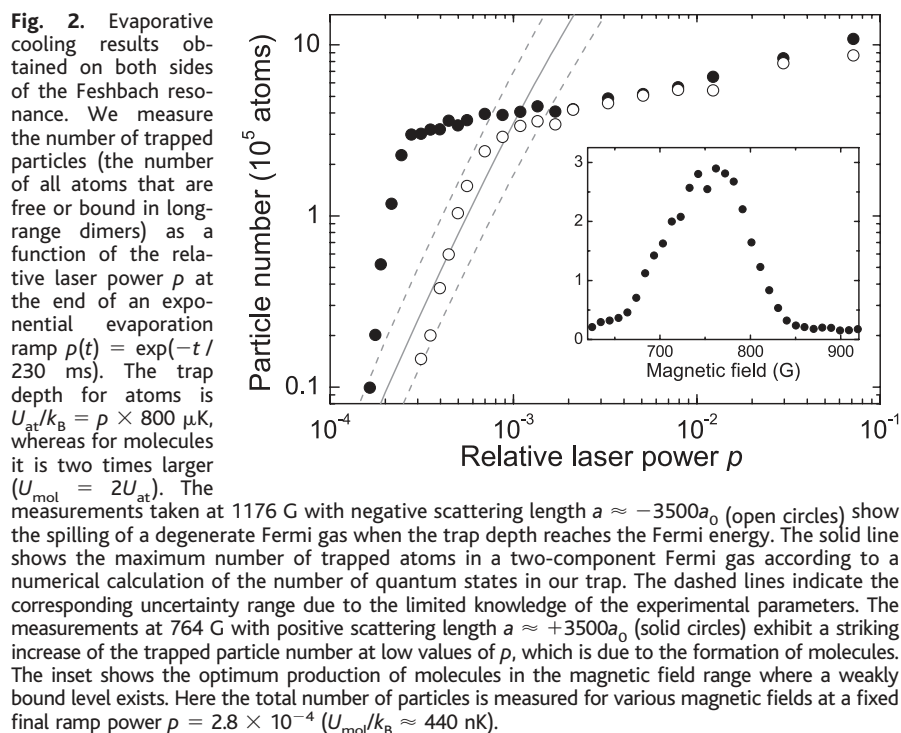
## REPORTS

ceeds in a very similar way as that described in (17, 20). The measured atom number  $N$  (26) first follows a scaling law  $N/N_0 = p^\alpha$  (27), with  $\alpha \approx 0.25$ . In this regime, the temperature of the gas is typically a factor of 10 below the trap depth (27), and the elastic collision rate stays well above  $10^4 \text{ s}^{-1}$ . The crossover to Fermi degeneracy, where the thermal energy  $k_B T$  reaches the Fermi energy  $E_F = \hbar \bar{\omega} (3N)^{1/3}$ , takes place at  $p \approx 0.05$  ( $U_{\text{at}}/k_B \approx 40 \text{ } \mu\text{K}$ ). By further decreasing  $p$ , the trap depth  $U_{\text{at}} \propto p$  decreases faster than the Fermi energy  $E_F \propto p^{1/3}$ . A threshold occurs when  $E_F$  reaches  $U_{\text{at}}$  and the trap is filled up to the "rim." Further decrease of  $p$  then leads to a spilling of atoms out of the trap and thus to a rapid decrease of  $N$  with  $p$ . Our data (Fig. 2) clearly show this spilling effect for  $p < 1 \times 10^{-3}$  ( $U_{\text{at}}/k_B < 800 \text{ nK}$ ). Modeling the spilling curves provides us with an upper bound of  $k_B T < 0.2 E_F$  for the temperature in terms of the Fermi energy. In the regime of a completely filled shallow trap, the number of atoms in the two-component spin mixture is given by two times the number of quantum states in the trap. A numerical calculation, shown in Fig. 2, confirms this interpretation of our data.

The same evaporation procedure is performed at a magnetic field of 764 G, where the scattering length  $a \approx +3500a_0$  (23) has essentially the same magnitude but opposite sign. Here the weakly bound dimers have a binding energy of  $\sim 2 \text{ } \mu\text{K}$ , and their formation has been observed in several experiments (12, 13, 21). In order to detect the molecules, we dissociate them and measure the number of resulting atoms (26). For this purpose, we abruptly turn on the full trap power, which strongly heats the sample and leads to collisional dissociation. In order to ensure that we dissociate all molecules, we also apply a magnetic field ramp across the Feshbach resonance (13). The number of atoms measured after the dissociation process thus yields the number of free atoms together with atoms having formed molecules.

Below  $p = 1 \times 10^{-3}$  the measured atom numbers (solid circles in Fig. 2) show a striking difference in comparison with the case of the degenerate Fermi gas. Down to a power level of  $p = 3 \times 10^{-4}$  ( $U_{\text{mol}}/k_B \approx 480 \text{ nK}$ ), the trap holds almost all particles and contains up to 20 times more atoms than would be possible for fermions. Hence, the trapped sample can no longer be an atomic Fermi gas. The trap is filled with bosonic molecules in the weakly bound state (28). The lifetime of the molecular ensemble, for which we measure about 20 s at a fixed trap depth of  $U_{\text{mol}}/k_B \approx 560 \text{ nK}$ , exceeds the time scale of elastic collisions ( $\sim 100 \text{ } \mu\text{s}$ ) by several orders of magnitude. This highlights the fact that the molecular cloud exists in a thermal equilibrium state.

The formation of molecules during the evaporative cooling process can be understood



in terms of a chemical atom-molecule equilibrium (29, 30). Exothermal three-body recombination processes compete with dissociation by endothermal two-body processes. When the gas is cooled down, the equilibrium shifts to an increasing fraction of molecules. Because atom-atom, atom-molecule, and molecule-molecule collisions have comparable cross sections near the resonance (16), evaporation continues at about the same speed. In the final stage of cooling, all relevant energies, such as the thermal energy  $k_B T$  and the trap depths  $U_{\text{at}}$  and  $U_{\text{mol}}$ , are far below the binding energy  $\hbar^2/(ma^2)$ , so that in chemical equilibrium one is left with an essentially pure sample of molecules. The fact that the binding energy of  $\sim 2 \text{ } \mu\text{K}$  at our optimized magnetic field of 764 G is a few times larger than the final trap depth (inset, Fig. 1) fits well into this picture.

The observation that a large number of  $N_{\text{mol}} \approx 1.5 \times 10^5$  molecules is confined in our very shallow, only 480 nK deep trap under thermal equilibrium conditions already shows that a molecular BEC is formed. The trap offers about 10 times more quantum states for dimers as compared to the case of atoms discussed before (31). Because we observe a factor of  $\sim 20$  more particles than for the degenerate atomic Fermi gas, the molecular gas is necessarily quantum degenerate. Because of the high elastic collision rates, which stay well above  $10^3 \text{ s}^{-1}$  even for very shallow traps, the sample is also thermalized. The temperature then is a small fraction of the trap depth. According to standard evaporation theory (27), we can typically assume  $T \approx 0.1 U_{\text{mol}}/k_B \approx 50 \text{ nK}$ . This is well below the critical temperature for BEC, for

which we calculate  $T_C = \hbar \bar{\omega} k_B^{-1} (N_{\text{mol}}/1.202)^{1/3} = 280 \text{ nK}$ . Because the condensate fraction is given by  $1 - (T/T_C)^3$ , these arguments show that the molecular BEC must be almost pure.

To investigate the molecular condensate, we have studied a characteristic collective excitation mode (32, 33). For a cigar-shaped sample in the Thomas-Fermi limit, well fulfilled in our experiment, such a quadrupolar mode is expected at a frequency of  $\sqrt{5/2} \omega_z = 2\pi \times 33.8 \text{ Hz}$ . We perform our measurement at  $p = 3.5 \times 10^{-4}$  ( $U_{\text{mol}}/k_B \approx 560 \text{ nK}$ ) with a trapped sample of  $\sim 10^5$  molecules. We apply a sinusoidal modulation to the magnetic field with an amplitude of 3.5 G to modulate the molecular scattering length  $a_m \propto a$  (16) with a relative amplitude of about 5%. After 2 s of continuous excitation, we measure the remaining number of particles in the trap. The resonance manifests itself in a sharp dip in the number of particles (Fig. 3). The observed resonance frequency of 33.6 Hz is in remarkable agreement with the expectation. We point out that a noncondensed gas deep in the hydrodynamic regime would show a similar frequency of 33.2 Hz (34), but thermalization in our shallow trap excludes this scenario (35). The measured collective excitation frequency rules out a gas in the collisionless regime, which would show its resonant loss at  $2\omega_z = 2\pi \times 42.8 \text{ Hz}$ , and thus again confirms the thermalization of the sample. The observed narrow resonance width of  $\sim 1 \text{ Hz}$  shows a very low damping rate and is consistent with an almost pure BEC (33, 36).

An essential property of a BEC is its mean field potential  $U_{\text{MF}} = 4\pi n a_m \hbar^2/(2m)$  resulting

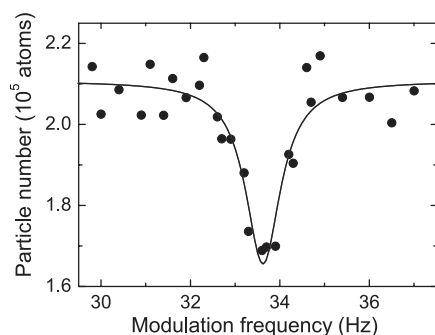


**Fig. 3.** Resonance of a collective excitation mode at  $\sqrt{5/2} \omega_z$ . The oscillation is excited by magnetic modulation of the molecular BEC mean field. The solid curve shows a Lorentzian fit to the data.

from  $s$ -wave interactions; here  $n$  denotes the molecular density. For our molecular BEC with large positive  $a_m$ , the mean field is repulsive and thus stabilizes the BEC against collapse and decay. In a trap of finite depth, however, the mean field repulsion limits the maximum number of trappable molecules. When the chemical potential  $\mu$  reaches the trap depth, a similar spilling effect is expected as we see for the Fermi gas, but for weaker traps. The decrease of our molecular signal (Fig. 2) below  $p = 3 \times 10^{-4}$  ( $U_{\text{mol}}/k_B \approx 480$  nK) may be explained by such a spilling effect.

We used spilling in a controlled way to demonstrate the mean field of the molecular BEC and to investigate its dependence on the magnetic field. After producing the BEC at a magnetic field of  $B_1 = 772$  G and  $p = 3.5 \times 10^{-4}$  ( $U_{\text{mol}}/k_B \approx 560$  nK), we adiabatically tilt the vertical trapping potential by application of a magnetic field gradient  $B'$  that is smoothly ramped up within 50 ms. The number of remaining particles as a function of the applied field gradient (Fig. 4) shows the loss of molecules resulting from the reduced trap depth. When the magnetic field is kept at the evaporation field of  $B_1 = 772$  G, where  $a = 4100a_0$  (23), even very weak gradients lead to loss (open circles in Fig. 4). This indicates that the chemical potential is close to the potential depth, so that the trap is full. The chemical potential can be lowered by reducing the scattering length. For this purpose, we ramp the magnetic field to a smaller value. A spilling curve taken at  $B_2 = 731$  G, where  $a = 2200a_0$  (23), indeed shows a markedly different behavior (solid circles in Fig. 4). Here small gradients do not lead to any loss and the curve thus shows a flat top. For gradients  $|B'|$  exceeding 0.65 G/cm, molecules get spilled until everything is lost at  $|B'| = 1.3$  G/cm. The sharp onset of the spilling confirms the essentially pure nature of the BEC.

A comparison of the two spilling curves in Fig. 4 provides us with information on the ratio of the scattering lengths  $a_m$  at the two magnetic fields  $B_1$  and  $B_2$ . In the spilling region above  $|B'| = 0.65$  G/cm, the trap is full in both cases,

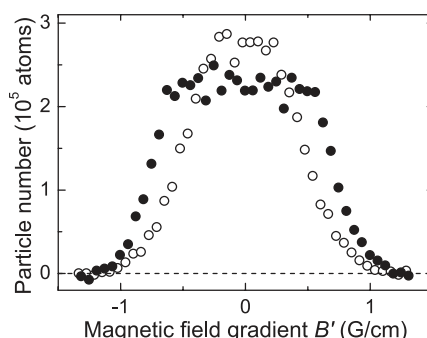


**Fig. 4.** Controlled spilling of the BEC by application of a magnetic field gradient  $B'$ . This variable gradient is applied in addition to the constant gradient of 1.1 G/cm that we use for gravity compensation. The data are taken at the two different magnetic fields  $B_1 = 772$  G (open circles) and  $B_2 = 731$  G (solid circles), where the mean field of the BEC is different by a factor of  $\sim 2$ .

and the trapped particle number is inversely proportional to  $a_m$ . Comparing the two spilling curves in that region, we obtain a scattering length ratio of  $a_m(B_1)/a_m(B_2) = 2.4(2)$ . This factor is indeed close to the factor of 1.9 (23) expected from the proportionality of atomic and molecular scattering lengths  $a_m \propto a$  (16) and the dependence of  $a$  shown in Fig. 1. This observation demonstrates the mean field of the molecular BEC together with its magnetic tunability.

The ability to control interactions in a Bose condensed ensemble of paired fermionic atoms has many exciting prospects (37, 38). It opens up unique ways to cool a fermionic gas far below the Fermi temperature (39) and to study different regimes of superfluidity (40–43). The experimental exploration of the strongly interacting crossover regime between a BEC-like and a Cooper-paired phase is a particular challenge and promises more insight into the physical mechanisms underlying superconductivity.

#### References and Notes

- M. Anderson, J. Ensher, M. Matthews, C. Wieman, E. Cornell, *Science* **269**, 198 (1995).
- K. Davis et al., *Phys. Rev. Lett.* **75**, 3969 (1995).
- C. Bradley, C. Sackett, J. Tollett, R. Hulet, *Phys. Rev. Lett.* **75**, 1687 (1995).
- R. Wynar, R. S. Freeland, D. J. Han, C. Ryu, D. J. Heinzen, *Science* **287**, 1016 (2000).
- E. A. Donley, N. R. Claussen, S. T. Thompson, C. E. Wieman, *Nature* **417**, 529 (2002).
- C. Chin, A. J. Kerman, V. Vuletić, S. Chu, *Phys. Rev. Lett.* **90**, 033201 (2003).
- J. Herbig et al., *Science* **301**, 1510 (2003); published online 21 August 2003 (10.1126/science.1088876).
- S. Dürr, T. Volz, A. Marte, G. Rempe, preprint available at <http://arxiv.org/abs/cond-mat/0307440>.
- K. Xu, et al. preprint available at <http://arxiv.org/abs/cond-mat/0310027>.
- C. A. Regal, C. Ticknor, J. L. Bohn, D. S. Jin, *Nature* **424**, 47 (2003).
- K. E. Strecker, G. B. Partridge, R. G. Hulet, *Phys. Rev. Lett.* **91**, 080406 (2003).
- J. Cubizolles, T. Bourdel, S. J. J. M. F. Kokkelmans, G. V. Shlyapnikov, C. Salomon, preprint available at <http://arxiv.org/abs/cond-mat/0308018>.

- S. Jochim et al., *Phys. Rev. Lett.*, in press (preprint available at <http://arxiv.org/abs/cond-mat/0308095>).
- S. Inouye et al., *Nature* **392**, 151 (1998).
- C. A. Regal, M. Greiner, D. S. Jin, preprint available at <http://arxiv.org/abs/cond-mat/0308606>.
- D. S. Petrov, C. Salomon, G. V. Shlyapnikov, preprint available at <http://arxiv.org/abs/cond-mat/0309010>.
- S. Granade, M. E. Gehm, K. M. O'Hara, J. E. Thomas, *Phys. Rev. Lett.* **88**, 120405 (2002).
- K. M. O'Hara et al., *Phys. Rev. A* **66**, 041401 (2002).
- S. Jochim et al., *Phys. Rev. Lett.* **89**, 273202 (2002).
- K. M. O'Hara, S. L. Hemmer, M. E. Gehm, S. R. Granade, J. E. Thomas, *Science* **298**, 2179 (2002); published online 7 November 2002 (10.1126/science.1079107).
- T. Bourdel et al., *Phys. Rev. Lett.* **91**, 020402 (2003).
- M. Houbiers, H. T. C. Stoof, W. McAlexander, R. Hulet, *Phys. Rev. A* **57**, R1497 (1998).
- The position of the Feshbach resonance is known to within a few tens of Gauss. All numbers given for the scattering lengths and binding energies are subject to a corresponding systematic error.
- K. Dieckmann et al., *Phys. Rev. Lett.* **89**, 203201 (2002).
- A. Mosk et al., *Opt. Lett.* **26**, 1837 (2001).
- We measure the atom number via fluorescence detection after recapture into a magneto-optical trap. In order to avoid molecule formation and loss when the Feshbach tuning field is ramped down before detection, we heat the sample by abruptly turning on the full laser power of the optical dipole trap. At low phase-space densities, the thermal gas is not affected by the downward Feshbach ramp (13).
- K. M. O'Hara, M. E. Gehm, S. R. Granade, J. E. Thomas, *Phys. Rev. A* **64**, 051403 (2001).
- We know that only the weakly bound state is populated, because the release of binding energy in a three-body process would otherwise lead to immediate trap loss. Moreover, our dissociation-based detection is sensitive only to molecules in this state.
- C. Chin, R. Grimm, preprint available at <http://arxiv.org/abs/cond-mat/0309078>.
- S. J. J. M. F. Kokkelmans, G. V. Shlyapnikov, C. Salomon, preprint available at <http://arxiv.org/abs/cond-mat/0308384>.
- For the harmonically approximated trap with same frequencies and twice the depth, the molecules have eight times more quantum states than the atoms. The lower  $\omega_z$  at 764 G as compared to 1176 G gives another factor of 1.24.
- S. Stringari, *Phys. Rev. Lett.* **77**, 2360 (1996).
- D. M. Stamper-Kurn, H.-J. Miesner, S. Inouye, M. R. Andrews, W. Ketterle, *Phys. Rev. Lett.* **81**, 500 (1998).
- D. Guéry-Odelin, F. Zambelli, J. Dalibard, S. Stringari, *Phys. Rev. A* **60**, 4851 (1999).
- A noncondensed ensemble in the hydrodynamic regime, where the elastic collision rate exceeds all other time scales, would rapidly cool down by evaporation to temperatures far below the trap depth and thus form a BEC.
- D. S. Jin, M. R. Matthews, J. R. Ensher, C. E. Wieman, E. A. Cornell, *Phys. Rev. Lett.* **78**, 764 (1997).
- L. Pitaevskii, S. Stringari, *Science* **298**, 2144 (2002).
- A. Cho, *Science* **301**, 750 (2003).
- L. D. Carr, G. V. Shlyapnikov, Y. Castin, preprint available at <http://arxiv.org/abs/cond-mat/0308306>.
- H. T. C. Stoof, M. Houbiers, C. Sackett, R. Hulet, *Phys. Rev. Lett.* **76**, 10 (1996).
- M. Holland, S. J. J. M. F. Kokkelmans, M. L. Chiofalo, R. Walser, *Phys. Rev. Lett.* **87**, 120406 (2001).
- E. Timmermans, K. Furuya, P. W. Milonni, A. K. Kerman, *Phys. Lett. A* **285**, 228 (2001).
- Y. Ohashi, A. Griffin, *Phys. Rev. Lett.* **89**, 130402 (2002).
- We thank P. Zoller for very useful discussions and for stimulating the measurement of the collective excitation frequency. We acknowledge support by the Austrian Science Fund (FWF) within Spezialforschungsbeirich 15 (project part 15) and by the European Union through the Cold Molecules Training and Mobility of Researchers Network under contract no. HPRN-CT-2002-00290. C.C. is a Lise-Meitner fellow of the FWF.

3 November 2003; accepted 11 November 2003

Published online 13 November 2003;

10.1126/science.1093280

Include this information when citing this paper.



## **Appendix G**

### **Crossover from a Molecular Bose-Einstein Condensate to a Degenerate Fermi Gas**



# Crossover from a Molecular Bose-Einstein Condensate to a Degenerate Fermi Gas

M. Bartenstein,<sup>1</sup> A. Altmeyer,<sup>1</sup> S. Riedl,<sup>1</sup> S. Jochim,<sup>1</sup> C. Chin,<sup>1</sup> J. Hecker Denschlag,<sup>1</sup> and R. Grimm<sup>1,2</sup>

<sup>1</sup>*Institut für Experimentalphysik, Universität Innsbruck, Technikerstraße 25, 6020 Innsbruck, Austria*

<sup>2</sup>*Institut für Quantenoptik und Quanteninformation, Österreichische Akademie der Wissenschaften, 6020 Innsbruck, Austria*

(Received 8 January 2004; revised manuscript received 2 February 2004; published 23 March 2004)

We demonstrate a reversible conversion of a  $^6\text{Li}_2$  molecular Bose-Einstein condensate to a degenerate Fermi gas of atoms by adiabatically crossing a Feshbach resonance. By optical *in situ* imaging, we observe a smooth change of the cloud size in the crossover regime. On the Feshbach resonance, the ensemble is strongly interacting and the measured cloud size is 75(7)% of the one of a noninteracting zero-temperature Fermi gas. The high condensate fraction of more than 90% and the adiabatic crossover suggest our Fermi gas to be cold enough to form a superfluid.

DOI: 10.1103/PhysRevLett.92.120401

PACS numbers: 03.75.Mn, 05.30.Fk, 32.80.Pj, 34.50.-s

Bose-Einstein condensation (BEC) of molecules formed by fermionic atoms was recently demonstrated [1–4]. The tunability of interactions in such systems provides a unique possibility to explore the Bose-Einstein condensate to Bardeen-Cooper-Schrieffer (BEC-BCS) crossover [5], an intriguing interplay between the superfluidity of bosons and Cooper pairing of fermions. While the BEC and BCS limits are both well understood, the crossover takes place in a strongly interacting regime, which represents a challenge for many-body theory.

Feshbach resonances [6] play a central role to control two-body interaction and have been used for conversion between fermionic atoms and bosonic molecules [7–10]. They are also the experimental key to investigate phenomena related to the BEC-BCS crossover. For example, it has been predicted in Ref. [11] that a pure molecular BEC can be converted into a superfluid Fermi gas by an adiabatic passage over the Feshbach resonance. Moreover, in the crossover regime where the interactions are unitarity limited, a universal behavior is expected [12,13]. Ultracold gases in that regime may provide new insights into other strongly interacting systems such as high- $T_c$  superconductors,  $^3\text{He}$  superfluids, and neutron stars.

A spin mixture of  $^6\text{Li}$  atoms in the lowest two hyperfine sublevels is an excellent system to investigate the crossover [14,15] based on a broad Feshbach resonance at a magnetic field of  $B = 850$  G [16–18]. An efficient formation of ultracold molecules has been realized by three-body recombination [10,19], or by sweeping the magnetic field across the resonance [8]. The long lifetime of the molecules permits efficient evaporation [1,8,10] and facilitates slow, adiabatic changes of the system.

In this work, we explore the regime where the BEC-BCS crossover is expected by analyzing the density profiles of the trapped cloud at different magnetic fields. Our experimental setup is described in Ref. [1]. We load  $2 \times 10^6$  precooled  $^6\text{Li}$  atoms into a single focused-beam dipole trap, which is generated by a 10 W Yb:YAG laser operating at a wavelength of 1030 nm. We evaporatively

cool the cloud by exponentially lowering the trap depth with a time constant of 460 ms. The radial and axial trap frequencies are  $\omega_r/2\pi = 110 \text{ Hz}(P/\text{mW})^{1/2}$  and  $\omega_z/2\pi = (600B/\text{kG} + 0.94P/\text{mW})^{1/2} \text{ Hz}$ , respectively, where  $P$  is the laser power. The curvature of the magnetic field that we use for Feshbach tuning results in a magnetic contribution to the axial trapping. In the low power range where the molecular BEC is formed ( $P < 50$  mW), the axial confinement is predominantly magnetic. During the whole evaporation process, the magnetic field is kept at  $B = 764$  G. At this field the molecular binding energy is  $\sim k_B \times 2 \mu\text{K}$ , where  $k_B$  is Boltzmann's constant. For the scattering length of elastic molecule-molecule collisions, we expect  $a_{\text{mol}} = 2200a_0$ , based on the predicted relation of  $a_{\text{mol}} = 0.6a$  [20] and an atomic scattering length of  $a = 3500a_0$  [17]. Here  $a_0$  is Bohr's radius. Using radio-frequency spectroscopy which allows us to distinguish signals from atoms and molecules [7], we observe a complete atom to molecule conversion when the thermal energy of the particles is reduced to values well below the molecular binding energy.

For detection we apply *in situ* absorption imaging to record spatial density profiles of the trapped ensemble. To image at high magnetic fields, we illuminate the cloud for 20  $\mu\text{s}$  with a probe beam (intensity 0.5 mW/cm<sup>2</sup>) tuned to the atomic  $|2S_{1/2}, m_J = -1/2, m_I = 0\rangle \rightarrow |2P_{3/2}, m'_J = -3/2, m'_I = 0\rangle$  transition. The probe beam dissociates the molecules and is used to image the resulting atom cloud [3]. Compared to the absorption imaging of unbound atoms, we found that the detection efficiency of the molecules approaches 100% at fields higher than 750 G and  $\sim 50\%$  at 650 G. The difference is due to the Franck-Condon wave function overlap, which favors fields closer to the resonance where the interatomic separation in the molecular state is larger. In our cigar-shaped trap, the radial cloud size is on the order of our imaging resolution of 10  $\mu\text{m}$ , while the axial cloud size of typically  $\sim 100 \mu\text{m}$  can be accurately measured. We therefore obtain axial density distributions from images integrated radially.



To measure the condensate fraction, we adiabatically reduce the magnetic field from 764 to 676 G in a 200-ms linear ramp after completion of the evaporation ramp. This reduces the scattering length  $a_{\text{mol}}$  and thus increases the visibility of the characteristic bimodal distribution. Figure 1(a) shows a bimodal profile observed in this way with  $N_{\text{mol}} = N/2 = 4 \times 10^5$  molecules remaining at a final evaporation ramp power of 28 mW. A Gaussian fit to the thermal wings (dashed line) yields a temperature of  $T = 430$  nK, which is a factor of 7.5 below the calculated trap depth of  $3.2 \mu\text{K}$ . The observed condensate fraction of  $\sim 20\%$  is consistent with  $1 - (T/T_c)^3$ , where  $T_c = 0.8k_B^{-1}\hbar\bar{\omega}(N_{\text{mol}}/1.202)^{1/3} = 500$  nK is the critical temperature,  $\bar{\omega} = (\omega_r^2\omega_z)^{1/3}$  is the mean vibration frequency, and the factor of 0.8 takes into account the  $\sim 20\%$  downshift in  $T_c$  due to interactions [21].

We obtain pure molecular condensates when we continue the evaporation process down to final power levels of a few mW. Figure 1(b) shows an essentially pure condensate of  $N_{\text{mol}} = 2.0 \times 10^5$  molecules obtained at a final power of 3.8 mW, where the trap depth is 450 nK. The density profile is well fit by a Thomas-Fermi density distribution  $\propto (1 - z^2/z_{\text{TF}}^2)^2$  with a radius  $z_{\text{TF}} = 105 \mu\text{m}$ . The corresponding peak molecular density is  $1.2 \times 10^{13} \text{ cm}^{-3}$ . In the image a thermal component is not discernable. A careful analysis of the profile provides us with a lower bound of 90% for the condensate fraction. For the chemical potential of the BEC, we obtain  $\mu = \frac{1}{2}m_{\text{mol}}\omega_z^2 z_{\text{TF}}^2 = k_B \times 130$  nK. Here  $m_{\text{mol}} = 2m$  is the mass of the  $^6\text{Li}$  dimer. Based on the prediction  $a_{\text{mol}} = 0.6a = 650a_0$ , the calculated chemical potential of  $\frac{1}{2}(15\hbar^2 N_{\text{mol}} \bar{\omega}^3 a_{\text{mol}} \sqrt{m_{\text{mol}}})^{2/5} = k_B \times 155$  nK is consistent

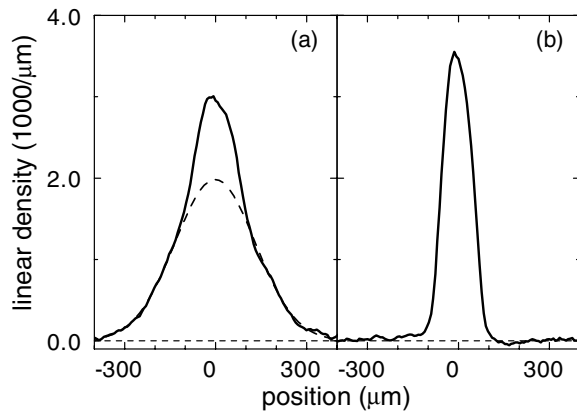


FIG. 1. Axial density profiles of a partially condensed (a) and fully condensed (b) molecular cloud. The profiles are derived from averaging seven *in situ* images taken at a magnetic field of  $B = 676$  G after evaporation at the production field of 764 G. (a) When the evaporation ramp is stopped with  $4 \times 10^5$  molecules at a final laser power of 28 mW, a characteristic bimodal distribution is observed with a condensate fraction of  $\sim 20\%$ . The dashed curve shows Gaussian fit to the thermal fraction. (b) At a final laser power of 3.8 mW, an essentially pure condensate of  $2 \times 10^5$  molecules is obtained.

with the observed value of  $k_B \times 130$  nK considering the experimental uncertainty. In particular, the particle number is calibrated to within a factor of 1.5 through fluorescence imaging [10].

The pure molecular BEC at 764 G serves as our starting point for exploring the crossover to the degenerate Fermi gas. Before we change the magnetic field, we first adiabatically increase the trap power from 3.8 to 35 mW in a 200-ms exponential ramp. The higher power provides a trap depth of  $\sim k_B \times 2 \mu\text{K}$  for the atoms, which is roughly a factor of 2 above the Fermi energy, and avoids spilling of the Fermi gas produced at magnetic fields above the resonance [1]. The compression increases the peak density of the condensate by a factor of 2.5. All further experiments reported here are performed in the recompressed trap with  $\omega_r/2\pi = 640$  Hz and  $\omega_z/2\pi = (600B/\text{kG} + 32)^{1/2}$  Hz.

We measure the lifetime of the BEC in the compressed trap at 764 G to be 40 s. The peak molecular density is estimated to be  $n_{\text{mol}} = (15/8\pi)(\omega_r/\omega_z)^2 N_{\text{mol}}/z_{\text{TF}}^3 = 1.0(5) \times 10^{13} \text{ cm}^{-3}$ . This provides an upper bound for the binary loss coefficient of  $1 \times 10^{-14} \text{ cm}^3/\text{s}$ , and is consistent with previous measurements in thermal molecular gases [8,10] together with the predicted scattering length scaling [20] and the factor-of-2 suppression of binary collision loss in a condensate.

For exploring the crossover to a Fermi gas we apply slow magnetic-field ramps. To ensure their adiabaticity, we performed several test experiments. In one series of measurements we ramped up the field from 764 to 882 G and back to 764 G with variable ramp speed. This converts the molecular BEC into a strongly interacting Fermi gas and vice versa. Therefore substantial changes are expected in the cloud size. After the up-and-down ramp, we observe an axial oscillation of the ensemble at the quadrupolar excitation frequency [1,22]. This collective oscillation is the lowest excitation mode of the system and is thus sensitive to nonadiabaticity effects. We observe axial oscillations with relative amplitudes of  $> 5\%$  for ramp speeds above 1.2 G/ms. For ramp speeds of 0.6 G/ms and lower, the axial oscillation was no longer visible.

We also checked the reversibility of the crossover process by linearly ramping up the magnetic field from 764 to 1176 G and down again to 764 G within 2 s (ramp speed of  $\pm 0.41$  G/ms). In Fig. 2, we compare the axial profile taken after this ramp (●) with the corresponding profile obtained after 2 s at fixed magnetic field (○). The comparison does not show any significant deviation. This highlights that the conversion into a Fermi gas and its back-conversion into a molecular BEC are lossless and proceed without noticeable increase of the entropy.

To investigate the spatial profile of the trapped gas in different regimes, we start with the molecular BEC at 764 G and change the magnetic field in 1-s linear ramps to final values between 740 and 1440 G. Images are then taken at the final ramp field. To characterize the size of



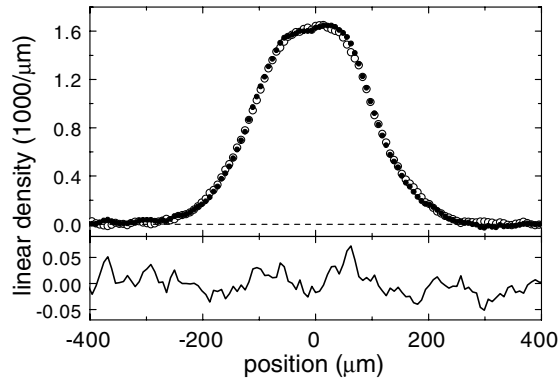


FIG. 2. Axial profile of a molecular BEC at 764 G (●) after its conversion into a Fermi gas at 1176 G and subsequent back conversion. Two 1-s magnetic field ramps are applied in this reversible process. For reference we show the corresponding profile observed without the magnetic field ramp (○). The density profiles are obtained by averaging over 50 images. The difference shown in the lower graph is consistent with the drifts of a residual interference pattern in the images.

the trapped gas, we determine the root-mean-squared axial size  $z_{\text{rms}}$ . This rms size is related to the axial radius  $z_{\text{TF}}$  by  $z_{\text{rms}} = z_{\text{TF}}/\sqrt{7}$  in the case of a pure BEC in the Thomas-Fermi limit and by  $z_{\text{rms}} = z_{\text{TF}}/\sqrt{8}$  in the cases of zero-temperature noninteracting or strongly interacting Fermi gases [23].

Figure 3(b) shows how the measured axial size  $z_{\text{rms}}$  changes with the magnetic field. For comparison, Fig. 3(a) displays the magnetic-field dependence of the atomic scattering length  $a$ . Up to 950 G, an increase in  $z_{\text{rms}}$  is due to the crossover from the molecular BEC to the degenerate Fermi gas. For higher magnetic fields, the axial cloud size of the Fermi gas shrinks with  $B$  as the axial magnetic confinement increases ( $\omega_z \propto \sqrt{B}$ ).

For the following discussions, we normalize the observed size to the one expected for a noninteracting Fermi gas. In particular, this removes the explicit trap dependence. In Fig. 3(c), we show the normalized axial size  $\zeta = z_{\text{rms}}/z_0$ , where  $z_0 = (E_F/4m\omega_z^2)^{1/2}$  is the rms axial size of a noninteracting zero-temperature Fermi gas with  $N = 4 \times 10^5$  atoms. The Fermi energy  $E_F = \hbar^2 k_F^2/2m = \hbar\bar{\omega}(3N)^{1/3}$  amounts to  $k_B \times 1.1 \mu\text{K}$  at 850 G, and the Fermi wave number  $k_F$  corresponds to a length scale of  $k_F^{-1} = 3600a_0$ .

Below the Feshbach resonance, the observed dependence of the cloud size agrees well with the mean-field behavior of a BEC in the Thomas-Fermi limit. In this regime, the normalized size is given by  $\zeta = 0.688(a_{\text{mol}}/a)^{1/5}(E_F/E_b)^{1/10}$ , where  $E_b = \hbar^2/ma^2$  is the molecular binding energy. Figure 3(c) shows the corresponding curve (solid line) calculated with  $a_{\text{mol}}/a = 0.6$  [20]. This BEC limit provides a reasonable approximation up to  $\sim 800$  G; here the molecular gas interaction parameter is  $n_{\text{mol}}a_{\text{mol}}^3 \approx 0.08$ . Alternatively, the interaction strength can be expressed as  $k_F a \approx 1.9$ .

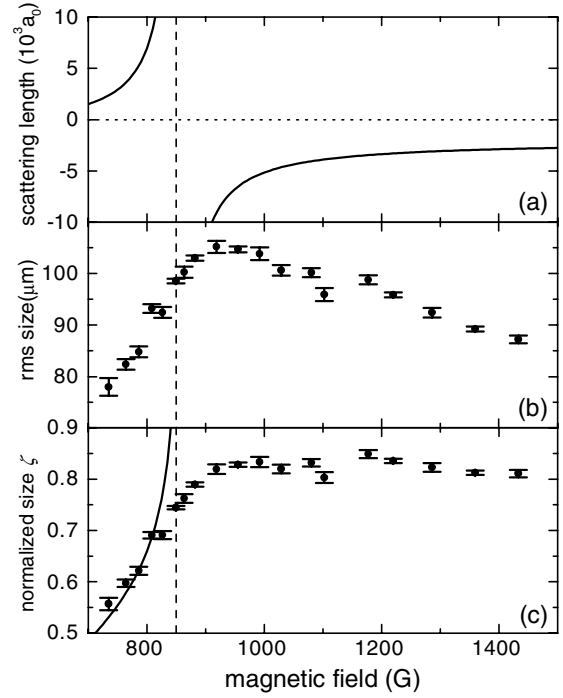


FIG. 3. Axial cloud size measurements across the Feshbach resonance. In (a) the atomic scattering length  $a$  is shown according to [17]; the resonance at 850 G is marked by the vertical dashed line. The data in (b) display the measured rms cloud sizes. In (c), the same data are plotted after normalization to a noninteracting Fermi gas. The solid line shows the expectation from BEC mean-field theory with  $a_{\text{mol}} = 0.6a$ . In (b) and (c), the error bars show the statistical error of the size measurements from typically five individual images.

The crossover to the Fermi gas is observed in the vicinity of the Feshbach resonance between 800 and 950 G; here  $\zeta$  smoothly increases with the magnetic field until it levels off at 950 G, where the interaction strength is characterized by  $k_F a \approx -1.9$ . Our results suggest that the crossover occurs within the range of  $-0.5 \leq (k_F a)^{-1} \leq 0.5$ , which corresponds to the strongly interacting regime. The smoothness of the crossover is further illustrated in Fig. 4. Here the spatial profiles near the resonance show the gradually increasing cloud size without any noticeable new features.

On resonance a universal regime is realized [12–14], where scattering is fully governed by unitarity and the scattering length drops out of the description. Here the normalized cloud size can be written as  $\zeta = (1 + \beta)^{1/4}$ , where  $\beta$  parametrizes the mean-field contribution to the chemical potential in terms of the local Fermi energy [14]. At 850 G our measured value of  $\zeta = 0.75 \pm 0.07$  provides  $\beta = -0.68_{-0.10}^{+0.13}$ . Here the total error range includes all statistic and systematic uncertainties with the particle number giving the dominant contribution. Note that the uncertainty in the Feshbach resonance position is not included in the errors [18]. Our experimental results reveal a stronger interaction effect than previous measurements that yielded  $\beta = -0.26(7)$  at  $T = 0.15T_F$  [14]

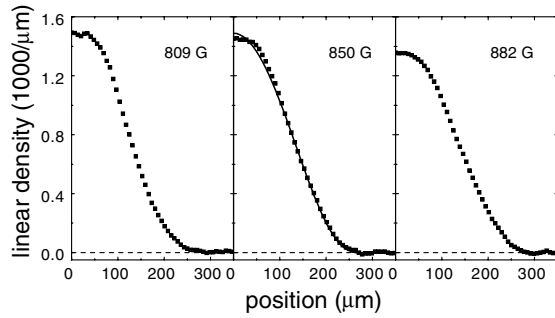


FIG. 4. Observed axial density profiles near the Feshbach resonance, averaged over 50 images and symmetrized to reduce imaging imperfections. The rms cloud sizes are 93, 99, and 103  $\mu\text{m}$  at  $B = 809, 850,$  and  $882$  G, respectively. For comparison, the on-resonance data at 850 G are shown together with a fit by the expected profile  $\propto (1 - z^2/z_{\text{TF}}^2)^{5/2}$ . The small deviation near the top is due to a residual interference pattern in the images.

and  $\beta \approx -0.3$  at  $T = 0.6T_F$  [15]. Our value of  $\beta$  lies within the range of the theoretical predictions for a zero-temperature Fermi gas:  $-0.67$  [12,24],  $-0.43$  [24], and, in particular,  $-0.56(1)$  from a recent quantum Monte Carlo calculation [25].

Beyond the Feshbach resonance, in the Fermi gas regime above 950 G, we observe an essentially constant normalized cloud size of  $\zeta = 0.83 \pm 0.07$ . In this regime, the interaction parameter  $k_F a$  is calculated to vary between  $-2$  (at 950 G) and  $-0.8$  (at 1440 G), which allows us to estimate  $\zeta$  to vary between 0.90 and 0.95 based on the interaction energy calculations in Ref. [12]. Our observed values are somewhat below this expectation, which requires further investigation.

In summary, we have demonstrated the smooth crossover from a molecular condensate of  $^6\text{Li}$  dimers to an atomic Fermi gas. Since the conversion is adiabatic and reversible, the temperature of the Fermi gas can be estimated from the conservation of entropy [11]. Our high condensate fraction of  $> 90\%$  suggests a very small entropy which in the Fermi gas limit corresponds to an extremely low temperature of  $k_B T < 0.04E_F$ . In this scenario, superfluidity can be expected to extend from the molecular BEC regime into the strongly interacting Fermi gas regime above the Feshbach resonance where  $k_F a \lesssim -0.8$ . Our experiment thus opens up intriguing possibilities to study atomic Cooper pairing and superfluidity in resonant quantum gases.

We thank G.V. Shlyapnikov, W. Zwerger, and S. Stringari and his group for very useful discussions. We acknowledge support by the Austrian Science Fund (FWF) within SFB 15 (project part 15) and by the European Union in the frame of the Cold Molecules TMR Network under Contract No. HPRN-CT-2002-00290. C.C. thanks the FWF for financial support.

- [1] S. Jochim *et al.*, Science **302**, 2101 (2003); published online 13 November 2003 ([www.sciencemag.org/cgi/content/abstract/1093280v1](http://www.sciencemag.org/cgi/content/abstract/1093280v1)).
- [2] M. Greiner, C. A. Regal, and D. S. Jin, Nature (London) **426**, 537 (2003).
- [3] M. Zwierlein *et al.*, Phys. Rev. Lett. **91**, 250401 (2003).
- [4] T. Bourdel *et al.*, cond-mat/0403091.
- [5] A. J. Leggett, in *Modern Trends in the Theory of Condensed Matter*, edited by A. Pekalski and R. Przystawa (Springer-Verlag, Berlin, 1980); P. Nozières and S. Schmitt-Rink, J. Low Temp. Phys. **59**, 195 (1985); M. Drechsler and W. Zwerger, Ann. Phys. (Leipzig) **1**, 15 (1992); E. Timmermans, K. Furuya, P. W. Milonni, and A. K. Kerman, Phys. Lett. A **285**, 228 (2001); M. Holland, S. J. M. F. Kokkelmans, M. L. Chiofalo, and R. Walser, Phys. Rev. Lett. **87**, 120406 (2001); Y. Ohashi and A. Griffin, Phys. Rev. Lett. **89**, 130402 (2002); R. Combescot, Phys. Rev. Lett. **91**, 120401 (2003); A. Perali, P. Pieri, and G. C. Strinati, Phys. Rev. A **68**, 031601(R) (2003); J. Stajic *et al.*, cond-mat/0309329.
- [6] E. Tiesinga, B. J. Verhaar, and H. T. C. Stoof, Phys. Rev. A **47**, 4114 (1993); S. Inouye *et al.*, Nature (London) **392**, 151 (1998).
- [7] C. A. Regal, C. Ticknor, J. L. Bohn, and D. S. Jin, Nature (London) **424**, 47 (2003).
- [8] J. Cubizolles *et al.*, Phys. Rev. Lett. **91**, 240401 (2003).
- [9] K. E. Strecker, G. B. Partridge, and R. G. Hulet, Phys. Rev. Lett. **91**, 080406 (2003).
- [10] S. Jochim *et al.*, Phys. Rev. Lett. **91**, 240402 (2003).
- [11] L. D. Carr, G. V. Shlyapnikov, and Y. Castin, cond-mat/0308306.
- [12] H. Heiselberg, Phys. Rev. A **63**, 043606 (2001).
- [13] T.-L. Ho, Phys. Rev. Lett. **92**, 090402 (2004).
- [14] K. M. O'Hara *et al.*, Science **298**, 2179 (2002); M. E. Gehm *et al.*, Phys. Rev. A **68**, 011401 (2003).
- [15] T. Bourdel *et al.*, Phys. Rev. Lett. **91**, 020402 (2003).
- [16] M. Houbiers, H. T. C. Stoof, W. McAlexander, and R. Hulet, Phys. Rev. A **57**, R1497 (1998).
- [17] K. M. O'Hara *et al.*, Phys. Rev. A **66**, 041401(R) (2002).
- [18] The resonance position is uncertain within a few 10 G.
- [19] C. Chin and R. Grimm, cond-mat/0309078.
- [20] D. S. Petrov, C. Salomon, and G. V. Shlyapnikov, cond-mat/0309010.
- [21] S. Giorgini, L. P. Pitaevskii, and S. Stringari, Phys. Rev. A **54**, R4633 (1996).
- [22] S. Stringari, Phys. Rev. Lett. **77**, 2360 (1996).
- [23] We fit the density profiles with the function  $\rho(z) = \rho_0(1 - z^2/z_r^2)^\alpha$ , where  $\rho_0$ ,  $z_r$ , and  $2 \leq \alpha \leq 2.5$  are free parameters. This function interpolates between the density profile of a pure BEC in the Thomas-Fermi limit with  $\alpha = 2$  and a zero-temperature noninteracting or strongly interacting Fermi gas with  $\alpha = 2.5$ . The rms cloud size  $z_{\text{rms}}$  is obtained from  $z_r$  and  $\alpha$  by  $z_{\text{rms}} = z_r/\sqrt{3 + 2\alpha}$ .
- [24] G. A. Baker, Phys. Rev. C **60**, 054311 (1999).
- [25] J. Carlson, S.-Y. Chang, V. R. Pandharipande, and K. E. Schmidt, Phys. Rev. Lett. **91**, 050401 (2003).

## **Appendix H**

### **Collective Excitations of a Degenerate Gas at the BEC-BCS Crossover**



## Collective Excitations of a Degenerate Gas at the BEC-BCS Crossover

M. Bartenstein,<sup>1</sup> A. Altmeyer,<sup>1</sup> S. Riedl,<sup>1</sup> S. Jochim,<sup>1</sup> C. Chin,<sup>1</sup> J. Hecker Denschlag,<sup>1</sup> and R. Grimm<sup>1,2</sup>

<sup>1</sup>*Institut für Experimentalphysik, Universität Innsbruck, Technikerstraße 25, 6020 Innsbruck, Austria*

<sup>2</sup>*Institut für Quantenoptik und Quanteninformation, Österreichische Akademie der Wissenschaften, 6020 Innsbruck, Austria*

(Received 29 March 2004; published 19 May 2004)

We study collective excitation modes of a fermionic gas of  ${}^6\text{Li}$  atoms in the BEC-BCS crossover regime. While measurements of the axial compression mode in the cigar-shaped trap close to a Feshbach resonance confirm theoretical expectations, the radial compression mode shows surprising features. In the strongly interacting molecular BEC regime, we observe a negative frequency shift with increasing coupling strength. In the regime of a strongly interacting Fermi gas, an abrupt change in the collective excitation frequency occurs, which may be a signature for a transition from a superfluid to a collisionless phase.

DOI: 10.1103/PhysRevLett.92.203201

PACS numbers: 34.50.-s, 05.30.Fk, 32.80.Pj, 39.25.+k

The crossover from a Bose-Einstein condensate (BEC) to a Bardeen-Cooper-Schrieffer (BCS) superfluid has for decades attracted considerable attention in many-body theory [1]. Bose-Einstein condensates of molecules formed by fermionic atoms of  ${}^6\text{Li}$  and  ${}^{40}\text{K}$  [2–5] provide a unique system to experimentally explore this BEC-BCS crossover. In such ultracold gases magnetically tuned scattering resonances, known as Feshbach resonances, allow one to control and vary the interaction strength over a very broad range. Recent experiments have entered the crossover regime and yield results on the interaction strength by measuring the cloud size [6] and expansion energy [5]. Moreover, two experiments [7,8] have demonstrated the condensed nature of fermionic atom pairs in the crossover regime.

Important questions are related to superfluidity in the crossover regime [9]. When a molecular BEC is converted into an ultracold Fermi gas [6], one can expect ultralow temperatures and superfluidity to extend far into the Fermi gas regime [10]. Detection tools to probe superfluidity in this regime are therefore requested. The investigation of collective excitation modes [11] is well established as a powerful method to gain insight into the physical behavior of ultracold quantum gases in different regimes of Bose [12] and Fermi gases [13]. A recent paper [14] points out an interesting dependence of the collective frequencies in the BEC-BCS crossover of a superfluid Fermi gas. Superfluidity implies a hydrodynamic behavior which can cause substantial changes in the excitation spectrum and in general very low damping rates. However, in the crossover regime the strong interaction between the particles also results in hydrodynamic behavior in the normal, nonsuperfluid phase. Therefore the interpretation of collective modes in the BEC-BCS crossover in terms of superfluidity is not straightforward and needs careful investigation to identify the different regimes.

In this Letter, we report on measurements of fundamental collective excitation modes in the BEC-BCS crossover for various coupling strengths in the low-

temperature limit. In Ref. [2], we have already presented a first measurement of the collective excitation of a molecular BEC in the limit of strong coupling. As described previously [2,6], we work with a spin mixture of  ${}^6\text{Li}$  atoms in the two lowest internal states. For exploring different interaction regimes, we use a broad Feshbach resonance, the position of which we determined to 837(5) G [15]. The different interaction regimes can be characterized by the coupling parameter  $1/(k_F a)$ , where  $a$  represents the atom-atom scattering length and  $k_F$  is the Fermi wave number. Well below the Feshbach resonance ( $B < 700$  G), we can realize the molecular BEC regime with  $1/(k_F a) \gg 1$ . On resonance, we obtain the unitarity-limited regime of a universal fermionic quantum gas with  $1/(k_F a) = 0$  [16]. An interacting Fermi gas of atoms is realized beyond the resonance where  $1/(k_F a) < 0$ .

The starting point of our experiments is a cigar-shaped molecular BEC produced by evaporative cooling in an optical dipole trap in the same way as described in Ref. [6]. Radially the sample is confined by a 35-mW laser beam (wavelength 1030 nm) focused to a waist of 25  $\mu\text{m}$ . The radial vibration frequency is  $\omega_r \approx 2\pi \times 750$  Hz. The axial vibration frequency is  $\omega_z = 2\pi \times (601B/\text{kG} + 11)^{1/2}$  Hz, where the predominant contribution stems from magnetic confinement caused by the curvature of the Feshbach tuning field  $B$ , and a very small additional contribution arises from the weak axial optical trapping force.

For exploring collective excitations in the BEC-BCS crossover regime, we ramp the magnetic field from the evaporation field of 764 G, where the molecular BEC is formed, to fields between 676 and 1250 G within 1 s. In previous work [6], we have shown that the conversion to an atomic Fermi gas proceeds in an adiabatic and reversible way, i.e., without increase of entropy. From the condensate fraction in the BEC limit, for which we measure more than 90% [6], we can give upper bounds for the temperature in both the BEC limit and the non-interacting Fermi gas limit of  $T < 0.46T_{\text{BEC}}$  and  $T < 0.03T_F$  [10], respectively. Here  $T_{\text{BEC}}$  ( $T_F$ ) denotes the

critical temperature (Fermi temperature). With a total number of atoms  $N \approx 4 \times 10^5$  (free atoms and atoms bound to molecules) and a geometrically averaged trap frequency at 837 G of  $\bar{\omega} = (\omega_r^2 \omega_z)^{1/3} \approx 2\pi \times 230$  Hz, we calculate a Fermi energy  $E_F = \hbar^2 k_F^2 / 2m = \hbar \bar{\omega} (3N)^{1/3} = k_B \times 1.2 \mu\text{K}$  for a noninteracting cloud, where  $m$  is the mass of an atom and  $k_B$  is Boltzmann's constant.

To excite the *axial* compression mode at a given magnetic field, we increase the optical confinement in a 10-ms time interval by a factor of 1.5. The laser power is varied slow enough for the radial motion to follow adiabatically, but fast enough to induce axial oscillations. The relative amplitude of the resulting axial oscillation is kept small, typically  $\sim 10\%$ . We observe the oscillation by *in situ* imaging of the cloud [6] after a variable hold time  $t$  at constant trap parameters. To determine the collective oscillation frequency  $\Omega_z$  and the damping rate  $\Gamma_z$ , we fit a damped harmonic oscillation  $z(t) = z_0 + A_z \exp(-\Gamma_z t) \times \sin(\Omega_z t + \phi_z)$  to the observed time evolution of the cloud size, where  $z_0$ ,  $A_z$ , and  $\phi_z$  are additional fit parameters.

The measured oscillation frequencies and damping rates are shown in Fig. 1. The data are normalized to the axial trap frequency  $\omega_z$ , as determined by excitation of the axial sloshing mode. We point out that the axial confinement is harmonic because of the dominant magnetic trapping, and we can measure  $\omega_z$  with a  $10^{-3}$  precision. In the BEC limit, the measured collective fre-

quencies are in agreement with the expected  $\Omega_z/\omega_z = \sqrt{5}/2 = 1.581$  [11,17]. With increasing magnetic field, we observe a decrease in the collective excitation frequency until a minimum is reached at about 900 G, i.e., in the regime of a strongly interacting Fermi gas where  $1/(k_F a) \approx -0.5$ . With further increasing magnetic field and decreasing interaction strength, we then observe a gradual increase of the collective frequency toward  $\Omega_z/\omega_z = 2$ . The latter value is expected for a collisionless degenerate Fermi gas, where the elastic collision rate is strongly reduced by Pauli blocking. Because of the large damping rates in the transition regime between hydrodynamic and collisionless behavior, the excitation frequencies cannot be determined with high accuracy. The observed axial damping is consistent with a gradual transition between these two regimes [18].

The insets of Fig. 1 show a zoom-in of the data for the resonance region between 750 and 900 G. The collective frequency that we measure on resonance exhibits the small 2% down-shift expected for the unitarity limit ( $\Omega_z/\omega_z = \sqrt{12}/5 = 1.549$ ) [14]. For the damping rate, we observe a clear minimum at a magnetic field of 815(10) G, which is close to the resonance position. It is interesting to note that this damping minimum coincides with the recent observation of a maximum fraction of condensed fermionic atom pairs in Ref. [18]. For the minimum damping rate, we obtain the very low value of  $\Gamma_z/\omega_z \approx 0.0015$ , which corresponds to a  $1/e$  damping time of  $\sim 5$  s.

To excite the *radial* compression mode, we reduce the optical confinement for 50  $\mu\text{s}$ , which is short compared with the radial oscillation period of 1.3 ms. In this short interval the cloud slightly expands radially, and then begins to oscillate when the trap is switched back to the initial laser power. The relative oscillation amplitude is  $\sim 10\%$ . To detect the radial oscillation, we turn off the trapping laser after various delay times  $t$  and measure the radial size  $r(t)$  after 1.5 ms of expansion. The measured radial size  $r(t)$  reflects the oscillating release energy. From the corresponding experimental data, we extract the excitation frequency  $\Omega_r$  and damping  $\Gamma_r$  by fitting the radial cloud size to  $r(t) = r_0 + A_r \exp(-\Gamma_r t) \sin(\Omega_r t + \phi_r)$ , where  $r_0$ ,  $A_r$ , and  $\phi_r$  are additional fit parameters. Typical radial oscillation curves are shown in Fig. 2.

The magnetic-field dependence of the radial excitation frequency  $\Omega_r$  and the damping rate  $\Gamma_r$  is shown in Fig. 3. Here we normalize the data to the trap frequency  $\omega_r$ , which we obtain by measuring the radial sloshing mode at the given magnetic field [19]. This normalization suppresses anharmonicity effects in the measured compression mode frequency to below 3% [21]. For low magnetic fields, the measured frequency ratio approaches the BEC limit [11,22] ( $\Omega_r/\omega_r = 2$ ). With increasing magnetic field, i.e., increasing interaction strength, we observe a large down-shift of the frequency. On resonance ( $B = 837$  G), we observe  $\Omega_r/\omega_r = 1.62(2)$ . Above resonance, i.e., with the gas entering the strongly interacting Fermi

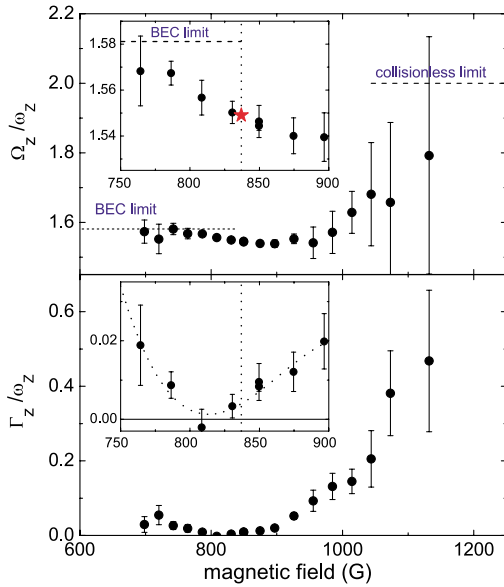


FIG. 1 (color online). Measured frequency  $\Omega_z$  and damping rate  $\Gamma_z$  of the axial compression mode, normalized to the trap frequency  $\omega_z$ . In the upper graph, the dashed lines indicate the BEC limit of  $\Omega_z/\omega_z = \sqrt{5}/2$  and the collisionless Fermi gas limit with  $\Omega_z/\omega_z = 2$ . The insets show the data in the resonance region. Here the vertical dotted line indicates the resonance position at 837(5) G. The star marks the theoretical prediction of  $\Omega_z/\omega_z = \sqrt{12}/5$  in the unitarity limit. In the lower inset, the dotted line is a third-order polynomial fit to the data.

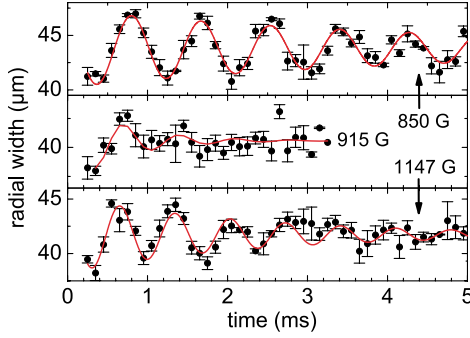


FIG. 2 (color online). Oscillations of the radial compression mode at different magnetic fields in the strongly interacting Fermi gas regime. The solid lines show fits by damped harmonic oscillations.

gas regime, the oscillation frequency further decreases until a maximum shift of almost 30% [ $\Omega_r/\omega_r = 1.42(5)$ ] is reached at  $B = 890$  G. With further increasing magnetic field, i.e., decreasing interaction strength, an abrupt change to  $\Omega_r/\omega_r \approx 2$  is observed. For  $B > 920$  G our data are consistent with a Fermi gas in the collisionless regime. The damping of the radial compression mode is small in the BEC limit and reaches a minimum close to the unitarity regime. At  $B = 910$  G, where the abrupt change occurs, we observe very strong damping (see also middle trace in Fig. 2).

We have performed further experiments to check our data on the radial compression mode for systematic effects. We have repeated the measurements after recompressing the trap to 9 times higher trap laser power

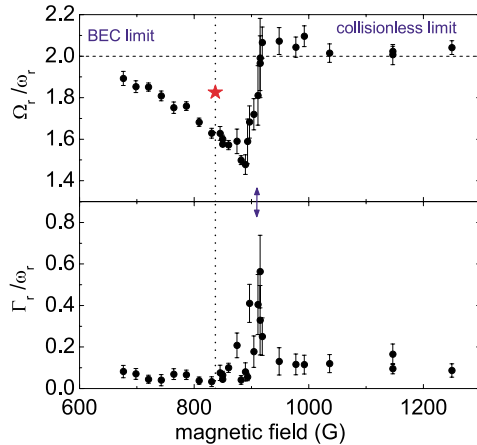


FIG. 3 (color online). Measured frequency  $\Omega_r$  and damping rate  $\Gamma_r$  of the radial compression mode, normalized to the trap frequency (sloshing mode frequency)  $\omega_r$ . In the upper graph, the dashed line indicates  $\Omega_r/\omega_r = 2$ , which corresponds to both the BEC limit and the collisionless Fermi gas limit. The vertical dotted line marks the resonance position at 837(5) G. The star indicates the theoretical expectation of  $\Omega_r/\omega_r = \sqrt{10}/3$  in the unitarity limit. A striking change in the excitation frequency occurs at  $\sim 910$  G (arrow) and is accompanied by anomalously strong damping.

( $\omega_r \approx 2.4$  kHz). The corresponding data confirm all our observations in the shallower trap. In particular, the negative frequency shift and the sudden change in the collective frequency show up in essentially the same way. The recompressed trap also allows us to eliminate a small residual anharmonicity shift from our measurement of the collective frequency at 837 G, and we obtain  $\Omega_r/\omega_r = 1.67(3)$  for the harmonic trap limit. We have also checked that the frequency of the compression mode in the resonance region does not depend on the way we prepare the ultracold gas. Direct evaporation at a fixed magnetic field, without starting from a molecular BEC, leads to the same collective frequency. Preliminary measurements at higher temperatures, however, show a trend towards smaller frequency shifts in the radial compression mode and to smoother changes of the collective frequency.

Our measurements on the radial compression mode show *three surprises*. The corresponding features, which we discuss in the following, cannot be explained on the basis of available theoretical models and suggest new physics in the BEC-BCS crossover regime.

*Surprise one.*—For a strongly interacting BEC, Ref. [23] has predicted up-shifts of the collective frequencies with increasing coupling strength based on beyond mean-field theory corrections [24]. Applying these predictions to a molecular BEC in the crossover regime, the collective excitation frequencies should follow  $\delta\Omega_i/\Omega_i = c_i\sqrt{n_m a_m^3}$  ( $i = z, r$ ), where  $n_m$  is the peak molecular number density and  $a_m = 0.6a$  [25] is the molecule-molecule scattering length. For our highly elongated trap geometry, the numerical factors are  $c_r = 5c_z = 0.727$ . In contrast to these expectations, we observe a strong frequency down-shift in the radial direction. Using the above formula to fit the first four data points, we obtain a negative coefficient of  $c_r = -1.2(3)$ . For the axial oscillation we obtain  $c_z = -0.04(5)$ . Note that a substantial down-shift in radial direction is observed even at the low magnetic field of 676 G where the molecular gas parameter is relatively small ( $n_m a_m^3 = 0.001$ ). Apparently, the beyond mean-field theory of a BEC is not adequate to describe the transition from a molecular BEC to a strongly interacting gas in the BEC-BCS crossover.

*Surprise two.*—The universal character of the strongly interacting quantum gas on resonance suggests a simple equation of state for which one expects  $\Omega_z/\omega_z = \sqrt{12/5} = 1.549$  and  $\Omega_r/\omega_r = \sqrt{10/3} = 1.826$  for the collective excitation frequencies [14]. While our measurements confirm the predicted axial frequency, we obtain a different frequency in the radial direction of  $\Omega_r/\omega_r = 1.67(3)$ .

*Surprise three.*—The abrupt change of the excitation frequency and the large damping rate are not expected in a normal degenerate Fermi gas, where the collective excitation frequency is expected to vary smoothly from the hydrodynamic regime to the collisionless one. Furthermore, for the damping rate of the radial mode in the

transition regime, a maximum value of  $\Gamma_r/\omega_r = 0.09$  is calculated in Ref. [18]. Our measured damping rate of  $\Gamma_r/\omega_r \approx 0.5$  is clearly inconsistent with this prediction for the normal (nonsuperfluid) hydrodynamic regime. However, both the sudden change of the collective frequency and a strong damping are expected for a transition from the superfluid to the normal phase [26].

In conclusion, our experiments demonstrate that the collective modes of a degenerate gas in the BEC-BCS crossover region show a pronounced dependence on the coupling strength and thus provide valuable information on the physical behavior of the system. For the axial compression mode, the frequency shift observed in the unitarity limit confirms theoretical expectations. However, the radial compression mode reveals a surprising behavior. In the strongly interacting BEC regime, the observed frequency shifts have an opposite sign as compared to expectations from beyond mean-field theory and the frequency shift on resonance is even larger than expected. The most striking feature is an abrupt change of the radial collective frequency in the regime of a strongly attractive Fermi gas where  $1/(k_F a) \approx -0.5$ . The transition is accompanied by very strong damping. The observation supports an interpretation in terms of a transition from a hydrodynamic to a collisionless phase. A superfluid scenario for the hydrodynamic case seems plausible in view of current theories on resonance superfluidity [9] and the very low temperatures provided by the molecular BEC [10]. A definite answer, however, to the sensitive question of superfluidity requires further careful investigations, e.g., on the temperature dependence of the phase transition.

We warmly thank S. Stringari for stimulating this work and for many useful discussions. We also thank W. Zwerger and M. Baranov for very useful discussions. We acknowledge support by the Austrian Science Fund (FWF) within SFB 15 (project part 15) and by the European Union in the frame of the Cold Molecules TMR Network under Contract No. HPRN-CT-2002-00290. C.C. thanks the FWF for financial support.

*Note added.*—A recent paper by John Thomas' group [27] reports on measurements of the radial compression mode in the resonance region, which show much weaker frequency shifts than we observe. This apparent discrepancy needs further investigation.

- 
- [1] A.J. Leggett, in *Modern Trends in the Theory of Condensed Matter*, edited by A. Pekalski and R. Przystawa (Springer-Verlag, Berlin, 1980); P. Nozières and S. Schmitt-Rink, *J. Low Temp. Phys.* **59**, 195 (1985); E. Timmermans, K. Furuya, P.W. Milonni, and A.K. Kerman, *Phys. Lett. A* **285**, 228 (2001); J.N. Milstein, S.J.J.M.F. Kokkelmans, and M.J. Holland, *Phys. Rev. A* **66**, 043604 (2002); Y. Ohashi and A. Griffin, *Phys. Rev.*

- Lett.* **89**, 130402 (2002); R. Combescot, *Phys. Rev. Lett.* **91**, 120401 (2003); A. Perali, P. Pieri, and G.C. Strinati, *Phys. Rev. A* **68**, 031601(R) (2003); J. Stajic *et al.*, *cond-mat/0309329*.
- [2] S. Jochim *et al.*, *Science* **302**, 2101 (2003).
- [3] M. Greiner, C.A. Regal, and D.S. Jin, *Nature (London)* **426**, 537 (2003).
- [4] M.W. Zwierlein *et al.*, *Phys. Rev. Lett.* **91**, 250401 (2003).
- [5] T. Bourdel *et al.*, *cond-mat/0403091*.
- [6] M. Bartenstein *et al.*, *Phys. Rev. Lett.* **92**, 120401 (2004).
- [7] C.A. Regal, M. Greiner, and D.S. Jin, *Phys. Rev. Lett.* **92**, 040403 (2004).
- [8] M.W. Zwierlein *et al.*, *Phys. Rev. Lett.* **92**, 120403 (2004).
- [9] M. Holland *et al.*, *Phys. Rev. Lett.* **87**, 120406 (2001).
- [10] L.D. Carr, G.V. Shlyapnikov, and Y. Castin, *Phys. Rev. Lett.* **92**, 150404 (2004).
- [11] S. Stringari, *Phys. Rev. Lett.* **77**, 2360 (1996).
- [12] L. Pitaevski and S. Stringari, *Bose-Einstein Condensation* (Clarendon, Oxford, 2003), and references therein.
- [13] G.M. Bruun and C.W. Clark, *Phys. Rev. Lett.* **83**, 5415 (1999); G.M. Bruun and B.R. Mottelson, *Phys. Rev. Lett.* **87**, 270403 (2001); A. Minguzzi and M.P. Tosi, *Phys. Rev. A* **63**, 023609 (2001).
- [14] S. Stringari, *Europhys. Lett.* **65**, 749 (2004).
- [15] We determined the resonance position by measuring the molecular binding energy using radio-frequency spectroscopy as introduced in C.A. Regal, C. Ticknor, J.L. Bohn, and D.S. Jin, *Nature (London)* **424**, 47 (2003).
- [16] H. Heiselberg, *Phys. Rev. A* **63**, 043606 (2001).
- [17] M.-O. Mewes *et al.*, *Phys. Rev. Lett.* **77**, 988 (1996).
- [18] L. Vichi, *J. Low Temp. Phys.* **121**, 177 (2000).
- [19] We excite the radial sloshing mode by pulsed application of a vertical magnetic gradient. With increasing magnetic field and, thus, increasing radial cloud size, the anharmonicity of the Gaussian-shaped radial potential leads to a decrease of the sloshing mode frequency. For  $\omega_r/2\pi$ , we observe a corresponding decrease from 765 Hz at 676 G to 710 Hz at magnetic fields above 1.2 kG; at 837 G we obtain 740 Hz. Our measurements of the sloshing mode frequency agree well with an expected scaling of the lowest-order anharmonicity correction with the squared cloud size [20].
- [20] S. Stringari (private communication).
- [21] The anharmonicity corrections to frequencies of both the compression mode ( $\Omega_r$ ) and the sloshing mode ( $\omega_r$ ) scale in the same way with the increasing cloud size with a slightly larger prefactor for the compression mode [20]. Our normalization  $\Omega_r/\omega_r$  reduces the anharmonicity effect by typically a factor of 5.
- [22] F. Chevy *et al.*, *Phys. Rev. Lett.* **88**, 250402 (2002).
- [23] L. Pitaevski and S. Stringari, *Phys. Rev. Lett.* **81**, 4541 (1998).
- [24] T.D. Lee, K.W. Huang, and C.N. Yang, *Phys. Rev.* **106**, 1135 (1957).
- [25] D.S. Petrov, C. Salomon, and G.V. Shlyapnikov, *cond-mat/0309010*.
- [26] M.A. Baranov and D.S. Petrov, *Phys. Rev. A* **62**, 041601 (2000).
- [27] J. Kinast *et al.*, *Phys. Rev. Lett.* **92**, 150402 (2004).



## **Appendix I**

### **Observation of the Pairing Gap in a Strongly Interacting Fermi Gas**



16. A. vanOtterlo *et al.*, *Phys. Rev. B* **52**, 16176 (1995).
17. G. Schmid, S. Todo, M. Troyer, A. Dorneich, *Phys. Rev. Lett.* **88**, 167208 (2002).
18. A. Görlitz, *Phys. Rev. Lett.* **87**, 130402 (2001).
19. M. Greiner, I. Bloch, O. Mandel, T. W. Hänsch, T. Esslinger, *Appl. Phys. B* **73**, 769 (2001).
20. M. T. DePue, C. McCormick, S. L. Winoto, S. Oliver, D. S. Weiss, *Phys. Rev. Lett.* **82**, 2262 (1999).
21. B. L. Tolra *et al.*, *Phys. Rev. Lett.* **92**, 190401 (2004).
22. H. Moritz, T. Söferle, M. Köhl, T. Esslinger, *Phys. Rev. Lett.* **91**, 250402 (2003).
23. T. Söferle, H. Moritz, C. Schori, M. Köhl, T. Esslinger, *Phys. Rev. Lett.* **92**, 130403 (2004).
24. B. Paredes *et al.*, *Nature* **429**, 277 (2004).
25. V. Dunjko, V. Lorent, M. Olshanii, *Phys. Rev. Lett.* **86**, 5413 (2001).
26. M. Greiner, O. Mandel, T. Esslinger, T. W. Hänsch, I. Bloch, *Nature* **415**, 39 (2002).
27. T. Kinoshita, T. Wenger, D. S. Weiss, in preparation.
28. D. J. Han, M. T. DePue, D. S. Weiss, *Phys. Rev. A* **63**, 023405 (2001).
29. M. T. DePue, S. L. Winoto, D. J. Han, D. S. Weiss, *Opt. Commun.* **180**, 73 (2000).
30. S. L. Winoto, M. T. DePue, N. E. Bramall, D. S. Weiss, *Phys. Rev. A*, **59**, R19 (1999).
31. We thank M. Olshanii, K. Gibble, and J. Banavar for

useful discussions and V. Dunjko for providing us with the exact 1D Bose gas theory curves. This work was supported by the NSF grant no. PHY-0137477.

#### Supporting Online Material

www.sciencemag.org/cgi/content/full/1100700/DC1  
SOM Text  
Table S1

25 May 2004; accepted 20 July 2004

Published online 29 July 2004;

10.1126/science.1100700

Include this information when citing this paper.

# Observation of the Pairing Gap in a Strongly Interacting Fermi Gas

C. Chin,<sup>1</sup> M. Bartenstein,<sup>1</sup> A. Altmeyer,<sup>1</sup> S. Riedl,<sup>1</sup> S. Jochim,<sup>1</sup>  
J. Hecker Denschlag,<sup>1</sup> R. Grimm<sup>1,2\*</sup>

We studied fermionic pairing in an ultracold two-component gas of <sup>6</sup>Li atoms by observing an energy gap in the radio-frequency excitation spectra. With control of the two-body interactions through a Feshbach resonance, we demonstrated the dependence of the pairing gap on coupling strength, temperature, and Fermi energy. The appearance of an energy gap with moderate evaporative cooling suggests that our full evaporation brought the strongly interacting system deep into a superfluid state.

The spectroscopic observation of a pairing gap in the 1950s marked an important experimental breakthrough in research on superconductivity (1). The gap measurements provided a key to investigating the paired nature of the particles responsible for the frictionless current in metals at very low temperatures. The ground-breaking Bardeen-Cooper-Schrieffer (BCS) theory, developed at about the same time, showed that two electrons in the degenerate Fermi sea can be coupled by an effectively attractive interaction and will form a delocalized, composite particle with bosonic character. BCS theory predicted that the gap in the low-temperature limit is proportional to the critical temperature  $T_c$  for the phase transition, in agreement with the experimental measurements. In general, the physics of superconductivity and superfluidity go far beyond the weak-coupling limit of BCS theory. In the limit of strong coupling, paired fermions form localized bosons, and the system can undergo Bose-Einstein condensation (BEC). The BCS limit and the BEC limit are connected by a smooth BCS-BEC crossover, which has been a subject of great theoretical interest for more than three decades (2–5). The formation of pairs generally represents a key ingredient of superfluidity in fermionic sys-

tems, and the gap energy is a central quantity to characterize the pairing regime.

The rapid progress in experiments with ultracold degenerate Fermi gases (6) has opened up a unique testing ground to study phenomena related to pairing and superfluidity at densities typically a billion times below the ones in usual condensed-matter systems. In cold-atom experiments, magnetically tuned scattering resonances (Feshbach resonances) serve as a powerful tool to control the two-body coupling strength in the gas (7). On the basis of such a resonance, a strongly interacting degenerate Fermi gas was recently realized (8). A major breakthrough then followed, with the creation of Bose-Einstein condensates of molecular dimers composed of fermionic atoms (9–13), which corresponds to the realization of a BEC-type superfluid in the strong coupling limit. By variation of the coupling strength, subsequent experiments (12, 14–18) began to explore the crossover to a BCS-type system. This BEC-BCS crossover is closely linked to the predicted “resonance superfluidity” (19–22) and a “universal” behavior of a Fermi gas with resonant interactions (23, 24). The observation of the condensation of atom pairs (15, 16) and measurements of collective oscillations (17, 18) support the expected superfluidity at presently attainable temperatures in Fermi gases with resonant interactions.

We prepared our ultracold gas of fermionic <sup>6</sup>Li atoms in a balanced spin-mixture of the two lowest sub-states |1> and |2> of the electronic 1s<sup>2</sup> 2s ground state, employing methods of laser

cooling and trapping and subsequent evaporative cooling (9). A magnetic field  $B$  in the range between 650 to 950 G was applied for Feshbach tuning through a broad resonance centered at the field  $B_0 \approx 830$  G. In this high-field range, the three lowest atomic levels form a triplet of states |1>, |2>, and |3>, essentially differing by the orientation of the nuclear spin ( $m_I = 1, 0, -1$ , where  $m_I$  is the nuclear magnetic quantum number). In the resonance region with  $B < B_0$ , the s-wave scattering length  $a$  for collisions between atoms in states |1> and |2> is positive. Here, two-body physics supports a weakly bound molecular state with a binding energy  $E_b = \hbar^2/(ma^2)$ , where  $\hbar$  is Planck’s constant  $h$  divided by  $2\pi$  and  $m$  is the atomic mass. Molecules formed in this state can undergo BEC (9–13). At  $B = B_0$ , the two-body interaction is resonant ( $a \rightarrow \pm\infty$ ), corresponding to a vanishing binding energy of the molecular state. Beyond the resonance ( $B > B_0$ ), the scattering length is negative ( $a < 0$ ), which leads to an effective attraction. Here, two-body physics does not support a weakly bound molecular level, and pairing can only occur because of many-body effects.

Our experimental approach (9, 14) facilitated preparation of the quantum gas in various regimes with controlled temperature, Fermi energy, and interaction strength. We performed evaporative cooling under conditions (25) in which an essentially pure molecular Bose-Einstein condensate containing  $N = 4 \times 10^5$  paired atoms could be created as a starting point for the experiments. The final laser power of the evaporation ramp allowed us to vary the temperature  $T$ . The Fermi energy  $E_F$  (Fermi temperature  $T_F = E_F/k_B$ , with Boltzmann’s constant  $k_B$ ) was controlled by a recompression of the gas, which we performed by increasing the trap laser power after the cooling process (25). We then varied the interaction strength by slowly changing the magnetic field to the desired final value. The adiabatic changes applied to the gas after evaporative cooling proceeded with conserved entropy (14). Lacking a reliable method to determine the temperature  $T$  of a deeply degenerate, strongly interacting Fermi gas in a direct way, we characterized the system by the temperature  $T'$  measured after an isentropic conversion into the BEC limit (25). For

<sup>1</sup>Institut für Experimentalphysik, Universität Innsbruck, Technikerstraße 25, 6020 Innsbruck, Austria.

<sup>2</sup>Institut für Quantenoptik und Quanteninformation, Österreichische Akademie der Wissenschaften, 6020 Innsbruck, Austria.

\*To whom correspondence should be addressed. E-mail: rudolf.grimm@uibk.ac.at

a deeply degenerate Fermi gas, the true temperature  $T$  is substantially below our observable  $T'$  (25, 26), but a general theory for this relation is not yet available.

Radio-frequency (RF) spectroscopy has been introduced as a powerful tool to study interaction effects in ultracold Fermi gases (27–29). Molecular binding energies have been measured for  $^{40}\text{K}$  atoms (29), for which the potential of the method to observe fermionic pairing gap energies has also been pointed out. RF spectroscopy has been applied to  $^6\text{Li}$  atoms to study interaction effects up to magnetic fields of 750 G (28). One important observation was the absence of mean-field shifts in the strongly interacting regime. This effect can be attributed to the fact that, in the relevant magnetic-field range, all s-wave scattering processes between  $^6\text{Li}$  atoms in the states  $|1\rangle$ ,  $|2\rangle$ , and  $|3\rangle$  are simultaneously unitarity-limited. This property of  $^6\text{Li}$  is very favorable for RF spectroscopy because it suppresses shifts and broadening by mean-field effects.

We drove RF transitions from state  $|2\rangle$  to the empty state  $|3\rangle$  at  $\sim 80$  MHz and monitored the loss of atoms in state  $|2\rangle$  after weak excitation by a 1-s RF pulse, using state-selective absorption imaging (14). Our experiment was optimized to obtain a resolution of  $\sim 100$  Hz, corresponding to an intrinsic sensitivity to interaction effects on the scale of  $\sim 5$  nK, which is more than two orders of magnitude below the typical Fermi temperatures.

We recorded RF spectra for different degrees of cooling and in various coupling regimes (Fig. 1). We realized the molecular regime at  $B = 720$  G ( $a = +120$  nm). For the resonance region, we examined two different magnetic fields, because the precise resonance location  $B_0$  is not exactly known. Our two values  $B = 822$  G (16) and  $837$  G (13, 18) may be considered as lower and upper bounds for  $B_0$ . We also studied the regime beyond the resonance with a large negative scattering length at  $B = 875$  G ( $a \approx -600$  nm). Spectra taken in a “hot” thermal sample at  $T \approx 6T_F$  (where  $T_F = 15$   $\mu\text{K}$ ) show the narrow atomic  $|2\rangle \rightarrow |3\rangle$  transition line (Fig. 1, top) and serve as a frequency reference. We present our spectra as a function of the RF offset with respect to the bare atomic transition frequency.

Spectral signatures of pairing have been theoretically considered (30–34). A clear signature of the pairing process is the emergence of a double-peak structure in the spectral response as a result of the coexistence of unpaired and paired atoms. The pair-related peak is located at a higher frequency than the unpaired-atoms signal, because energy is required for pair breaking. For understanding of the spectra, both the homogeneous line shape of the pair signal (31, 33) and the inhomogeneous line broadening due to the density distribution in the harmonic trap need to be taken into account

(34). As an effect of inhomogeneity, fermionic pairing due to many-body effects takes place predominantly in the central high-density region of the trap, and unpaired atoms mostly populate the outer region of the trap where the density is low (34–36). The spectral component corresponding to the pairs thus shows a large inhomogeneous broadening in addition to the homogeneous width of the pair-breaking signal. For the unpaired atoms, the homogeneous line is narrow and the effects of inhomogeneity and mean-field shifts are negligible. These arguments explain why the RF spectra in general show a relatively sharp peak for the unpaired atoms together with a broader peak attributed to the pairs.

We observed clear double-peak structures already at  $T'/T_F = 0.5$ , which we obtained with moderate evaporative cooling down to a laser power of  $P = 200$  mW (Fig. 1, middle,  $T_F = 3.4$   $\mu\text{K}$ ). In the molecular regime  $B = 720$  G, the sharp atomic peak was well separated from the broad dissociation signal (29), which showed a molecular binding energy of  $E_b = h \times 130$  kHz  $= k_B \times 6.2$   $\mu\text{K}$ . For  $B \rightarrow B_0$ , the peaks began to overlap. In the resonance region [822 G and 837 G (Fig. 1)], we still observed a relatively narrow atomic peak at the original position together with a pair signal. For magnetic fields beyond the resonance, we could resolve the double-peak structure for fields up to  $\sim 900$  G.

For  $T'/T_F < 0.2$ , realized with a deep evaporative cooling ramp down to an optical

trap power of  $P = 3.8$  mW, we observed the disappearance of the narrow atomic peak in the RF spectra (Fig. 1, bottom,  $T_F = 1.2$   $\mu\text{K}$ ). This shows that essentially all atoms were paired. In the BEC limit (720 G), the dissociation line shape is identical to the one observed in the trap at higher temperature and Fermi energy. Here the localized pairs are molecules with a size much smaller than the mean interparticle spacing, and the dissociation signal is independent of the density. In the resonance region [822 G and 837 G (Fig. 1)], the pairing signal shows a clear dependence on density (Fermi energy), which becomes even more pronounced beyond the resonance (875 G). We attribute this to the fact that the size of the pairs becomes comparable to or larger than the interparticle spacing. In addition, the narrow width of the pair signal in this regime (Fig. 1, bottom,  $B = 875$  G) indicates a pair localization in momentum space to well below the Fermi momentum  $\hbar k_F = \sqrt{2mE_F}$  and thus a pair size exceeding the interparticle spacing.

To quantitatively investigate the crossover from the two-body molecular regime to the fermionic many-body regime, we measured the pairing energy in a range between 720 and 905 G. The measurements were performed after deep evaporative cooling ( $T'/T_F < 0.2$ ) for two different Fermi temperatures,  $T_F = 1.2$   $\mu\text{K}$  and  $T_F = 3.6$   $\mu\text{K}$  (Fig. 2). As an effective pairing gap, we defined  $\Delta\nu$  as the frequency difference between the pair-signal maximum and the bare atomic resonance. In the BEC limit, the effective

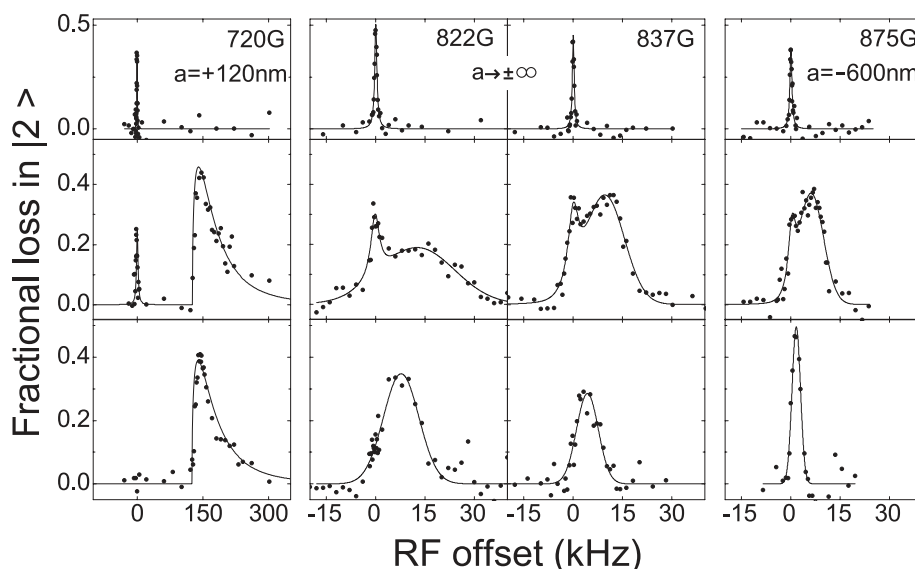


**Fig. 1.** RF spectra for various magnetic fields and different degrees of evaporative cooling. The RF offset ( $k_B \times 1$   $\mu\text{K} \approx h \times 20.8$  kHz) is given relative to the atomic transition  $|2\rangle \rightarrow |3\rangle$ . The molecular limit is realized for  $B = 720$  G (first column). The resonance regime is studied for  $B = 822$  G and  $B = 837$  G (second and third columns). The data at 875 G (fourth column) explore the crossover on the BCS side. Top row, signals of unpaired atoms at  $T' \approx 6T_F$  ( $T_F = 15$   $\mu\text{K}$ ); middle row, signals for a mixture of unpaired and paired atoms at  $T' = 0.5T_F$  ( $T_F = 3.4$   $\mu\text{K}$ ); bottom row, signals for paired atoms at  $T' < 0.2T_F$  ( $T_F = 1.2$   $\mu\text{K}$ ). The true temperature  $T$  of the atomic Fermi gas is below the temperature  $T'$ , which we measured in the BEC limit. The solid lines are introduced to guide the eye.

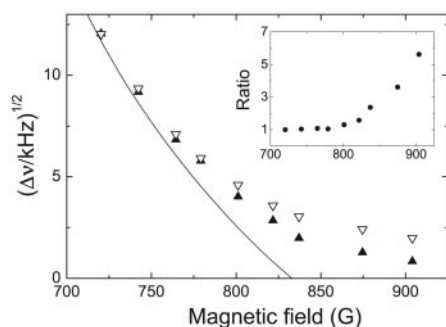


**Fig. 2.** Measurements of the effective pairing gap  $\Delta\nu$  as a function of the magnetic field  $B$  for deep evaporative cooling and two different Fermi temperatures,  $T_F = 1.2 \mu\text{K}$  (solid symbols) and  $3.6 \mu\text{K}$  (open symbols). The solid line shows  $\Delta\nu$  for the low-density limit, where it is essentially given by the molecular binding energy (25). Inset: The ratio of the effective pairing gaps measured at the two different Fermi energies.

tive pairing gap  $\Delta\nu$  simply reflects the molecular binding energy  $E_b$  (Fig. 2, solid line) (25). With an increasing magnetic field, in the BEC-BCS crossover,  $\Delta\nu$  shows an increasing deviation from this low-density molecular limit and smoothly evolves into a density-dependent many-body regime where  $\hbar\Delta\nu < E_F$ .

A comparison of the pairing energies at the two different Fermi energies (Fig. 2, inset) provides further insight into the nature of the pairs. In the BEC limit,  $\Delta\nu$  is solely determined by  $E_b$  and thus does not depend on  $E_F$ . In the universal regime on resonance,  $E_F$  is the only energy scale, and we indeed observed the effective pairing gap  $\Delta\nu$  to increase linearly with the Fermi energy. We found a corresponding relation  $\hbar\Delta\nu \approx 0.2 E_F$ . Beyond the resonance, where the system is expected to change from a resonant to a BCS-type behavior,  $\Delta\nu$  was found to depend more strongly on the Fermi energy and the observed gap ratio further increased. We interpret this in terms of the increasing BCS character of pairing, for which an exponential dependence  $\hbar\Delta\nu/E_F \propto \exp(-\pi/2k_F|a|)$  is expected.

In a further series of measurements (Fig. 3), we applied a controlled heating method to study the temperature dependence of the gap in a way that allowed us to keep all other parameters constant. After production of a pure molecular Bose-Einstein condensate ( $T' < 0.2T_F$ ) in the usual way, we adiabatically changed the conditions to  $B = 837 \text{ G}$  and  $T_F = 1.2 \mu\text{K}$ . We then increased the trap laser power by a factor of nine ( $T_F$  increased to  $2.5 \mu\text{K}$ ), using exponential ramps of different durations. For fast ramps, this recompression was nonadiabatic and increased the entropy. By variation of the ramp time, we explored a range from our lowest temperatures up to  $T'/T_F = 0.8$ . The emergence of the gap with decreasing temperature is clearly visible in the RF spectra (Fig. 3). The marked increase of  $\Delta\nu$  for decreasing temperature is

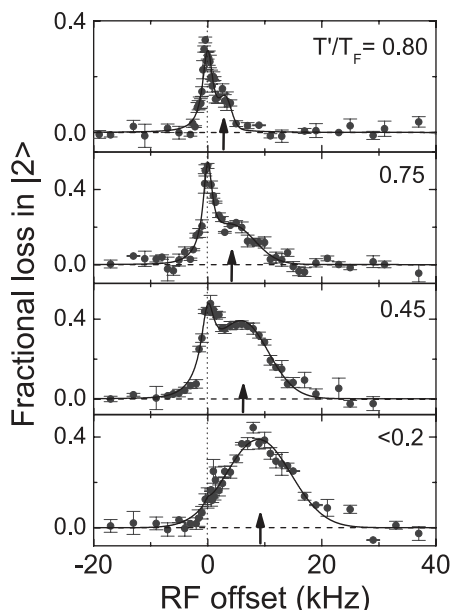


**Fig. 3.** RF spectra measured at  $B = 837 \text{ G}$  and  $T_F = 2.5 \mu\text{K}$  for different temperatures  $T'$  adjusted by controlled heating. The solid lines are fits to guide the eye, using a Lorentzian curve for the atom peak and a Gaussian curve for the pair signal. The vertical dotted line marks the atomic transition, and the arrows indicate the effective pairing gap  $\Delta\nu$ .

in good agreement with theoretical expectations for the pairing gap energy (5).

The conditions of our experiment were theoretically analyzed for the case of resonant two-body interaction (34). The calculated RF spectra are in agreement with our experimental results and demonstrate how a double-peak structure emerges as the gas is cooled below  $T/T_F \approx 0.5$  and how the atomic peak disappears with further decreasing temperature. In particular, the work clarifies the role of the “pseudo-gap” regime (5, 22), in which pairs are formed before superfluidity is reached. According to the calculated spectra, the atomic peak disappears at temperatures well below the critical temperature for the phase-transition to a superfluid. A recent theoretical study of the BCS-BEC crossover at finite temperature (36) predicted the phase-transition to a superfluid to occur at a temperature that on resonance is only  $\sim 30\%$  below the point where pair formation sets in.

We have observed fermionic pairing already after moderate evaporative cooling. With much deeper cooling applied, the unpaired atom signal disappeared from our spectra. This observation shows that pairing takes place even in the outer region of the trapped gas where the density and the local Fermi energy are low. Our results thus strongly suggest that a resonance superfluid is formed in the central region of the trap (34). Together with the observations of resonance condensation of fermionic pairs (15, 16) and weak damping of collective excitations (17,

18), our observation of the pairing gap provides a strong case for superfluidity in experiments on resonantly interacting Fermi gases.

## References and Notes

1. M. Tinkham, *Introduction to Superconductivity* (McGraw-Hill, New York, ed. 2, 1996).
2. D. M. Eagles, *Phys. Rev.* **186**, 456 (1969).
3. A. J. Leggett, in *Modern Trends in the Theory of Condensed Matter*, A. Pekalski, R. Przystawa, Eds. (Springer-Verlag, Berlin, 1980), pp. 13–27.
4. P. Nozières, S. Schmitt-Rink, *J. Low Temp. Phys.* **59**, 195 (1985).
5. Q. Chen, J. Stajic, S. Tan, K. Levin, in preparation (available at <http://arxiv.org/abs/cond-mat/0404274>).
6. A. Cho, *Science* **301**, 750 (2003).
7. S. Inouye et al., *Nature* **392**, 151 (1998).
8. K. M. O'Hara, S. L. Hemmer, M. E. Gehm, S. R. Granade, J. E. Thomas, *Science* **298**, 2179 (2002); published online 7 Nov 2002 (10.1126/science.1079107).
9. S. Jochim et al., *Science* **302**, 2101 (2003); published online 13 November 2003 (10.1126/science.1093280).
10. M. Greiner, C. A. Regal, D. S. Jin, *Nature* **426**, 537 (2003).
11. M. W. Zwierlein et al., *Phys. Rev. Lett.* **91**, 250401 (2003).
12. T. Bourdel et al., *Phys. Rev. Lett.* **93**, 050401 (2004).
13. R. Hulet, paper presented at the Kauli Institute for Theoretical Physics Conference on Quantum Gases, Santa Barbara, CA, 10 to 14 May 2004.
14. M. Bartenstein et al., *Phys. Rev. Lett.* **92**, 120401 (2004).
15. C. A. Regal, M. Greiner, D. S. Jin, *Phys. Rev. Lett.* **92**, 040403 (2004).
16. M. W. Zwierlein et al., *Phys. Rev. Lett.* **92**, 120403 (2004).
17. J. Kinast, S. L. Hemmer, M. E. Gehm, A. Turlapov, J. E. Thomas, *Phys. Rev. Lett.* **92**, 150402 (2004).
18. M. Bartenstein et al., *Phys. Rev. Lett.* **92**, 203201 (2004).
19. M. Holland, S. J. J. M. F. Kokkelmans, M. L. Chiofalo, R. Walser, *Phys. Rev. Lett.* **87**, 120406 (2001).
20. E. Timmermans, K. Furuya, P. W. Milonni, A. K. Kerman, *Phys. Lett. A* **285**, 228 (2001).
21. Y. Ohashi, A. Griffin, *Phys. Rev. Lett.* **89**, 130402 (2002).
22. J. Stajic et al., *Phys. Rev. A* **69**, 063610 (2004).
23. H. Heiselberg, *Phys. Rev. A* **63**, 043606 (2001).
24. T.-L. Ho, *Phys. Rev. Lett.* **92**, 090402 (2004).
25. Materials and methods are available as supporting material on Science Online.
26. L. D. Carr, G. V. Shlyapnikov, Y. Castin, *Phys. Rev. Lett.* **92**, 150404 (2004).
27. C. Regal, D. Jin, *Phys. Rev. Lett.* **90**, 230404 (2003).
28. S. Gupta et al., *Science* **300**, 1723 (2003); published online 8 May 2003 (10.1126/science.1085335).
29. C. A. Regal, C. Ticknor, J. L. Bohn, D. S. Jin, *Nature* **424**, 47 (2003).
30. P. Törmä, P. Zoller, *Phys. Rev. Lett.* **85**, 487 (2000).
31. J. Kinnunen, M. Rodríguez, P. Törmä, *Phys. Rev. Lett.* **92**, 230403 (2004).
32. H. P. Büchler, P. Zoller, W. Zwerger, in preparation (available at <http://arxiv.org/abs/cond-mat/0404116>).
33. R. B. Diener, T.-L. Ho, in preparation (available at <http://arxiv.org/abs/cond-mat/0405174>).
34. J. Kinnunen, M. Rodríguez, P. Törmä, *Science* **305**, 1131; published online 22 July 2004 (10.1126/science.1100782).
35. A. Bulgac, in preparation (available at <http://arxiv.org/abs/cond-mat/0309358>).
36. A. Perali, P. Pieri, L. Pisani, G. C. Strinati, *Phys. Rev. Lett.* **92**, 220404 (2004).
37. We thank P. Törmä for a stimulating exchange of results and very useful discussions and W. Zwerger and H. P. Büchler for many stimulating discussions. Supported by the Austrian Science Fund (FWF) within special forschungsbereich 15 (project part 15) and by the European Union in the frame of the Cold Molecules Training and Mobility of Researchers Network under contract no. HPRN-CT-2002-00290. C.C. is a Lise-Meitner research fellow of the FWF.

## Supporting Online Material

[www.sciencemag.org/cgi/content/full/1100818/DC1](http://www.sciencemag.org/cgi/content/full/1100818/DC1)  
Materials and Methods  
References and Notes

27 May 2004; accepted 13 July 2004  
Published online 22 July 2004;  
10.1126/science.1100818  
Include this information when citing this paper.



# References

- [Abr97] E. R. I. Abraham, W. I. McAlexander, J. M. Gerton, R. G. Hulet, R. Côté, and A. Dalgarno, *Triplet s-wave resonance in  $^6\text{Li}$  collisions and scattering lengths of  $^6\text{Li}$  and  $^7\text{Li}$* , Phys. Rev. A **55**, R3299 (1997).
- [And95] M. H. Anderson, J. R. Ensher, M. R. Matthews, C. E. Wieman, and E. A. Cornell, *Observation of Bose-Einstein Condensation in a Dilute Atomic Vapor*, Science **269**, 198 (1995).
- [And97] M. R. Andrews, C. G. Townsend, H.-J. Miesner, D. S. Durfee, D. M. Kurn, and W. Ketterle, *Observation of Interference Between Two Bose-Einstein Condensates*, Science **275**, 637 (1997).
- [And98] B. P. Anderson and M. A. Kasevich, *Macroscopic Quantum Interference from Atomic Tunnel Arrays*, Science **282**, 1686 (1998).
- [Ari77] E. Arimondo, M. Inguscio, and P. Violino, *Experimental determination of the hyperfine structure in the alkali atoms*, Rev. Mod. Phys. **49**, 31 (1977).
- [AS01] J. R. Abo-Shaeer, C. Raman, J. M. Vogels, and W. Ketterle, *Observation of Vortex Lattices in Bose-Einstein Condensates*, Science **292**, 476 (2001).
- [Bak99] G. A. Baker, *Neutron matter model*, Phys. Rev. C **60**, 054311 (1999).
- [Bar57] J. Bardeen, L. N. Cooper, and J. R. Schrieffer, *Theory of Superconductivity*, Phys. Rev. **108**, 1175 (1957).
- [Bar04a] M. Bartenstein, *From Molecules to Cooper Pairs: Experiments in the BEC-BCS crossover*, Ph.D. thesis, Universität Innsbruck (2004), to be published.
- [Bar04b] M. Bartenstein, A. Altmeyer, S. Riedl, S. Jochim, C. Chin, J. Hecker Denschlag, and R. Grimm, *Collective excitations of a degenerate gas at the BEC-BCS crossover*, Phys. Rev. Lett. **92**, 203201 (2004).
- [Bar04c] M. Bartenstein, A. Altmeyer, S. Riedl, S. Jochim, C. Chin, J. Hecker Denschlag, and R. Grimm, *Crossover from a Molecular Bose-Einstein Condensate to a Degenerate Fermi Gas*, Phys. Rev. Lett. **92**, 120401 (2004).



## References

- [Bar04d] M. Bartenstein, A. Altmeyer, S. Riedl, R. G. S. Jochim, C. Chin, J. Hecker Denschlag, R. Grimm, A. Simoni, E. Tiesinga, C. Williams, and P. Julienne, *Precise determination of  $^6\text{Li}$  cold collision parameters by radio-frequency spectroscopy on weakly bound molecules* (2004), to be published.
- [Bou03] T. Bourdel, J. Cubizolles, L. Khaykovich, K. M. F. Magalhães, S. J. J. M. F. Kokkelmans, G. V. Shlyapnikov, and C. Salomon, *Measurement of the Interaction Energy near a Feshbach Resonance in a  $^6\text{Li}$  Fermi Gas*, Phys. Rev. Lett. **91**, 020402 (2003).
- [Bou04] T. Bourdel, L. Khaykovich, J. Cubizolles, J. Zhang, F. Chevy, M. Teichmann, L. Tarruell, S. J. J. M. F. Kokkelmans, and C. Salomon, *Experimental Study of the BEC-BCS Crossover Region in Lithium 6*, Phys. Rev. Lett. **93**, 050401 (2004).
- [Bra95] C. C. Bradley, C. A. Sackett, J. J. Tollett, and R. G. Hulet, *Evidence of Bose-Einstein Condensation in an Atomic Gas with Attractive Interactions*, Phys. Rev. Lett. **75**, 1687 (1995), *ibid.* **79**, 1170 (1997).
- [Bra97] C. C. Bradley, C. A. Sackett, and R. G. Hulet, *Bose-Einstein Condensation of Lithium: Observation of Limited Condensate Number*, Phys. Rev. Lett. **78**, 985 (1997).
- [Bre31] G. Breit and I. Rabi, *Measurement of nuclear spin*, Phys. Rev. **38**, 2082 (1931).
- [Bur99] S. Burger, K. Bongs, S. Dettmer, W. Ertmer, K. Sengstock, A. Sanpera, G. V. Shlyapnikov, and M. Lewenstein, *Dark Solitons in Bose-Einstein Condensates*, Phys. Rev. Lett. **83**, 5198 (1999).
- [Bur02] K. Burnett, P. S. Julienne, P. D. Lett, E. Tiesinga, and C. J. Williams, *Quantum encounters of the cold kind*, Nature **417**, 225 (2002).
- [Car03] J. Carlson, S.-Y. Chang, V. R. Pandharipande, and K. E. Schmidt, *Superfluid Fermi Gases with Large Scattering Length*, Phys. Rev. Lett. **91**, 050401 (2003).
- [Car04] L. D. Carr, G. Shlyapnikov, and Y. Castin, *Achieving a BCS Transition in an Atomic Fermi Gas*, Phys. Rev. Lett. **92**, 150404 (2004).
- [Che04] Q. Chen, J. Stajic, S. Tan, and K. Levin, *BCS-BEC Crossover: From High Temperature Superconductors to Ultracold Superfluids* (2004), <http://www.arxiv.org/cond-mat/0404274>.



- [Chi00] C. Chin, V. Vuletić, A. J. Kerman, and S. Chu, *High Resolution Feshbach Spectroscopy of Cesium*, Phys. Rev. Lett. **85**, 2717 (2000).
- [Chi01] C. Chin, *Cooling, Collisions and Coherence of Cold Cesium Atoms in a Trap*, Ph.D. thesis, Stanford University (2001).
- [Chi04a] C. Chin, M. Bartenstein, A. Altmeyer, S. Riedl, S. Jochim, J. Hecker Denschlag, and R. Grimm, *Observation of the pairing gap in a strongly interacting Fermi gas*, Science **305**, 1128 (2004), published online 22 July 2004; 10.1126/science.1100818.
- [Chi04b] C. Chin and R. Grimm, *Thermal equilibrium and efficient evaporation of an ultracold atom-molecule mixture*, Phys. Rev. A **69**, 033612 (2004).
- [Cho03] A. Cho, *Ultracold Atoms Spark a Hot Race*, Science **301**, 750 (2003), News Focus.
- [Cor00] S. L. Cornish, N. R. Claussen, J. L. Roberts, E. A. Cornell, and C. E. Wieman, *Stable  $^{85}\text{Rb}$  Bose-Einstein Condensates with Widely Tunable Interactions*, Phys. Rev. Lett. **85**, 1795 (2000).
- [Cub03] J. Cubizolles, T. Bourdel, S. Kokkelmans, G. Shlyapnikov, and C. Salomon, *Production of Long-Lived Ultracold  $\text{Li}_2$  Molecules from a Fermi Gas*, Phys. Rev. Lett. **91**, 240401 (2003).
- [Dal99a] F. Dalfovo, S. Giorgini, L. P. Pitaevskii, and S. Stringari, *Theory of Bose-Einstein condensation in trapped gases*, Rev. Mod. Phys. **71**, 463 (1999).
- [Dal99b] J. Dalibard, *Collisional dynamics of ultra-cold atomic gases*, in: M. Inguscio, S. Stringari, and C. E. Wieman (Eds.), *Proceedings of the International School of Physics - Enrico Fermi*, 321, IOS Press, 1999.
- [Dav95] K. B. Davis, M.-O. Mewes, M. R. Andrews, N. J. van Druten, D. S. Durfee, D. M. Kurn, and W. Ketterle, *Bose-Einstein Condensation in a Gas of Sodium Atoms*, Phys. Rev. Lett. **75**, 3969 (1995).
- [DeM99a] B. DeMarco, J. L. Bohn, J. P. Burke, Jr., M. Holland, and D. S. Jin, *Measurement of  $p$ -Wave Threshold Law Using Evaporatively Cooled Fermionic Atoms*, Phys. Rev. Lett. **82**, 4208 (1999).
- [DeM99b] B. DeMarco and D. S. Jin, *Onset of Fermi Degeneracy in a Trapped Atomic Gas*, Science **285**, 1703 (1999).

## References

- [Den00] J. Denschlag, J. E. Simsarian, D. L. Feder, C. W. Clark, L. A. Collins, J. Cubizolles, L. Deng, E. W. Hagley, K. Helmerson, W. P. Reinhardt, S. L. Rolston, B. I. Schneider, and W. D. Phillips, *Generating Solitons by Phase Engineering of a Bose-Einstein Condensate*, Science **287**, 97 (2000).
- [Die02] K. Dieckmann, C. A. Stan, S. Gupta, Z. Hadzibabic, C. H. Schunck, and W. Ketterle, *Decay of an Ultracold Fermionic Lithium Gas near a Feshbach Resonance*, Phys. Rev. Lett. **89**, 203201 (2002).
- [Don01] E. A. Donley, N. R. Claussen, S. L. Cornish, J. L. Roberts, E. A. Cornell, and C. E. Wieman, *Dynamics of collapsing and exploding Bose-Einstein condensates*, Nature **412**, 295 (2001).
- [Don02] E. A. Donley, N. R. Claussen, S. T. Thompson, and C. E. Wieman, *Atom-molecule coherence in a Bose-Einstein condensate*, Nature **417**, 529 (2002).
- [Dre83] R. Drever, J. Hall, F. V. Kowalski, J. Hough, G. Ford, A. Munley, and H. Ward, *Laser phase and frequency stabilization using an optical resonator*, Appl. Phys. B **31**, 97 (1983).
- [Dür04] S. Dür, A. Volz, T. Marte, and G. Rempe, *Observation of Molecules Produced from a Bose-Einstein Condensate*, Phys. Rev. Lett. **92**, 020406 (2004).
- [Eag69] D. M. Eagles, *Possible Pairing without Superconductivity at Low Carrier Concentrations in Bulk and Thin-Film Superconducting Semiconductors*, Phys. Rev. **186**, 456 (1969).
- [Els00] T. Elsässer, *Stehwellenfalle in einem Resonator*, diploma thesis, Max-Planck-Institut für Kernphysik, Heidelberg (2000).
- [Fed96] P. O. Fedichev, M. W. Reynolds, and G. V. Shlyapnikov, *Three-Body Recombination of Ultracold Atoms to a Weakly Bound s Level*, Phys. Rev. Lett. **77**, 2921 (1996).
- [Fes58] H. Feshbach, *A Unified Theory of Nuclear Reactions*, Ann. Phys. **5**, 337 (1958).
- [Geh03a] M. E. Gehm, *Preparation of an Optically-Trapped Degenerate Fermi Gas of  $^6\text{Li}$ : Finding the Route to Degeneracy*, Ph.D. thesis, Duke University (2003).

- [Geh03b] M. E. Gehm, S. L. Hemmer, S. R. Granade, K. M. OHara, , and J. E. Thomas, *Mechanical stability of a strongly interacting Fermi gas of atoms*, Phys. Rev. A **68**, 011401(R) (2003).
- [Ger00] J. M. Gerton, D. Strekalov, I. Prodan, and R. G. Hulet, *Direct observation of growth and collapse of a Bose-Einstein condensate with attractive interactions*, Nature **408**, 692 (2000).
- [Gio96] S. Giorgini, L. P. Pitaevskii, and S. Stringari, *Condensate fraction and critical temperature of a trapped interacting Bose gas*, Phys. Rev. A **54**, R4633 (1996).
- [GO99] D. Guéry-Odelin, F. Zambelli, J. Dalibard, and S. Stringari, *Collective oscillations of a classical gas confined in harmonic traps*, Phys. Rev. A **60**, 4851 (1999).
- [Gor61] L. P. Gorkov and T. K. Melik-Barkhudarov, *Contribution to the theory of superfluidity in an imperfect Fermi gas*, Sov. Phys. JETP **13**, 1018 (1961).
- [Gra02] S. R. Granade, M. E. Gehm, K. M. O'Hara, and J. E. Thomas, *All-Optical Production of a Degenerate Fermi Gas*, Phys. Rev. Lett. **88**, 120405 (2002).
- [Gre02] M. Greiner, O. Mandel, T. Esslinger, T. W. Hänsch, and I. Bloch, *Quantum phase transition from a superfluid to a Mott insulator in a gas of ultracold atoms*, Nature **415**, 39 (2002).
- [Gre03] M. Greiner, C. A. Regal, and D. S. Jin, *Emergence of a molecular Bose-Einstein condensate from a Fermi gas*, Nature **426**, 540 (2003), doi:10.1038/nature02199; Published online 26 November 2003.
- [Gri93] G. F. Gribakin and V. V. Flambaum, *Calculation of the scattering length in atomic collisions using the semiclassical approximation*, Phys. Rev. A **48**, 546 (1993).
- [Gri96] A. Griffin, *Conserving and gapless approximations for an inhomogeneous Bose gas at finite temperatures*, Phys. Rev. B **53**, 9341 (1996).
- [Gri00] R. Grimm, M. Weidemüller, and Y. Ovchinnikov, *Optical dipole traps for neutral atoms*, Adv. At. Mol. Opt. Phys. **42** (2000).
- [Gro61] E. P. Gross, *Structure in Quantized Vortex in Boson Systems*, Il Nuovo Cimento **20**, 454 (1961).

## References

- [Had03] Z. Hadzibabic, S. Gupta, C. A. Stan, C. H. Schunck, M. W. Zwierlein, K. Dieckmann, and W. Ketterle, *Fiftyfold Improvement in the Number of Quantum Degenerate Fermionic Atoms*, Phys. Rev. Lett. **91**, 160401 (2003).
- [Hän80] T. W. Hänsch and B. Couillaud, *Laser frequency stabilization by polarization spectroscopy of a reflecting reference cavity*, Opt. Commun. **35**, 441 (1980).
- [Hei01] H. Heiselberg, *Fermi systems with long scattering lengths*, Phys. Rev. A **63**, 043606 (2001).
- [Hen03] G. C. Hendl, *Atom - Atom Wechselwirkung in einem ultrakalten, fermionischen Gas*, diploma thesis, Universität Innsbruck (2003).
- [Her03] J. Herbig, T. Kraemer, M. Mark, T. Weber, C. Chin, H.-C. Nägerl, and R. Grimm, *Preparation of a Pure Molecular Quantum Gas*, Science **301**, 1510 (2003), published online 21 August 2003; 10.1126/science.1088876.
- [Ho04] T.-L. Ho, *Universal Thermodynamics of Degenerate Quantum Gases in the Unitarity Limit*, Phys. Rev. Lett. **92**, 090402 (2004).
- [Hol01] M. Holland, S. J. J. M. F. Kokkelmans, M. L. Chiofalo, and R. Walser, *Resonance Superfluidity in a Quantum Degenerate Fermi Gas*, Phys. Rev. Lett. **87**, 120406 (2001).
- [Hou98] M. Houbiers, H. T. C. Stoof, W. I. McAlexander, and R. G. Hulet, *Elastic and inelastic collisions of Li-6 atoms in magnetic and optical traps*, Phys. Rev. A **57**, R1497 (1998).
- [Hul04] R. Hulet, *Conversion of an Atomic Fermi Gas to a Molecular Bose Einstein Condensate* (2004).
- [Ino98] S. Inouye, M. R. Andrews, J. Stenger, H.-J. Miesner, D. M. Stamper-Kurn, and W. Ketterle, *Observation of Feshbach resonances in a Bose-Einstein condensate*, Nature **392**, 151 (1998).
- [Jin97] D. S. Jin, M. R. Matthews, J. R. Ensher, C. E. Wieman, and E. A. Cornell, *Temperature-Dependent Damping and Frequency Shifts in Collective Excitations of a Dilute Bose-Einstein Condensate*, Phys. Rev. Lett. **78**, 764 (1997).
- [Joc00] S. Jochim, *Aufbau einer Apparatur zum magnetooptischen Einfang von fermionischen Lithiumatomen*, diploma thesis, Max-Planck-Institut für Kernphysik, Heidelberg (2000).

- [Joc02] S. Jochim, M. Bartenstein, G. Hendl, J. Hecker Denschlag, R. Grimm, A. Mosk, and M. Weidemüller, *Magnetic Field Control of Elastic Scattering in a Cold Gas of Fermionic Lithium Atoms*, Phys. Rev. Lett. **89**, 273202 (2002).
- [Joc03a] S. Jochim, M. Bartenstein, A. Altmeyer, G. Hendl, S. Riedl, C. Chin, J. Hecker Denschlag, and R. Grimm, *Bose-Einstein Condensation of Molecules*, Science **301**, 2101 (2003), published online 13 November 2003; 10.1126/science.1093280.
- [Joc03b] S. Jochim, M. Bartenstein, A. Altmeyer, G. Hendl, C. Chin, J. Hecker Denschlag, and R. Grimm, *Pure Gas of Optically Trapped Molecules Created from Fermionic Atoms*, Phys. Rev. Lett. **91**, 240402 (2003).
- [Jul92] P. Julienne, A. Smith, and K. Burnett, *Theory of collisions between laser-cooled atoms*, Advances in Atomic, Molecular, and Optical Physics **30**, 141 (1992).
- [Kaw93] J. Kawanaka, K. Shimizu, H. Takuma, and F. Shimizu, *Quadratic collisional loss rate of a  $^7\text{Li}$  trap*, Phys. Rev. A **48**, R883 (1993).
- [Ket99] W. Ketterle, D. S. Durfee, and D. M. Stamper-Kurn, *Making, probing and understanding Bose-Einstein condensates*, in: M. Inguscio, S. Stringari, and C. E. Wieman (Eds.), *Proceedings of the International School of Physics - Enrico Fermi*, 67, IOS Press, 1999.
- [Kha02] L. Khaykovich, F. Schreck, G. Ferrari, T. Bourdel, J. Cubizolles, L. D. Carr, Y. Castin, and C. Salomon, *Formation of a Matter-Wave Bright Soliton*, Science **296**, 1290 (2002).
- [Kin04a] J. Kinast, S. L. Hemmer, M. E. Gehm, A. Turlapov, and J. E. Thomas, *Evidence for Superfluidity in a Resonantly Interacting Fermi Gas*, Phys. Rev. Lett. **92**, 150402 (2004).
- [Kin04b] J. Kinnunen, M. Rodriguez, and P. Törmä, *Pairing gap and in-gap excitations in trapped fermionic superfluids*, Science **305**, 1131 (2004), published online 22 July 2004; 10.1126/science.1100782.
- [Kok04] S. J. J. M. F. Kokkelmans, G. V. Shlyapnikov, and C. Salomon, *Degenerate atom-molecule mixture in a cold Fermi gas*, Phys. Rev. A **69**, 031602(R) (2004).
- [Lan77] L. D. Landau and E. M. Lifshitz, *Quantum Mechanics: Non-Relativistic Theory*, Pergamon Press, Oxford, 1977, 3rd ed.

## References

- [Lan80] L. D. Landau and E. M. Lifshitz, *Statistical Physics, Part I*, Pergamon Press, Oxford, 1980, 3rd ed.
- [Leg80] A. J. Leggett, *Diatomic Molecules and Cooper Pairs*, in: A. Pekalski and R. Przystawa (Eds.), *Modern Trends in the Theory of Condensed Matter*, 13–27, Springer-Verlag, Berlin, 1980.
- [Lid92] D. R. Lide (Ed.), *Handbook of Chemistry and Physics*, CRC Press, Inc., 1992, 73rd ed.
- [Lof02] T. Loftus, C. A. Regal, C. Ticknor, J. L. Bohn, and D. S. Jin, *Resonant Control of Elastic Collisions in an Optically Trapped Fermi Gas of Atoms*, Phys. Rev. Lett. **88**, 173201 (2002).
- [Lui96] O. J. Luiten, M. W. Reynolds, and J. T. M. Walraven, *Kinetic theory of the evaporative cooling of a trapped gas*, Phys. Rev. A **53**, 381 (1996).
- [Mar04] B. Marcelis, E. G. M. van Kempen, B. J. Verhaar, and S. J. J. M. F. Kokkelmans, *Feshbach resonances with large background scattering length: interplay with open-channel resonances*, Phys. Rev. A **70**, 012701 (2004).
- [Min97] A. Minguzzi, S. Conti, and M. P. Tosi, *The internal energy and condensate fraction of a trapped interacting Bose gas*, J. Phys., Condens. Matter **9**, L33 (1997).
- [Mod03] G. Modugno, F. Ferlaino, R. Heidemann, G. Roati, and M. Inguscio, *Production of a Fermi gas in an optical lattice*, Phys. Rev. A **66**, 011601 (2003).
- [Mon93] C. R. Monroe, E. A. Cornell, C. A. Sackett, C. J. Myatt, and C. E. Wieman, *Measurement of Cs-Cs Elastic Scattering at  $T = 30\mu K$* , Phys. Rev. Lett. **70**, 414 (1993).
- [Mor01] H. Moritz, *Fermionisches Lithium in einer Resonatordipolfalle*, diploma thesis, Max-Planck-Institut für Kernphysik, Heidelberg (2001).
- [Mos01] A. Mosk, S. Jochim, H. Moritz, T. Elsässer, M. Weidemüller, and R. Grimm, *Resonator-Enhanced Optical Dipole Trap for Fermionic Lithium Atoms*, Opt. Lett. **26**, 1837 (2001).
- [Nar98] M. Naraschewski and D. M. Stamper-Kurn, *Analytical description of a trapped semi-ideal Bose gas at finite temperature*, Phys. Rev. A **58**, 2423 (1998).

- [O'H01] K. M. O'Hara, M. E. Gehm, S. R. Granade, and J. E. Thomas, *Scaling laws for evaporative cooling in time-dependent optical traps*, Phys. Rev. A **64**, 051403(R) (2001).
- [O'H02a] K. M. O'Hara, S. L. Hemmer, M. E. Gehm, S. R. Granade, and J. E. Thomas, *Observation of a Strongly Interacting Degenerate Fermi Gas of Atoms*, Science **298**, 2179 (2002).
- [O'H02b] K. M. O'Hara, S. L. Hemmer, S. R. Granade, M. E. Gehm, J. E. Thomas, V. Venturi, E. Tiesinga, and C. J. Williams, *Measurement of the zero crossing in a Feshbach resonance of fermionic  $^6\text{Li}$* , Phys. Rev. A **66**, 041401(R) (2002).
- [Oha02] Y. Ohashi and A. Griffin, *BCS-BEC Crossover in a Gas of Fermi Atoms with a Feshbach Resonance*, Phys. Rev. Lett. **89**, 130402 (2002).
- [Pet00] D. S. Petrov, M. Holzmann, and G. V. Shlyapnikov, *Bose-Einstein Condensation in Quasi-2D Trapped Gases*, Phys. Rev. Lett. **84**, 2551 (2000).
- [Pet01] D. S. Petrov and G. V. Shlyapnikov, *Interatomic collisions in a tightly confined Bose gas*, Phys. Rev. A **64**, 012706 (2001).
- [Pet02] C. J. Pethik and H. Smith, *Bose-Einstein Condensation in Dilute Gases*, Cambridge University Press, 2002.
- [Pet03a] D. S. Petrov, *Three-body problem in Fermi gases with short-range inter-particle interaction*, Phys. Rev. A **67**, 010703(R) (2003).
- [Pet03b] D. S. Petrov, M. A. Baranov, and G. V. Shlyapnikov, *Superfluid transition in quasi-two-dimensional Fermi gases*, Phys. Rev. A **67**, 031601(R) (2003).
- [Pet04] D. Petrov, C. Salomon, and G. Shlyapnikov, *Weakly bound dimers of fermionic atoms*, Phys. Rev. Lett. **93**, 090404 (2004).
- [Pit61] L. P. Pitaevskii, *Vortex lines in an imperfect Bose gas*, Sov. Phys. JETP **13**, 451 (1961).
- [Pit03] L. Pitaevskii and S. Stringari, *Bose-Einstein Condensation*, Oxford University Press, 2003.
- [Reg03] C. A. Regal, C. Ticknor, J. L. Bohn, and D. S. Jin, *Creation of ultracold molecules from a Fermi gas of atoms*, Nature **424**, 47 (2003).
- [Reg04] C. A. Regal, M. Greiner, and D. S. Jin, *Observation of Resonance Condensation of Fermionic Atom Pairs*, Phys. Rev. Lett. **92**, 040403 (2004).

## References

- [Rie04] S. Riedl, *Untersuchung stark wechselwirkender fermionischer Quantengase mittels Absorptionsabbildung*, diploma thesis, Universität Innsbruck (2004), to be published.
- [Sak94] J. J. Sakurai, *Modern Quantum Mechanics*, Addison-Wesley, 1994, revised ed.
- [Sch99] U. Schünemann, H. Engler, R. Grimm, M. Weidemüller, and M. Zielonkowski, *Simple scheme for tunable frequency offset locking of two lasers*, Rev. Sci. Instr. **70**, 242 (1999).
- [Sch01] F. Schreck, L. Khaykovich, K. L. Corwin, G. Ferrari, T. Bourdel, J. Cubizolles, and C. Salomon, *Quasipure Bose-Einstein Condensate Immersed in a Fermi Sea*, Phys. Rev. Lett. **87**, 080403 (2001).
- [Sch02] F. Schreck, *Mixtures of ultracold gases: Fermi sea and Bose-Einstein condensate of lithium isotopes*, PhD thesis, Ecole Normale Supérieure, Paris (2002).
- [Sin02] K. Singer, S. Jochim, M. Mudrich, A. Mosk, and M. Weidemüller, *Low-cost mechanical shutter for light beams*, Rev. Sci. Instr. **73**, 4402 (2002).
- [Ste99] J. Stenger, S. Inouye, A. P. Chikkatur, D. M. Stamper-Kurn, D. E. Pritchard, and W. Ketterle, *Bragg Spectroscopy of a Bose-Einstein Condensate*, Phys. Rev. Lett. **82**, 4569 (1999).
- [Str96] S. Stringari, *Collective Excitations of a Trapped Bose-Condensed Gas*, Phys. Rev. Lett. **77**, 2360 (1996).
- [Str02] K. E. Strecker, G. B. Partridge, A. G. Truscott, and R. G. Hulet, *Formation and propagation of matter-wave soliton trains*, Nature **417**, 150 (2002).
- [Str03] K. E. Strecker, G. B. Partridge, and R. G. Hulet, *Conversion of an Atomic Fermi Gas to a Long-Lived Molecular Bose Gas*, Phys. Rev. Lett. **91**, 080406 (2003).
- [Str04] S. Stringari, *Collective oscillations of a trapped Fermi gas near a Feshbach resonance*, Europhys. Lett. **65**, 749 (2004).
- [Sun03] H. Suno, B. D. Esry, and C. H. Greene, *Recombination of Three Ultracold Fermionic Atoms*, Phys. Rev. Lett. **90**, 053202 (2003).
- [Tie93] E. Tiesinga, B. J. Verhaar, and H. T. C. Stoof, *Threshold and resonance phenomena in ultracold ground-state collisions*, Phys. Rev. A **47**, 4114 (1993).



- [Tim97] E. Timmermans, P. Tommasini, and K. Huang, *Variational Thomas-Fermi theory of a nonuniform Bose condensate at zero temperature*, Phys. Rev. A **55**, 3645 (1997).
- [Tim01] E. Timmermans, K. Furuya, P. W. Milonni, and A. K. Kerman, *Prospect of creating a composite Fermi-Bose superfluid*, Phys. Lett. A **285**, 228 (2001).
- [Tru01] A. G. Truscott, K. E. Strecker, W. I. McAlexander, G. B. Partridge, and R. G. Hulet, *Observation of Fermi Pressure in a Gas of Trapped Atoms*, Science **291**, 2570 (2001).
- [Ven01] V. Venturi, E. Tiesinga, and C. Williams (2001), private communication; this calculation was constrained by the zero crossing of the scattering length at 530 G, resulting in a resonance position of 856 G.
- [Web03] T. Weber, J. Herbig, M. Mark, H.-C. Nägerl, and R. Grimm, *Three-body recombination at large scattering lengths in an ultracold atomic gas*, Phys. Rev. Lett. **91**, 123201 (2003).
- [Wei99] J. Weiner, V. S. Bagnato, S. Zilio, and P. S. Julienne, *Experiments and theory in cold and ultracold collisions*, Rev. Mod. Phys. **71** (1999).
- [Xu01] G. Xu, *Manipulation and Quantum Control of Ultracold Atoms and Molecules for Precision Measurements*, Ph.D. thesis, University of Texas, Austin (2001).
- [Xu03] K. Xu, T. Mukaiyama, J. R. Abo-Shaeer, J. K. Chin, D. E. Miller, and W. Ketterle, *Formation of Quantum-Degenerate Sodium Molecules*, Phys. Rev. Lett. **91**, 210402 (2003).
- [Yan96] Z.-C. Yan, J. F. Babb, A. Dalgarno, and G. W. F. Drake, *Variational calculations of dispersion coefficients for interactions among H, He, and Li atoms*, Phys. Rev. A **54**, 2824 (1996).
- [Zwi03] M. W. Zwierlein, C. A. Stan, C. H. Schunck, S. M. F. Raupach, S. Gupta, Z. Hadzibabic, and W. Ketterle, *Observation of Bose-Einstein Condensation of Molecules*, Phys. Rev. Lett. **91**, 250401 (2003).
- [Zwi04] M. Zwierlein, C. A. Stan, C. H. Schunck, S. M. F. Raupach, A. J. Kerman, and W. Ketterle, *Condensation of Pairs of Fermionic Atoms near a Feshbach Resonance*, Phys. Rev. Lett. **92**, 120403 (2004).



## Thanks!!!

This thesis would not have been realized without the help of a large number of people for whom I would like to express my gratitude here.

First of all, I would like to thank my advisor, Rudi Grimm who guided me through this thesis. Without all the great ideas he contributed throughout my thesis work we could not have come so far.

It all started in January 1999 when Rudi and Matthias Weidemüller were courageous enough to give me the chance to start the lithium-6 project with my diploma thesis at the Max-Planck-Institut für Kernphysik in Heidelberg. Later in the year, I was joined by Thilo Elsässer as a diploma student and by Allard Mosk as a postdoc. During his thesis Thilo designed and set up the first version of our optical resonator that is used now to trap large numbers of ultracold lithium atoms. At the beginning of my PhD thesis work we had our first operating  $^6\text{Li}$  magneto-optical trap and Henning Moritz joined our small team. During his diploma thesis we struggled hard and spent many nights in the lab to achieve a decent lifetime in our resonator enhanced dipole trap which was finally achieved with a new, ultrastable Nd:YAG laser. During all the time that I spent in Heidelberg and way beyond that time, Allard contributed tremendously to the success of the experiment. I learned a lot from him and I was always amazed about how many ideas he would come up with in a single day! During all the time at the Max-Planck-Institut we enjoyed the generous support of Dirk Schwalm, our research director, whose door was always open.

During summer 2001 I moved to Innsbruck together with the experiment, where Johannes Hecker Denschlag and Rudi were already waiting to continue the project. In Fall 2001, I was joined by Markus Bartenstein as a second PhD student on the lithium project and since then we have formed a great and effective team. He proved his organizational skills not only as a chairman of the Young Atoms Opticians conference! We've built waterproof magnetic field coils that finally did a surprisingly good job and show no signs of ageing after more than two years. Together with Gerhard Hendl, who joined us as a diploma student we tracked down all kinds of problems that hindered us from doing great experiments. A lot of our electronics boxes carry his brand name "Chicken" (Hendl is the Tyrolean word for Chicken), and thanks to his cooling water protection system we were saved from burning coils or cooling water disasters. By early summer 2003 we had a stable experiment that allowed us to do some real physics. And when we were joined by Alexander Altmeyer as a PhD student, Cheng Chin as a postdoc, and a little later by Stefan Riedl as a diploma student, our team became almost invincible. I must not forget to also thank the U.S. immigration authorities for refusing to extend Cheng's visa to the United States, which made him join our group! I will never forget the message Cheng left in the lab after we had for the first time formed a significant amount of molecules: "Selim, the fun begins!". Yes, Cheng, you were right, after this day we never faced a major difficulty on our way to the

molecular BEC, which we achieved about half a year later. During the paper-writing that followed, Rudi was faster than all the rest of us and Johannes was by far the most critical reader who found all the important flaws before we submitted.

I owe great thanks also to all the other people in our group, Markus Hammes, Tino Weber, David Rychtarik, Marcel Mudrich and Kilian Singer started their PhD work with me in Heidelberg. Hanns-Christoph Nägerl, Jens Herbig and Matthias Theiss were already in Innsbruck when I joined them. Gregor Thalhammer, Bastian Engeser, Michael Mark, Klaus Winkler, Tobias Kraemer, Michael Hellwig, Peter Unterwaditzer, Karl Pilch and last but not least, Reece Geursen joined us over the years. All of them contributed a lot to the work that is presented in this thesis through sharing ideas, discussing problems, borrowing equipment and providing moral support when things went wrong.

Of course also the “non-scientific” staff of our institute supported us tremendously. Christine Götsch-Obmascher, our group’s secretary helped with all the organizational stuff and Anton Schönherr and Stefan Haslwanter did great work in the mechanical workshop.

It was always great to share the free time with my colleagues and friends, going to the mountains, snowboarding, or simply gathering for “Flugzeuge grillen” at Innsbruck’s exclusive “Hawaii beach” behind the airport. A special highlight was Johannes’ party at the Hafelekar.

Finally I would like to thank all my family for supporting me in any possible way. Without them I would not have been able to do this work.

I am most thankful to my girl friend Julika, who had to travel so many times from Heidelberg during the past three years, and who sometimes had to be quite patient when I spent all day in the lab even during weekends and when I was not really talkative on the phone. She gave me all the moral support that I needed to overcome all the crises that occurred. I’m proud of you!